Université de Lille 1 SCIENCES ET TECHNOLOGIES

iemn

HABILITATION À DIRIGER DES RECHERCHES
DE
L'UNIVERSITÉ DE LILLE 1

Spécialité : **Sciences pour l'ingénieur**

présentée par

Michaël BAUDOIN

Acoustofluidique micro-échelle

APPENDIX : PUBLICATIONS

Soutenance prévue le **16 Novembre 2015** devant le jury composé de

M.	José	**BICO**	ESPCI	Rapporteur
M.	Olivier	**BOU MATAR**	Ecole Centrale de Lille	Garant
M.	Ayache	**BOUAKAZ**	Inserm	Rapporteur
M.	Henrik	**BRUUS**	DTU	Examinateur
M.	Lionel	**BUCHAILLOT**	CNRS	Invité
M.	Benjamin	**DOLLET**	CNRS	Rapporteur
M.	Jacques	**MAGNAUDET**	CNRS	Examinateur
M.	Philippe	**PERNOD**	Ecole Centrale de Lille	Invité
M.	Stéphane	**ZALESKI**	Université Paris 6	Examinateur
M.	Farzam	**ZOUESHTIAGH**	Université Lille 1	Examinateur

An extended coupled phase theory for the sound propagation in polydisperse concentrated suspensions of rigid particles

Michael Baudoin[a)]
Institut Jean Le Rond D'Alembert (IJLRDA), UMR CNRS 7190 and Institut des NanoSciences de Paris (INSP), UMR CNRS 7588, Université Pierre et Marie Curie - Paris 6, 4 place Jussieu, 75252 Paris Cedex 05, France

Jean-Louis Thomas
INSP, CNRS and Université Pierre et Marie Curie - Paris 6, 75252 Paris Cedex 05, France

François Coulouvrat and Daniel Lhuillier
IJLRDA, CNRS and Université Pierre et Marie Curie - Paris 6, 75252 Paris Cedex 05, France

(Received 15 November 2006; revised 7 March 2007; accepted 15 March 2007)

An extension of the classical coupled phase theory is proposed to account for hydrodynamic interactions between neighboring rigid particles, which are essential to describe properly the sound propagation in concentrated suspensions. Rigorous ensemble-averaged equations are derived for each phase and simplified in the case of acoustical wave propagation. Then, closure is achieved by introducing a self-consistent scheme originally developed by Buyevich and Shchelchkova [Prog. Aerosp. Sci. **18**, 121–151 (1978)] for incompressible flows, to model the transfer terms between the two phases. This provides an alternative to the effective medium self-consistent theory developed by Spelt *et al.* [J. Fluid Mech. **430**, 51–86 (2001)] in which the suspension is considered as a whole. Here, a significantly simpler formulation is obtained in the long wavelength regime. Predictions of this self-consistent theory are compared with the classical coupled phase theory and with experimental data measuring the attenuation in concentrated suspensions of silica in water. Our calculation is shown to give a good description of the attenuation variation with volume fraction. This theory is also extended to the case of polydisperse suspensions. Finally, the link between the self-consistent theory and the different orders of the multiple scattering theory is clarified. © *2007 Acoustical Society of America.* [DOI: 10.1121/1.2723648]

PACS number(s): 43.35.Bf [AJS] Pages: 3386–3397

I. INTRODUCTION

The propagation of sound waves through dilute suspensions of different natures has been the subject of many studies since the pioneering article of Sewell[1] in 1910 who considered immovable rigid particles suspended in a gas. Several phenomena can be involved in the attenuation and dispersion of sound, depending on the particles nature and the wave frequency. In hydrosols, the acoustic damping is mainly induced by the visco-inertial terms (Lamb[2]).

To study the influence of particles on the sound propagation in suspensions, two methods have been principally developed. First, the scattering theory, also called ECAH theory based on the work of Epstein and Carhart[3] and Allegra and Hawley.[4] In this model, a spherical particle is considered and the waves propagating inside and outside the particle are decomposed into three modes: compressional, shear, and thermal ones. Potentials are expressed in terms of Bessel functions series satisfying the boundary conditions at the particle surface. Second, there is the coupled phase theory[5,6] based on the two-phase hydrodynamic equations. The primary advantage of the scattering theory is to be valid over the whole frequency range, although some difficulties arise with the series truncation due to the nonuniform convergence of the Bessel series.[7] The coupled phase theory gives a good framework to incorporate phenomena that would be difficult to include in the scattering theory such as mass transfers or chemical reactions. Moreover, it also leads to an explicit dispersion equation that is simpler to interpret physically and calculate, which can be useful when dealing with the inverse problem.

These theories agree well with experimental data in dilute suspensions, but they both neglect some parts, of the "multiple scattering" whose importance increases with concentration. The coupled phase theory inherently integrates "multiple scattering" but only at first order (cf. Sec. II C). Thus, it neglects interactions that occur when the viscous or/and thermal boundary layer of neighboring particles overlap one another. The ECAH theory was originally considering a simple superposition of each particle contribution and was therefore not considering "multiple scattering."

To incorporate the "reverberant multiple scattering" (in the sense of geometrical redirection of energy), the multiple scattering theory[8–13] has been introduced into the ECAH theory.[14]

To account for "dissipative multiple scattering," that is to say overlapping of thermal waves in the case of emulsions, Hemar *et al.*[15] have introduced a so-called "core-shell model:" the particle is surrounded by a cell of pure fluid,

a)Electronic mail: baudoin@lmm.jussieu.fr

 0001-4966/2007/121(6)/3386/12/$23.00

where the presence of the particle is rather unlikely, which is itself embedded in an effective medium. Such models show a good agreement with experiments, but they require the introduction of several unknown parameters. The first one is the radius of the pure medium cell b. Many investigators choose $b=a/\alpha_d^{1/3}$ (where a is the particle radius and α_d is the volume fraction occupied by the particles), although this value is not appropriate for randomly distributed spheres. It would be more adequate for systems in which the distance between particles is almost uniform (cf. Refs. 16 and 17). Then, the effective properties of the medium must also be introduced. In the work by Hemar *et al.* and in the article by Hipp *et al.*,[18] the volume averaged parameters are introduced, but one could also choose a different set of effective parameters. The primary advantage of the present study is that the effective properties are introduced in a consistent way. One can note that the multiple scattering theory and the "core-shell model" have been merged in the article by McClements and Hermann.[19] The results of this model have then been compared in detail with the classical coupled phase theory by Evans and Attenborough.[6]

Finally, and to the authors' knowledge, the only articles dealing with the overlapping of visco-inertial potentials are the articles by Dukhin and Goetz[20] and by Spelt *et al.*[17] The first one is the so-called cell model,[21,22] which is based on empirical grounds. Although it provides a relatively good estimation of viscous interactions between neighboring particles, there is no rigorous justification of this procedure. Moreover, it does not integrate the intrinsic (bulk) losses in the formulation. The second one, as the present work, uses the self-consistent approximation, but the suspension is considered as a whole. Its advantage is to give a theory that is valid whatever the frequency of the incident wave and the nature of the particle. The present work is limited to the long wavelength regime (LWR) but provides a simpler expression to describe the attenuation and dispersion in suspensions of rigid particles. This work also differs in the expression of the closure relations that are not limited to plane waves. These considerations will be developed in Sec. II D 4.

In this paper, we will first derive the ensemble averaged conservation equations and simplify them in the case of acoustical wave propagation. Then we will introduce the self-consistent scheme originally developed by Buyevich[23,24] for an incompressible flow and we will discuss the link between the closure assumptions introduced here in the effective medium theory (EMT), and the one introduced in the multiple scattering theory (MST). Once the semi-analytical dispersion equation is established, the results are compared to the experimental data of Hipp *et al.*[25] Finally, the equations will be extended to the case of polydisperse solutions.

II. THEORY

In the coupled phase theory, averaged conservation equations are written down separately for each phase. These equations are coupled by the transfer terms between the two phases. In the case of rigid particles in a liquid matrix, the thermal transfer and intrinsic absorption can be neglected as they are both proportional to γ_c-1, where γ_c is the specific heat ratio of the continuous phase that is almost equal to one in liquids. Thus, only the mass and momentum conservation equations are required. In this section, we will consider a monodisperse suspension of spherical rigid particles isotropically distributed.

A. Ensemble-averaged equations

The ensemble-averaged equations are calculated from the local constitutive equations of the continuous and dispersed phases by using a configurational average.[24]

If the interfaces between the two phases have no mass, one can introduce the generalized functions for density and momentum based on the "fine-grained" definition in each phase under the form

$$\begin{bmatrix} \rho' \\ \rho' \boldsymbol{v}' \end{bmatrix} = \sum_{k=c,d} \chi_k \begin{bmatrix} \rho_k' \\ \rho_k' \boldsymbol{v}_k' \end{bmatrix},$$

where c,d denote respectively the continuous and dispersed phase, ρ_k' and $\boldsymbol{v}_k'$ are the "fine grained" density and velocity, and χ_k is the phase function defined by

$$\chi_k(\boldsymbol{x},t) = \begin{cases} 1 & \text{if } \boldsymbol{x} \text{ is in phase } k \text{ at time } t, \\ 0 & \text{otherwise}, \end{cases} \tag{1}$$

with of course $\chi_c=1-\chi_d$.

If interface forces due to the surface tension are neglected and no external force field is considered, the generalized mass and momentum conservation equations can be written under the form

$$\frac{\partial \rho'}{\partial t} + \operatorname{div}(\rho' \boldsymbol{v}') = 0, \tag{2}$$

$$\frac{\partial}{\partial t}(\rho' \boldsymbol{v}') + \operatorname{div}(\rho' \boldsymbol{v}' \otimes \boldsymbol{v}') = \operatorname{div}(\boldsymbol{\Pi}'), \tag{3}$$

where $\boldsymbol{\Pi}'$ is the generalized stress tensor:

$$\boldsymbol{\Pi}' = \sum_{k=c,d} \chi_k \boldsymbol{\Pi}_k',$$

Π_k' being the stress tensor in the kth phase.

To obtain separate averaged equations for each phase, Eqs. (2) and (3) are multiplied by the phase function and then averaged via the configurational average:

$$\langle G'(\boldsymbol{x},t) \rangle = \int G'(\boldsymbol{x},t|\boldsymbol{x}_1,\ldots,\boldsymbol{x}_N) p(t,\boldsymbol{x}_1,\ldots,\boldsymbol{x}_N) d\boldsymbol{x}_1 \cdots d\boldsymbol{x}_N;$$

where $p(t,\boldsymbol{x}_1,\cdots,\boldsymbol{x}_N)dx_1 \cdots dx_N$ is the probability of finding the first particle center in the vicinity of $\boldsymbol{x}_1$ at t, while at the same time the second particle is in the vicinity of $\boldsymbol{x}_2$ and so forth. Considering indistinguishable particles, this expression can be rewritten as the probability $p(t,C_N)dC_N$ of finding the N particles in the vicinity of $C_N=(\boldsymbol{x}_1,\ldots,\boldsymbol{x}_N)$, regardless of their order.

The left hand side of Eqs. (2) and (3) are of the form

$$\frac{\partial G'}{\partial t} + \mathrm{div}(G'\boldsymbol{v}').$$

Providing that the fluctuations $G''=G'-\langle G'\rangle$ of the local field G' relative to the mean field $\langle G'\rangle$ are neglected and as long as no phase change occurs, the previously described average yields[26]

$$\left\langle \chi_k \left[\frac{\partial G'}{\partial t} + \mathrm{div}(G'\boldsymbol{v}') \right] \right\rangle = \frac{\partial}{\partial t}(\alpha_k G_k) + \mathrm{div}(\alpha_k G_k v_k), \tag{4}$$

with $\alpha_k=\langle\chi_k\rangle$ the mean volume fraction occupied by phase k, and G_k the phasic average of the variable G':

$$G_k = \langle \chi_k G'\rangle/\alpha_k. \tag{5}$$

The next fundamental step is to express $\langle\chi_c\mathrm{div}(\boldsymbol{\Pi}')\rangle$ and $\langle\chi_d\mathrm{div}(\boldsymbol{\Pi}')\rangle$ in terms of quantities that we will be able to calculate for a test particle in order to achieve closure. Our derivation is based on the theory developed by Buyevich,[24,27] here modified to account for the compressibility of the continuous phase as required for sound propagation. From $\chi_c = 1-\chi_d$, we easily obtain

$$\langle\chi_c\mathrm{div}(\boldsymbol{\Pi}')\rangle = \mathrm{div}\langle\boldsymbol{\Pi}'\rangle - \langle\chi_d\mathrm{div}(\boldsymbol{\Pi}')\rangle \tag{6}$$

with $\langle\boldsymbol{\Pi}'\rangle = \langle\chi_c\boldsymbol{\Pi}'\rangle + \langle\chi_d\boldsymbol{\Pi}'\rangle$.

In the continuous phase, the "fine-grained" stress tensor expression is the one of a Newtonian fluid, and thus

$$\langle\chi_c\boldsymbol{\Pi}'\rangle = -\alpha_c p_c \boldsymbol{I} + 2\mu_c\langle\chi_c\boldsymbol{D}'\rangle + \lambda_c\langle\chi_c\mathrm{div}(\boldsymbol{v}')\rangle\boldsymbol{I}, \tag{7}$$

where p_c is the phasic average of the local pressure, $\boldsymbol{D}'$ is the strain rate tensor, $\boldsymbol{I}$ is the unit tensor, and μ_c and $\zeta_c=\lambda_c+2\mu_c/3$ are respectively the shear and bulk viscosities of the continuous phase.

Owing to the rigidity of the particles, the strain rates $\boldsymbol{D}'$ and the volume variation $\mathrm{div}(\boldsymbol{v}')$ vanish inside the particle, and thus we obtain

$$\langle\chi_c\boldsymbol{D}'\rangle = \langle\boldsymbol{D}'\rangle - \langle\chi_d\boldsymbol{D}'\rangle = \langle\boldsymbol{D}'\rangle \equiv \boldsymbol{D}, \tag{8}$$

$$\langle\chi_c\mathrm{div}(\boldsymbol{v}')\rangle = \mathrm{div}\langle\boldsymbol{v}'\rangle - \langle\chi_d\mathrm{div}(\boldsymbol{v}')\rangle = \mathrm{div}\langle\boldsymbol{v}'\rangle = \mathrm{div}(\boldsymbol{v}), \tag{9}$$

with $\boldsymbol{v}=\alpha_c\boldsymbol{v_c}+\alpha_d\boldsymbol{v_d}$ and $\boldsymbol{D}=1/2(\nabla\boldsymbol{v}+\nabla^t\boldsymbol{v})$.

From Eqs. (7)–(9), we get

$$\langle\boldsymbol{\Pi}'\rangle = -\alpha_c p_c\boldsymbol{I} + 2\mu_c\boldsymbol{D} + \lambda_c\mathrm{div}(\boldsymbol{v})\boldsymbol{I} + \langle\chi_d\boldsymbol{\Pi}'\rangle. \tag{10}$$

Finally, by taking into acount (4), (6), and (10) in Eqs. (2) and (3), the following system of mass and momentum conservation stands:

$$\frac{\partial}{\partial t}(\alpha_c\rho_c) + \mathrm{div}(\alpha_c\rho_c\boldsymbol{v_c}) = 0, \tag{11}$$

$$\frac{\partial}{\partial t}(\alpha_d\rho_d) + \mathrm{div}(\alpha_d\rho_d\boldsymbol{v_d}) = 0, \tag{12}$$

$$\frac{\partial}{\partial t}(\alpha_c\rho_c\boldsymbol{v_c}) + \mathrm{div}(\alpha_c\rho_c\boldsymbol{v_c}\otimes\boldsymbol{v_c}) = \mathrm{div}(\boldsymbol{\Pi}) - \boldsymbol{F}, \tag{13}$$

$$\frac{\partial}{\partial t}(\alpha_d\rho_d\boldsymbol{v_d}) + \mathrm{div}(\alpha_d\rho_d\boldsymbol{v_d}\otimes\boldsymbol{v_d}) = \boldsymbol{F}, \tag{14}$$

with the expressions of the effective stress tensor $\boldsymbol{\Pi}=\langle\boldsymbol{\Pi}'\rangle$ given by Eq. (10) and the effective force $\boldsymbol{F}$ given by

$$\boldsymbol{F} = \langle\chi_d\mathrm{div}(\boldsymbol{\Pi}')\rangle. \tag{15}$$

B. The test particle problem

Thus, only the quantities $\langle\chi_d\boldsymbol{\Pi}'\rangle$ and $\langle\chi_d\mathrm{div}(\boldsymbol{\Pi}')\rangle$ remain to be expressed in terms of the averaged fields to achieve closure. To address this issue, the link between these expressions and the so-called test particle problem must be established. Let us introduce some notations that will be useful in this problem.

First, the conditional averages with one or two (or more) particles positions being known are defined by

$$\langle G'\rangle_{\boldsymbol{x}'}(\boldsymbol{x},t) = \int G'(\boldsymbol{x},t|C_N)p(t,C_{N-1}|\boldsymbol{x}')\,dC_{N-1},$$

$$\langle G'\rangle_{\boldsymbol{x}',\boldsymbol{x}''}(\boldsymbol{x},t) = \int G'p(t,C_{N-2}|\boldsymbol{x}',\boldsymbol{x}'')\,dC_{N-2}.$$

Then, we can introduce the unconditional probability density $p(t,\boldsymbol{x}')$ of finding one of the N sphere centers in $\boldsymbol{x}'$ at t, and $p(t,\boldsymbol{x}';\boldsymbol{x}'')$ the same probability but conditioned by the presence of another sphere center in $\boldsymbol{x}''$:

$$p(t,\boldsymbol{x}') = \sum_{j=1}^{N}\int\cdots\int p(t,C_N)_{x^j=\boldsymbol{x}'}\prod_{i\neq j}d\boldsymbol{x}^i,$$

$$p(t,\boldsymbol{x}';\boldsymbol{x}'') = \sum_{j\neq k}\int\cdots\int p(t,C_N)_{x^j=\boldsymbol{x}',x^k=\boldsymbol{x}''}\prod_{i\neq j,k}d\boldsymbol{x}^i.$$

We can note that $p(t,\boldsymbol{x}')$ is nothing but the mean concentration number of particles by volume, which will be noted $n(t,\boldsymbol{x}')$ in the rest of this paper.

From the above definitions, Buyevich and Shchelchkova[24] establish the link between quantities averaged over the dispersed phase and integrals over a test particle surface or volume:

$$\langle\chi_d G'\rangle(\boldsymbol{x},t) = \int_{|\boldsymbol{x}-\boldsymbol{x}'|\leq a} n(t,\boldsymbol{x}')\langle G'\rangle_{\boldsymbol{x}'}(\boldsymbol{x},t)\,d\boldsymbol{x}'. \tag{16}$$

With this equation and providing that the macroscopic scale L (that is to say, the wavelength λ in acoustics) is much larger than the radius a of the particle, they obtain the following formula:

$$\alpha_d(t,\boldsymbol{x}) = \langle\chi_d\rangle(t,\boldsymbol{x}) \approx 4/3\,\pi a^3 n(t,\boldsymbol{x}), \tag{17}$$

$$\boldsymbol{F} = \langle\chi_d\mathrm{div}(\boldsymbol{\Pi}')\rangle \approx \frac{3\alpha_d}{4\pi a^3}\oint\langle\boldsymbol{\Pi}'\rangle_x\cdot\mathbf{n}\,dS, \tag{18}$$

where $\mathbf{n}$ is the normal vector. Equation (18) clearly shows that $\boldsymbol{F}$ is nothing but the force applied on a test sphere by a fictitious medium, whose properties significantly differ from

the pure ambient fluid, as they include the influence of the other distributed spheres.

Finally, with a complex reasoning that we will not reproduce here, they prove that if no external torque acts on the particle, and the inertial terms due to the particle rotation can be neglected (assumptions well satisfied for acoustical waves), $\langle \chi_d \mathbf{\Pi}' \rangle$ can be expressed by the following surface integral over the test sphere surface:

$$\langle \chi_d \mathbf{\Pi}' \rangle \approx \frac{3\alpha_d}{4\pi a^3} \oint^{(s)} \boldsymbol{a} \otimes (\boldsymbol{n} \cdot \langle \mathbf{\Pi}' \rangle_{\boldsymbol{x}}) \, dS, \tag{19}$$

where the superscript (s) means that only the symmetric part of the tensor appearing in the integrand is considered.

C. The self-consistent closure scheme

The link between constitutive equations and the test particle problem is now established via (18) and (19). To compute these expressions, one should first determine the boundary conditions and secondly derive a set of equations for the conditionally averaged fields. The first issue can be solved by the following considerations:

- As no phase changes occur, the conditionally averaged velocity is equal to the velocity of the test sphere on the particle surface ($r=a$).
- Far from the test particle (when $r \to \infty$), the perturbation of the fields induced by the presence of the heterogeneity vanishes so that the conditionally averaged fields asymptotically coincide with the unconditionally averaged fields:

$$\langle G' \rangle_{\boldsymbol{x}'} \to \langle G' \rangle \quad \text{when } r \to \infty . \tag{20}$$

To address the second issue, the same equations can be derived for the conditionally averaged field as for the averaged field, but, this time, constitutive equations are expressed in terms of the averaged field with two particle positions being known:

$$\boldsymbol{F}_{\boldsymbol{x}'} = \int_{\boldsymbol{x}''} \int_{|\boldsymbol{x}-\boldsymbol{x}'| \le a} n(t,\boldsymbol{x}',\boldsymbol{x}'') \langle \mathrm{div}(\mathbf{\Pi}') \rangle_{\boldsymbol{x}',\boldsymbol{x}''} \, d\boldsymbol{x}' \, d\boldsymbol{x}'',$$

$$\langle \chi_d \mathbf{\Pi}' \rangle_{\boldsymbol{x}'} = \int_{\boldsymbol{x}''} \int_{|\boldsymbol{x}-\boldsymbol{x}'| \le a} n(t,\boldsymbol{x}',\boldsymbol{x}'') \langle (\mathbf{\Pi}') \rangle_{\boldsymbol{x}',\boldsymbol{x}''} \, d\boldsymbol{x}' \, d\boldsymbol{x}''.$$

Of course, one could also calculate the averaged equations with the position of two particles being known and so on. In such a way, one would obtain an infinite hierarchy of mutually dependent equations conditioned by the position of an increasing number of particles. So the problem arises of an efficient truncation or closure of this hierarchy. A truncation at the first level would result in the calculation of the constitutive equations when the particles are embedded in the pure ambient fluid. Here, mutual interactions of two or more spheres are completely left out. This approximation is usually used in dilute mixtures and corresponds to the classical version of the coupled phase theory. However, even at this level, a part of the multiple scattering is included because the particles are excited by the mean field (cf. Fig. 1).

At the next level, binary interactions of pairs of spheres are accounted for, while ternary, quadruple, and higher order loops are neglected. To achieve closure at this level, one should calculate the constitutive equations when two particles positions are known, which is not an easy matter.

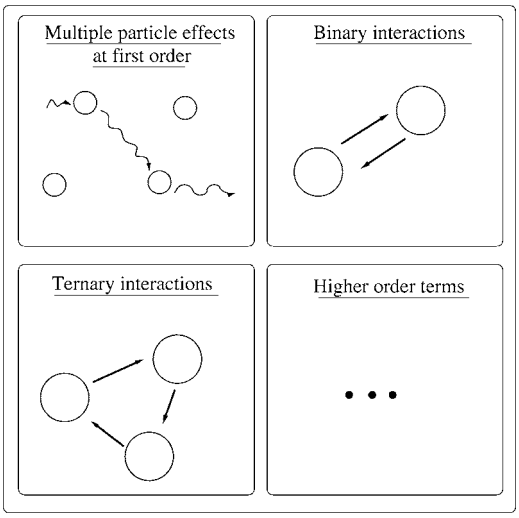

FIG. 1. Different orders of multiple scattering.

Of course, one could theoretically truncate this hierarchy at any order to integrate higher order loops, but the complexity of the calculation would greatly increase with the order. Anyway, this procedure would result in a polynomial expansion with respect to the particle concentration α_d and will thus be limited to relatively dilute mixtures. Moreover, nothing ensures that mutual interaction between n particles are dominant over interactions between $n+1$ particles when the concentration increases.

To overcome these limitations, Buyevich proposed a self-consistent scheme.[16,24] The starting point of this procedure is that, anyway, the resolution of the previous mutually dependent equations would result in an infinite polynomial series for the effective mixture properties. Instead of truncating the hierarchy at a certain level, the particles are supposed to be embedded in this *final* effective medium. Thanks to this procedure and by introducing a plausible form for integrals (18) and (19), the effective properties will be computed with an iterative scheme. All orders of interaction will thus be included in this formulation. Moreover, the correlations of particles in position can also be incorporated according to the choice of the expression of the conditional volume fraction.

D. Application to the propagation of an acoustic wave

1. Linearized equations

We will now adapt the previous system to the propagation of an acoustic wave. In this case, Eqs. (11)–(15) can be linearized. If we denote the equilibrium state with a subscript "o", the following equations stand:

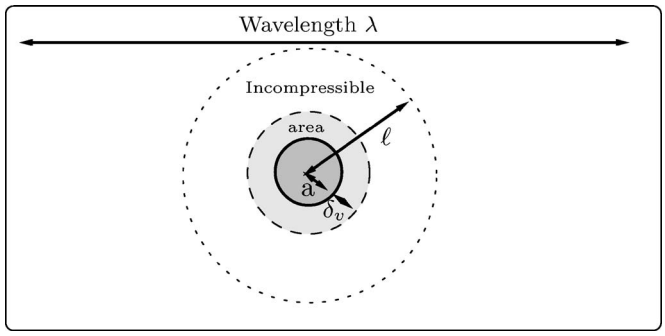

FIG. 2. The mesoscopic scale.

mass conservation:

$$\rho_{co}\left(\boxed{\frac{\partial \alpha_c}{\partial t}}+\alpha_{co}\mathrm{div}(\boldsymbol{v_c})\right)+\boxed{\alpha_{co}\frac{\partial \rho_c}{\partial t}}=0, \tag{21}$$

$$\boxed{\frac{\partial \alpha_d}{\partial t}}+\alpha_{do}\mathrm{div}(\boldsymbol{v_d})=0, \tag{22}$$

$$\alpha_d = 1-\alpha_c; \tag{23}$$

momentum conservation:

$$\alpha_{co}\rho_{co}\frac{\partial \boldsymbol{v_c}}{\partial t}=-\nabla(\alpha_c p_c)+\mu_c\Delta \mathbf{v}+\boxed{(\lambda_c+\mu_c)\boldsymbol{\nabla}\mathrm{div}(\boldsymbol{v})} + \mathrm{div}\langle\chi_d\boldsymbol{\Pi}'\rangle-\boldsymbol{F}, \tag{24}$$

$$\alpha_{do}\rho_{do}\frac{\partial \boldsymbol{v_d}}{\partial t}=\boldsymbol{F}. \tag{25}$$

In these expressions, all terms linked to the compressibility of the continuous phase have been outlined.

2. The long wavelength regime (LWR)

To perform the explicit calculation of constitutive equations, we will consider the LWR. In this case, we can introduce a mesoscopic scale l around the test particle where the compressibility of the continuous phase can be neglected and such as, when $r\to l$, the perturbation induced by the test particle vanishes (cf. Fig. 2):

$$a+\delta_v \ll l \ll \lambda,$$

where λ is the acoustic wavelength and $\delta_v=\sqrt{2\mu_c/\omega\rho_c}$ is the thickness of the viscous boundary layer. This inequality is always satisfied in the cases treated in this paper. At distances smaller than l (cf. Fig. 2), all (outlined) compressible terms can be neglected and, after Fourier transform, we obtain

$$\mathrm{div}(\boldsymbol{v_c})=\mathrm{div}(\boldsymbol{v_d})=0, \tag{26}$$

$$-\alpha_{co}\rho_{co}(i\omega)\boldsymbol{v_c}=-\nabla(\alpha_c p_c)+\mu_c\Delta\boldsymbol{v}+\mathrm{div}\langle\chi_d\boldsymbol{\Pi}'\rangle-\boldsymbol{F}, \tag{27}$$

$$-\alpha_{do}\rho_{do}(i\omega)\boldsymbol{v_d}=\boldsymbol{F}. \tag{28}$$

The same equations can be derived for the conditionally averaged field, but, this time, the conditional volume fraction at equilibrium $\alpha_{do,\boldsymbol{x}'}$ replaces the unconditional one:

$$\mathrm{div}(\alpha_{co,\boldsymbol{x}'}\boldsymbol{v_{c,x}}')=\mathrm{div}(\alpha_{do,\boldsymbol{x}'}\boldsymbol{v_{d,x}}')=0, \tag{29}$$

$$-\alpha_{co,\boldsymbol{x}'}\rho_{co}(i\omega)\boldsymbol{v_{c,x}}'=-\nabla(\alpha_{c,\boldsymbol{x}'}p_{c,\boldsymbol{x}'})+\mu_c\Delta\boldsymbol{v}_{\boldsymbol{x}'} + div\langle\chi_d\boldsymbol{\Pi}'\rangle_{\boldsymbol{x}'}-\boldsymbol{F}_{\boldsymbol{x}'}, \tag{30}$$

$$-\alpha_{do,\boldsymbol{x}'}\rho_{do}(i\omega)\boldsymbol{v_{d,x}}'=\boldsymbol{F}_{\boldsymbol{x}'}. \tag{31}$$

3. Correlations of particles in position

The difference between $\alpha_{do,\boldsymbol{x}'}$ and α_{do} stems from the correlations of particles in position, that is to say, the perturbation of the particle repartition induced by the presence of a test sphere in $\boldsymbol{x}'$. The simplest approximation consists in neglecting this difference:

$$\alpha_{do,\boldsymbol{x}'}=\alpha_{do}, \tag{32}$$

and thus ignoring the non-overlapping property of the spheres. For the sake of simplicity, we will adopt this hypothesis and we will precisely discuss its validity in Sec. III. Of course, more elaborate expressions[16] can be derived to describe properly the repartition of particles within groups of several spheres (cf. the Kirkwood and Percus-Yevick models as reviewed in the book by Croxton[28]) and therefore include the correlations of position.

4. The self-consistent condition

Even if the equations have been simplified in the incompressible region, we still have to deal with the entire hierarchy of equations, and we therefore need to close the system. For that purpose, we will use the condition expressed in the Sec. II C: the particles will be supposed to be embedded in the *final* effective medium (made of the whole series expansion). Let us apply this condition to our case.

First, Eqs. (29)–(31) can be rewritten in a convective reference frame related to the velocity of the test particle center, that is to say $\boldsymbol{v_d}|_{r=0}$:

$$\mathrm{div}(\boldsymbol{V_{c,x}}')=\mathrm{div}(\boldsymbol{V_{d,x}}')=0, \tag{33}$$

$$-\alpha_{co}\rho_{co}(i\omega)\boldsymbol{V_{c,x}}'=-\nabla(\alpha_{c,\boldsymbol{x}'}p_{c,\boldsymbol{x}'})+\mu_c\Delta\boldsymbol{V}_{\boldsymbol{x}'} + \mathrm{div}\langle\chi_d\boldsymbol{\Pi}'\rangle_{\boldsymbol{x}'}-\boldsymbol{F}_{\boldsymbol{x}'}-\alpha_{co}\rho_{co}\nabla\Psi, \tag{34}$$

$$-\alpha_{do}\rho_{do}(i\omega)\boldsymbol{V_{d,x}}'=\boldsymbol{F}_{\boldsymbol{x}'}-\alpha_{do}\rho_{do}\nabla\Psi, \tag{35}$$

with

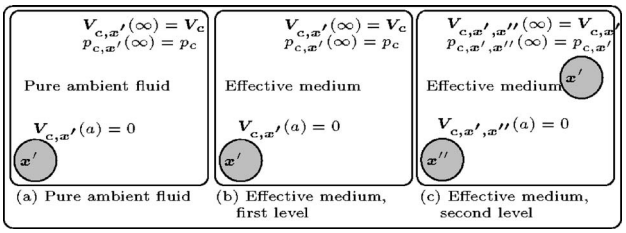

FIG. 3. Calculation of closure terms at different levels of the hierarchy.

$$\{\boldsymbol{V}_{\boldsymbol{d},\boldsymbol{x}'}, \boldsymbol{V}_{\boldsymbol{c},\boldsymbol{x}'}\} = \{\boldsymbol{v}_{\boldsymbol{d},\boldsymbol{x}'}, \boldsymbol{v}_{\boldsymbol{c},\boldsymbol{x}'}\} - \boldsymbol{v}_{\boldsymbol{d}}|_{r=0},$$

$$\Psi = -i\omega \boldsymbol{r} \cdot \boldsymbol{v}_{\boldsymbol{d}}|_{r=0}. \tag{36}$$

The terms proportional to $\nabla\Psi$ appearing in these equations are due to the change of reference frame. The boundary conditions can also be rewritten:

$$\boldsymbol{V}_{\boldsymbol{c},\boldsymbol{x}'} \to 0 \quad \text{when } r \to a, \tag{37}$$

$$\boldsymbol{V}_{\boldsymbol{c},\boldsymbol{x}'} \to \boldsymbol{V}_{\boldsymbol{c}} \quad \text{and} \quad p_{c,\boldsymbol{x}'} \to p_c \quad \text{when } r \to \infty. \tag{38}$$

Then, integrands (18) and (19) can be calculated for a particle embedded in a pure incompressible fluid, with boundary conditions (37) and (38) [cf. Fig. 3(a)]. The first integrand (18) corresponds to the classical calculation of the force applied on a moving sphere embedded in an unsteady nonuniform velocity field, sometimes called the Basset-Boussinesq-Oseen force.[29] The calculation of the second integrand (19) is less usual and can be found in some papers by Buyevich:[29,23]

$$\boldsymbol{F} = m_1(\boldsymbol{V}_{\boldsymbol{c}} - \boldsymbol{V}_{\boldsymbol{d}}) + m_2 \Delta \boldsymbol{V}_{\boldsymbol{c}} + m_3 \nabla \Psi, \tag{39}$$

$$\mathrm{div}\langle \chi_d \boldsymbol{\Pi}' \rangle = -\nabla(\alpha_d p_c) + m_0 \Delta \boldsymbol{V}_{\boldsymbol{c}}, \tag{40}$$

where m_0, m_1, m_2, and m_3 depend on the properties of the pure ambient fluid (μ_c, ρ_{co}) and on frequency ω. In these expressions, $m_1(\boldsymbol{V}_{\boldsymbol{c}} - \boldsymbol{V}_{\boldsymbol{d}})$ corresponds to the sum of the Stokes drag, the Basset hereditary, and the total inertial forces; $m_2 \Delta \boldsymbol{V}_{\boldsymbol{c}}$ is the Oseen correction due to the nonuniformity of the ambient fluid velocity; and $m_3 \nabla \Psi$ comes from the change of reference frame.

In the effective medium, the same relations stand:

$$\boldsymbol{F} = m_1^*(\boldsymbol{V}_{\boldsymbol{c}} - \boldsymbol{V}_{\boldsymbol{d}}) + m_2^* \Delta \boldsymbol{V}_{\boldsymbol{c}} + m_3^* \nabla \Psi, \tag{41}$$

$$\mathrm{div}\langle \chi_d \boldsymbol{\Pi}' \rangle = -\nabla(\alpha_d p_c) + m_0^* \Delta \boldsymbol{V}_{\boldsymbol{c}}, \tag{42}$$

but m_0^*, m_1^*, m_2^*, and m_3^* depend on the effective properties of the surrounding fluid (μ_{eff}, ρ_{eff1}, ρ_{eff2}), where ρ_{eff1} and ρ_{eff2} are some effective volume fractions, respectively linked to the inertial phenomena and the change of frame of reference, and μ_{eff} is the effective viscosity of the suspension.

Here arises the problem of determining these effective properties and this is the fundamental point in which our theory differs from the so-called "core shell model." These effective densities and viscosity will be calculated in a consistent way instead of being empirically introduced.

The expressions of $\boldsymbol{F}$ and $\mathrm{div}\langle \chi_d \boldsymbol{\Pi}' \rangle$ come from the calculation of integrands (18) and (19) in the *final* effective medium with boundary conditions (37) and (38) as illustrated by Fig. 3(b). At the next level of the hierarchy, the particles are also embedded in the *final* effective medium and the boundary conditions become [cf. Fig. 3(c)]

$$\boldsymbol{V}_{\boldsymbol{c},\boldsymbol{x}',\boldsymbol{x}''} \to 0 \quad \text{when } r \to a, \tag{43}$$

$$\boldsymbol{V}_{\boldsymbol{c},\boldsymbol{x}',\boldsymbol{x}''} \to \boldsymbol{V}_{\boldsymbol{c},\boldsymbol{x}'} \quad \text{and } p_{c,\boldsymbol{x}',\boldsymbol{x}''} \to p_{c,\boldsymbol{x}'} \quad \text{when } r \to \infty. \tag{44}$$

This is exactly the same problem, but the boundary conditions are expressed in terms of the conditionally averaged fields instead of the averaged fields. So $\boldsymbol{F}_{\boldsymbol{x}'}$ and $\mathrm{div}\langle \chi_d \boldsymbol{\Pi}' \rangle$ will be related to $\boldsymbol{V}_{\boldsymbol{c},\boldsymbol{x}'}, \boldsymbol{V}_{\boldsymbol{d},\boldsymbol{x}'}$, and $\nabla\Psi$ with *exactly the same coefficients* m_0^*, m_1^*, m_2^*, and m_3^*:

$$\boldsymbol{F}_{\boldsymbol{x}'} = m_1^*(\boldsymbol{V}_{\boldsymbol{c},\boldsymbol{x}'} - \boldsymbol{V}_{\boldsymbol{d},\boldsymbol{x}'}) + m_2^* \Delta \boldsymbol{V}_{\boldsymbol{c},\boldsymbol{x}'} + m_3^* \nabla \Psi, \tag{45}$$

$$\mathrm{div}\langle \chi_d \boldsymbol{\Pi}' \rangle_{\boldsymbol{x}'} = -\nabla(\alpha_{d,\boldsymbol{x}'} p_{c,\boldsymbol{x}'}) + m_0^* \Delta \boldsymbol{V}_{\boldsymbol{c},\boldsymbol{x}'}. \tag{46}$$

It is the equality of these coefficients at every order of the hierarchy that expresses the self-consistent condition. With this condition, there is no need to truncate the hierarchy at a finite order because the system is already closed as we will see.

To determine the expressions of the effective parameters in a consistent way, previous equations must be combined properly to obtain a final system of equations in the effective medium similar to the equations that would stand in the pure medium, that is to say,

$$\mathrm{div}(\boldsymbol{V}_{\boldsymbol{c},\boldsymbol{x}'}) = 0, \tag{47}$$

$$-\rho_{\mathrm{eff1}}(i\omega)\boldsymbol{V}_{\boldsymbol{c},\boldsymbol{x}'} = -\nabla p_{c,\boldsymbol{x}'} + \mu_{\mathrm{eff}} \Delta \boldsymbol{V}_{\boldsymbol{c},\boldsymbol{x}'} - \rho_{\mathrm{eff2}} \nabla \Psi. \tag{48}$$

If we replace relations (45) and (46) in Eqs. (33)–(35), we obtain together with Eq. (48) a set of 11 equations. On the other hand, we have 11 unknown parameters: the six components of velocities $\boldsymbol{V}_{\boldsymbol{d},\boldsymbol{x}'}$ and $\boldsymbol{V}_{\boldsymbol{c},\boldsymbol{x}'}$, the three effective parameters ρ_{eff1}, ρ_{eff2}, and μ_{eff}, the volume fraction $\alpha_{d,\boldsymbol{x}'}$, and the pressure $p_{c,\boldsymbol{x}'}$. Therefore, the effective properties can be expressed in terms of the coefficients m_k^* (for more details, cf. the original derivation by Buyevich[23]):

$$\rho_{\mathrm{eff1}} = \alpha_{co}\rho_{co} + \frac{\alpha_{do}\rho_{do} m_1^*}{m_1^* - i\omega\alpha_{do}\rho_{do}}, \tag{49}$$

$$\mu_{\mathrm{eff}} = \alpha_{co}\mu_c + m_0^* + \frac{\alpha_{do}\rho_{do} i\omega m_2^* + \alpha_{do}\mu_c(m_1^* - i\omega m_2^* \rho_{\mathrm{eff1}}/\mu_{\mathrm{eff}})}{m_1^* - i\omega\alpha_{do}\rho_{do}}, \tag{50}$$

$$\rho_{\mathrm{eff2}} = \alpha_{co}\rho_{co} + \alpha_{do}\rho_{do}\frac{m_1^* - m_3^* i\omega}{m_1^* - i\omega\alpha_{do}\rho_{do}}. \tag{51}$$

Now Eqs. (47) and (48) can be solved[29,23] with boundary conditions (37) and (38) to calculate integrands (18) and (19). We will obtain the same expressions as in the case of the pure fluid, but the effective properties (μ_{eff}, ρ_{eff1}, ρ_{eff2}) will stand instead of the pure fluid properties (μ_c, ρ_{co}):

$$m_0^* = \frac{5\alpha_{do}\mu_{\text{eff}}\exp(\beta)}{2(1+\beta)}, \tag{52}$$

$$m_1^* = \frac{9\alpha_{do}}{2a^2}(1+\beta+\beta^2/3)\mu_{\text{eff}}, \tag{53}$$

$$m_2^* = \frac{9\alpha_{do}}{2\beta^2}(\exp(\beta)-(1+\beta+\beta^2/3))\mu_{\text{eff}}, \tag{54}$$

$$m_3^* = \alpha_{do}\rho_{\text{eff2}}, \tag{55}$$

with

$$\beta^2 = -(i\omega)\rho_{\text{eff1}}a^2/\mu_{\text{eff}}. \tag{56}$$

Thus, coefficients m_k^* are expressed in terms of the effective properties and the system is closed. There only remains to solve numerically the self-consistent system formed by Eqs. (49)–(55) in the complex plane. This can be achieved by a simple iterative procedure, but some more elaborate schemes such as the so-called "Globally Convergent Newton's Method" can also be used.

We can notice that in the steady regime, we simply obtain

$$\rho_{\text{eff1}} = \rho_{\text{eff2}} = \alpha_{co}\rho_{co} + \alpha_{do}\rho_{do} \equiv \rho, \quad \mu_{\text{eff}} = \mu_c/(1-5/2\alpha_{do}).$$

This simple case illustrates the strength of the self-consistent scheme. A truncation of the hierarchy at the first order would have given the well-known Einstein formula:

$$\mu_{\text{eff}} = \mu_c(1+5/2\alpha_{do}) + O(\alpha_{do}^2).$$

It can be simply obtained from the expression (50) of μ_{eff} by replacing the coefficients m_k^* by their expression in the pure fluid m_k and by taking the asymptotic limit when $\omega=0$.

A truncation at order n would have given a formula of the form

$$\mu_{\text{eff}} = 1+5/2\alpha_{do} + \sum_{i=2}^{n} K_i\alpha_{do}^i + O(\alpha_{do}^{n+1}).$$

Thus all these formulas are limited to $\alpha_{do} \ll 1$. With the self-consistent theory, we directly obtain the whole series expression.

To conclude this part we would like to point out some differences with other models. First, we can note that the above steady effective properties are commonly used in the "core shell" model. Thus, the evolution of these parameters with frequency is neglected, contrary to the present study. Then, one of the differences with the model proposed by Spelt *et al.*[17] is that, in our theory, the relation between the closure terms and the averaged fields (expressed by coefficients m_k^*) is deduced from the pure fluid expressions. In the article by Spelt *et al.*, the authors say that each closure relation can be expressed in terms of any of the averaged fields as these field are also related to each other through algebraic equations that depend on the frequency and the effective wave number. This is a correct argument but only for plane waves because more complicated relations stand between averaged fields when dealing with spherical or more complicated wavefronts.

E. Dispersion equation for a plane acoustic wave

Now, we will derive the dispersion equation for a plane wave such as $G=G_o+\tilde{G}e^{i(k_* x-\omega t)}$, where $\tilde{G}$ is the amplitude of the wave, G_o is the equilibrium state, and k_* is the complex effective wave number. In this case, from Eqs. (21)–(25) and the expression of closure relations (41) and (42) we get the final system:

mass conservation:

$$-i\omega(\rho_{co}\tilde{\alpha}_c + \alpha_{co}\tilde{\rho}_c) + ik_*\alpha_{co}\rho_{co}\tilde{v}_c = 0, \tag{57}$$

$$i\omega\tilde{\alpha}_c + ik_*\alpha_{do}\tilde{v}_d = 0; \tag{58}$$

momentum conservation:

$$i\omega\alpha_{co}\rho_{co}\tilde{v}_c - ik_*\tilde{p}_c = k_*^2(\lambda_c+2\mu_c)(\alpha_{co}\tilde{v}_c+\alpha_{do}\tilde{v}_d) + k_*^2 m_0^*\tilde{v}_c + [m_1^*(\tilde{v}_c-\tilde{v}_d) - k_*^2 m_2^*\tilde{v}_c - i\omega m_3^*\tilde{v}_d], \tag{59}$$

$$-i\alpha_{do}\rho_{do}\omega\tilde{v}_d = m_1^*(\tilde{v}_c-\tilde{v}_d) - k_*^2 m_2^*\tilde{v}_c - i\omega m_3^*\tilde{v}_d; \tag{60}$$

state equation:

$$\tilde{p}c = c_{co}^2\tilde{\rho}_c, \tag{61}$$

where c_{co} is the sound velocity at rest in the continuous phase and parameters m_k^* can be numerically calculated from expressions (49)–(55) as mentioned earlier. This system is therefore a linear system of five equations, with five unknowns, $\tilde{\alpha}_c$, $\tilde{\rho}_c$, $\tilde{v}_c$, $\tilde{v}_d$, and $\tilde{p}_c$, and is consequently well posed. If we introduce the following parameters,

$$M_k^* = \frac{m_k^*}{\alpha_{do}\rho_{do}}, \quad d_r = \frac{\alpha_{do}\rho_{do}}{\alpha_{co}\rho_{co}}, \quad \text{and} \quad r = \frac{\rho_{co}}{\rho_{do}},$$

we get from (60)

$$\tilde{v}_d = [h_v - k_*^2 h_c]\tilde{v}_c \tag{62}$$

with

$$h_v = \frac{M_1^*}{M_1^* + i\omega(M_3^*-1)} \quad \text{and} \quad h_c = \frac{M_2^*}{M_1^* + i\omega(M_3^*-1)}.$$

Finally, by combining the conservation equations, we obtain the following bicubic equation, which can easily be solved to calculate the effective wave number:

$$Ak_*^4 + Bk_*^2 + C = 0, \tag{63}$$

$$A = d_r h_c\left[\frac{(\lambda_c+2\mu_c)}{\rho_{do}i\omega} + \frac{rc_{co}^2}{\alpha_{co}\omega^2}\right], \tag{64}$$

$$B = -d_r\left[h_c + \frac{M_0^* + (\lambda_c+2\mu_c)(\alpha_{co}+\alpha_{do}h_v)}{i\omega}\right] - \frac{c_{co}^2}{\alpha_{co}\omega^2}[1+d_r r h_v], \tag{65}$$

$$C = 1 + d_r h_v. \tag{66}$$

This calculation can be simplified because $h_v/k_*^2 h_c \gg 1$. This can be proved either by calculating it numerically or by noticing that this ratio is of the form of an effective acoustic Reynolds number, which is therefore large compared to unity. Thus, all terms proportional to h_c in the preceding equations can be neglected and we finally obtain

$$\left(\frac{k_*}{\omega} c_{co}\right)^2 = I(\omega) V(\omega),$$

$$I(\omega) = \left[1 - \frac{\alpha_{co} d_r i\omega}{c_{co}^2 (1 + d_r r h_v)} \times \left[M_0^* + \frac{(\lambda_c + 2\mu_c)(\alpha_{co} + \alpha_{do} h_v)}{\alpha_{do}\rho_{do}}\right]\right]^{-1},$$

$$V(\omega) = \left[1 + d_r \frac{(\alpha_{co} - r)h_v - \alpha_{co} r}{1 + d_r r h_v}\right].$$

In this expression $I(w)$ corresponds to the intrinsic (bulk) losses in the medium and $V(\omega)$ to the visco-inertial interactions between the two phases.

III. COMPARISON WITH EXPERIMENTS AND OTHER THEORIES

In this section, we will first compare the effective medium theory (EMT) with the multiple scattering theory (MST) from a theoretical point of view. Then, we will compare the predictions of our theory with the experimental data of Hipp *et al.*[25] and also with the "classical coupled phase theory" in which the calculation of the closure terms is based on the pure ambient fluid parameters instead of the effective ones.

A. Theoretical comparison with the multiple scattering theory

The hierarchy appearing in the EMT is similar to the hierarchy that also appears in the MST [see Ref. 11, Eq. (2.13)]. However, in the EMT the hierarchy is a succession of mutually dependent equations governing the conditionally averaged fields, whereas in the MST the hierarchy concerns the exciting field. This is one of the fundamental points in which these two theories differ.

Before delving into this crucial problem, let us clarify the terminology used here. The exciting field ($G_j'^E$) acting on the jth particle is the sum of the original field that would exist in the absence of particles (G'^0), and the wave scattered by every particle ($G_k'^S$) except the jth:

$$G_j'^E(\boldsymbol{x}, t|\boldsymbol{x_1}, \ldots, \boldsymbol{x_N}) = G'^0(\boldsymbol{x}, t) + \sum_{k \neq j} G_k'^S(\boldsymbol{x}, t|\boldsymbol{x_1}, \ldots, \boldsymbol{x_N}). \tag{67}$$

Note that this deterministic formulation is exact and that only the last scattering event of the particle j is omitted. Thus $G_k'^S$ may involve previous scattering by the jth particle. Otherwise, resonant scattering between a cluster of particles, i.e., loops, would be neglected.

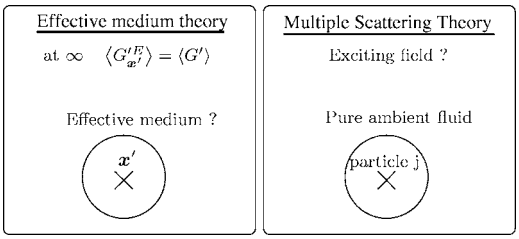

FIG. 4. Comparison between the self-consistent theory and the multiple scattering theory.

In the linear regime, the wave scattered by the jth particle can be related to the exciting field acting on it by the introduction of a linear operator T_j so that

$$G_j'^E(\boldsymbol{x}, t|\boldsymbol{x_1}, \ldots, \boldsymbol{x_N}) = G'^0(\boldsymbol{x}, t) + \sum_{k \neq j} T_k G_k'^E(\boldsymbol{x}, t|\boldsymbol{x_1}, \ldots, \boldsymbol{x_N}). \tag{68}$$

The introduction of this operator is a crucial step in the MST and it means that this theory is limited to the linear regime whereas the EMT is not. We can also note that the operator T_j is computed by using the properties of the pure ambient fluid.

The following relation stands between the total field (G'), the exciting field acting on the jth particle ($G_j'^E$), and the wave scattered by the same particle ($G_j'^S$):

$$G'(\boldsymbol{x}, t|\boldsymbol{x_1}, \ldots, \boldsymbol{x_N}) = G_j'^E(\boldsymbol{x}, t|\boldsymbol{x_1}, \ldots, \boldsymbol{x_N}) + G_j'^S(\boldsymbol{x}, t|\boldsymbol{x_1}, \ldots, \boldsymbol{x_N}). \tag{69}$$

Now we can clarify the previous assertion. In the EMT, a test particle is considered in $\boldsymbol{x}'$, and the value of the averaged exciting field acting on it is known far from the particle as the influence of the test particle vanishes:

$$\langle G'^{,E}_{\boldsymbol{x}'}\rangle_{\boldsymbol{x}'} \to \langle G'\rangle \quad \text{when } r \to \infty \quad \text{as } \langle G'^{,S}_{\boldsymbol{x}'}\rangle_{\boldsymbol{x}'} \to 0, \tag{70}$$

where $G'^{,E}_{\boldsymbol{x}'}$ and $G'^{,S}_{\boldsymbol{x}'}$ are respectively the exciting field acting on the particle located in $\boldsymbol{x}'$ and the wave scattered by this particle. This relation corresponds to the boundary condition (20). The fundamental problem here is thus to determine the expression of the effective medium surrounding the particle to perform integrands (18) and (19).

In the multiple scattering theory, we suppose that all particles are embedded in the pure ambient fluid (by introducing the operator T) and the problem, in this case, is to determine the form of the exciting field. These two approaches can be summarized by Fig. 4. We will now show that, at the lowest level, these two theories are equivalent. For that purpose, let us recall the assumptions implicitly made by Foldy[8] (and listed by Waterman and Truell[11]), when he identifies the average of the exciting field with the average of the total field to achieve closure. The starting point of his derivation is Eq. (68).

(1) Its first assumption is that the exciting field acting on the jth particle is the total field that would exist if this particle was not there:

$$G_j'^E(\boldsymbol{x},t|\boldsymbol{x}_1,\ldots,\boldsymbol{x}_N) = G'(\boldsymbol{x},t|\boldsymbol{x}_1,\ldots,\boldsymbol{x}_{j-1},\boldsymbol{x}_{j+1},\ldots\boldsymbol{x}_N),$$

Here, Foldy neglects all mutual interactions of the particles (loops) as the jth particle cannot influence the other particles that produce the exciting field.

(2) Then he assumes that the probability density conditioned by the position of one particle $p(t,\boldsymbol{x}_1,\ldots,\boldsymbol{x}_{j-1},\boldsymbol{x}_{j+1},\ldots,\boldsymbol{x}_N|\boldsymbol{x}_j)$ is equal to the unconditional probability: $p(t,\boldsymbol{x}_1,\ldots,\boldsymbol{x}_{j-1},\boldsymbol{x}_{j+1},\ldots,\boldsymbol{x}_N)$. This assumption leads to the statistical independence so that the correlations of particles in position are neglected and thus the particles can overlap one another.
(3) His third hypothesis is not restrictive; he assumes that the contributions of a single particle on the mean field can be neglected. This will be valid whenever the number N of particles appearing in the statistical average process is large enough, as the contribution of a single particle is of the order $1/N$.

Of course the first and second hypotheses are linked: to account properly for interactions of two or more particles, one should determine the correlations in position. But they are also undoubtedly distinct. One could, for example, estimate the interactions of pairs with an inaccurate distribution of the particles, for example by supposing that they can overlap one another. This would lead to an expression that would not be valid for too concentrated solutions but that would nevertheless incorporate pair interactions.

Assumptions 1–3 lead to the simple relation:

$$\langle G_j'^E(\boldsymbol{x},t)\rangle_j = \langle G'(\boldsymbol{x},t)\rangle. \tag{71}$$

So, the average of the exciting field acting on the jth particle is equal to the mean field, and the particle is embedded in the pure ambient fluid. This situation is therefore equivalent to the first level of the EMT hierarchy. However, even at this level, there is still a fundamental difference between these two theories. In the coupled phase theory, averaged equations are derived with respect to the volume fraction occupied by each phase. In the derivation of Foldy, however, the particles are supposed to be pointlike. Thus the decrease of the volume fraction occupied by the continuous phase due to the increase of the number of particles is not accounted for. The difference between these two theories can be neglected when the number of particles is large but the corresponding volume fraction is small. However, this difference becomes important when the particles occupy a large volume fraction: in the coupled phase theory when $\alpha_{do}\to 1$, only the intrinsic absorption in the dispersed phase remains whereas in the theory of Foldy the effects are maximum.

To account for interactions of pairs of particles, Lax introduced the so-called "quasi-crystalline approximation"[10] according to which the averaged exciting field acting on the jth particle when the position of two particles is known (j,k) is approximately equal to the averaged exciting field acting on the jth particle when only the position of the latter is known

$$\langle G_j'^E(\boldsymbol{x},t)\rangle_{jk} \approx \langle G_j'^E\rangle_j. \tag{72}$$

This approximation comes within the scope of a more general frame in which the averaged exciting field with n positions of particles being known is supposed to be approximately equal to the averaged exciting field with $n-1$ known positions.

To conclude this part, we can underline the fact that such a procedure will always result in a polynomial development with respect to the particle concentration and will thus be limited to relatively dilute mixtures whereas the EMT is not.

B. Comparison with the classical coupled phase theory and experimental data

Figure 5 compares the results obtained with our theory with the experimental data of Hipp *et al.*[14] and also with the "classical coupled phase theory." In this figure, we can see how much the predictions are improved by the introduction of the effective parameters instead of the pure fluid values, for low frequencies, when the interactions between the particles are strong because of the overlapping of boundary layers. However, when the frequency increases, some differences between the predictions and the experiments appear. They may be explained by the following considerations.

When the correlations of particles in position are considered, the more we approach the test particle, the more unlikely is the presence of another particle because they cannot overlap one another. So, it means that the conditional volume fraction $\alpha_{do,\boldsymbol{x}'}\to 0$ when $r\to a$. On the opposite, far from the test particle, the modification of the particle distribution induced by the presence of the test sphere vanishes so that $\alpha_{do,\boldsymbol{x}'}\to\alpha_{do}$ when $r\to\infty$. The transition between these two regimes appears approximately when $r\approx 2a$, which is the characteristic length that can be introduced because of the non-overlapping property of the particles. On the other hand, we can notice that the boundary layer thickness δ_v is inversely proportional to the square root of the frequency, so that when the frequency increases, this thickness decreases.

In our model, the correlations of particles in position are not considered and thus the effective properties do not depend on the distance from the particle surface. As long as $\delta_v \gg a$, approximating the effective medium surrounding the particle by homogeneous parameters based on the approximation $\alpha_{do,\boldsymbol{x}'}(r)=\alpha_{do}$ is accurate. But when $\delta v\approx a$, the variations of the conditional volume fraction with the distance r from the particle center cannot be neglected anymore. When $\delta_v \ll a$, the parameters of the effective medium in the boundary layer are even very close to the pure fluid values as almost no particles are present in this region. Consequently, the approximation that consists in taking the pure fluid parameters (ρ_{co},μ_c) to calculate the closure terms should give better results in this frequency range. To verify the validity of this hypothesis, we have plotted the attenuation curves for larger particles (cf. Fig. 6). In this case the characteristic frequency coresponding to $\delta_v=a$ is equal to $f_c=11$ MHz, whereas for Fig. 5 it was equal to 101 MHz.

On the above curves, we can observe the transition between the two asymptotic limits, around the characteristic frequency f_c, therefore corroborating our hypothesis. Our

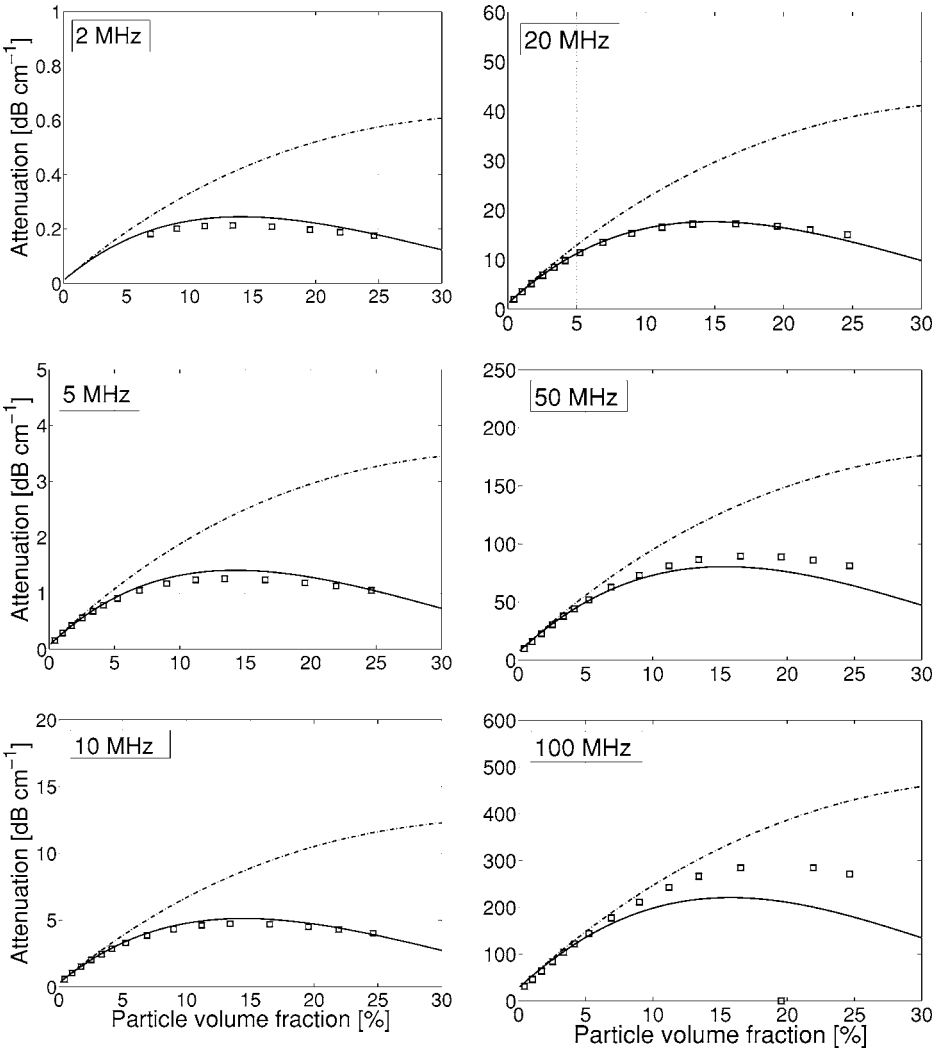

FIG. 5. Attenuation as a function of the volume fraction at various frequencies for silica particles of 56-nm radius in water. The solid lines correspond to our theory (—), the broken line to the classical coupled phase theory (- · -), and the symbols to the experimental data.

analysis shows how important the correlations in position are in the calculation of the effective parameters in acoustics. Thus, their integration in the calculation of coefficients m_k^* should give the smooth transition between these two limiting cases.

To conclude this section, we also plotted the curves with and without the intrinsic (bulk) losses, which are often neglected in the coupled phase models (cf. Fig. 7). These effects prove to be important for volume fraction up to 6% and must therefore be included correctly in formulation.

IV. EXTENSION TO THE POLYDISPERSE CASE

In this section, we will extend previous equations to polydisperse suspensions by using the same procedure as the one introduced by Gubaidullin and Nigmatulin[30] in their treatment of polydisperse aerosols. When a polydisperse suspension is considered, the probability $p(t,\boldsymbol{x})$ of finding any particle in x at t is replaced by the probability $p(t,\boldsymbol{x},a)$ of finding a particle of radius a in x at t. In this case, the properties of the dispersed phase also depend on the particule radius. So instead of introducing directly the phasic average over the whole dispersed phase $\langle \chi_d G' \rangle / \alpha_d$, we will split it into two steps:

- first, an average over all particles with the same radius $G_p(a) = \langle \chi_a G' \rangle / \alpha_p(a)$, where

$$\chi_a(\boldsymbol{x},t) = \begin{cases} 1 & \text{if } \boldsymbol{x} \text{ is in a particle of size } a \text{ at time } t, \\ 0 & \text{otherwise,} \end{cases}$$

  and $\alpha_p(a) = \langle \chi_a(\boldsymbol{x},t) \rangle$ is the volume fraction occupied by particles of radius a,
- and second, an average $\langle \rangle_a$ over all the particles sizes:

$$G_d = \frac{1}{\alpha_d} \langle G_p(a) \rangle_a = \frac{1}{\alpha_d} \int_{a_{\min}}^{a_{\max}} \alpha_p(a) G_p(a)\, da.$$

We can now derive the equations in the polydisperse case. The equations of the continuous phase will remain the same, but the momentum conservation equation of the dispersed phase will be derived for each particle size so that the set of Eqs. (57)–(61) becomes

mass conservation:

$$-i\omega(\rho_{co}\tilde{\alpha}_c + \alpha_{co}\tilde{\rho}_c) + ik_*\alpha_{co}\rho_{co}\tilde{v}_c = 0,$$

$$i\omega\tilde{\alpha}_c + ik_*\alpha_{do}\langle \tilde{v}_p \rangle_a = 0;$$

momentum conservation:

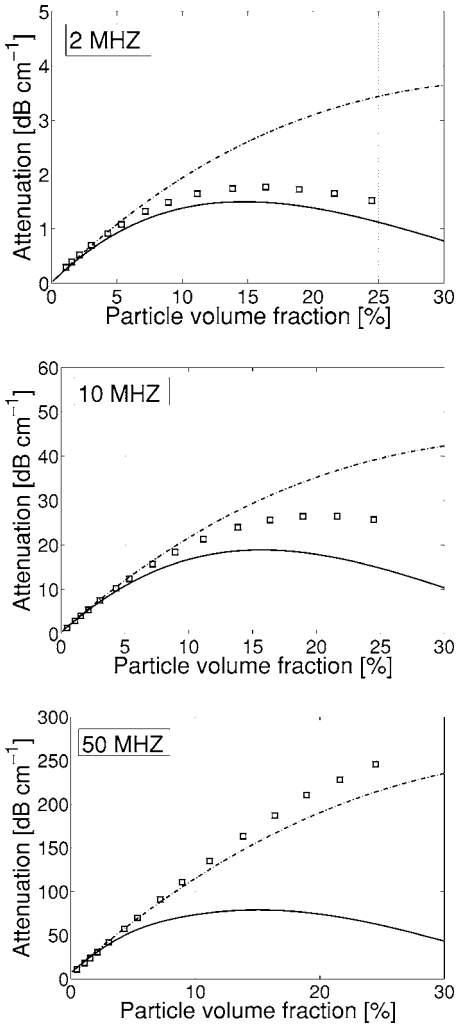

FIG. 6. Attenuation as a function of the volume fraction at various frequencies for silica particles of 164.5-nm radius in water. The solid lines correspond to our theory (—), the broken line to the classical coupled phase theory (- · -), and the symbols to the experimental data.

$$
\begin{aligned}
&i\omega\alpha_{co}\rho_{co}\tilde{v}_c - ik_*\tilde{p}_c \\
&\quad = k_*^2(\lambda_c + 2\mu_c)(\alpha_{co}\tilde{v}_c + \alpha_{do}\langle\tilde{v}_p\rangle_a) + k_*^2\langle m_0^*\rangle_a\tilde{v}_c \\
&\qquad + \langle m_1^*(\tilde{v}_c - \tilde{v}_p)\rangle_a - k_*^2\langle m_2^*\rangle_a\tilde{v}_c - i\omega\langle m_3^*\tilde{v}_p\rangle_a, \\
&\qquad - i\alpha_{do}\rho_{do}\omega\tilde{v}_p = m_1^*(\tilde{v}_c - \tilde{v}_p) - k_*^2 m_2^*\tilde{v}_c - i\omega m_3^*\tilde{v}_p;
\end{aligned}
$$

state equation:

$$\tilde{p}_c = c_{co}^2\tilde{\rho}_c.$$

In these equations, the coefficients m_k^* depend on the particle size and must therefore be calculated for each radius a.

Then we can express the velocity of the dispersed phase $\tilde{v}_p$ in terms of the velocity of the continuous $\tilde{v}_c$ phase, which is independent of the particle radius:

$$\tilde{v}_p = [h_v(a) - k_*^2 h_c(a)]\tilde{v}_c.$$

In this way, we can extract the continuous phase properties from the average $\langle\rangle_a$. If we now combine the conservation equations, we finally obtain the same dispersion equation as in the monodisperse case but with respectively $\langle h_v\rangle_a$, $\langle h_c\rangle_a$, and $\langle M_0^*\rangle_a$ instead of h_v, h_c, and M_0^*. Thus, only the average

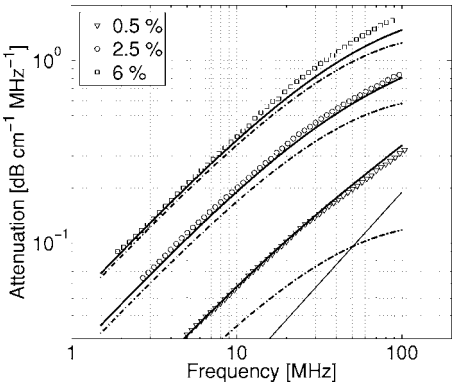

FIG. 7. Attenuation as a function of the frequency at different volume fractions for silica particles of 56-nm radius in water. The solid lines correspond to the complete theory (—), the broken line to the theory without intrinsic losses (- · -), the symbols to the experimental data, and the thin straight line to the intrinsic losses in water.

of these three parameters must be calculated to extend the validity of our dispersion relation to the polydisperse case.

V. CONCLUSION

The coupled phase theory has been improved to consider polydisperse suspensions and viscous interactions with the use of an effective medium, self-consistent theory. Our derivation is based on Buyevich's incompressible hydrodynamic model extended here to acoustical waves propagation. This theory turns out in practice to be very effective, as it amounts finally to a dispersion relation, which can be used directly for measurements or simulations. When compared with experiments, this model provides an accurate description of the attenuation at low frequencies, for concentrated suspensions for which interactions between particles are strong. In particular, the self-consistent approach has the ability to take properly into account interactions at all orders, such as the overlapping of viscous boundaries layers and the loops in the sense of the multiple scattering theory (MST) of waves. The link between the MST and the effective medium theory (EMT) has also been clarified.

Finally, our derivation could be extended to higher frequencies (or equivalently larger particles) and higher volume fractions by taking into account the correlations of particles in position, which would affect the effective properties of the medium. Its validity could even be enlarged to the high frequency regime by including the compressibility of the liquid when calculating the closure terms.[31,32]

ACKNOWLEDGMENTS

The authors would like to thank A. K. Hipp, G. Storti, and M. Morbidelli (Department of Chemical Engineering, ETH Zürich) for kindly providing us with the results of their experiments.

[1]C. J. T. Sewell, "On the extinction of sound in a viscous atmosphere by small obstacles of cylindrical and spherical form," Philos. Trans. R. Soc. London **210**, 239–270 (1910).
[2]H. Lamb, *Hydrodynamics* (Dover, New York, 1945).
[3]P. S. Epstein and R. R. Carhart, "The absorption of sound in suspensions and emulsions. I. Waterfog in air," J. Acoust. Soc. Am. **25**(3), 553–565

(l953).
[4]J. R. Allegra and S. A. Hawley, "Attenuation of sound in suspensions and emulsions: Theory and experiments," J. Acoust. Soc. Am. **51**, 1545–1564 (1972).
[5]A. H. Harker and J. A. G. Temple, "Velocity and attenuation of ultrasound in suspensions of particles in fluids," J. Phys. D **21**, 1576–l588 (1988).
[6]J. M. Evans and K. Attenborough, "Coupled phase theory for sound propagation in emulsions," J. Acoust. Soc. Am. **102**(1), 278–282, (1997).
[7]O. G. Harlen, M. J. Holmes, M. J. W. Povey, Y. Qiu, and B. D. Sleeman, "A low frequency potential scattering description of acoustic propagation in dispersions," SIAM J. Appl. Math. **61**(6), 1906–1931 (2001).
[8]L. L. Foldy, "The multiple scattering of waves. I. General theory of isotropic scattering by randomly distributed scatterers," Phys. Rev. **67**, 107–119 (1945).
[9]M. Lax, "Multiple scattering of waves," Rev. Mod. Phys. **23**, 287–310 (l951).
[10]M. Lax, "Multiple scattering of waves. II. The effective field in dense systems," Phys. Rev. **85**, 621–629 (1952).
[11]P. C. Waterman and R. Truell, "Multiple scattering of waves," J. Math. Phys. **2**, 512–537 (1961).
[12]V. Twersky, "On scattering of waves by random distributions. I. Free-space scatterer formalism," J. Math. Phys. **3**, 700–715 (1962).
[13]P. Lloyd and M. V. Berry, "Wave propagation through an assembly of spheres. IV. Relations between different multiple scattering theories," Proc. Phys. Soc. London **91**, 678–688 (1967).
[14]A. K. Hipp, G. Storti, and M. Morbidelli, "On multiple-particle effects in the acoustic characterization of colloidal dispersions," J. Phys. D **32**, 568–576 (1999).
[15]Y. Hemar N. Herrmann, P. Lemaréchal, R. Hocquart, and F. Lequeux, "Effective medium model for ultrasonic attenution due to the thermo-elastic effect in concentrated emulsions," J. Phys. II **7**, 637–647 (1997).
[16]Yu. A. Buyevich, "Heat and mass transfer in disperse media. II. Constitutive equations," Int. J. Heat Mass Transfer **35**(10), 2453–2463 (1992).
[17]P. D. M. Spelt, M. A. Norato, A. S. Sangani, M. S. Greenwood, and L. L. Tavlarides, "Attenuation of sound in concentrated suspensions: theory and experiments," J. Fluid Mech. **430**, 51–86. (2001).
[18]A. K. Hipp, G. Storti, and M. Morbidelli, "Acoustic characterization of concentrated suspensions and emulsions. 1. model analysis," Langmuir **18**, 391–404 (2002).
[19]D. J. McClements, Y. Hemar, and N. Herrmann, "Incorporation of thermal overlap effects into multiple scattering theory," J. Acoust. Soc. Am. **2**, 915–918 (1999).
[20]A. S. Dukhin and P. J. Goetz, "Acoustic spectroscopy for concentrated polydisperse colloids with high density contrast," Langmuir **12**, 4987–4997 (1996).
[21]J. Happel and H. Brenner, *Low Reynolds Number Hydrodynamics* (Martinus Nijhoff, Dordrecht, 1973).
[22]T. A. Strout, "Attenuation of sound in high-concentration suspensions: development and application of an oscillatory cell model," Ph.D. thesis, The University of Maine, 1991.
[23]Yu. A. Buyevich, "Interphase interaction in fine suspension flow," Chem. Eng. Sci. **50**(4), 641–650 (1995).
[24]Yu. A. Buyevich and I. N. Shchelchkova, "Flow of dense suspensions," Prog. Aerosp. Sci. **18**, 121–151 (1978).
[25]A. K. Hipp, G. Storti, and M. Morbidelli, "Acoustic characterization of concentrated suspensions and emulsions. 2. experimental validation," Langmuir, **18**, 391–404 (2002).
[26]D. A. Drew "Mathematical modelling of two-phase flow," Annu. Rev. Fluid Mech. **15**, 261–292 (1983).
[27]Yu. A. Buyevich and T. G. Theofanous, "Ensemble averaging in the mechanics of suspensions," FED (Am. Soc. Mech. Eng.) **243**, 41–60 (1997).
[28]C. A. Croxton, *Liquid State Physics. A Statistical Mechanical Introduction* (Cambridge U. P. Cambridge, 1974).
[29]Yu. A. Buyevich and V. G. Markov, "Rheology of concentrated mixtures of fluids with small particles," J. Appl. Math. Mech. **36**(3), 452–464 (1972).
[30]D. A. Gubaidullin and R. I. Nigmatulin, "On the theory of acoustic waves in polydispersed gaz-vapor-droplet suspensions," Int. J. Multiphase Flow **26**, 207–228 (2000).
[31]S. Temkin, "Viscous attenuation of sound in dilute suspensions of rigid particles," J. Acoust. Soc. Am. **100**(2), 825–831 (1996).
[32]S. Temkin and C.-M. Leung, "On the velocity of a rigid sphere in a sound wave," J. Sound Vib. **49**(1), 75–92 (1976).

On the influence of spatial correlations on sound propagation in concentrated solutions of rigid particles

Michael Baudoin[a)]
Université Pierre et Marie Curie-Paris 6, Institut Jean Le Rond D'Alembert (IJLRDA), UMR CNRS 7190 and Institut des NanoSciences de Paris (INSP), UMR CNRS 7588, 4 place Jussieu, 75252 Paris Cedex 05, France

Jean-Louis Thomas
INSP, CNRS, and Université Pierre et Marie Curie-Paris 6, 4 place Jussieu, Paris 75005, France

François Coulouvrat
IJLRDA, CNRS, and Université Pierre et Marie Curie-Paris 6, 4 place Jussieu, Paris 75005, France

(Received 29 May 2007; revised 26 March 2008; accepted 31 March 2008)

In a previous paper [J. Acoust. Soc. Am. **121**, 3386–3387 (2007)], a self-consistent effective medium theory has been used to account for hydrodynamic interactions between neighboring rigid particles, which considerably affect the sound propagation in concentrated solutions. However, spatial correlations were completely left out in this model. They correspond to the fact that the presence of one particle at a given position locally affects the location of the other ones. In the present work, the importance of such correlations is demonstrated within a certain frequency range and particle concentration. For that purpose, spatial correlations are integrated in our two-phase formulation by using a closure scheme similar to the one introduced by Spelt *et al.* ["Attenuation of sound in concentrated suspensions theory and experiments," J. Fluid Mech. **430**, 51–86 (2001)]. Then, the effect is shown through a careful comparison of the results obtained with this model, the ones obtained with different self-consistent approximations and the experiments performed by Hipp *et al.* ["Acoustical characterization of concentrated suspensions and emulsions. 2. Experimental validation," Langmuir, **18**, 391–404 (2002)]. With the present formulation, an excellent agreement is reached for all frequencies (within the limit of the long wavelength regime) and for concentrations up to 30% without any adjustable parameter.
 [DOI: 10.1121/1.2912445]

PACS number(s): 43.35.Bf [AJS] Pages: 4127–4139

I. INTRODUCTION

A precise prediction of the attenuation and dispersion of acoustical waves induced by the presence of particles in suspensions of different natures would be of great interest for acoustic spectroscopy.[1,2] Although the propagation in dilute suspensions is now well described (see Ref. 3 for bubbles, the ECAH theory,[4,5] and the coupled phase theory[6] for emulsions and the models of Gubaidullin and Nigmatulin,[7] Gumerov *et al.*,[8] and Duraiswami and Prosperetti[9] for aerosols), there remain some difficulties in concentrated suspensions as the interactions between neighboring particles must be taken into account. For that purpose, different methods have been used: first, numerical methods which are generally based on the so called "multipole expansion" (see Refs. 10 and 11 for the Helmholtz equation, and Refs. 12–15 for the Stokes and Brinkman equations). Although this numerical treatment of the problem is required for the study of particular configurations (when the particles are not homogeneously distributed), it does not take advantage of the average homogeneous distribution of the particles for randomly distributed spheres. That is why, a statistical treatment of the equations is interesting in this case. First, a hierarchy of mutually dependent averaged equations can be derived (see Ref. 16 for the multiple scattering theory developed for the Helmholtz equation and Ref. 17 for the two-phase Navier–Stokes equations). Then arises the problem of the efficient closure of this hierarchy. In many papers, this hierarchy is truncated at a certain order (generally at first or second order[18–20]). At first order, mutual interactions between neighboring particles are completely left out. At second order, only mutual interactions between two particles are taken into account. This truncation of the hierarchy cannot be used for concentrated suspensions because in this case, mutual interactions between N particles cannot be neglected compared to mutual interactions between $N+1$ particles. In order to avoid this truncation, self-consistent effective medium theories have been widely used in many branches of physics (see Ref. 21 for acoustical waves in bubbly liquids, Ref. 22 for elastic waves in composites, and Refs. 23–25 for two-phase flow, etc.). These methods consist of calculating the constitutive equations by considering a test particle surrounded by an effective medium whose properties are determined in a consistent way. To take into account spatial correlations (that is to say the modification of the particles location due to the presence of the test sphere), different approximations have been introduced (see Refs. 25–27 for a comparison of the different

a)Electronic mail: baudoin@lmm.jussieu.fr.

ones). Some take into account the continuous variation of the conditional volume fraction with the distance from the test particle and others approximate this variation by a step function and therefore reduce to "core shell models." A core-shell approximation (originally introduced by Dodd *et al.*[28]) has been successfully used by Spelt *et al.*[29] to compute the propagation of acoustical waves in suspensions of different natures. In their work, the suspension is considered as a whole and the plane acoustical wave impinging a test particle is decomposed according to the ECAH theory[4,5] into compressional, thermal, and viscous modes. Therefore, this model can be used for a large range of frequencies and different kinds of suspensions.

In the following, the same closure scheme (self-consistent approximation with core-shell approximation) is introduced to compute the exchange terms in our two-phase formulation. However, simpler equations are obtained by considering only the scattering mechanisms and pole orders necessary for the study of rigid particle in the long wavelength regime (LWR). Moreover, vectorial expressions of the closure terms (force and stresslet) are obtained and the acceleration of the particles is taken into account. These expressions can therefore be used for other purposes than plane acoustical waves. We must note that for a plane acoustical wave propagating in suspensions of rigid particles in the LWR, the two models should correspond.

The present model is used to study the influence of spatial correlations on the sound propagation in solutions of rigid particles. In the first section, we recall the linearized two-phase equations obtained in a previous paper[30] to describe the sound propagation in solutions of rigid particles. Then, we derive the equations for the conditionally averaged fields which should be solved to take into account spatial correlations and, in particular, the continuous variation of the conditional volume fraction with the distance from the test particle. To perform the explicit calculation of the dispersion equation, a simplification of this problem is used: the conditional volume fraction is approximated by a step function. In this way, a "core-shell" model is obtained but with a "core radius" related to the particle volume fraction and radius by a complex function calculated from Percus–Yevick (PY) theory for hard spheres.[31,32] The results are finally compared to the experiments of Hipp *et al.*[33] performed in solutions of silica particles for different frequencies, particle sizes, and concentration and an excellent agreement is reached.

II. COUPLED PHASE THEORY

A. Linearized ensemble averaged equations and the hierarchy of balance equations

In a precedent paper,[30] ensemble averaged equations have been derived to describe the propagation of acoustical waves in homogeneous solutions of monodisperse rigid particles. They were obtained from local-instant balance equations in each phase by the introduction of the phasic function:

$$\chi_k(\mathbf{x},t) = \begin{cases} 1 & \text{if } \mathbf{x} \text{ is in phase } k \text{ at time } t \\ 0 & \text{otherwise,} \end{cases}$$

which allows to broaden the validity of local balance equations to every position and time, and by the use of a statistical average (noted $\langle\ \rangle$ hereafter) such as

$$\langle G'(\mathbf{x},t)\rangle = \int G'(\mathbf{x},t|C_N)p(t,C_N)dC_N,$$

where $p(t,C_N)dC_N$ is the probability of finding the N particles in the vicinity of $C_N=(\mathbf{x}_1,\ldots,\mathbf{x_N})$, regardless of their order and $G'=\Sigma_k\chi_k G'_k$ is a local function generalized to every position and time by the use of the phasic function.

Once linearized, the balance equations stand under the following form.

Mass conservation,

$$\rho_{co}\left(\frac{\partial\alpha_c}{\partial t} + \alpha_{co}\,\mathrm{div}(\mathbf{v_c})\right) + \alpha_{co}\frac{\partial\rho_c}{\partial t} = 0, \tag{1}$$

$$\rho_{do}\left(\frac{\partial\alpha_d}{\partial t} + \alpha_{do}\,\mathrm{div}(\mathbf{v_d})\right) + \alpha_{do}\frac{\partial\rho_d}{\partial t} = 0, \tag{2}$$

$$\alpha_d = 1 - \alpha_c. \tag{3}$$

Momentum conservation,

$$\alpha_{co}\rho_{co}\frac{\partial\mathbf{v_c}}{\partial t} = -\nabla(\alpha_c p_c) + \mu_c\Delta\mathbf{v} + (\lambda_c+\mu_c)\,\nabla\ \mathrm{div}(\mathbf{v}) + \mathrm{div}\,\mathbf{S} - \mathbf{F}, \tag{4}$$

$$\alpha_{do}\rho_{do}\frac{\partial\mathbf{v_d}}{\partial t} = \mathbf{F}. \tag{5}$$

Equations of state,

$$\rho_c = p_c/c_{co}^2, \tag{6}$$

$$\rho_d = p_c/c_{do}^2. \tag{7}$$

In these equations, the subscripts o, c, and d denote, respectively, the equilibrium state, and the continuous and the dispersed phases, $\alpha_k=\langle\chi_k\rangle$ is the volume fraction of phase k while $\rho_k=\langle\chi_k\rho'\rangle$ is its mean density and $\mathbf{v_k}=\langle\chi_k\rho'\mathbf{v}'\rangle/\langle\chi_k\rho'\rangle$ its mean velocity. Finally, p_c, μ_c, and $\zeta_c=\lambda_c+2\mu_c/3$ are, respectively, the pressure, the shear, and the bulk viscosities of the continuous phase, c_{ko} the sound speed in phase k, $\mathbf{v}=\alpha_{co}\mathbf{v_c}+\alpha_{do}\mathbf{v_d}$ the average velocity of the suspension, $\mathbf{F}=\langle\chi_d\,\mathrm{div}(\mathbf{\Pi}')\rangle$ the interphase force, and $\mathbf{S}=\langle\chi_d\mathbf{\Pi}'\rangle$ the average of the local generalized stress tensor $\mathbf{\Pi}'=\Sigma_{k=c,d}\chi_k\Pi'_k$. We can note that in Eq. (2) (mass conservation for the dispersed phase), the compressibility of the particles has been taken into account in order to give a correct prediction of both attenuation and dispersion for concentrated suspensions of silica nanoparticle. Even if these particles are 35 times less compressible than water (ratio 2, 2 for density, 4 for the sound speed, and therefore 35 for the compressibility $\xi=1/\rho c^2$), their departure from a perfectly rigid behavior might have an influence on the effective sound speed in concentrated suspensions. However, this modifica-

tion does not affect the attenuation curves and they will only induce a global shift of the effective sound speed as we are far from the particle resonances in the frequency range considered here.

To achieve closure, the interphase force $\mathbf{F}$ and the stresslet $\mathbf{S}$ must be expressed in terms of the averaged fields. The first step is to establish the link between these expressions and the so-called test particle problem. This particular issue was addressed by Buyevich and Shchelchkova:[24]

$$\mathbf{F} = \langle \chi_d \, \mathrm{div}(\mathbf{\Pi}') \rangle \approx \frac{3\alpha_d}{4\pi a^3} \oint \langle \mathbf{\Pi}' \rangle_{\mathbf{x}} \, . \, \mathbf{n} dS, \tag{8}$$

$$\mathbf{S} = \langle \chi_d \mathbf{\Pi}' \rangle \approx \frac{3\alpha_d}{4\pi a^3} \oint^{(s)} \mathbf{a} \otimes (\mathbf{n} \, . \, \langle \mathbf{\Pi}' \rangle_{\mathbf{x}}) dS, \tag{9}$$

where a is the radius of the particle, $\mathbf{n}$ the normal vector, and $\langle \, \rangle_{\mathbf{x}}$ the statistical average conditioned by the knowledge of the position of one particle in $\mathbf{x}$:

$$\langle G' \rangle_{\mathbf{x}}(\mathbf{x}', t) = \int G'(\mathbf{x}', t | C_N) p(t, C_{N-1} | \mathbf{x}) dC_{N-1}.$$

With these expressions, the interphase force and stresslet are related to the conditionally averaged fields. One could therefore decide to derive the balance equations for the conditionally averaged fields. The same equations would be obtained, but now the conditional force $\mathbf{F}_{\mathbf{x}}$ and stresslet $\mathbf{S}_{\mathbf{x}}$ would depend on the averaged fields with the positions of two particles being known and so on. In this way, an infinite hierarchy of interdependent equations, similar to the cluster expansion which appears in statistical physics, would be disclosed. It was rigorously established by Hinch[17] in 1977.

Now arises the problem of the efficient closure of this hierarchy. The first idea consists of truncating this hierarchy at a certain order. At first order, the constitutive Eqs. (8) and (9) are calculated for a sphere embedded in the pure continuous phase. In this case, interactions between particles are completely left out. This is the approximation classically used in two-phase models.[6,34] At second order, the conditional force $\mathbf{F}_{\mathbf{x}}$ and stresslet $\mathbf{S}_{\mathbf{x}}$ are calculated for a cluster of two spheres lying in the pure continuous phase. In this case, binary interactions of pairs of sphere are taken into account while ternary or higher order interactions are completely left out. One could of course calculate these expressions for higher order clusters but this method is limited. First, because the calculation of the constitutive equations becomes more and more difficult when the size of the cluster increases. Second, because interactions between $N+1$ particles are no more negligible compared to interactions between N particles in very concentrated solutions, and thus the whole hierarchy must be considered.

It is the merit of the pioneering work of Lundgren[23] and Buyevich *et al.*[24,35] to have proposed an alternative *self-consistent effective medium theory* that takes into account interactions at all order within a certain approximation. These self-consistent schemes have then been extended to even more concentrated medium, when spatial correlations must be considered. For this purpose, different approximations have been introduced and they are compared in a paper by Sangani and Yao.[26,27] In our precedent paper,[30] a self-consistent effective medium theory had been used to take into account the influence of hydrodynamic interactions between particles on the propagation of acoustical waves in suspensions of rigid particles. However, spatial correlations were not considered and the theory will now be modified to include these effects.

B. The long wavelength regime

Before delving into this crucial problem, the balance equations will be simplified in the neighborhood of a test particle, lying at position $\mathbf{x}$ to calculate the surface integrals (8) and (9). For that purpose, a mesoscopic scale l such that $a \ll l \ll \lambda$ can be introduced whenever the wavelength λ is much larger than the radius a of the particle, that is to say in the LWR. Within a cell of characteristic length l around the test particle, all terms linked to the compressibility of the continuous phase can be neglected and thus Eqs. (1)–(7) reduce to the following form after Fourier transform:

$$\mathrm{div}(\mathbf{v_c}) = \mathrm{div}(\mathbf{v_d}) = 0, \tag{10}$$

$$-\alpha_{co}\rho_{co}(i\omega)\mathbf{v_c} = -\nabla(\alpha_c p_c) + \mu_c \Delta \mathbf{v} + \mathrm{div}\, \mathbf{S} - \mathbf{F}, \tag{11}$$

$$-\alpha_{do}\rho_{do}(i\omega)\mathbf{v_d} = \mathbf{F}. \tag{12}$$

If we rewrite them in the convective frame of reference related to the velocity of the test particle, we simply obtain

$$\mathrm{div}(\mathbf{V_c}) = \mathrm{div}(\mathbf{V_d}) = 0, \tag{13}$$

$$-\alpha_{co}\rho_{co}(i\omega)\mathbf{V_c} = -\nabla(\alpha_c p_c) + \mu_c \Delta \mathbf{V} + \mathrm{div}\, \mathbf{S} - \mathbf{F} - \alpha_{co}\rho_{co} \nabla \Psi, \tag{14}$$

$$-\alpha_{do}\rho_{do}(i\omega)\mathbf{V_d} = \mathbf{F} - \alpha_{do}\rho_{do} \nabla \Psi, \tag{15}$$

where $\mathbf{V_k} = \mathbf{v_k} - \mathbf{v_d}|_{r=0}$ is the average velocity of phase k in the new frame of reference, $\Psi = -i\omega \mathbf{r}$. $\mathbf{v_d}|_{r=0}$ is a function introduced to take into account the acceleration of the test particle, $\mathbf{r} = \mathbf{x}' - \mathbf{x}$ is the distance from the test particle, and ω the frequency of the propagating wave.

Similar balance equations can also be derived for the conditionally averaged fields but this time, the conditional volume fraction $\alpha_{ko,\mathbf{x}}$ of phase k stands instead of the unconditional one:

$$\mathrm{div}(\alpha_{co,\mathbf{x}}\mathbf{V_{c,x}}) = \mathrm{div}(\alpha_{do,\mathbf{x}}\mathbf{V_{d,x}}) = 0, \tag{16}$$

$$-\alpha_{co,\mathbf{x}}\rho_{co}(i\omega)\mathbf{V_{c,x}} = -\nabla(\alpha_{c,\mathbf{x}} p_{c,\mathbf{x}}) + \mu_c \Delta \mathbf{V_x} + \mathrm{div}\, \mathbf{S_x} - \mathbf{F_x} - \alpha_{co,\mathbf{x}}\rho_{co} \nabla \Psi, \tag{17}$$

$$-\alpha_{do,\mathbf{x}}\rho_{do}(i\omega)\mathbf{V_{d,x}} = \mathbf{F_x} - \alpha_{do,\mathbf{x}}\rho_{do} \nabla \Psi, \tag{18}$$

where $\mathbf{V_{k,x}} = \mathbf{v_{k,x}} - \mathbf{v_d}|_{r=0}$.

On the test sphere ($r=a$), the conditional velocity of the continuous phase is null and far from it ($r \to \infty$), the influence of the test particle vanishes. We therefore obtain the following boundary conditions:

$$\mathbf{V_{c,x}} = 0 \quad \text{in } r = a, \tag{19}$$

$$\{\mathbf{V_{c,x}}, \mathbf{V_{d,x}}, p_{c,\mathbf{x}}\} \to \{\mathbf{V_c}, \mathbf{V_d}, p_c\} \quad \text{when } r \to \infty. \tag{20}$$

III. SPATIAL CORRELATIONS

A. The conditional volume fraction

For pointlike particle, there would be no difference between the conditional volume fraction $\alpha_{do,\mathbf{x}}$ and the unconditional one α_{do}. However, the nonoverlapping property of hard spheres modifies the distribution of particles in the neighborhood of the test particle. We will now see how the conditional volume fraction can be estimated for hard spheres.

First, the so-called distribution function $p(t,\mathbf{x}|\mathbf{x}')$ (which is nothing but the probability of finding one of the sphere center in $\mathbf{x}'$ when another particle is lying in $\mathbf{x}$) can be calculated with models inherited from statistical physics such as the PY (Refs. 31 and 32 or hypernetted chain[36,37] (HNC) models. Numerical methods (for example, Monte Carlo simulations) could also be used but PY theory provides accurate and easily computable estimate of this function.

Then the conditional volume fraction $\alpha_{do,\mathbf{x}}(\mathbf{x}')$ can be deduced from the distribution function $p(t,\mathbf{x}|\mathbf{x}')$ with the following formula[38] for hard spheres:

$$\alpha_{do,\mathbf{x}}(\mathbf{x}') = \int_{|\mathbf{x}''-\mathbf{x}'|\leqslant a} p(t,\mathbf{x}''|\mathbf{x}) d\mathbf{x}''. \tag{21}$$

For isotropically distributed spheres, the distribution function depends only on the distance $r'=|\mathbf{x}''-\mathbf{x}|$ and thus this formula reduces to

$$\alpha_{do,\mathbf{x}}(r) = \int_{\max(2a,r-a)}^{r+a} p(t,r') \frac{\pi r'}{r} [2rr' - r'^2 - r^2 + a^2] dr', \tag{22}$$

with $r=|\mathbf{x}'-\mathbf{x}|$. Figure 1 illustrates the evolution of the distribution function and the conditional volume fraction with the distance r from the test particle center, calculated from PY theory for hard spheres. We can note that the nonoverlapping condition does not mean that some parts of the particles cannot lie in the region $a \leqslant r \leqslant 2a$ but just that the centers of the particles are excluded from it. That is why the volume fraction progressively increases in this region contrarily to the distribution function which is null.

B. The self-consistent effective medium closure scheme

We will now apply the self-consistent condition (called method A in papers from Chang *et al.*[25,39] and Yao and Sangani[26,27]) in order to close the infinite hierarchy previously described. We can note that contrarily to the scheme proposed by Buyevich[38,40] (called method B in the papers of Chang *et al.*), closure will be obtained for the conditionaly averaged field and not for the perturbation (as defined by Buyevich in his paper).

To achieve closure, the force $\mathbf{F}$ and the stresslet $\mathbf{S}$ must necessarily be expressed in terms of the average fields and their space and time derivatives of appropriate tensor dimensionality.

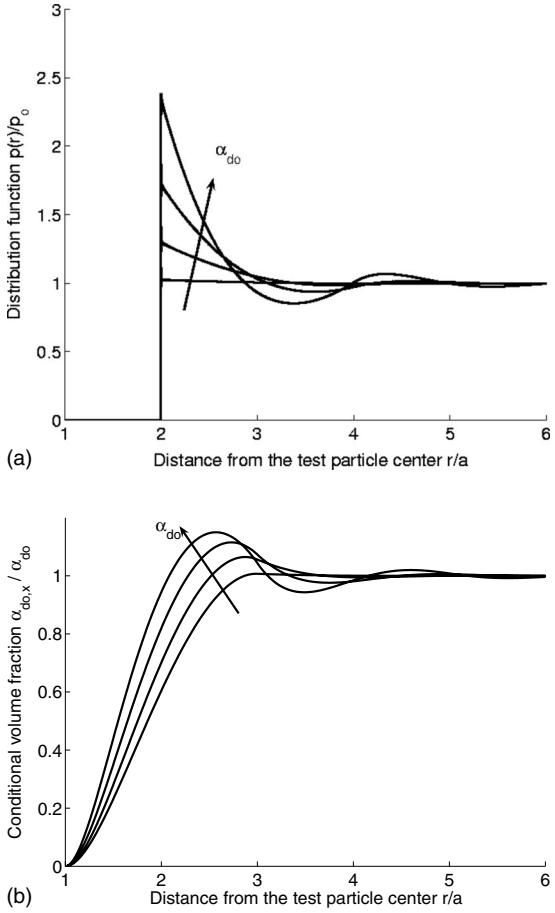

FIG. 1. Evolution of the distribution function and the conditional volume fraction with the distance r/a from the test particle center for volume fraction α_{do} of, respectively, 1%, 10%, 20%, and 30%. These curves are calculated with PY theory.

$$\mathbf{F} = f\langle \mathbf{V_c}, \mathbf{V_d}, \nabla p_c, \nabla \psi, \Delta \mathbf{V_c}, \Delta \mathbf{V_d}, \dots \rangle, \tag{23}$$

$$\mathrm{div}(\mathbf{S}) = s\langle \mathbf{V_c}, \mathbf{V_d}, \nabla p_c, \nabla \psi, \Delta \mathbf{V_c}, \Delta \mathbf{V_d}, \dots \rangle. \tag{24}$$

Since the two-phase equations considered here are linear, f and s must be linear functions of their arguments. Moreover, these functions must depend on the frequency ω to take into account the time derivatives in the Fourier space. For a moving sphere embedded in a pure ambient fluid, the expressions of f and s are well known:[41,42]

$$\mathbf{F} = \alpha_{do}[n_1(\mathbf{V_c} - \mathbf{V_d}) + n_2 \Delta \mathbf{V_c} + n_3 \nabla \Psi], \tag{25}$$

$$\mathrm{div}(\mathbf{S}) = \nabla(\alpha_d p_c) + \alpha_{do} n_o \Delta \mathbf{V_c}, \tag{26}$$

where n_o, n_1, n_2, and n_3 are the coefficients that depend on the pure fluid properties ($\mu_c \rho_{co}$) and on the frequency ω. In these expressions, $n_1(\mathbf{V_c}-\mathbf{V_d})$ corresponds to the sum of the Stokes drag, the Basset hereditary, and the total inertial forces, $n_2 \Delta \mathbf{V_c}$ is the Faxen correction due to the nonuniformity of the ambient fluid velocity, and $n_3 \nabla \Psi$ is due to the acceleration of the test particle.

If we now take into account the influence of the other distributed spheres, the particle is no more embedded in the pure fluid but in an effective medium whose properties are unknown at this stage of the derivation. In this case, the force $\mathbf{F}$ and the stresslet $\mathbf{S}$ will be related to the averaged fields in

the same way but with new coefficients $\tilde{n}_k$ which depend on the effective properties of the surrounding fluid $(\mu_{\text{eff}}, \rho_{\text{eff1}}, \rho_{\text{eff2}})$:

$$\mathbf{F} = \alpha_{do}[\tilde{n}_1(\mathbf{V_c} - \mathbf{V_d}) + \tilde{n}_2 \Delta \mathbf{V_c} + \tilde{n}_3 \nabla \Psi], \tag{27}$$

$$\text{div}(\mathbf{S}) = \nabla(\alpha_d p_c) + \alpha_{do} \tilde{n}_0 \Delta \mathbf{V_c}, \tag{28}$$

where ρ_{eff1} and ρ_{eff2} are some effective densities, respectively, linked to the inertial phenomena and the change of frame of reference, and μ_{eff} is the effective viscosity of the solution. We must underline how important is the hypothesis of homogeneity of the suspension at this stage of the derivation because an inhomogeneous distribution of the particles might induce extra forces related to the gradient of the volume fraction.

The self-consistent condition consists of keeping the *same* coefficients $\tilde{n}_k$ to express $\mathbf{F_x}$ and $\mathbf{S_x}$ in terms of the conditionally averaged fields:

$$\mathbf{F_x} = \alpha_{do,\mathbf{x}}[\tilde{n}_1(\mathbf{V_{c,x}} - \mathbf{V_{d,x}}) + \tilde{n}_2 \Delta \mathbf{V_{c,x}} + \tilde{n}_3 \nabla \Psi], \tag{29}$$

$$\text{div}(\mathbf{S_x}) = \nabla(\alpha_{d,\mathbf{x}} p_{c,\mathbf{x}}) + \alpha_{do,\mathbf{x}} \tilde{n}_0 \Delta \mathbf{V_{c,x}}. \tag{30}$$

Of course, the conditional volume fraction replaces the unconditional one because the distribution of the particles is modified by the presence of the test sphere.

Now, the effective properties of the surrounding fluid must be determined in a consistent way. For that purpose, Eqs. (13)–(15) [with the expressions of $\mathbf{F}$ and $\mathbf{S}$ given by Eqs. (27) and (28)] must be properly combined to obtain a final set of equations in the effective medium similar to the equations which would stand in a pure fluid:

$$\text{div}(\mathbf{V_c}) = 0, \tag{31}$$

$$-\rho_{\text{eff1}}(i\omega)\mathbf{V_c} = -\nabla p_c + \mu_{\text{eff}} \Delta \mathbf{V_c} - \rho_{\text{eff2}} \nabla \Psi. \tag{32}$$

As mentioned earlier by the authors,[30] Eqs. (31), (32), and (13)–(15) form a closed system and thus the effective properties can be expressed in terms of the properties of the continuous and dispersed phases, and the coefficients $\tilde{n}_k$ (see Ref. 41 for more details about this calculation):

$$\rho_{\text{eff1}} = \alpha_{co}\rho_{co} + \frac{\alpha_{do}\rho_{do}\tilde{n}_1}{\tilde{n}_1 - i\omega\rho_{do}}, \tag{33}$$

$$\mu_{\text{eff}} = \alpha_{co}\mu_c + \alpha_{do}\tilde{n}_0 + \frac{\alpha_{do}\rho_{do} i\omega \tilde{n}_2 + \alpha_{do}\mu_c(\tilde{n}_1 - i\omega\tilde{n}_2\rho_{\text{eff1}}/\mu_{\text{eff}})}{\tilde{n}_1 - i\omega\rho_{do}}, \tag{34}$$

$$\rho_{\text{eff2}} = \alpha_{co}\rho_{co} + \alpha_{do}\rho_{do}\frac{\tilde{n}_1 - \tilde{n}_3 i\omega}{\tilde{n}_1 - i\omega\rho_{do}}. \tag{35}$$

Our expression of μ_{eff} slightly differs from the expression obtained by Buyevich because of a different choice in the definition of $\tilde{n}_0$, which is more appropriate for our study.

The final step consists of calculating integrals (8) and (9) to express the coefficients $\tilde{n}_k$ in terms of the effective properties of the surrounding fluid. For that purpose, Eqs. (16)–(18) with $\mathbf{F_x}$ and $\mathbf{S_x}$ given by Eqs. (29) and (30) have to be solved.

The solution of Eqs. (31) and (32) for the averaged fields (equivalent to the so-called Brinkman equations) is well known: it was independently solved by Howells[43] for porous media and Buyevich and Markov[35] for the calculation of the force applied on a moving sphere embedded in an unsteady nonuniform velocity field. However, the resolution of the equations for the conditionally averaged fields would be a challenging task because the variation of the conditional volume fraction with the distance r introduces new terms in the equation.

C. Approximation of the conditional volume fraction by a step function

To simplify this calculation, the evolution of the volume fraction obtained with PY theory in Sec. III A will be approximated by a step function:

$$\alpha_{co,\mathbf{x}} = \chi_p + \alpha_{co}\chi_e, \tag{36}$$

$$\alpha_{do,\mathbf{x}} = \alpha_{do}\chi_e, \tag{37}$$

where

$$\chi_p = \begin{cases} 1 & \text{if } a < r < R_c \\ 0 & \text{if } r > R_c \end{cases}, \quad \chi_e = \begin{cases} 0 & \text{if } a < r < R_c \\ 1 & \text{if } r > R_c, \end{cases}$$

and R_c is given by the following formula:

$$\int_{r=a}^{2a} \alpha_{do,\mathbf{x}}(r)d\mathbf{r} + \int_{r=2a}^{\infty} (\alpha_{do,\mathbf{x}}(r) - \alpha_{do})d\mathbf{r} = \int_{R_c<r<2a} \alpha_{do} d\mathbf{r}. \tag{38}$$

With this definition of R_c, the volume occupied by the particles is conserved and also the asymptotic behavior when $r \to \infty$. In this way, a "core-shell" model is obtained (see Fig. 2). The particle is surrounded by a layer of pure fluid which is itself embedded in a homogeneous effective medium. The condition (38) introduced here to calculate the evolution of the "core radius" R_c with the volume fraction (as illustrated by Fig. 3) is equivalent to the one introduced by Spelt *et al.*[29] The only difference is that these authors expressed R_c in terms of the number density, but it does not affect its estimation.

We can now split the conditionally averaged fields into their value in the pure fluid layer and their value in the homogeneous effective medium:

$$\alpha_{co,\mathbf{x}}\mathbf{V_{c,x}} = \chi_p \mathbf{V^p_{c,x}} + \chi_e \alpha_{co} \mathbf{V^e_{c,x}},$$

$$\alpha_{do,\mathbf{x}}\mathbf{V_{d,x}} = \chi_e \alpha_{do} \mathbf{V^e_{d,x}},$$

$$p^e_{c,x} = \chi_p p^p_{c,x} + \chi_e p^e_{c,x},$$

and thus deduce the balance equations in both parts. In the pure fluid layer $(a<r<R)$,

$$\text{div}(\mathbf{V^p_{c,x}}) = 0, \tag{39}$$

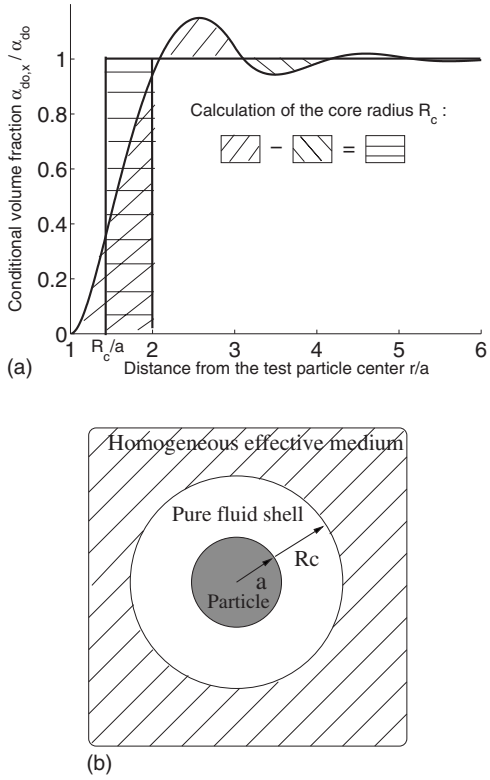

FIG. 2. Approximation of the conditional volume fraction by a step function: core shell model.

$$-\rho_{co}(i\omega)\mathbf{V}^{\mathbf{p}}_{\mathbf{c},\mathbf{x}} = -\nabla p^{p}_{c,x} + \mu_c \Delta \mathbf{V}^{\mathbf{p}}_{\mathbf{c},\mathbf{x}} - \rho_{co}\nabla\Psi. \tag{40}$$

In the homogeneous effective medium ($r>R$),

$$\mathrm{div}(\mathbf{V}^{\mathbf{e}}_{\mathbf{c},\mathbf{x}}) = 0, \tag{41}$$

$$-\rho_{\mathrm{eff}1}(i\omega)\mathbf{V}^{\mathbf{e}}_{\mathbf{c},\mathbf{x}} = -\nabla p^{e}_{c,x} + \mu_{\mathrm{eff}}\Delta \mathbf{V}^{\mathbf{e}}_{\mathbf{c},\mathbf{x}} - \rho_{\mathrm{eff}2}\nabla\Psi. \tag{42}$$

The problem is therefore reduced to the study of a particle embedded in a pure fluid shell (with a viscosity μ_c and a density ρ_{co}), which is itself surrounded by a homogeneous effective medium (with effective properties μ_{eff}, $\rho_{\mathrm{eff}1}$, and $\rho_{\mathrm{eff}2}$).

Now, the boundary conditions must be expressed for the different fields. On the particle surface ($r=a$), the conditionally averaged velocity of the continuous phase is equal to zero that is to say

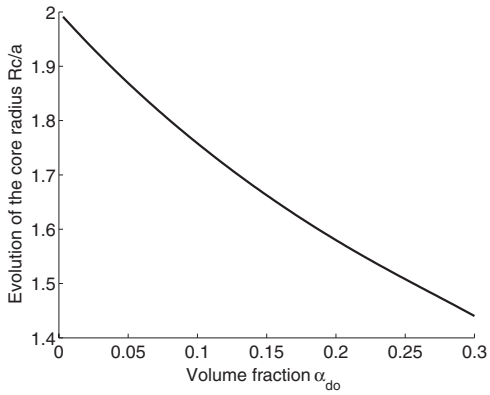

FIG. 3. Evolution of the core radius with the volume fraction.

$$\alpha_{co,\mathbf{x}}\mathbf{V}_{\mathbf{c},\mathbf{x}} = \mathbf{V}^{\mathbf{p}}_{\mathbf{c},\mathbf{x}} = 0.$$

Then, the mass conservation equation for the mean velocity [$\mathrm{div}(\mathbf{V}_{\mathbf{x}})=0$] imposes the following condition at the core-shell surface ($r=R_c$):

$$\mathbf{V}^{\mathbf{p}}_{\mathbf{c},\mathbf{x}} = \alpha_{co}\mathbf{V}^{\mathbf{e}}_{\mathbf{c},\mathbf{x}} + \alpha_{do}\mathbf{V}^{\mathbf{e}}_{\mathbf{d},\mathbf{x}}, \tag{43}$$

where $\mathbf{V}^{\mathbf{e}}_{\mathbf{d},\mathbf{x}}$ can be expressed in terms of $\mathbf{V}^{\mathbf{e}}_{\mathbf{c},\mathbf{x}}$ and $\nabla\Psi$ through Eq. (18).

The momentum conservation gives the following condition in $r=R_c$:

$$\mathbf{\Pi}^{\mathbf{p}}_{\mathbf{x}} \cdot \mathbf{n} = \mathbf{\Pi}^{\mathbf{e}}_{\mathbf{x}} \cdot \mathbf{n}, \tag{44}$$

where $\mathbf{n}$ is the normal vector to the surface of the core and $\mathbf{\Pi}^{\mathbf{p}}_{\mathbf{x}}$ and $\mathbf{\Pi}^{\mathbf{e}}_{\mathbf{x}}$ are, respectively, the strain tensors in the pure layer and in the homogeneous effective medium:

$$\mathbf{\Pi}^{\mathbf{p}}_{\mathbf{x}} = -p^{p}_{c,x} + 2\mu_c\mathbf{D}^{\mathbf{p}}_{\mathbf{c},\mathbf{x}} \quad \text{with } \mathbf{D}^{\mathbf{p}}_{\mathbf{c},\mathbf{x}} = 1/2(\nabla\mathbf{V}^{\mathbf{p}}_{\mathbf{c},\mathbf{x}} + \nabla^t\mathbf{V}^{\mathbf{p}}_{\mathbf{c},\mathbf{x}}),$$

$$\mathbf{\Pi}^{\mathbf{e}}_{\mathbf{x}} = -p^{e}_{c,x} + 2\mu_{\mathrm{eff}}\mathbf{D}^{\mathbf{e}}_{\mathbf{c},\mathbf{x}} \quad \text{with } \mathbf{D}^{\mathbf{e}}_{\mathbf{c},\mathbf{x}} = 1/2(\nabla\mathbf{V}^{\mathbf{e}}_{\mathbf{c},\mathbf{x}} + \nabla^t\mathbf{V}^{\mathbf{e}}_{\mathbf{c},\mathbf{x}}).$$

Finally, far from the test particle ($r\to\infty$), the perturbation induced by its presence vanishes so that

$$\{\mathbf{V}^{\mathbf{e}}_{\mathbf{c},\mathbf{x}}, p^{e}_{c,x}\} \to \{\mathbf{V}_{\mathbf{c}}, p_c\}. \tag{45}$$

With Eqs. (31), (32), and (39)–(45), we have derived all the equations and boundary conditions necessary to compute integrals (8) and (9), which reduce to

$$\mathbf{F} = \frac{3\alpha_d}{4\pi a^3}\oint \mathbf{\Pi}^{\mathbf{p}}_{\mathbf{x}} \cdot \mathbf{n} dS, \tag{46}$$

$$\mathbf{S} = \frac{3\alpha_d}{4\pi a^3}\oint^{(s)} \mathbf{a}\otimes(\mathbf{n}\cdot\mathbf{\Pi}^{\mathbf{p}}_{\mathbf{x}})dS. \tag{47}$$

D. Calculation of the closure terms

To solve these equations, the velocity and pressure fields must be expressed in terms of spherical functions according to the method developed by Buyevich and Markov.[42] The details of this calculation can be found in Appendixes A and B. In this section, we only give the final expressions of the coefficient $\tilde{n_k}$ which result from the identification of the expression of $\mathbf{F}$ and $\mathbf{S}$ calculated in the Appendix and formulas (27) and (28).

1. Expression of $\tilde{n}_0$

$$\tilde{n}_0 = 3\frac{\mu_c\beta_c}{\beta_{\mathrm{eff}}}\left[\left(\dot{S}_2(\gamma) + \left(\frac{4}{\gamma}+\frac{\gamma}{2}\right)S_2(\gamma)\right)V_{C_1} + \left(\dot{Q}_2(\gamma) + \left(\frac{4}{\gamma}+\frac{\gamma}{2}\right)Q_2(\gamma)\right)V_{C_2} - \left(\frac{10}{\gamma}+\gamma\right)V_{C_3} - \gamma V_{C_4}\right],$$

where

$$S_2(X) = \frac{(X^2-3X+3)e^X - (X^2+3X+3)e^{-X}}{2X^4},$$

$$Q_2(X) = \frac{(X^2+3X+3)e^{-X}}{X^4},$$

and

$$\epsilon = \beta_{\text{eff}} a, \quad \gamma = \beta_c a,$$

$$\eta = \beta_{\text{eff}} R_c, \quad \delta = \beta_c R_c,$$

$$\beta_c^2 = -(i\omega)\rho_{co}/\mu_c, \quad \beta_{\text{eff}}^2 = -(i\omega)\rho_{\text{eff }1}/\mu_{\text{eff}},$$

$$\kappa = \beta_c \mu_c / \beta_{\text{eff}} \mu_{\text{eff}}.$$

Finally, $V_C = [V_{C_1} V_{C_2} V_{C_3} V_{C_4} V_{C_5} V_{C_6}]^t$ is a column vector whose expression is given by

$$V_C = M_2^{-1} V_{A2}, \tag{48}$$

where the expressions of M_2 and V_{A2} are given in Appendix C.

2. Expression of $\tilde{n}_1$, $\tilde{n}_2$, and $\tilde{n}_3$

$$\tilde{n}_1 = -\mu_c \beta_c^2 [S_1(\gamma) V_{E_1} + Q_1(\gamma) V_{E_2} - V_{E_3} - V_{E_4}], \tag{49}$$

$$\tilde{n}_2 = \frac{\mu_c \beta_c^2}{\beta_{\text{eff}}^2} [S_1(\gamma)(3V_{D_1} + V_{E_1}) + Q_1(\gamma)(3V_{D_2} + V_{E_2}) - (3V_{D_3} + V_{E_3}) - (3V_{D_4} + V_{E_4})], \tag{50}$$

$$\tilde{n}_3 = \rho_{co} + \mu_c \beta_c^2 [S_1(\gamma) V_{F_1} + Q_1(\gamma) V_{F_2} - V_{F_3} - V_{F_4}], \tag{51}$$

where

$$S_1(X) = \frac{(X-1)e^X + (X+1)e^{-X}}{2X^3},$$

$$Q_1(X) = \frac{(X+1)e^{-X}}{X^3},$$

and V_D, V_E, and V_F are some column vectors whose expressions are given by

$$V_D = M_1^{-1} V_{A1}, \tag{52}$$

$$V_E = M_1^{-1} V_{M1}, \tag{53}$$

$$V_F = M_1^{-1} V_{P1}, \tag{54}$$

where the expression of M_1, V_{A1}, V_{M1}, and V_{P1} are given in Appendix C.

With these expressions, the coefficients $\tilde{n_k}$ are related to the effective parameters μ_{eff}, $\rho_{\text{eff}1}$, and $\rho_{\text{eff}2}$, which are themselves related to the coefficients $\tilde{n_k}$ through Eqs. (33)–(35). Thus, the system is closed and the coefficients $\tilde{n_k}$ can be calculated either with a simple iterative procedure or with more elaborate numerical schemes such as the "globally convergent Newton's method."

IV. RESULTS AND COMPARISON WITH EXPERIMENTS

A. Final dispersion equation

Then, the expression of the force (27) and the stresslet (28) can be substituted in the linearized system (1)–(7), and the dispersion equation can be derived for a plane wave by considering fields of the form: $G = G_o + \bar{G} e^{i(k_* x - \omega t)}$, where $\bar{G}$ is the amplitude of the wave, G_o the equilibrium state, and k_* the complex effective wave number. As calculated in a previous paper,[30] the effective wave number k_* is the solution of the following quadratic equation:

$$Ak_*^4 + Bk_*^2 + C = 0,$$

$$A = d_r h_c \left[\frac{(\lambda_c + 2\mu_c)}{\rho_{do} i\omega} + \frac{r c_{co}^2}{\alpha_{co}\omega^2} \right],$$

$$B = -d_r \left[h_c + \frac{N_0^* + (\lambda_c + 2\mu_c)(\alpha_{co} + \alpha_{do} h_v)/\alpha_{do}\rho_{do}}{i\omega} \right] - \frac{c_{co}^2}{\alpha_{co}\omega^2} \frac{[1 + d_r r h_v]}{[1 + \alpha_{do}\xi_d/\alpha_{co}\xi_c]}, \tag{55}$$

$$C = 1 + d_r h_v,$$

where

$$h_v = \frac{N_1^*}{N_1^* + i\omega(N_3^* - 1)}, \quad h_c = \frac{N_2^*}{N_1^* + i\omega(N_3^* - 1)}$$

and

$$N_k^* = \frac{n_k^*}{\rho_{do}}, \quad d_r = \frac{\alpha_{do}\rho_{do}}{\alpha_{co}\rho_{co}}, \quad r = \frac{\rho_{co}}{\rho_{do}}.$$

We can note that the coefficient $\alpha_{do}\rho_{do}$ was missing in the expression of B in our previous paper (just in the manuscript, the good expression had been considered for the computation). We can also note that a new coefficient $[1 + \alpha_{do}\xi_d/\alpha_{co}\xi_c]$ (with ξ_k the compressibility of phase k) appears, as we have taken into account the compressibility of the dispersed phase in Eq. (2).

B. Comparison of the different theories with experiments

Now, the results of this corrected effective medium theory (that take into account spatial correlations) can be compared to previous results[30] obtained with the same theory but without spatial correlations (that is to say when a homogeneous effective medium is considered around the test particle) and also with the classical coupled phase theory (when the test particle is supposed to be surrounded by the pure continuous phase). For that purpose, we will consider the experiments performed by Hipp *et al.*[33] who measured the attenuation of acoustical waves in solutions of silica particle in water for different concentrations, frequencies, and particle sizes. Before analyzing these curves, let us recall some elements which will be useful to understand the influence of spatial correlations. When an acoustical wave propagates through a solution of rigid particles, the particles do not

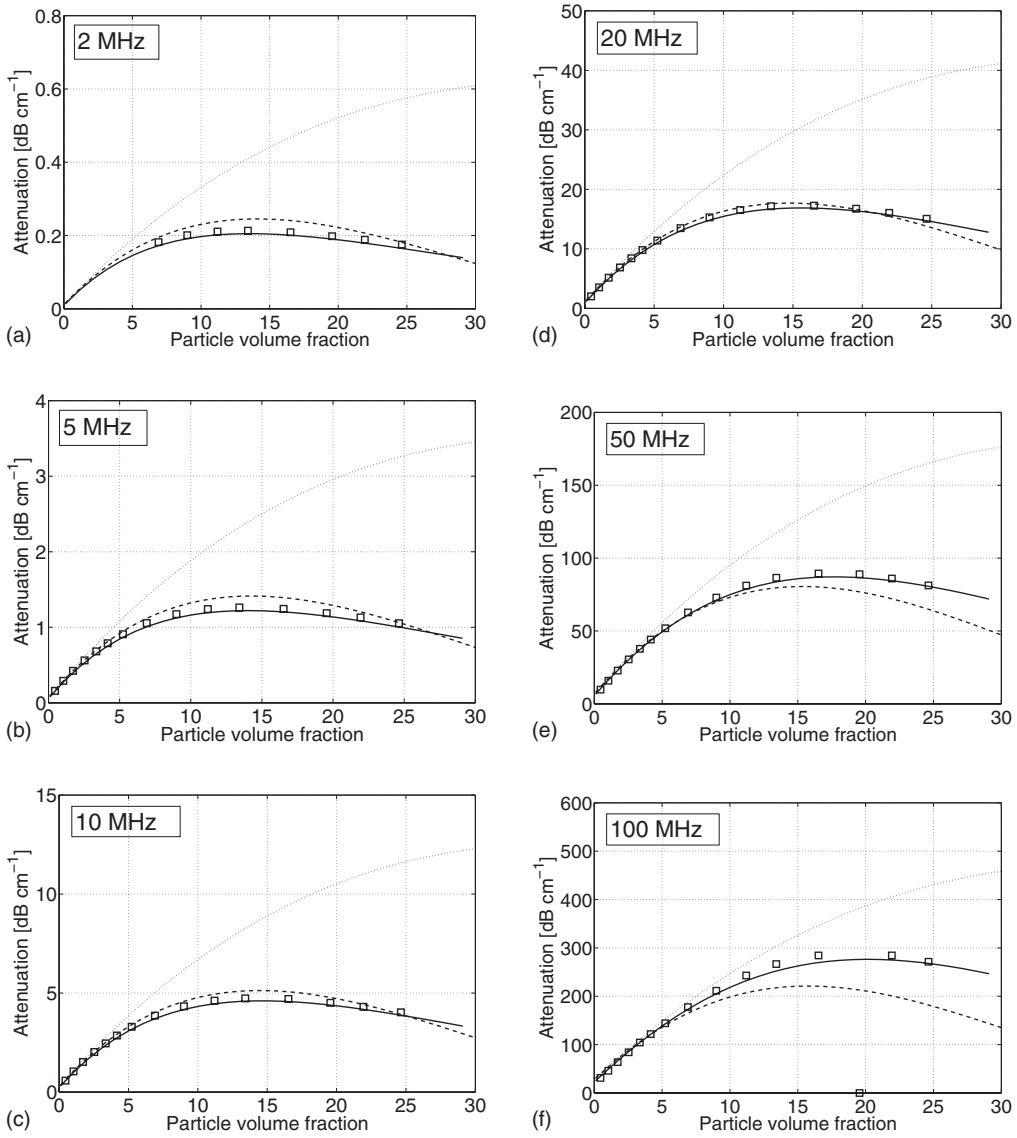

FIG. 4. Attenuation as a function of the volume fraction at various frequencies for silica particles of 56 nm radius in water. The solid lines (-) correspond to the new effective theory, the broken lines (–) to the effective theory without spatial correlationss, the dotted line (..) to the classical coupled phase theory, and the symbols to the experimental data.

move with the same velocity as the surrounding fluid because of the difference of density between them and the surrounding fluid. As a consequence, a dipolar wave is scattered and a part of the energy of the impinging wave is therefore redirected, inducing a loss of spatial coherence. Some energy is also dissipated because of the viscosity of the surrounding fluid which slows down the movement of the particle and therefore converts energy from the compressional propagation mode to a viscous lossy mode. The combination between these two scattering mechanisms is referred to as the "viscoinertial" phenomena. The characteristic length for the decrease of the viscous lossy wave is the size of the boundary layer δ_v which is related to the frequency ω according to the following formula:

$$\delta_v = \sqrt{\frac{2\mu_c}{\omega\rho_c}}.$$

In concentrated suspensions, viscous interactions between neighboring particles may appear according to their concentration and the frequency of the propagating wave. As long as $\delta_v \ll R_c - a$, the properties of the fluid in the boundary layer are very close to the properties of the surrounding pure fluid (because $\alpha_{do,\mathbf{x}} \approx 0$ in this area) and thus the force and the stresselet can be estimated by considering a particle embedded in the pure liquid (as it is done in the classical coupled phase theory). However, when $\delta_v \gg R_c - a$, the variation of the effective properties due to the spatial correlations only concerns a thin part of the boundary layer and thus the approximation of the surrounding fluid by a homogeneous effective medium for the calculation of the closure terms (as it was done in a previous paper[30]) should give good results. As $R_c - a \approx a$, the transition between these two limiting case should happen when $\delta_v \approx a$. For the two suspensions considered here, the corresponding characteristic frequencies are, respectively, of $f_c = 101$ MHz for Fig. 4 and $f_c = 11$ MHz for Fig. 5. Finally, as δ_v is inversely proportional to the frequency, the condition $\delta_v \ll a$ correspond to high frequencies $f \gg f_c$ and the condition $\delta_v \gg a$ to low frequencies $f \ll f_c$.

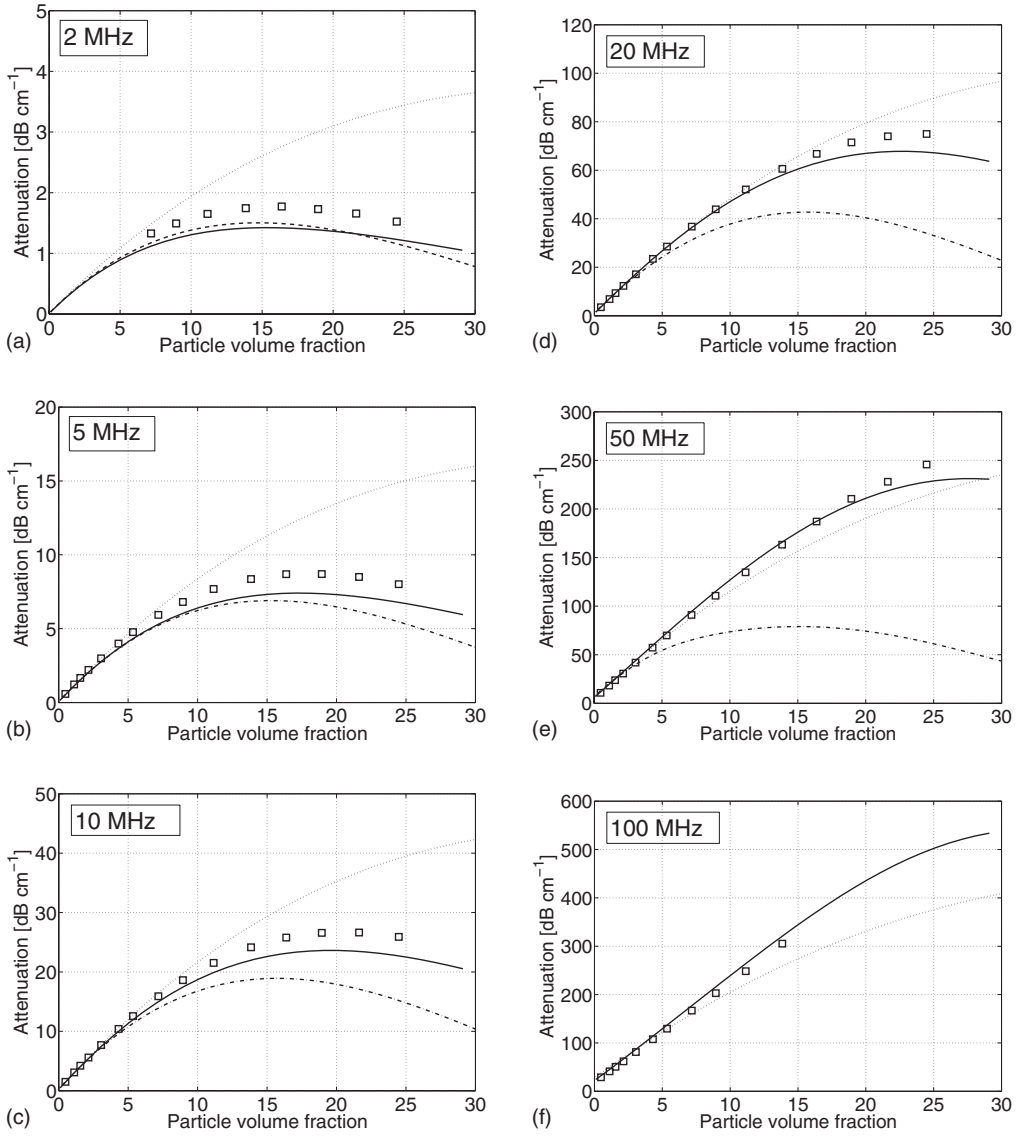

FIG. 5. Attenuation as a function of the volume fraction at various frequencies for silica particles of 164.5 nm radius in water. The solid lines (-) correspond to the new effective theory, the broken lines (–) to the effective theory without spatial correlationss, the dotted line (..) to the classical coupled phase theory, and the symbols to the experimental data.

Effectively, we can see on the different figures that for frequencies $f \ll f_c$, the experimental data are close to the results obtained with the homogeneous effective medium[30] (dash dotted lines), whereas for frequencies $f \gg f_c$, the results are closer to the curves obtained with the classical coupled phase theory (dotted line). As a consequence, none of these theories can properly describe the sound propagation in concentrated suspensions for a wide range of frequencies and particle sizes. For high frequencies and particle concentration, the homogeneous effective theory even gives unphysical effective parameters; that is why we have not plotted the corresponding curves (see Fig. 5 at 100 MHz). With the introduction of spatial correlations, we obtain a model (solid lines) which gives good results for both limiting cases. As expected, the results are less accurate for the transition ($f \approx f_c$) because the progressive evolution of the conditional volume fraction has been approximated by a step function. We can note at this point that equivalent results should be obtained with the model of Spelt *et al.*[29] based on the ECAH[4,5] decomposition. Of course, for low volume fraction ($\alpha_{do} < 5\%$), all these theories give the same results because in this case, the effective properties of the surrounding fluid are close to the properties of the pure fluid. Concerning the remaining discrepancies between our theory and the experiments, different phenomena might explain them such as the polydispersity of the solution or collisions between neighboring particles. Another possible effect might be the increase of the importance of thermal effects in concentrated suspension. It is well known that in dilute suspensions of silica particles in water, viscoinertial effects are more important than thermal ones[44,45] because the first ones are proportional to $(1-r)=O(1)$ in these suspensions and thermal effects to $(\gamma-1) \ll 1$ (where γ is the specific heat ratio). However, viscous interactions make the attenuation induced by viscoinertial effects decrease. In the same way, there will also be some thermal interactions due to the overlapping of viscous boundary layer, which will make the attenuation induced by this scattering mechanism decrease. However, as the viscous boundary layer δ_v is usually larger than the thermal boundary

layer δ_t for aqueous solutions (see, for example, Hipp *et al.*[46]), viscoinertial interactions will be more important than thermal interactions and therefore thermal attenuation might become more significant in concentrated suspensions. It would be interesting to investigate this question in a future work.

To conclude this discussion, we can notice that unlike interactions of compressional waves, viscous coupling tends to diminish the attenuation induced by the suspension when the concentration increases, which is quite unusual.

V. CONCLUSION

An effective medium coupled phase theory has been derived to properly describe the sound propagation in concentrated suspensions of rigid particles. An excellent agreement is obtained between this theory and the experimental data of Hipp *et al.* who measured the attenuation induced by the presence of silica particles in water for different particle sizes, concentration up to 30%, and frequencies between 2 and 100 MHz. Moreover, the influence of spatial correlations on the propagation in solutions of rigid particles has been clearly identified. This theory could be improved by considering the exact evolution of the conditional volume fraction with the distance from the test particle center instead of the core-shell aproximation. It could be also extended to polydisperse suspensions but it would require the knowledge of the distribution function in polydisperse suspensions which is not an easy matter.[47] Finally, we can underline that the expressions obtained here for the force and the stresslet could also be used for hydrodynamic studies of concentrated suspensions of particles, as long as the characteristic macroscopic length of the flow is much larger than the size of the particles, and as long as the flow does not modify the distribution of the particles.

ACKNOWLEDGMENTS

The authors would like to thank A. K. Hipp, G. Storti, and M. Morbidelli (Department of Chemical Engineering, ETH Zürich) for kindly providing us with the results of their experiments and D. Lhuillier (Institut Jean le Rond D'Alembert, CNRS) for numerous and fruitful discussions.

APPENDIX A: RESOLUTION OF THE SYSTEM

First, we can subtract Eqs. (31) and (32) for the averaged fields from Eqs. (41) and (42) for the conditionally averaged fields in the region $r>R_c$ to obtain equations for the perturbation due to the presence of the test sphere:

$$\mathrm{div}(\mathbf{V_c^{e*}}) = 0, \tag{A1}$$

$$-\rho_{\mathrm{eff}\,1}(i\omega)\mathbf{V_c^{e*}} = -\nabla p_c^{e*} + \mu_{\mathrm{eff}}\Delta\mathbf{V_c^{e*}}, \tag{A2}$$

where

$$\mathbf{V_c^{e*}} = \mathbf{V_{c,x}^{e}} - \mathbf{V_c},$$

$$p_c^{e*} = p_{c,x}^{e} - p_c.$$

Then, the boundary conditions can easily be rewritten in terms of the perturbation fields:

$$\mathbf{V_{c,x}^{p}} = 0 \quad \text{in } r = a \tag{A3}$$

$$\mathbf{V_{c,x}^{p}} - \alpha_{co}\mathbf{V_c^{e*}} - \alpha_{do}\mathbf{V_d^{e*}} = \alpha_{co}\mathbf{V_c} + \alpha_{do}\mathbf{V_d} \quad \text{in } r = R_c, \tag{A4}$$

$$\mathbf{\Pi_x^p}\,.\,\mathbf{n} - \mathbf{\Pi^{e*}}\,.\,\mathbf{n} = \mathbf{\Pi_c}\,.\,\mathbf{n} \quad \text{in } r = R_c, \tag{A5}$$

$$\{\mathbf{V_c^{e*}}, p_c^{e*}\} \to 0 \quad \text{when } r \to \infty. \tag{A6}$$

Equations (31), (32), (39), (40), (A1), and (A2) can all be written under the form

$$\mathrm{div}(\mathbf{U}) = 0, \tag{A7}$$

$$(\Delta - \beta^2)\mathbf{U} = \nabla R, \tag{A8}$$

where

$$\{U = \mathbf{V_c}, R = 1/\mu_{\mathrm{eff}}(p_c + \rho_{\mathrm{eff}\,2}\psi), \beta = \beta_{\mathrm{eff}}\} \quad \text{for the first set of equations,}$$

$$\{U = \mathbf{V_{c,x}^{p}}, R = 1/\mu_c(p_{c,x}^{p} + \rho_{co}\psi), \beta = \beta_c\} \quad \text{for the second,}$$

$$\{U = \mathbf{V_c^{e*}}, R = 1/\mu_{\mathrm{eff}}(p_c^{e*}), \beta = \beta_{\mathrm{eff}}\} \text{ for the third one.}$$

Then the velocity and pressure fields can be expressed in terms of spherical functions:

$$U(\mathbf{r}) = \sum_{k=0}^{\infty}\left[F_k(r)s_k(\theta,\phi)\frac{\mathbf{r}}{r} + G_k(r)r\,\nabla\, s_k(\theta,\phi) + H_k(r)\mathbf{r} \times \nabla s_k(\theta,\phi)\right], \tag{A9}$$

$$R(\mathbf{r}) = \sum_{k=0}^{\infty} L_k(r)s_k(\theta,\phi), \tag{A10}$$

where r, θ, and ϕ are the spherical coordinates. $F_k s_k$ denotes the summation

$$F_k s_k = F_k^0(r)P_k(\cos(\theta)) + \sum_{k'=1}^{k}\left[F_{k+}^{k'}(r)P_k^{k'}(\cos(\theta))\cos(k'\phi)\right. \tag{A11}$$

$$\left. + F_{k-}^{k'}(r)P_k^{k'}(\cos(\theta))\sin(k'\phi)\right], \tag{A12}$$

and P_k and $P_k^{k'}$ are, respectively, the principal and associated Legendre functions. Of course, $G_k s_k$ and $H_k s_k$ denote similar summations.

As the inertial terms due to the rotation of the particle are neglected $H_k=0$ and because of the symmetry of the problem (which is invariant by any rotation of ϕ angle), only the principal Legendre functions are required:

$$F_k s_k = F_k^0(r) P_k(\cos(\theta)), \tag{A13}$$

$$G_k s_k = G_k^0(r) P_k(\cos(\theta)). \tag{A14}$$

Then, by replacing the preceding expressions of $\mathbf{U}$ and R in the conservation Eqs. (A7) and (A8), Buyevich and Markov[42] obtain the following expressions for F_k^0 and G_k^0:

$$F_k^0 = A_k S_k(\xi) + B_k Q_k(\xi) - k M_k \left(\frac{\xi}{\beta}\right)^{k-1} + (k+1) N_k \left(\frac{\xi}{\beta}\right)^{-k-2}, \tag{A15}$$

$$G_k^0 = \frac{2}{k(k+1)} A_k \left(S_k(\xi) + \frac{\xi}{2}\dot{S}_k(\xi)\right) + \frac{2}{k(k+1)} B_k \left(Q_k(\xi) + \frac{\xi}{2}\dot{Q}_k(\xi)\right) - M_k \left(\frac{\xi}{\beta}\right)^{k-1} - N_k \left(\frac{\xi}{\beta}\right)^{-k-2}, \tag{A16}$$

where the coefficients A_k, B_k, M_k, and N_k are some constants which must be determined from the boundary conditions for each order k; $\dot{S}_k$ and $\dot{Q}_k$ are the derivatives of S_k and Q_k with respect to ξ; and the expressions of S_k and Q_k are given by the following expressions:

$$S_k = 2^k \xi^{k-1} \frac{d^k}{d(\xi^2)^k} \frac{\sinh \xi}{\xi}, \tag{A17}$$

$$Q_k = (-2)^k \xi^{k-1} \frac{d^k}{d(\xi^2)^k} \frac{\exp(-\xi)}{\xi}, \tag{A18}$$

with $\xi \equiv \beta r$.

We can now introduce the following notations: the constants $\{A_k, B_k, M_k, N_k\}$ are, respectively, equal to the following:

- $\{a_k, b_k, m_k, n_k\}$ for the first set of equations (for the average fields in the original frame of reference),
- $\{a_k^p, b_k^p, m_k^p, n_k^p\}$ for the second set of equations (for the conditionally averaged field in the pure fluid shell), and
- $\{a_k^e, b_k^e, m_k^e, n_k^e\}$ for the third set of equations (for the perturbation in the effective homogeneous medium).

We can easily deduce from the boundary conditions that: (a) b_k and n_k are null because the averaged fields are bounded when $r \to 0$, and (b) a_k^e and m_k^e are null because the perturbation vanishes when $r \to \infty$.

Now, there only remains to express the relations between the remaining coefficients, deduced from the boundary conditions (A3)–(A6). At first order ($k=1$), we obtain

$$M_1 V_1 = a_1 V_{A1} + m_1 V_{M1} - (i\omega)\, v_d|_{r=0} V_{P1} \tag{A19}$$

and at second order ($k=2$)

$$M_2 V_2 = a_2 V_{A2} + m_2 V_{M2}, \tag{A20}$$

where the expression of the column vectors V_{A1}, V_{M1}, V_{A2}, and V_{M2} and the matrices M_1 and M_2 are given in Appendix C and the expressions of V_1 and V_2 are given by

$$V_1 = \begin{bmatrix} a_1^p \\ b_1^p \\ m_1^p \\ n_1^p/a^3 \\ b_1^e \\ n_1^e/R_c^3 \end{bmatrix}, \quad V_2 = \begin{bmatrix} a_2^p \\ b_2^p \\ am_2^p \\ n_2^p/a^4 \\ b_2^e \\ n_2^e/R_c^4 \end{bmatrix}.$$

APPENDIX B: CALCULATION OF THE FORCE AND THE STRESSLET

The next step consists of expressing the force $\mathbf{F}$ and the stresslet $\mathbf{S}$ in terms of the coefficients a_k^p, b_k^p, m_k^p, and n_k^p. It is important to note that only the coefficients of first order ($k=1$) are required for the calculation of the force and the coefficients of second order ($k=2$) for the calculation of the stresslet because the contribution of the other terms vanishes when the integration over the surface of the sphere is performed. The following expressions are obtained:

$$\mathbf{F} = \alpha_{do}\mu_c\beta_c^2 \left[S_1(\gamma) a_1^p + Q_1(\gamma) b_1^p - m_1^p - \frac{n_1^p}{a^3} \right] \mathbf{e_z} + \alpha_{do}\rho_{co} \nabla \Psi,$$

$$\mathbf{S} = \frac{\alpha_{do}\mu_c\beta_c}{5} (3\mathbf{e_z} \otimes \mathbf{e_z} - \mathbf{I}) \times \left[\left(\dot{S}_2(\gamma) + \left(\frac{4}{\gamma} + \frac{\gamma}{2} \right) S_2(\gamma) \right) a_2^p + \left(\dot{Q}_2(\gamma) + \left(\frac{4}{\gamma} + \frac{\gamma}{2} \right) Q_2(\gamma) \right) b_2^p - \left(\frac{10}{\gamma} + \gamma \right) am_2^p - \gamma \frac{n_2^p}{a^4} \right].$$

The final step consists of expressing the coefficients a_1, m_1, a_2, and m_2 in terms of the averaged fields in $r=0$:

$$a_1 \mathbf{e_z} = 3/\beta_{\text{eff}}^2 \, \Delta \mathbf{V_c}|_{r=0},$$

$$m_1 \mathbf{e_z} = 1/\beta_{\text{eff}}^2 \, \Delta \mathbf{V_c}|_{r=0} - \mathbf{V_c}|_{r=0},$$

$$a_2 (3\mathbf{e_z} \otimes \mathbf{e_z} - \mathbf{I}) = 30/\beta_{\text{eff}}^2 \, \nabla^s \Delta \mathbf{V_c}|_{r=0},$$

$$m_2 (3\mathbf{e_z} \otimes \mathbf{e_z} - \mathbf{I}) = - \nabla^s \mathbf{V_c}|_{r=0} + 1/\beta_{\text{eff}}^2 \, \nabla^s \Delta \mathbf{V_c}|_{r=0}.$$

Finally, with the relation $\Delta^2 \mathbf{V_c} = \beta_{\text{eff}}^2 \Delta \mathbf{V_c}$ [which can be easily deduced from Eqs. (31) and (32)] and by comparing the above expressions with Eqs. (27) and (28), we obtain the expression of the coefficients $\tilde{n}_k$.

APPENDIX C: EXPRESSION OF THE MATRICES M_1, M_2 AND THE VECTORS V_{A1}, V_{M1}, V_{P1}, V_{A2},V_{M2}

$$M_1 = \begin{bmatrix} S_1(\gamma) & Q_1(\gamma) & -1 & 2 & 0 & 0 \\ S_1(\gamma)+\gamma/2\dot{S}_1(\gamma) & Q_1(\gamma)+\gamma/2\dot{Q}_1(\gamma) & -1 & -1 & 0 & 0 \\ S_1(\delta) & Q_1(\delta) & -1 & 2(a/R_c)^3 & -\alpha_A Q_1(\eta) & -2\alpha_B \\ S_1(\delta)+(\delta/2)\dot{S}_1(\delta) & Q_1(\delta)+(\delta/2)\dot{Q}_1(\delta) & -1 & -(a/R_c)^3 & -\alpha_A(Q_1(\eta)+\eta/2\dot{Q}_1(\eta)) & \alpha_B \\ 2\kappa\dot{S}_1(\delta) & 2\kappa\dot{Q}_1(\delta) & -\kappa\delta & -\kappa(a/R_c)^3(\delta+12/\delta) & -2\dot{Q}_1(\eta) & \eta+12/\eta \\ \kappa(\delta/2\ddot{S}_1(\delta)+\dot{S}_1(\delta)) & \kappa(\delta/2\ddot{Q}_1(\delta)+\dot{Q}_1(\delta)) & 0 & 6\kappa a^3/\delta R_c^3 & -(\eta/2\ddot{Q}_1(\eta)+\dot{Q}_1(\eta)) & -6/\eta \end{bmatrix},$$

$$M_2 = \begin{bmatrix} S_2(\gamma) & Q_2(\gamma) & -2 & 3 & 0 & 0 \\ 1/3(S_2(\gamma)+\gamma/2\dot{S}_2(\gamma)) & 1/3(Q_2(\gamma)+(\gamma/2)\dot{Q}_2(\gamma)) & -1 & -1 & 0 & 0 \\ S_2(\delta) & Q_2(\delta) & -2R_c/a & 3(a/R_c)^4 & -\alpha_A Q_2(\eta) & -3\alpha_B \\ 1/3(S_2(\delta)+(\delta/2)\dot{S}_2(\delta)) & 1/3(Q_2(\delta)+(\delta/2)\dot{Q}_2(\delta)) & -R_c/a & -(a/R_c)^4 & -\alpha_A/3(Q_2(\eta)+(\eta/2)\dot{Q}_2(\eta)) & \alpha_B \\ 2\kappa\dot{S}_2(\delta) & 2\kappa\dot{Q}_2(\delta) & -\kappa R_c/a(\delta+4/\delta) & -\kappa a^4/R_c^4(\delta+24/\delta) & -2\dot{Q}_2(\eta) & (\eta+24/\eta) \\ \kappa((4/\delta+\delta/2)S_2(\delta)-\dot{S}_2(\delta)) & \kappa((4/\delta+\delta/2)Q_2(\delta)-\dot{Q}_2(\delta)) & -6\kappa R_c/a\delta & 24\kappa a^4/\delta R_c^4 & \dot{Q}_2(\eta)-(4/\eta+\eta/2)Q_2(\eta) & -24/\eta \end{bmatrix},$$

$$V_{A1} = \begin{bmatrix} 0 \\ 0 \\ \alpha_A S_1(\eta) \\ \alpha_A(S_1(\eta)+\eta/2\dot{S}_1(\eta)) \\ 2\dot{S}_1(\eta) \\ \dot{S}_1(\eta)+\eta/2\ddot{S}_1(\eta) \end{bmatrix}, \quad V_{M1} = \begin{bmatrix} 0 \\ 0 \\ -\alpha_B \\ -\alpha_B \\ -\eta \\ 0 \end{bmatrix}, \quad V_{P1} = \begin{bmatrix} 0 \\ 0 \\ \alpha_C \\ \alpha_C \\ (\rho_{\text{eff}2}-\rho_{co})R_c/\mu_{\text{eff}}\beta_{\text{eff}} \\ 0 \end{bmatrix},$$

$$V_{A2} = \begin{bmatrix} 0 \\ 0 \\ \alpha_A S_2(\eta) \\ \alpha_A/3(S_2(\eta)+\eta/2\dot{S}_2(\eta)) \\ 2\dot{S}_2(\eta) \\ (4/\eta+\eta/2)S_2(\eta)-\dot{S}_2(\eta) \end{bmatrix}, \quad V_{M2} = \begin{bmatrix} 0 \\ 0 \\ -2\alpha_B R_c \\ -2\alpha_B R_c \\ -(4/\eta+\eta/2)R_c \\ -\dfrac{6}{\eta}R_c \end{bmatrix},$$

with

$$\alpha_A = \alpha_{co} + \alpha_{do}(c_1+c_2), \quad \alpha_B = \alpha_{co} + \alpha_{do}c_1, \quad \alpha_C = \alpha_{do}\frac{\tilde{n}_3 - \rho_{do}}{\tilde{n}_1 - i\omega\rho_{do}},$$

$$c_1 = \frac{\tilde{n}_1}{\tilde{n}_1 - i\omega\rho_{do}}, \quad c_2 = \frac{\tilde{n}_2\beta_{\text{eff}}^2}{\tilde{n}_1 - i\omega\rho_{do}}.$$

[1] R. E. Challis, M. J. W. Povey, M. L. Mather, and A. K. Holmes, "Ultrasound techniques for characterizing colloidal dispersions," Rep. Prog. Phys. **68**, 1541–1637 (2005).

[2] A. S. Dukhin and P. J. Goetz, "Acoustic and electroacoustic spectroscopy for characterizing concentrated dispersions and emulsions," Adv. Colloid Interface Sci. **92**, 73–132 (2001).

[3] E. L. Carstensen and L. L. Foldy, "Propagation of sound through a liquid containing bubbles," J. Acoust. Soc. Am. **19**, 481–501 (1947).

[4] J. R. Allegra and S. A. Hawley, "Attenuation of sound in suspensions and emulsions: Theory and experiments," J. Acoust. Soc. Am. **51**, 1545–1564 (1972).

[5] P. S. Epstein and R. R. Carhart, "The absorption of sound in suspensions and emulsions. I. Waterfog in air," J. Acoust. Soc. Am. **25**, 553–565 (1953).

[6] J. M. Evans and K. Attenborough, "Coupled phase theory for sound propagation in emulsions," J. Acoust. Soc. Am. **102**, 278–282 (1997).

[7] D. A. Gubaidullin, and R. I. Nigmatulin, "On the theory of acoustic waves in polydispersed gaz-vapor-droplet suspensions," Int. J. Multiphase Flow **26**, 207–228 (2000).

[8] N. A. Gumerov, A. I. Ivandaev, and R. I. Nigmatulin, "Sound waves in monodisperse gas-particle or vapour-droplet mixtures," J. Fluid Mech. **193**, 53–74 (1988).

[9] R. Duraiswami and A. Prosperetti, "Linear pressure wave in fogs," J. Fluid Mech. **299**, 187–215 (1995).

[10] N. A. Gumerov and R. Duraiswami, "Computation of scattering from N spheres using multipole reexpansion," J. Acoust. Soc. Am. **112**(6), 2688–2701 (2002).

[11] N. A. Gumerov and R. Duraiswami, "Computation of scattering from clusters of spheres using fast multipole method," J. Acoust. Soc. Am. **117**,

1744–1761 (2005).
[12]A. J. C. Ladd, "Hydrodynamic interactions in a suspension of spherical particles," J. Chem. Phys. **88**(8), 5051–5063 (1988).
[13]A. J. C. Ladd, "Hydrodynamic interactions and the viscosity of suspensions of freely moving spheres," J. Chem. Phys. **90**, 1149–1157 (1989).
[14]A. J. C. Ladd, "Hydrodynamic transport coefficients of random dispersions of hard spheres," J. Chem. Phys. **93**, 3484–3494 (1990).
[15]G. Mo and A. S. Sangani, "A method for computing Stokes flow interactions among spherical objects and its application to suspensions of drops and porous particles," Phys. Fluids **6**, 1637–1652 (1994).
[16]L. L. Foldy, "The multiple scattering of waves. I. General theory of isotropic scattering by randomly distributed scatterers," Phys. Rev. **67**, 107–119 (1945).
[17]E. J. Hinch, "An averaged-equation approach to particle interactions in a fluid suspension," J. Fluid Mech. **83**, 695–720 (1977).
[18]F. S. Henyey, "Corrections to Foldy's effective medium theory for propagation in bubble clouds and other collections of very small scatterers," J. Acoust. Soc. Am. **105**(4), 2149–2153 (1999).
[19]A. S. Sangani, "A pairwise interaction theory for determining the linear acoustic properties of dilute bubbly liquids," J. Fluid Mech. **232**, 221–284 (1991).
[20]Z. Ye and L. Ding, "Acoustic dispersion and attenuation relations in bubbly mixture," J. Acoust. Soc. Am. **98**, 1629–1636 (1995).
[21]S. G. Kargl, "Effective medium approach to linear acoustics in bubbly liquids," J. Acoust. Soc. Am. **111**, 168–173 (2002).
[22]S. K. Kanaun, V. M. Levin, and F. J. Sabina, "Propagation of elastic waves in composites with random set of spherical inclusions," (effective medium approach), Wave Motion **40**, 69–88 (2004).
[23]T. S. Lundgren, "Slow flow through stationary random beds and suspensions of spheres," J. Fluid Mech. **51**, 273–299 (1972).
[24]Yu. A. Buyevich and I. N. Shchelchkova, "Flow of dense suspensions," Prog. Aerosp. Sci. **18**, 121–151 (1978).
[25]E. Chang, B. S. Yendler, and A. Acrivos, *Advances in Multiphase Media*, edited by G. Papanicolaou (SIAM, Philadelphia, PA, 1986).
[26]A. S. Sangani and C. Yao, "Transport processes in random arrays of cylinders. i thermal conduction," Phys. Fluids **31**, 2426–2444 (1988).
[27]A. S. Sangani and C. Yao, "Transport processes in random arrays of cylinders. II viscous flow," Phys. Fluids **31**, 2435–2444 (1998).
[28]T. L. Dodd, D. A. Hammer, A. S. Sangani, and D. L. Koch, "Numerical simulations of the effect of hydrodynamic interactions on diffusivities of integral membrane proteins," J. Fluid Mech. **293**, 147–180 (1995).
[29]P. D. M. Spelt, M. A. Norato, A. S. Sangani, M. S. Greenwood, and L. L. Tavlarides, "Attenuation of sound in concentrated suspensions, theory and experiments," J. Fluid Mech. **430**, 51–86 (2001).
[30]M. Baudoin, J. L. Thomas, F. Coulouvrat, and D. Lhuillier, "An extended coupled phase theory for the sound propagation in polydisperse suspensions of rigid particles," J. Acoust. Soc. Am. **121**, 3386–3397 (2007).
[31]J. K. Percus and G. J. Yevick, "Analysis of classical statistical mechanics by means of collective coordinates," Phys. Rev. **110**, 1–13 (1957).
[32]M. S. Wertheim, "Exact solution of the Percus-Yevick integral equation for hard spheres," Phys. Rev. Lett. **10**, 312–323 (1963).
[33]A. K. Hipp, G. Storti, and M. Morbidelli, "Acoustic characterization of concentrated suspensions and emulsions. 2. Experimental validation," Langmuir **18**, 391–404 (2002).
[34]R. I. Nigmatulin and J. C. Friedly, *Dynamics of Multiphase Media* (Hemisphere, Washington, 1991), Vols. **1** and **2**.
[35]Yu. A. Buyevich and V. G. Markov, "Continual mechanics of monodisperse suspensions, rheological equations of state for suspensions of moderate concentration," Prikl. Mat. Mekh. **37**, 1059–1077 (1973).
[36]T. Morita and K. Hiroike, "A new approach to the theory of classical fluids," Prog. Theor. Phys. **23**, 1003–1027 (1960).
[37]J. M. J. Van Leeuwen, J. Groeneveld, and J. De Boer, "New method for the calculation of the pair correlation function," Physica (Amsterdam) **25**, 792–808 (1959).
[38]Yu. A. Buyevich, "Heat and mass transfer in disperse media. II. Constitutive equations," Int. J. Heat Mass Transfer **35**(10), 2453–2463 (1992).
[39]E. Chang and A. Acrivos, "Rate of heat conduction from a heated sphere to a matrix containing passive spheres of a different conductivity," J. Appl. Phys. **59**(10), 3375–3382 (1986).
[40]Yu. A. Buyevich, "Heat and mass transfer in disperse media. I. Averaged field equations," Int. J. Heat Mass Transfer **35**(10), 2445–2452 (1992).
[41]Yu. A. Buyevich, "Interphase interaction in fine suspension flow," Chem. Eng. Sci. **50**, 641–650 (1995).
[42]Yu. A. Buyevich and V. G. Markov, "Rheology of concentrated mixtures of fluids with small particles," Prikl. Mat. Mekh. **36**, 480–493 (1972).
[43]I. D. Howells, "Drag due to the motion of a Newtonian fluid through a sparse random array of small fixed rigid objects," J. Fluid Mech. **64**, 449–475 (1974).
[44]A. K. Hipp, G. Storti, and M. Morbidelli, "Acoustic characterization of concentrated suspensions and emulsions. 1. Model analysis," Langmuir **18**, 391–404 (2002).
[45]S. Temkin, "Attenuation and dispersion of sound in dilute suspensions of spherical particles," J. Acoust. Soc. Am. **108**, 126–145 (2000).
[46]A. K. Hipp, G. Storti, and M. Morbidelli, "On multiple-particle effects in the acoustic characterization of colloidal dispersions," J. Phys. D **32**, 568–576 (1999).
[47]H. Hansen-Goos and R. Roth, "A new generalization of the Carnahan–Starling equation of state to additive mixture of hard spheres," J. Chem. Phys. **124**, 1–8 (2006).

PHYSICAL REVIEW E **81**, 036315 (2010)

Droplet displacements and oscillations induced by ultrasonic surface acoustic waves: A quantitative study

P. Brunet, M. Baudoin, O. Bou Matar, and F. Zoueshtiagh*
Institut d'Electronique de Microélectronique et de Nanotechnologies, UMR CNRS 8520, Cité Scientifique, Avenue Poincaré, BP 60069, 59652 Villeneuve d'Ascq, France
(Received 2 November 2009; published 18 March 2010)

We present an experimental study of a droplet interacting with an ultrasonic surface acoustic wave. Depending on the amplitude of the wave, the drop can either experience an internal flow with its contact line pinned, or (at higher amplitude) move along the direction of the wave also with internal flow. Both situations come with oscillations of the drop free surface. The physical origins of the internal mixing flow as well as the drop displacement and surface waves are still not well understood. In order to give insights of the underlying physics involved in these phenomena, we carried out an experimental and numerical study. The results suggest that the surface deformation of the drop can be related to a combination between acoustic streaming effect and radiation pressure inside the drop.

DOI: 10.1103/PhysRevE.81.036315 PACS number(s): 47.55.D−, 68.08.Bc, 47.35.Rs, 47.35.Pq

I. INTRODUCTION

A. General Issues

For discrete microfluidics in lab-on-chip devices, it is often necessary to handle small amount of liquids in the form of droplets. These elementary operations are the linear displacement, the splitting or the merging of droplets, or the production of a constant flow inside a drop. At the scale of a microliter drop or smaller, the main parameters governing the shape and flow dynamics, are the dynamic viscosity μ and the surface tension σ. Nonlinear effects originating from inertia are mostly negligible, so that the momentum conservation equation for the fluid reduces to the time-dependent Stokes equation. Consequently, it is hard to induce (chaotic) mixing and continuous resuspension of particles in a drop as the equation of flow motion is time reversible. Furthermore, during these operations, the drop is often in contact with ambient atmosphere and evaporation can significantly occur at the typical time scales of the operations. It is known that when the liquid contains colloidal particles or macromolecules, evaporation leads to a outwards flow in the drop, which in turn leads to a particle clustering in the vicinity of the contact line [1,2]. The "coffee rings" originate from this phenomenon, which in practical situation can strongly limit bioparticles detection in lab-on-chip devices (see, e.g., [3]) by forming deposits on DNA microarrays [4].

Another difficulty is to displace such small droplets. As their typical size is smaller than the capillary length $l_c = \sqrt{\sigma/\rho g}$, of the order of 1 to 2 mm for most liquids (ρ being the liquid density), the volume forces are generally overcome by the retention force, F_R, acting at the contact line of the substrate. This force scales with the contact-line perimeter [5],

$$F_R = \pi R \sigma (\cos(\theta_r) - \cos(\theta_a)) \quad (1)$$

Its strength is related to the contact angle hysteresis $\theta_a - \theta_r$, where θ_a and θ_r are respectively the advancing and receding contact angles. Real surfaces combining micro- or nanoscale roughness and chemical heterogeneities, can have significant hysteresis [6]. Furthermore, the aforementioned accumulation of particles near the contact line increases this hysteresis even more. The coffee-ring effect can be hindered by Marangoni forces if one uses a very volatile solvent [7], but with casual liquids and substrates used in biology, volume forces are too weak to resuspend continuously the particles or to move the drop in a controlled fashion.

One of the challenging issues is to provoke the continuous unpinning of the contact line of the drop to both prevent particle accumulation and to obliterate hysteresis. Various authors evidenced a similar unpinning effect with low-frequency mechanical vibrations [8–13], but it is required that the amplitude of vibrations be of the order of a millimeter to obtain the desired effect. Such vibrations can be unsupported by many fragile surrounding devices. Furthermore, as the pinning forces are often due to micron-sized roughness, it is intuitively more efficient to induce an unpinning flow from waves of shorter wavelength such as those produced by ultrasonic transducers, λ ranging from 1 to 300 microns.

B. Qualitative description of the phenomena

Recently, it has been found that the use of ultrasonic surface acoustic-so-called "Rayleigh" waves (SAW) transducers on piezoelectric substrates enables to both agitate inner fluid and to displace a droplet along the direction of the wave propagation [14–16]. SAW frequency generally ranges from 5 to 150 MHz, and depending on the operating frequency the dynamics of the droplet can show a host of different behaviors. At low frequencies—about 20 MHz, a "creeping and jumping" motion of the drop generally occurs, especially for low-viscosity liquids [17] [see Fig. 1(a)]. Due to a nonlinear coupling between the Rayleigh acoustic wave and the flow, the liquid inside is highly stirred in a rotating flow motion [see Fig. 1(b)], while the interface shows capillary waves. Although several experimental studies demonstrated the reliability of this technique, little is known about the detailed

*philippe.brunet@univ-lille1.fr

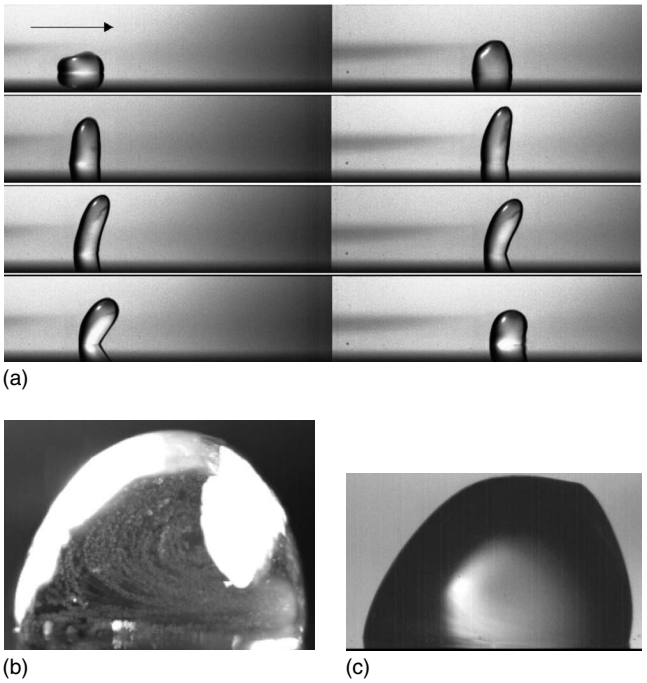

FIG. 1. (a) Successive snapshots of a water drop displaced by SAW, showing a periodic creeping and jumping flow. The arrow shows the direction of the displacement. (b) Particle tracking inside a steady drop subjected to SAW waves, obtained by time averaging. (c) Asymmetric shape of a drop moving under the action of SAW (W/G mixture 2), without oscillations. For the three images, the SAW propagates from left to right.

mechanisms that create both the internal flow and the droplet deformations. It is generally admitted that the SAW is radiated inside the droplet at a refraction angle ϕ_r, analogous to Snellius-Descartes law in optics,

$$\sin(\phi_r) = \frac{c_l}{c_s} \tag{2}$$

where c_l and c_s denote respectively the speed of sound in the liquid and the solid, and in turn generates acoustic streaming. The angle ϕ_r is around 25° for water and usual piezoelectric substrates. Regarding droplet dynamics by SAW, a fluid-dynamics analysis has been recently attempted [15], but results are mostly related to atomization occurring at high acoustic power. At high frequencies, around 100 MHz, a noticeable contribution on the understanding of drop deformation and displacement, is available in [18] (however at this frequency, no oscillations have been observed). It shows that the flow originates from a carrying force focused in a narrow region inside the drop, starting at the drop edge hit by the wave and directed toward the refraction angle.

In the general case, this force is partly due to nonlinear acoustic streaming [19,20]. The fluid trajectories are described qualitatively by the particle tracking snapshot such as that of Fig. 1(b). In the present frequency range, around 20 MHz, the liquid-air interface is also affected by SAW in three different ways.

First, the droplet's left-right symmetry is broken [see Fig. 1(c)] and the asymmetry is more pronounced for larger acoustic power. The asymmetry is responsible for the drop displacement as it makes the front and rear contact angles becoming, respectively, larger than θ_a and smaller than θ_r [6]. However, the relative contributions of acoustic streaming and radiation pressure on this asymmetry with respect to the frequency regime remain unclear.

Second, the periodic creeping-jumping motion [see Fig. 1(a)] has a well-defined frequency of the order of 50 to 200 Hz for usual droplet size, and comes with a continuous unpinning of the contact line. During the deformation cycle, the droplet is strongly stretched and flattened.

Finally, besides the global deformation, the droplet surface exhibits small deformations ("trembling") at a frequency of about of a few thousands Hertz. However, this is hardly visible on the pictures presented here.

In any case, the periodic deformations of the interface cannot be attributed to a steady flow. Instead, the acoustic radiation pressure which affects the shape of the liquid-vapor interface can be invoked for a possible origin of such deformations. Therefore, the periodic motion could be associated with dynamical eigenmodes of the droplet, where capillarity tends to restore a minimal surface energy.

The deep understanding of the involved phenomena is necessary in order to set up a droplet handling lab on chip with minimal acoustic power toward an optimization of the system. Especially interesting is the use of several combined transducers and short-time pulses in order to reduce heat (continuous appliance of SAW would cause much heat production) and to protect fragile bioparticles. The current available literature being insufficient for quantitative predictions, the present study aims to carry out quantitative measurements of the displacement and deformation of the drop. We present here such a quantitative study by varying parameters such as the droplet volume, the liquid viscosity and the amplitude of the acoustic wave. These results constitute a first step toward the understanding of the detailed coupled acoustic and hydrodynamic mechanisms.

II. EXPERIMENTAL SETUP

The setup is depicted in Fig. 2. We used a substrate with piezoelectric properties (lithium niobate, $LiNbO_3$), in order to generate powerful SAW. The transducer is an interdigitated transducer (IDT) which generates transverse-acoustic waves propagating along the surface. The interconnected fingers of the IDT are made of Titane covered by Gold, and designed by a lithographic technique detailed elsewhere [14]. We applied the periodic sinusoidal voltage with a high-frequency generator (IFR 2023A), amplified with a home-made amplifier. A SAW is generated providing that the voltage frequency is compatible with the space between each track of the IDT. Considering that the space between fingers $a/2$ is 43.75 μm, giving a wavelength $\lambda = 2a = 175$ μm, and that the sound velocity in $LiNbO_3$ is 3485 $\mathrm{m.s^{-1}}$ for transverse waves, the value of the frequency f_0 has to be around 19.5 MHz. In practice, we found the best actuation to droplets of any size for $f_0 = 20.375$ MHz and we kept this value for all experiments. The properties of the SAW ensure that the amplitude is not attenuated in its direction of propagation, and that it is localized near the surface.

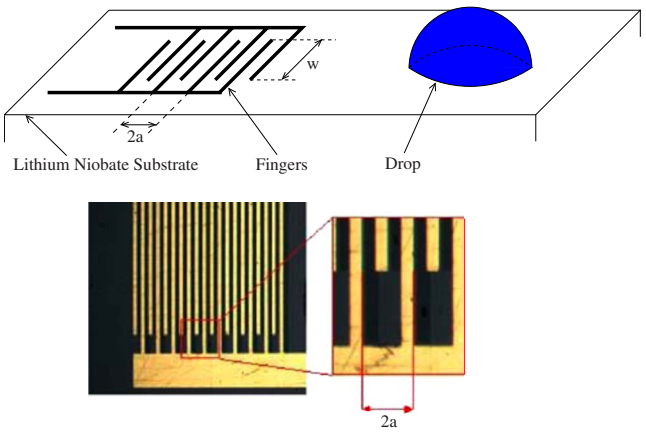

FIG. 2. (Color online) Scheme of the SAW interdigitated transducer that actuates with a droplet deposited on the substrate. The wave propagates from left to right. Below: the details of the network of fingers that compose the IDT.

In order to reduce the friction forces, and to study the simpler situation of partial wetting, we treated the surface with hydrophobic coating [monolayer of octadecyltrichlorosilane (OTS)]. The contact angles are: $\theta_a = 105°$ and $\theta_r = 95°$. This weak hysteresis helps to conduct experiments without the additional complexity of pearling at the trailing edge of a moving drop [22] that would have occurred otherwise. The droplet dynamics is acquired with a high-speed camera (Photron SA3) with a zoom lens completed by extension rings. This allows a maximal magnification of about 8 μm/pixel. The acquisition rate ranged from 2000 to 5000 im/s. To avoid evaporation, special care is devoted to use cold source of light (Schott KL2500) and to acquire pictures no later than a few seconds after the droplet has been put on the substrate.

The liquids used are deionized water and water/glycerol mixtures (W/G), which physical properties at 20 °C are given in Table I. Glycerol percent weight was varied from 50 to 70, increasing the viscosity by a factor of up to 11, whereas the surface tension stayed close to that of water.

The measurement of the normal displacement at the surface of the substrate gives the amplitude of the SAW. We used a technique of laser heterodyne interferometer of type Mach-Zender (SH130, B.M. Industries). In brief, the interferometer measures the Doppler shift between a reference beam and a secondary beam modulated at $f_M = 70$ MHz by an acousto-optic Bragg cell. The secondary beam is reflected onto the surface and hence, is modulated a second time by Doppler effect. The acoustic displacement d is then deduced from these measurements by extracting the relative amplitude between the peaks at f_M and $f_M \pm f_0$ in the power spectrum. The displacement d ranges from 0.3 to 2 nm for the usual experimental conditions.

TABLE I. Physical properties of liquids.

Liquid	Kin. viscos. ν (mm^2/s)	Surf. tension γ (N/m)	Density ρ (g/cm^3)
Water	1.00	0.072	1.00
W/G. mix 1	5.60	0.067	1.126
W/G. mix 2	11.50	0.066	1.161

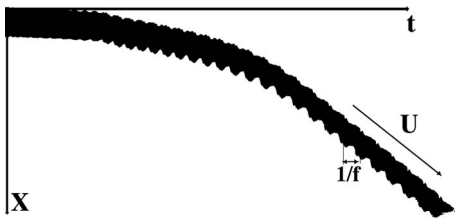

FIG. 3. Typical spatiotemporal diagram for a moving, creeping and jumping droplet like in Fig. 1(a).

III. RESULTS

For each experiment, the dynamics of the drop was extracted using the public domain image processing software ImageJ [23]. From a sequence of about 2000 images, we built spatiotemporal diagrams that allowed us to measure both the speed and the frequency of oscillations: we extracted the gray levels along a horizontal line cutting the base of the droplet, and we pilled the lines on top of each others (time axis is horizontal after a rotation of $\pi/2$). A typical motion of drop is pictured in Fig. 3 after binary treatment. The total time is about 250 ms. This diagram is then skeletonized to get the position versus time. The velocity U is the slope and the frequency f is extracted from a Fourier transform. It is noticeable that the drop does not start to move or oscillate immediately: it waits about 200 ms before it starts. During this relatively long transient, the oscillations progressively increase, as does the velocity.

A. Droplet displacement

We first present the velocity measurements, obtained by varying the acoustic amplitude d at constant volume [Fig. 4(a)] and by varying the droplet volume V at constant displacement d [Fig. 4(b)] for water. As stated earlier, the drop displacement results from a balance between driving forces—due to both the streaming and radiation pressure which induce a left/right asymmetry—and dissipation occurring near the contact line.

1. Influence of acoustic displacement

As expected, the larger d is, the faster the droplet moves. Also it turns out that d has to be larger than a certain threshold around 0.5 nm in order for the droplet to move. Below this threshold, the droplet stays at the same location but an internal flow motion is observed: this situation is illustrated in Fig. 1(b). The influence of d is strongly nonlinear: after a sharp increase just above threshold, U saturates at a volume-dependent value.

2. Influence of volume

Whatever the amplitude of the acoustic wave d, the influence of volume shows a maximal velocity at V about 5 μl

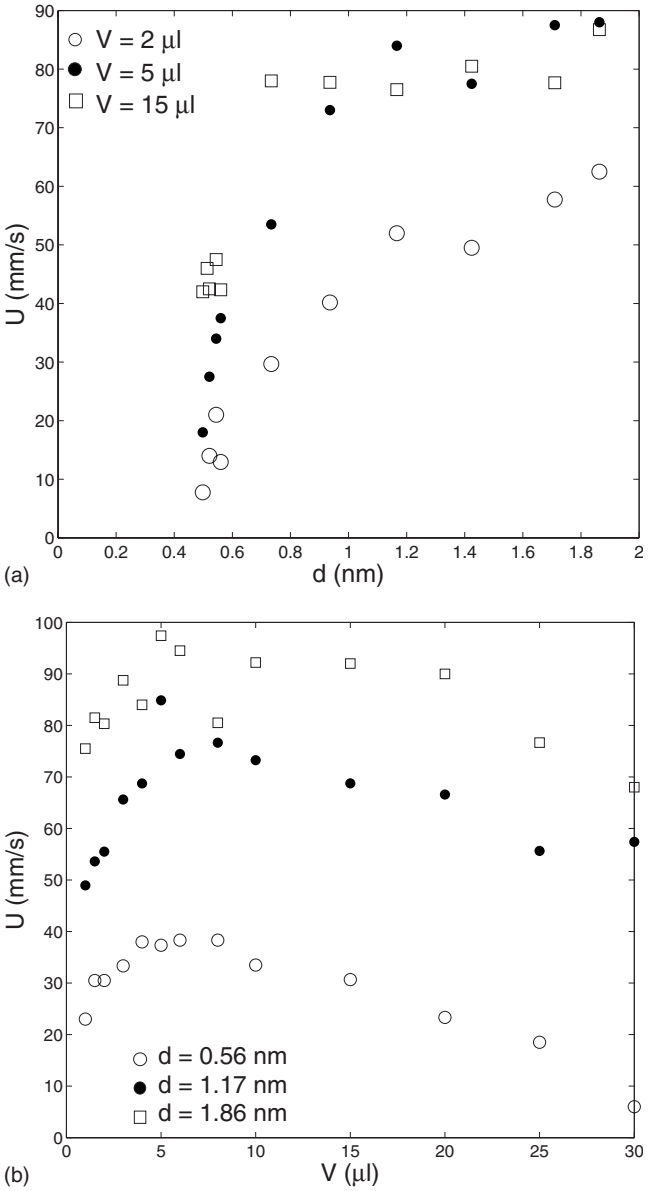

FIG. 4. (a) Drop velocity versus acoustic displacement d for three different volumes (water). (b) Drop velocity versus volume for three values of d.

[see Fig. 4(b)]. A tentative explanation of this behavior is developed in the Discussion part.

3. Influence of viscosity

To have a more complete understanding of the coupled acoustic and hydrodynamic effects, we used liquids of various viscosity (see Table I). Figure 5 shows velocity versus volume, for three liquids (water and W/G mixtures 1 and 2). The increase of viscosity leads to a decrease of the velocity as expected for moving droplets. Indeed it is known that viscosity is involved in the dissipation near the contact line [6] and, hence, an equal driving force displaces viscous drops at lower speed. It is natural to consider the dimensionless velocity, the capillary number

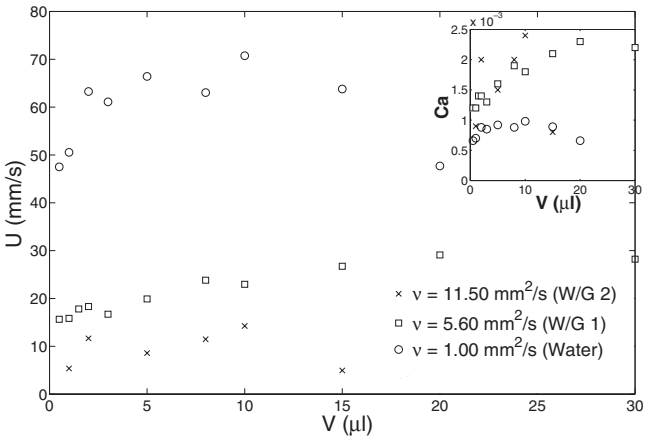

FIG. 5. Droplet velocity versus volume, for three different values of viscosity. d=0.99 nm. Inserted: the same measurements with the dimensionless velocity Ca.

$$\mathrm{Ca} = \frac{\mu U}{\sigma} \tag{3}$$

which is plotted in the insert of Fig. 5.

It turns out that the data for capillary numbers do not collapse well together, although the order of magnitude is around 1×10^{-3} for most measurements. This can be interpreted in the following way: the driving force is due (at least partially) to the acoustic streaming which involves bulk dissipation [20]. Hence, streaming effects are promoted by liquid viscosity. The increase of viscosity increases the contact-line dissipation [6], but it should also increase the driving force. Therefore, it is consistent that the values of Ca be slightly larger for more viscous liquids.

B. Creeping-jumping oscillatory motion

1. Influence of viscosity

First, it is noticeable that oscillations are more and more damped as the viscosity is increased by adding glycerol in the mixture. For instance with mixture 1, oscillations have very small amplitude and are barely measurable, whereas for mixture 2 oscillations completely vanished. Hence, the results of oscillations reported thereafter are for water as this is the only situation where they clearly appear like in Fig. 1(a).

2. Frequency

In Fig. 6, f is plotted versus volume for different acoustic displacement d. The results clearly show a sharp decrease of f with V, in the range V=0.5 to 5 μl. A power-law fit leads to an exponent close to one half: $f \sim V^{-1/2}$. This is reminiscent to what is predicted by the theory of Rayleigh-Lamb [21], for inertial-capillary modes of vibrations in a drop. Rayleigh's seminal calculation is valid for a spherical droplet and for small deformations,

$$f_n = \left(\frac{n(n-1)(n+2)\gamma}{3\pi\rho V} \right)^{1/2} \tag{4}$$

in which f_n denotes the resonance frequency of the n^{th} mode of oscillation.

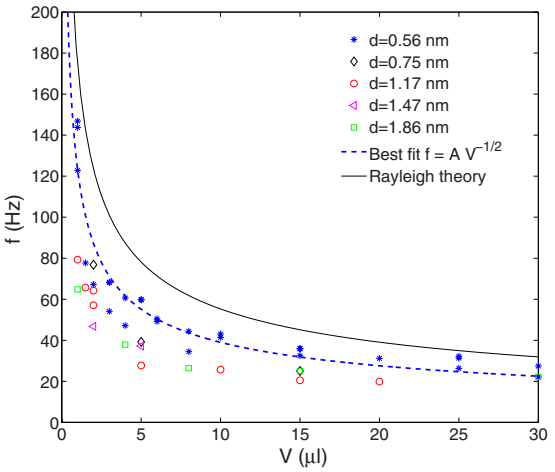

FIG. 6. (Color online) Frequency of the creeping-jumping oscillations versus volume, for various acoustic displacement d. The dashed blue curve is the best fit $f \sim V^{-1/2}$, and the black plain curve is the prediction by Rayleigh's theory.

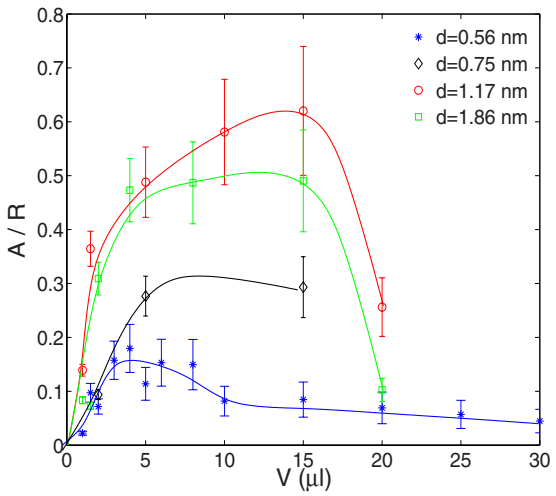

FIG. 7. (Color online) Amplitude of the creeping-jumping oscillations of water droplets versus volume, for various acoustic displacements. The curves are guidelines for the eyes.

The case $n=1$ corresponds to pure translation and $n=2$ corresponds to the lowest mode in which the drop is elongated with an elliptical shape. The morphology of the oscillations suggests a mode $n=2$ [see Fig. 1(a)]. To the best of our knowledge, the case of sessile drops has not been treated fully analytically. The pinning force acting at the contact line strongly constrains the structure of the capillary wave, making its computation more complex. However, Noblin *et al.* [11] showed that for moderate hysteresis and under strong enough vibrations, the contact line is constantly unpinned and the constraint due to retention force at the contact line [Eq. (1)] is released [8,9,11–13]. This is indeed what is observed in sequences such as Fig. 1(a). Hence, we compared out results to what is predicted by Eq. (4), also plotted in Fig. 6. It turns out that Rayleigh-Lamb's theory slightly overestimates the results although the order of magnitude is correctly predicted. This can be interpreted by the fact that SAW tend to induce large amplitude droplet oscillations which are out of the frame of Rayleigh's theory. Intuitively, large amplitude oscillations are of larger period than weak amplitude ones, and this is confirmed by the results of Fig. 6: larger d generates free-surface oscillations of larger amplitude and of smaller frequencies.

3. Amplitude

In Fig. 7, the relative amplitude of oscillations—i.e., the amplitude divided by the mean base radius of the drop—is plotted versus volume, for different acoustic displacements d. This amplitude is extracted from spatiotemporal diagrams such as that in Fig. 3 and corresponds to the maximal lateral deformation of the base of the drop. It turns out that the amplitude is maximal for a d-dependent value of volume. These results suggest that oscillations result from a balance between the wave-induced pressure reaching the interface and capillarity, as developed in Sec. IV.

IV. DISCUSSION—NUMERICAL RESULTS

The measurements presented here show several evidences that the dynamics of the drop is due to an interplay between acoustic streaming and radiation pressure. For water droplets at the tested frequency, the SAW induces both a left-right symmetry breakup leading to motion and the creeping-jumping oscillations (the high-frequency 'trembling' oscillations, mentioned earlier, will be treated in a further study). It is still unclear what the respective weight of streaming and radiation pressure are on the drop left/right asymmetry. Schindler *et al.* [18] showed that at high frequencies, acoustic streaming can lead to a conservative force potential in the drop toward the direction of propagation, headed to the top and inducing a deformation like in Fig. 1(c). However, the streaming flow cannot explain the creeping-jumping oscillations in which the free surface of the drop is pushed upwards.

The acoustic streaming inside the droplet comes from dissipation due to liquid shear (μ) and bulk (μ_b) viscosities. The internal streaming flow is more intense for larger viscosities and frequency [20]. On the contrary, the radiation pressure is directly proportional to the energy which reaches the free surface [20]. Consequently, the larger the viscous dissipation is, the smaller this energy is. The relative importance of both effects is strongly dependent on the structure of the acoustic wave diffracted in the drop and on how much the wave is attenuated.

It is relevant to compare the typical drop size with the length of attenuation of the acoustic wave which, in a fluid, is given by [20]

$$L = \frac{2\rho c_l^3}{(2\pi f_0)^2}\left(\frac{1}{\frac{4}{3}\mu + \mu_b}\right). \tag{5}$$

This length is plotted versus f_0 in Fig. 8, with respect to the drop size. The length L is equal or lower than the size of droplets for a frequency of about 125 MHz or above (see Fig. 8) and defines a range of frequency where radiation pressure is negligible. This is far beyond the values of f_0 used here and, therefore, both streaming and radiation pressure are effective in our study.

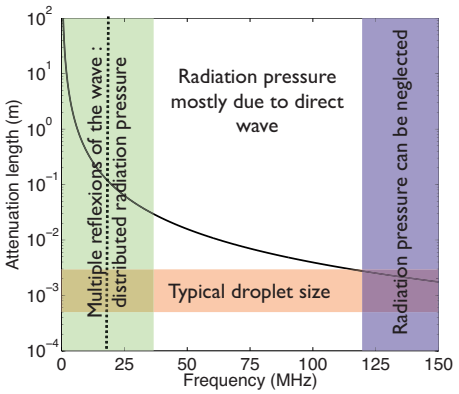

FIG. 8. (Color online) The different regimes of the relative influence of radiation pressure versus frequency. The plain curve stands for the attenuation length L in pure water (c_l=1476 m/s and μ_b=2.8×10^{-3} Pa.s) given by Eq. (5).

To confirm this trend, at least qualitatively, we carried out numerical simulations with a finite-elements software (COMSOL Multiphysics 3.4). The model uses a drop of half-spherical fixed shape (contact angle=90°, radius=2 mm) subjected to a SAW. The General Form Modes of COMSOL Multiphysics with two domains has been used, one for the piezoelectric substrate and one for the water droplet. In the water droplet, the linear equation of acoustic in a thermoviscous fluid has been considered. The boundary conditions used at the drop/ambient air interface are stress-free conditions. As we are interested in the linear radiation of the SAW propagating at the substrate surface into the water, the continuity of the normal stresses and displacements has been assumed between the piezoelectric substrate and the liquid [24]. This last point is justified by the fact that in our experiences the amplitude of SAW is always small in comparison to the acoustic wavelength.

Figure 9 shows the pressure distribution (a) in a water drop for f_0=20 MHz and in liquids where the attenuation is (b) 25 times larger and (c) 100 times larger, for the same f_0. When weakly attenuated, as in water for a frequency of 20 MHz [Fig. 9(a)], the wave structure is generally chaotic due to multiple reflections as the drop acts such as a chaotic cavity. If the radius is slightly modified, the wave structure is completely different except for the coherent part in the direct wave. To extract this coherent part we computed the wave structure for 15 droplets of radius ranging from 2 to 2.35 mm, and we averaged the contribution of each case. This calculation procedure, where stationary wave pattern are determined in nondeformable drops of increasing size, is justified by the fact that the time required for the wave to propagate across the 2 mm drop is about 2 μs, which is much lower than the observed characteristic deformation time of the drop.

The resulting data exhibit the coherent part of the wave, as shown in Fig. 10. In this case, the wave reaches the free surface whereas in the two other cases [Figs. 9(b) and 9(c)] it is strongly attenuated and hardly reaches the free surface. It is clear that radiation pressure will only operate in the first case. The third case is streaming dominated and should not show global free-surface oscillations. The action of radiation

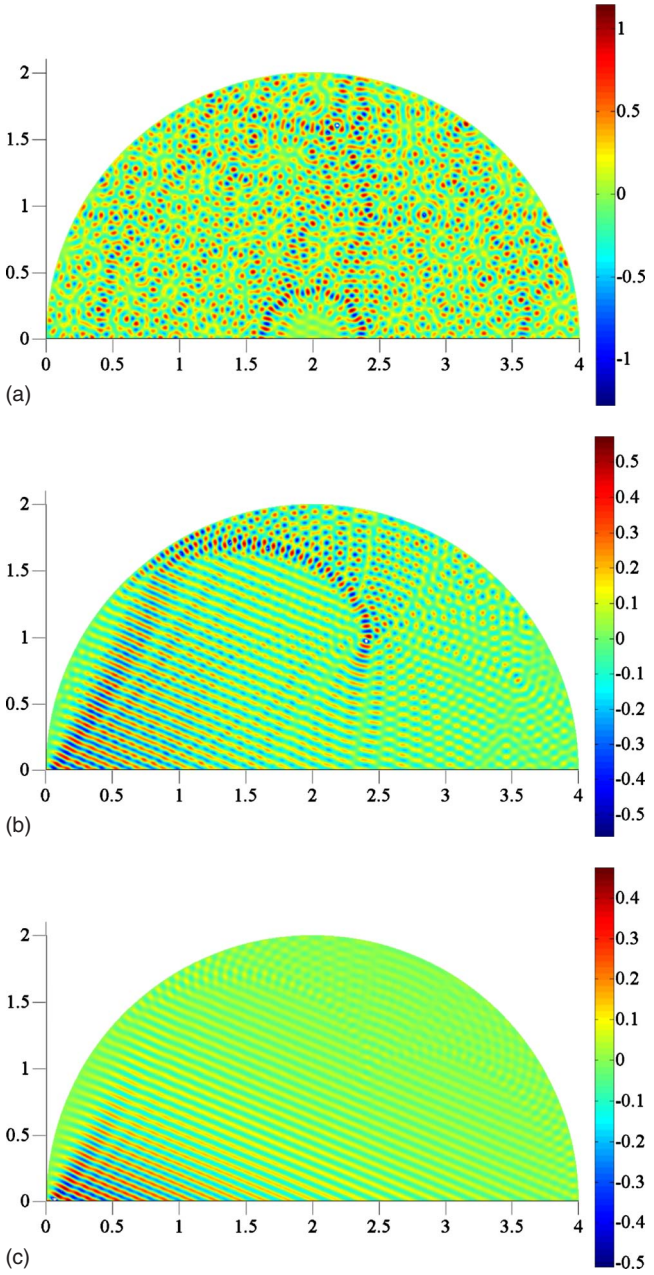

FIG. 9. (Color online) Numerical simulations of a SAW inside an nondeformable half-spherical drop, f_0=20.375 MHz and d=2 nm. Color levels stand for pressure (in gray-scale print version, darker gray stands for higher pressure in absolute value). (a) Weak attenuation in the case of water. (b) Intermediate attenuation, 25 times larger than (a). (c) Strong attenuation, 100 times larger than (a).

pressure is reminiscent to another study [25], although for much smaller frequencies and a different setup, where the free surface of a liquid layer is deformed by acoustic vibrations of a plate.

The coherent part of the wave is highly left-right asymmetric and the associated radiation pressure therefore contributes to the asymmetry of the droplet. On the contrary the chaotic part of the wave induces a radiation pressure homogeneously distributed on the surface of the wave. Therefore, only the direct coherent wave contributes to the displacement

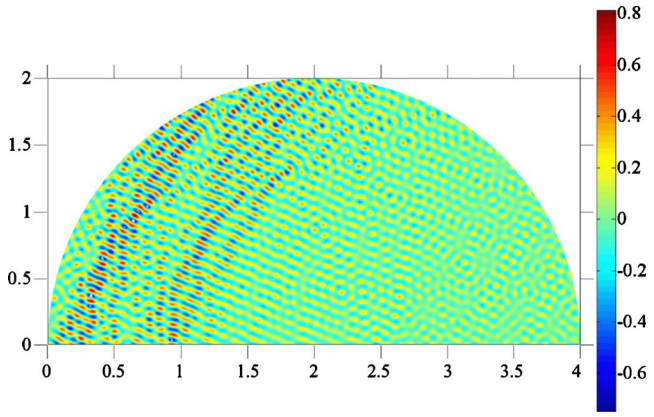

FIG. 10. (Color online) Pressure due to the coherent direct wave in the situation of Fig. 9(a), with chaotic multiple reflections. Obtained by averaging over several runs, see text for details. Color levels stand for pressure (in gray-scale print version, darker gray stands for higher pressure in absolute value).

of the droplet whereas the chaotic part should be the driving effect of the free-surface oscillations. The computations showed that the chaotic part vanishes for smaller f_0 than the coherent direct part. Indeed, for the existence of multiple reflections it is required that the length L be several times larger than the drop size. Therefore, we defined two other regimes: a 'multiple reflections' domain at lower f_0, and an intermediate regime where only the coherent part of the direct wave contributes to the radiation pressure.

The use of liquids more viscous than water have similar effects on the relative contribution of radiation pressure as the prescription of a higher frequency: it decreases L. In the cases displayed in Figs. 9(b) and 9(c), the corresponding frequencies would be 100 and 200 MHz, respectively. The use of W/G mixtures increases both μ and μ_b. The ratio between μ_b and μ is 2.8 for water, and it should be quite close to this value for W/G mixtures of low viscosity like ours. It is sensible to interpret the absence of oscillations for W/G droplets by a decrease of the length L: as the wave is more strongly attenuated when arriving at the droplet free surface, the radiation pressure is weaker than for water drops. In Fig. 8, the curve of L vs f_0 for W/G mixtures would be just translated downwards.

To observe the creeping-jumping oscillations, the radiation pressure has to be strong enough to cause the unpinning of the droplet contact line (otherwise, as the drop volume is constant, the height of the drop cannot vary significantly). Our measurements and computations suggest that the chaotic part of the wave is required to obtain such pressure: this condition is fulfilled only for frequencies included in the lowest range domain and for low-viscous liquids. This is to be related to the results of Fig. 6 for the selection of the frequency: once the radiation pressure pushes the top of the drop and shrinks its base surface, the contribution of this pressure decreases as the height of the drop increases. Therefore, the drop retracts under the action of capillary forces, leading to a frequency comparable to that of the first eigenmode of the drop driven by an inertial-capillary balance. The maxima of amplitude found for a d-dependent intermediate volume (Fig. 7) is consistent with this interpretation: surface tension hinders large oscillations for small drops, as capillary pressure, scaling with interface curvature, is bigger; whereas large drops are subjected to lesser radiation pressure because the acoustic wave is more damped before reaching the interface.

Finally, these calculations suggest a possible explanation for the maximal drop velocity for water, obtained for intermediate drop volume (see Fig. 4). If the drop is too small, only a part of the SAW is transferred to the droplet whereas a significant part of the acoustic energy goes on propagating in the solid after the drop [26]. On the contrary, drops of larger size collect most of the acoustic energy for their displacement and deformation. Bigger drops collect about the same amount of energy as intermediate drops, but they will be slowed down simply because they have more inertia. The drop optimal size is dictated by the attenuation length in the solid, in the X direction. This attenuation length is no more linked to the thermoviscous absorption in the liquid, but to the imaginary part k_i of the Rayleigh wave wave number, which is of leaky type when propagating in a substrate in contact with a liquid. For a lithium niobate substrate loaded by water $k_i \simeq 2.310\text{-}5 \times f_0$ Np/m [24,27], more than two orders of magnitude higher than the attenuation coefficient at $f_0 = 20$ MHz. This corresponds to the fact that the Rayleigh wave efficiently looses its energy by radiating in the liquid. The extraction of the amplitude at the solid-liquid interface gives an attenuation length of about 2.13 mm, corresponding to a drop volume of about 5 μl. This may explain the maxima of velocity observed in Fig. 4.

V. CONCLUSION

We have presented here a quantitative study of droplet dynamics, when actuated by a SAW. Most of previous studies of SAW ignored the effect of radiation pressure as they were carried out at higher frequencies. In our range of frequency and liquid viscosity, a combination between streaming and radiation pressure effects was observed and their respective contributions on the observed dynamics were studied. The free-surface oscillations are mostly due to radiation pressure, whereas internal flow is due to streaming. This is evidenced by both experiments at different viscosity, and computations. Contributions of both phenomena are of interest, for an optimal microfluidics mixing efficiency. Future studies will focus on the influence of frequency in order to determine the relative weight of both mechanisms in the drop's asymmetry.

[1] R. D. Deegan, O. Bakajin, T. F. Dupont, G. Huber, S. R. Nagel, and T. A. Witten, Nature (London) **389**, 827 (1997).
[2] R. D. Deegan, Phys. Rev. E **61**, 475 (2000).
[3] P. R. Nair and M. A. Alam, Appl. Phys. Lett. **88**, 233120 (2006).
[4] R. Blossey and A. Bosto, Langmuir **18**, 2952 (2002).
[5] E. B. Dussan V. and R. T.-P. Chow, J. Fluid Mech. **137**, 1 (1983).
[6] D. Bonn, J. Eggers, J. Indekeu, J. Meunier, and E. Rolley, Rev. Mod. Phys. **81**, 739 (2009).
[7] H. Hu and R. G. Larson, J. Phys. Chem. B. **110**, 7090 (2006).
[8] C. Andrieu, C. Sykes, and F. Brochard, Langmuir **10**, 2077 (1994).
[9] E. L. Decker and S. Garoff, Langmuir **12**, 2100 (1996).
[10] L. Dong, A. Chaudhury, and M. K. Chaudhury, Eur. Phys. J. E **21**, 231 (2006).
[11] X. Noblin, A. Buguin, and F. Brochard-Wyart, Eur. Phys. J. E **14**, 395 (2004).
[12] P. Brunet, J. Eggers, and R. D. Deegan, Phys. Rev. Lett. **99**, 144501 (2007).
[13] J. Long and P. Chen, Adv. Colloid Interface Sci. **127**, 55 (2006).
[14] A. Renaudin, P. Tabourier, V. Zhang, J. C. Camart, and C. Druon, Sens. Actuators B **113**, 389 (2006).
[15] A. Qi, L. Y. Yeo, and J. R. Friend, Phys. Fluids **20**, 074103 (2008).
[16] A. Wixforth, C. Strobl, C. Gauer, A. Toegl, J. Scriba, and Z. V. Guttenberg, Anal. Bioanal. Chem. **379**, 982 (2004).
[17] A. Renaudin, E. Galopin, V. Thomy, C. Druon, and F. Zoueshtiagh, Phys. Fluids **19**, 091111 (2007).
[18] M. Schindler, P. Talkner, and P. Hanggi, Phys. Fluids **18**, 103303 (2006).
[19] S. J. Lighthill, J. Sound Vib. **61**, 391 (1978).
[20] R. T. Beyer, *Nonlinear Acoustics* (Acoustical Society of America, New York, 1997).
[21] H. Lamb, *Hydrodynamics* (Cambridge University Press, Cambridge, England, 1932).
[22] T. Podgorski, J.-M. Flesselles, and L. Limat, Phys. Rev. Lett. **87**, 036102 (2001).
[23] W. Rusband, http://rsbweb.nih.gov/ij/
[24] J. J. Campbell and W. R. Jones, IEEE Trans. Sonics Ultrason. **17**, 71 (1970).
[25] J. Scortesse, J.-F. Manceau, and F. Bastien, J. Sound Vib. **254**, 927 (2002).
[26] Z. J. Jiao, X. Y. Huang, and N.-T. Nguyen, J. Phys. A: Math. Theor. **41**, 355502 (2008).
[27] S. Shiokawa, Y. Matsui, and T. Ueda, Jpn. J. Appl. Phys., Suppl. **29**, Suppl. 29-1), 137 (1990).

Medical Engineering & Physics 33 (2011) 849–856

Contents lists available at ScienceDirect

Medical Engineering & Physics

journal homepage: www.elsevier.com/locate/medengphy

The air–liquid flow in a microfluidic airway tree

Yu Song, Michael Baudoin, Paul Manneville, Charles N. Baroud*

LadHyX and Department of Mechanics, Ecole Polytechnique, CNRS UMR 7646, 91128 Palaiseau Cedex, France

ARTICLE INFO

Article history:
Received 13 January 2010
Received in revised form
28 September 2010
Accepted 4 October 2010

Keywords:
Two-phase flow
Airway tree
Liquid plugs
Microfluidics

ABSTRACT

Microfluidic techniques are employed to investigate air–liquid flows in the lung. A network of microchannels with five generations is made and used as a simplified model of a section of the pulmonary airway tree. Liquid plugs are injected into the network and pushed by a flow of air; they divide at every bifurcation until they reach the exits of the network. A resistance, associated with the presence of one plug in a given generation, is defined to establish a linear relation between the driving pressure and the total flow rate in the network. Based on this resistance, good predictions are obtained for the flow of two successive plugs in different generations. The total flow rate of a two-plug flow is found to depend not only on the driving pressure and lengths of the plugs, but also the initial distance between them. Furthermore, long range interactions between daughters of a dividing plug are observed and discussed, particularly when the plugs are flowing through the bifurcations. These interactions lead to different flow patterns for different forcing conditions: the flow develops symmetrically when subjected to constant pressure or high flow rate forcing, while a low flow rate driving yields an asymmetric flow.

1. Introduction

The lung is a dynamic organ where mechanical stresses play an important biological role. These stresses may arise in particular from the presence and transport of liquids within the airway tree. While liquid is always present on the inner surfaces of the pulmonary paths, it can form discrete plugs that occlude the airway in pathological situations [1]. Indeed, many respiratory pathologies, such as asthma, pneumonia, or respiratory distress syndrome, may involve the blockage of the airways by liquid plugs which impede the flow of air. Moreover, flows associated with the movement or rupture of liquid plugs can cause damage to endothelial cells which line the lung surface [2,3].

In addition to these pathologies where occlusion by the pulmonary fluids can occur, the instillation of liquid plugs into the pulmonary airway is common in medical treatments such as partial liquid ventilation and drug delivery [4]. It is of vital importance, for instance, in the case of Surfactant Replacement Therapy, where surfactant is injected as a liquid bolus into the lungs of premature neonates [5]. In these cases of drug delivery, the only available control over the plug distribution is at the entrance of the network, at the level of the patient's trachea. Once the bolus is injected, little is known about the ultimate distribution of liquid within the pulmonary tree, although some studies have attempted to predict surfactant dispersion by numerical or experimental models [6,7]. Variations in the paths taken by daughters of the initial surfactant plug may account for the inconsistent responses observed in such therapies [5].

One of the difficulties that arise is due to the interactions between the immiscible interfaces and the complex geometry of the lung. Indeed, the presence of surface tension introduces a nonlinear relationship between pressure drop and flow rate in a particular branch, through the addition of Laplace pressure terms [8,9]. While these nonlinearities already appear in flow through straight channels [10], they are amplified when plugs pass a bifurcation since the interfaces must strongly deform in this case [9]. This can lead to the existence of local blockage if the pressure is below a threshold value, or to plug rupture if the plug length is too small.

Microfluidics has already been proposed as a way to model branching geometry of the lung, at least in the generations where gravity and inertial effects are negligible [11]. These regions of the lung are characterized by length scales below the capillary length and small Reynolds numbers. The capillary length L_C, i.e. the scale below which the effects of gravity become small compared with surface tension effects, is generally around 2 mm for most liquids. The Reynolds number compares the effects of fluid inertia with viscous effects through the relation $Re = \rho_l UD/\eta$, where ρ_l is the liquid density, U is a characteristic velocity, D is the airway diameter, and η is the fluid viscosity. The two criteria $D < L_C$ and $Re < 1$ are met in the lung for a large range of generations, starting from about generation 9 to the respiratory bronchioles, around generation 20 [12]. The ability to fabricate complex microfluidic geometries using photo-lithography techniques therefore opens a wide range of pos-

* Corresponding author. Tel.: +33 169335261; fax: +33 169335292.
E-mail address: baroud@ladhyx.polytechnique.fr (C.N. Baroud).

1350-4533/$ – see front matter © 2010 IPEM. Published by Elsevier Ltd. All rights reserved.
doi:10.1016/j.medengphy.2010.10.001

sibilities for addressing questions of liquid distribution that are relevant for pulmonary flows, in the presence of different additional physical phenomena.

Below, we study the motion of liquid plugs in a connected tree of microchannels. We begin with a description of the experimental setup in Section 2. In Section 3, we derive an empirical relation for the resistance to flow due to a single plug in the network and show that this relation generalizes well for the case of a train of two plugs. Further, different behavior is observed for pressure vs. flow rate driving as the plug flows further into the network, since the resistance to flow is modified by the passage through successive bifurcations.

2. Experimental setup

Our experiments are conducted in a network consisting of branching microchannels that have rectangular cross-sections, as shown in Fig. 1. Soft lithography techniques are employed to make the channels of polydimethylsiloxane (PDMS) [13]. A thin flat layer of PDMS is spin-coated on a glass microscope slide and the channels are bonded on this PDMS layer in order to guarantee identical boundary condition at all four channel walls.

The network inlet consists of a Y-junction connected to the first generation for creating and injecting liquid plugs into the network. One inlet of the Y-junction is connected to a syringe filled with perfluorodecalin (PFD) and the syringe can be pushed by a pump. PFD is a fluorocarbon whose viscosity and surface tension are $\eta = 5 \times 10^{-3}$ Pa s and $\gamma = 20 \times 10^{-3}$ N/m, respectively. It presents good wetting properties on PDMS and does not swell the channels. Through the second inlet of the Y-junction, the air goes into the network and a constant driving is applied between the first and the last generations. Either constant pressure or constant flow rate can be applied. When pushing at constant pressure, the inlet of the air is connected to a computer-controlled pressure source (FLUIGENT, MFCS-8C). To apply a constant flow rate, a syringe is filled with water and connected to the air inlet through a flexible tube. Only a small volume of air near the network entrance is left in the tube in order to reduce the effects of air compressibility. A syringe pump ensures a constant flow rate of the water which then pushes the air into the network. Driving conditions for the experiments in this paper are given in Table 1.

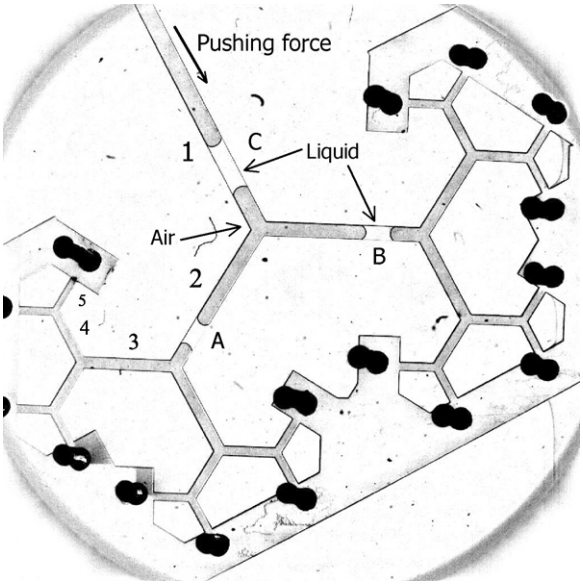

Fig. 1. Microscope image of the microfluidic network with five generations. Generations are numbered with Arabic numerals. The two early plugs (A and B) in generation 2 are the daughters of the first plug. A second plug (C) is moving in the first generation.

Table 1
Experimental conditions.

Number of plug(s)	Driving Condition
1	Pressure: $P_{dr} = 150, 250, 400$ Pa
1	Flow rate: $Q_{dr} = 2, 5, 20$ μL/min
2	Pressure: $P_{dr} = 500$ Pa

The height of all the branches in the network is 50 ± 2 μm and the width of the branch in the first generation is 720 μm. Channel widths of successive generations w_i decrease at a constant rate $w_{i+1} = \rho w_i$, where $\rho = 0.83$ is a constant parameter and the subscript denotes the generation number. This value of ρ preserves the ratio of mean diameters observed in the pulmonary airway [12]. It gives a width 342 μm for the last generation. The channel lengths also decrease linearly with the generation number, with a ratio 0.6. This value was chosen to preserve the ratio of plug length to branch length at each generation, thus reducing the number of variables in the problem, if the plugs divide symmetrically at the bifurcations. PFD plugs (bright regions) surrounded by air (gray regions) are indicated in Fig. 1. The plugs are injected into the first generation and pushed through the network, dividing into two daughters at every bifurcation. At the exits of the last generation, sixteen holes (black in Fig. 1) are punched to fix the exit condition at atmospheric pressure.

Experiments are recorded with a high speed camera (Photron Fastcam, 1024 PCI) through a stereomicroscope at 0.7× magnification. The resolution of the camera is 1024×1024 pixels, which yields 1 pixel for 24.8 μm. For the single plug experiments, images are taken at different rates (varying from 30 to 125 images per second) according to the driving conditions, thus ensuring that the plug positions can be traced with a good resolution. For two successive plugs under constant pressure driving, 125 images per second are recorded. From the image sequences thus obtained, the positions x_r of the rear interface of the plug are manually recorded while the plug is traveling in the network. Based on these measurements, the plug velocity is calculated as $U = [x_r(t) - x_r(t - dt)]/dt$, where dt is the time step between successive images. The fluid deposition on the walls is neglected in the calculation since it does not affect the flow significantly in our experimental conditions.

3. Movement in the straight sections

In this section, we focus on the velocity of a plug pushed at a constant pressure as it travels in the straight channels between two successive bifurcations. We first study the case of a single plug and its daughters in the network, then build a relation reproducing the results and show that it can be applied to the case of two successive plugs and their daughters.

3.1. A single plug in the network

A single plug is injected into the network and then pushed at a constant pressure P_{dr}. It divides into two at every bifurcation and velocities of all its daughters, measured in each branch, are recorded according to their position in the network (generation numbers i). The daughter plugs are constantly subjected to the same pressure difference and should therefore all move at the same speed which, in addition, should be constant during their passage in their respective branches. Variations from branch to branch and within a branch, to be attributed to imperfections in the micro-

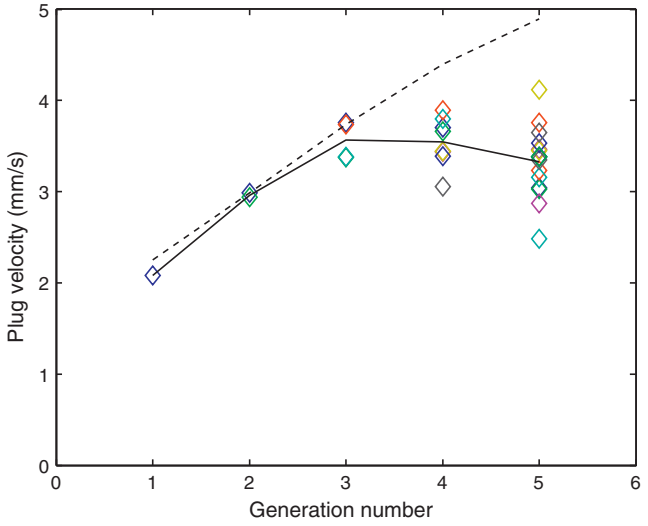

Fig. 2. Average plug velocity as a function of the generation number i (driving pressure 250 Pa). Symbols correspond to values recorded in each branch and the solid line to their average. The prediction from a previous study [9] is shown as a dashed line.

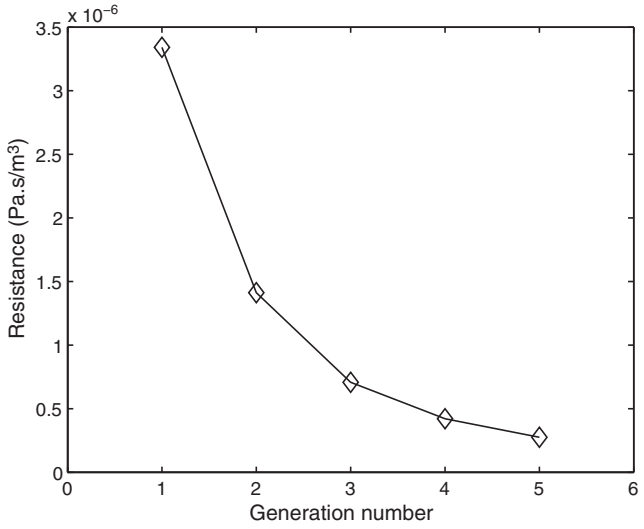

Fig. 3. Dependence of the resistance on the generation number.

fabrication, are observed however. As the channels get narrower, the flow becomes more sensitive to wall conditions, which brings bigger separations between data points in later generations. For each generation number i, values corresponding to the 2^{i-1} individual time-averages of the plug velocities are plotted in Fig. 2. The solid line drawn through these points thus gives the average value obtained over the 2^{i-1} branches.

At this stage, it is interesting to compare these observations to the theoretical prediction that could be made from the study of plug motion in straight channels in microfluidics conditions [9]. The formula in Eq. (11) of Ref. [9] is used to compute the velocity in all the generations by assuming that plugs divide equally at each bifurcation while taking into account the narrowing of the channels $w_i = w_1\rho^{i-1}$, hence $L_i = L_1/(2\rho)^{i-1}$. The result is given as a dashed line in Fig. 2, from which it is immediately seen that the plugs experience a resistance larger than predicted as they progress in the network. Since the formula is well validated in the case of long plugs, we attribute the discrepancy to the exponential shortening of the plugs with the generation number: for the experiment corresponding to the data in Fig. 2, the plug length in the last generation is $L_5 = 300\ \mu$m while the channel width is $w_5 = 342\ \mu$m. Plugs are therefore comparatively short and the resistance is underestimated in the last generations.

The limitations of the theory led us to develop an empirical relation that we now describe. As for an electrical network, we define a resistance R_iL_i associated with the presence of a daughter plug of length L_i in generation i, where the role of the voltage is played by the driving pressure P_{dr} and the role of the current intensity by the volumetric flow rate in each branch of that generation Q_i. We can therefore write $P_{dr} = R_iL_iQ_t = R_iL_iQ_iN_i$, where $N_i = 2^{i-1}$ is the number of branches in that generation and $Q_t = Q_iN_i$ is the total flow rate in the network. We assume further that each plug divides into two daughters of essentially equal lengths at every bifurcation, which is consistent with experimental observations, $L_i = L_1/(2\rho)^{i-1}$. Flow rate Q_i is calculated as $Q_i = U_ihw_i$, U_i being the plug velocity in that generation. The values of R_i can be computed from the measurements since the driving pressure, the initial length of the plug and the flow rate based on velocity measurements are known. They are found to decrease with the generation number, as shown in Fig. 3. This leads to an increase in the total flow rate Q_t as the plug reaches later generations (symbol ♦ in Fig. 4).

3.2. Two successive plugs

The relation just defined now allows us to analyze the dynamics when two plugs are injected successively. Like for two resistors mounted in series, the relation between the driving pressure and the volumetric flow rate can be written as $P_{dr} = R_i^{[1]}L_i^{[1]}Q_t^{[1]} + R_j^{[2]}L_j^{[2]}Q_t^{[2]} = (R_i^{[1]}L_i^{[1]} + R_j^{[2]}L_j^{[2]})Q_t$, where the superscripts '[1]' and '[2]' denote the first and the second plugs and the subscripts 'i' and 'j' indicate the position of the plugs in the network by the corresponding generation numbers. Using the values of R_i determined above and the initial lengths of two plugs, R_iL_i can be computed. Flow rates for a two-plug train for the driving pressure $P_{dr} = 500$ Pa are compared to the experimental findings in Fig. 4. Satisfactory agreement is obtained, indicating that the linear description of the flow in the network gives a good approximation in the current conditions.

Notice that although the lengths of the plugs and the driving pressure are kept the same, the total flow rate displays a clear dependence on the distance between the two plugs, as shown in Fig. 4. When the plugs get further apart, a higher flow rate is

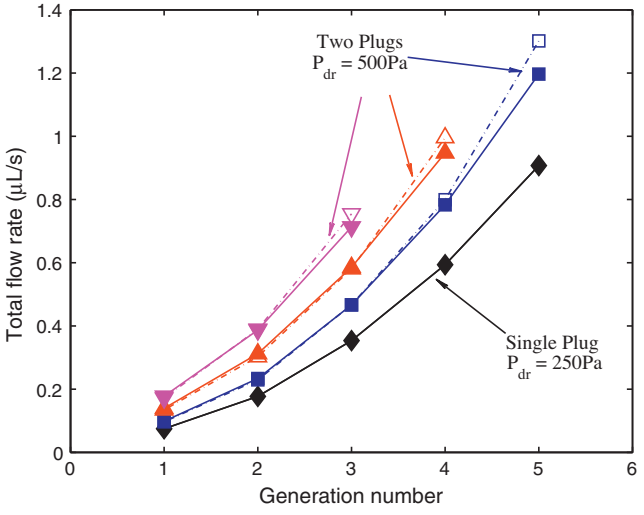

Fig. 4. Evolution of the total flow rate in a single plug experiment (♦) (driving pressure $P_{dr} = 250$ Pa) and two-plug experiments ($P_{dr} = 500$ Pa) when they always flow in the same generation (□), in two successive generations (△) and with a separation of one generation (▽). Open symbols denote experimental data and closed ones are values derived from the linear law.

observed. This can be understood by noting that the resistance due to the downstream plug decreases with generation number and thus the sum $(R_i^{[1]}L_i^{[1]} + R_j^{[2]}L_j^{[2]})$ also decreases.

4. Passage through a bifurcation and long range interactions

The passage of a plug in a bifurcation leads to highly nonlinear effects because of the strong modification of the shape of the interface. We begin by considering the details of the passage of a plug through a bifurcation before turning to how the behavior of one plug influences the passage of plugs elsewhere in the network.

4.1. One plug in one bifurcation

Consider a plug that just arrives at a bifurcation, as sketched in Fig. 5(a). The curvature of the front interface decreases before the rear one is affected by the bifurcation, which introduces a capillary pressure difference across the plug. This is a three-dimensional problem and the biggest curvature of the interface exists in the direction perpendicular to the plane of the network. However, we assume that the capillary pressure *difference* is mainly driven by curvature differences in the plane of the network. The pressure difference P_{cap} between the rear and front interfaces can be expressed as $P_{cap} = P_r - P_a = \gamma/r_r - \gamma/r_a$, where P_r, P_a denote the capillary pressures at the receding and advancing interfaces and r_r, r_a are the signed radii of curvature of the interfaces in the plane of the network. Before the plug touches the opposite wall, we have $r_a > r_r$ and r_a increases as the plug advances. So P_{cap} acquires increasing positive values. There exists a threshold pressure necessary to push a plug through a bifurcation, which is estimated as the maximum value of P_{cap}: $P_{thr} = P_{cap,\max} = \gamma/r_r - \gamma/r_{a,\max}$ where $r_{a,\max}$ is the maximum possible value of r_a, reached just before the front interface touches the corner of the opposite wall. Beyond this point, P_{cap} becomes negative ($r_a < r_r$) and pulls the daughter plug (Fig. 5(b)). When the plug has fully passed the bifurcation, P_{cap} cancels ($r_a \approx r_r$).

The threshold pressure P_{thr} can be computed from the network geometry:

$$P_{thr} = \frac{2\gamma\cos\theta}{w_i} - \frac{\gamma(\cos\theta - \sin\alpha)}{w_{i+1}} \quad (1)$$

where θ is the contact angle of PFD on PDMS (around 23°) and the bifurcation half-angle, α, is half the angle between the two branches of the same generation. Here $\alpha = 60°$ yields the threshold pressure $P_{thr} = 51$, 61, 74 and 89 Pa for the first to the fourth bifurcations, respectively. Although the values of P_{thr} depend on the value of the contact angle θ, a difference of 23° in the contact angle only changes the threshold by 2 Pa.

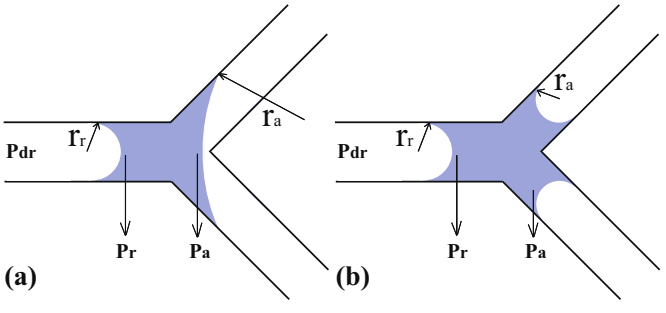

Fig. 5. Passage through a bifurcation. (a) A plug arrives at the bifurcation. The radius of curvature r_a is bigger than r_r and increasing while the plug is advancing. (b) After the front interface touches the next generation, r_a becomes smaller than r_r (notice that here $2\alpha = 90°$ for convenience).

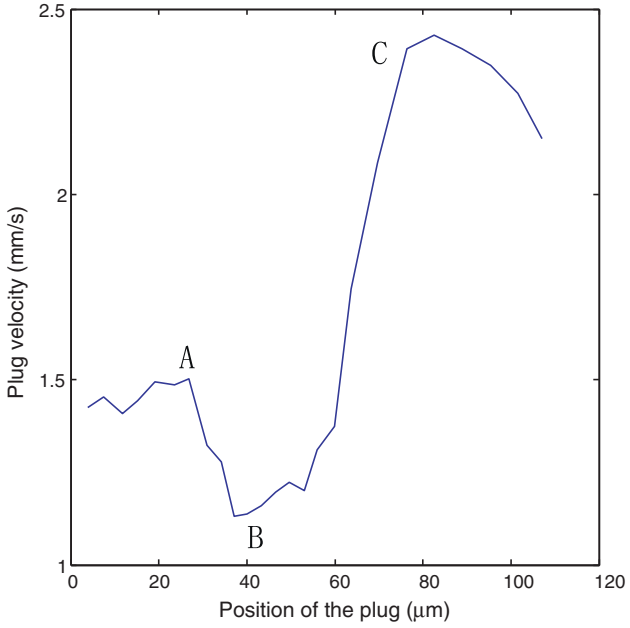

Fig. 6. Experimental measurements of plug velocity during the passage through a bifurcation. The position of the plug is defined as that of its rear interface.

When the plug is pushed at a constant pressure, the pressure difference across the plug can be expressed as $\Delta P = P_{dr} - P_{cap}$. The variation in P_{cap} will lead to variations of ΔP and also of the velocity of the plugs as they advance. In order to push a plug through a bifurcation, ΔP has to remain positive during the passage. This implies that the driving pressure has to be larger than the threshold pressure. Meanwhile, the velocity variations during the passage should account for the appearance of P_{cap}, which modifies the value of the effective driving pressure as ΔP.

Measurements of the velocity of a particular plug are shown in Fig. 6 when it is pushed at $P_{dr} = 250$ Pa and passes the second bifurcation in the network. The plug initially slows down after it enters the bifurcation (position A), after which its velocity rises quickly as the front interface reaches the opposite wall (position C), since $P_{cap} < 0$ and ΔP increases. Accordingly the passage of a plug through a bifurcation is always associated with a large spike in the velocity.

When the plug is forced at a constant flow rate, if the passage can be treated as a quasi-static process, we may write that $\Delta P = P_{cap}$ [14]. Variations in P_{cap} will therefore induce variations in the pressure upstream of the plug position such that ΔP will increase until the plug touches the opposite wall, where it rapidly switches to a negative value which pulls the plug into the daughter channels. The largest value reached by ΔP is $\Delta P = P_{thr}$.

4.2. Plug interactions

The connectivity of the branching tree implies that local pressure variations will lead to long range effects across different regions of the network. The fundamental unit to understand these interactions is shown in Fig. 7, where two daughters (I and II) of the same plug arrive at two bifurcations nearly simultaneously.

Assume that plug I touches the opposite wall slightly earlier than plug II. Then, its velocity as well as the flow rate in that branch increase according to the above analysis. In case of *constant pressure forcing*, the driving condition for plug II is not modified; this plug also slows down and then speeds up as it crosses the bifurcation, independently of plug I. This is no longer the case if the plugs are pushed at *constant flow rate Q*. When plug I passes the bifurcation

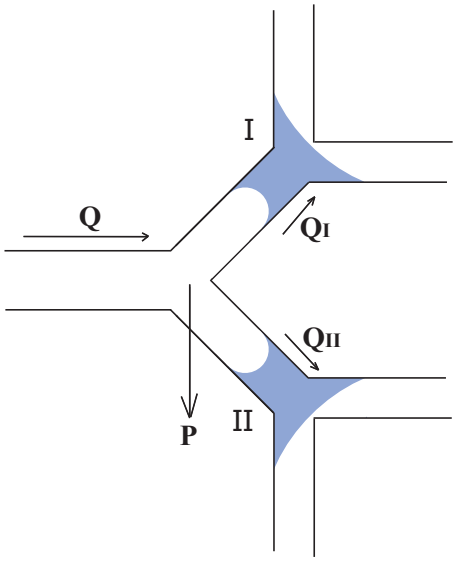

Fig. 7. The fundamental unit of long range interactions between two plugs.

shown in Fig. 7, the flow rate Q_I increases, forcing Q_{II} to decrease in order to conserve the value of $Q = Q_I + Q_{II}$. In fact, Q_{II} may become zero or even negative, which means that plug II may stop or even move backwards, depending on the value of Q.

5. Results

The flow behavior is studied by tracking the positions and velocities of daughter plugs along the paths shown in Fig. 8. In these experiments, a single plug is injected into the network and forced to divide into two at every bifurcation.

5.1. Constant pressure driving

A time sequence showing the successive divisions is shown in Fig. 9, when the plug is pushed at a constant driving pressure $P_{dr} = 250$ Pa. Only half of the network is shown for clarity. As seen in these images, the plug positions may vary slightly across the different generations but they mostly advance in synchrony through the bifurcations and across generations. These results are typical of many different experiments. A more quantitative measure of this synchronous flux is given by measuring the plug velocities as functions of time along the four paths, as shown in Fig. 10. As the daughter plugs advance in the network, their number increases and their velocities vary according to the analysis in Section 3.

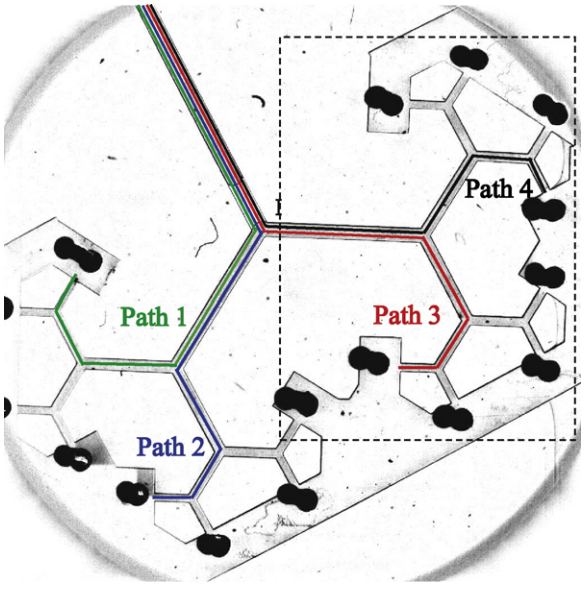

Fig. 8. Paths along which the plug positions and velocities are measured. The dashed box indicates the zone that is displayed in Figs. 9 and 11.

The spikes that appear in the velocity time series are the signatures of passages through the bifurcations, as explained above. By tracking the moment at which the spikes occur along each of the different paths, we see that the plugs reach the bifurcations and divide at roughly the same time. This is in spite of imperfections in the network which lead to slight asymmetry in the divisions and thus yield plugs of variable sizes. Moreover, a careful examination of the time series reveals small differences in the passage times through the second bifurcation. However, this difference is not amplified in later generations and the plugs all continue in a steady fashion. The flow remains globally symmetric during its evolution.

5.2. Constant flow rate driving

When the experiments are repeated by pushing the plug at a constant flow rate, the behavior may be strongly modified. In the experiment shown in Fig. 11, the driving flow rate is $Q_{dr} = 2\,\mu$L/min and two daughters are observed as they advance simultaneously in generation 2 (image (b)) but this synchrony is broken when they reach the bifurcation. At this stage, only one of the daughters divides and its daughters continue to flow in generation 3 (image (c)). However, the upstream plug catches up with its sister which gets blocked at the next bifurcation due to the higher threshold pressure.

The velocities of the plugs are displayed in Fig. 12 along the same paths as above. Due to flow rate conservation in the network, the plugs adjust their velocities while advancing and the acceleration in one path leads to a deceleration in the others. Here, an uneven division, which introduces daughters of different lengths, leads to significant velocity variations since a shorter daughter is easier to push forward than a longer one. Velocity differences are visible, for instance, in the case of the two daughters of the initial plug as they flow in generation 2: while the one in paths (3, 4) speeds up, the one in paths (1, 2) must slow down.

After one daughter passes a bifurcation and divides, a flow rate increase in the corresponding branches results in a slowing down of other daughters which become stuck at the bifurcations. Once the early plug that has divided reaches the next bifurcation, the threshold pressures at two successive bifurcations have to be compared and the plug with the lowest threshold will advance first. In this network, the threshold increases with generation number, which implies that the late plugs can catch up with the early ones. The most downstream plug must therefore wait at the bifurcation for all other plugs to reach the same bifurcation level before it can continue its journey. This is shown in the velocity evolution in Fig. 12, by the segments with zero velocities before the passage of a bifurcation.

At constant flow rate forcing $Q_{dr} = 2\,\mu$L/min, the air–liquid flow therefore remains symmetric but evolves through discrete steps. Plugs are never more than one generation apart due to the increasing threshold pressure, but they spend long periods of time stationary at bifurcations, waiting for plugs in the other branches to catch up.

5.3. Flow patterns in the network

Results of experiments repeated at different driving conditions are summarized in this section. As shown earlier, the flow is synchronous at $P_{dr} = 250$ Pa, but turns out to be asynchronous at

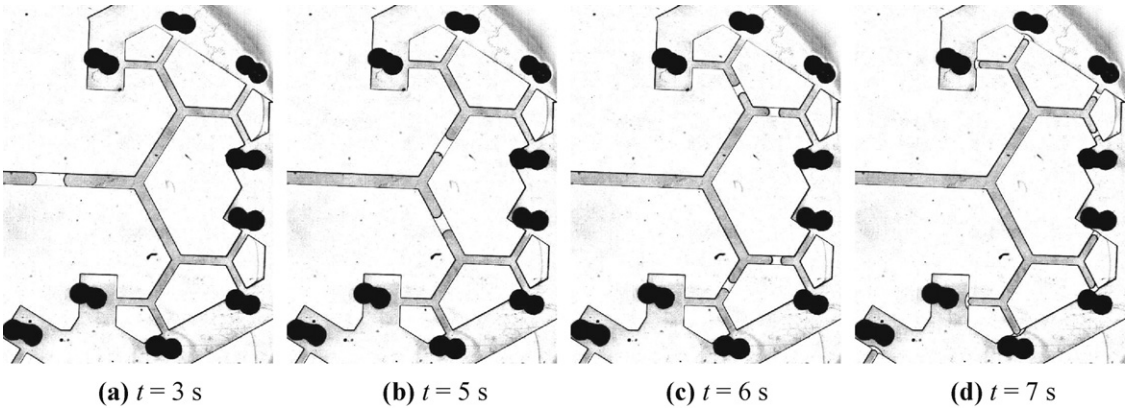

Fig. 9. Image sequence for the half network, obtained from the experiment of constant pressure driving.

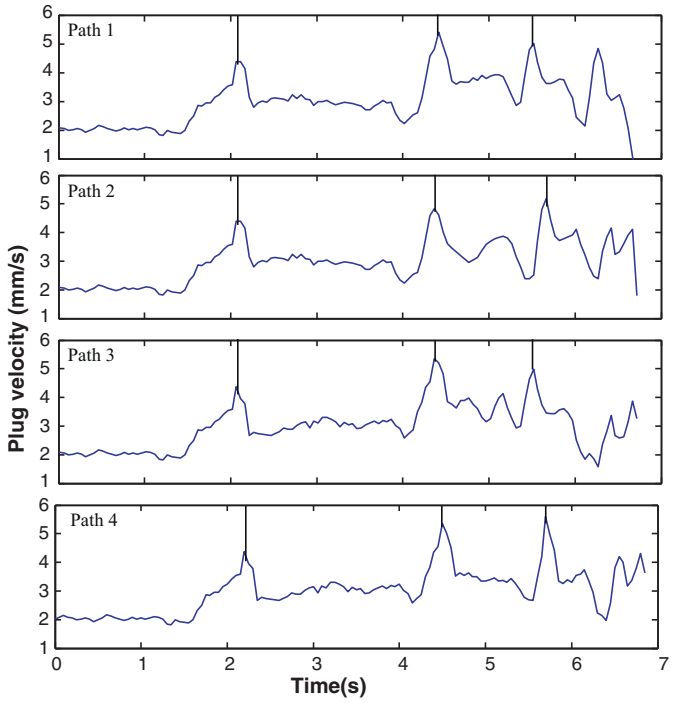

Fig. 10. Velocity variations along four paths under a constant pressure driving $P_{dr} = 250$ Pa. The vertical line indicates the time when the plug passes a bifurcation.

$Q_{dr} = 2$ μL/min. However, the flow pattern depends on not only the type of the driving condition but also the value of driving force.

The behavior described above can be summarized by measuring the time Δt_i separating the first and last plug divisions at a particular depth in the network. We normalize this time difference by the mean time taken to travel through the following generation (T_{i+1}) and write the normalized time $\overline{\Delta t_i}$. A value of $\overline{\Delta t_i} < 1$ indicates that the plugs advance nearly simultaneously through the generation $i+1$, while a value of $\overline{\Delta t_i} > 1$ implies that some plugs only divide once the early ones have already reached the next bifurcation. The results for different experiments are shown in Fig. 13, where each data point corresponds to an average over several experimental realizations.

Two distinct behaviors are observed. The division times for constant flow rate driving are above 1 at the second and third bifurcations for $Q = 2$ μL/min and at the third bifurcation for $Q = 5$ μL/min. This confirms that plugs pass one by one, waiting for each other to reach the next bifurcation. The transition to $\overline{\Delta t_i} > 1$ occurs when the pressure necessary to ensure the constant flow rate decreases below the local threshold, as described in Ref. [14]. Note that the values of $\overline{\Delta t_i}$ increase with generation number here because the number of sister plugs increases and since they must pass separately. In contrast, constant pressure driving yields values of $\overline{\Delta t_i}$ that are significantly below 1, indicating that plug divisions are nearly synchronous. This is the case for all of the data recorded here except for the lowest pressure value, at which $\overline{\Delta t_i} \sim 1.3$. This can be attributed to imperfections in the microfabrication. Indeed, depth variations of the channel, due to the uncertainty in the photolithography process, can lead to pressure differences between the front and the rear of a plug. When combined with low values of the

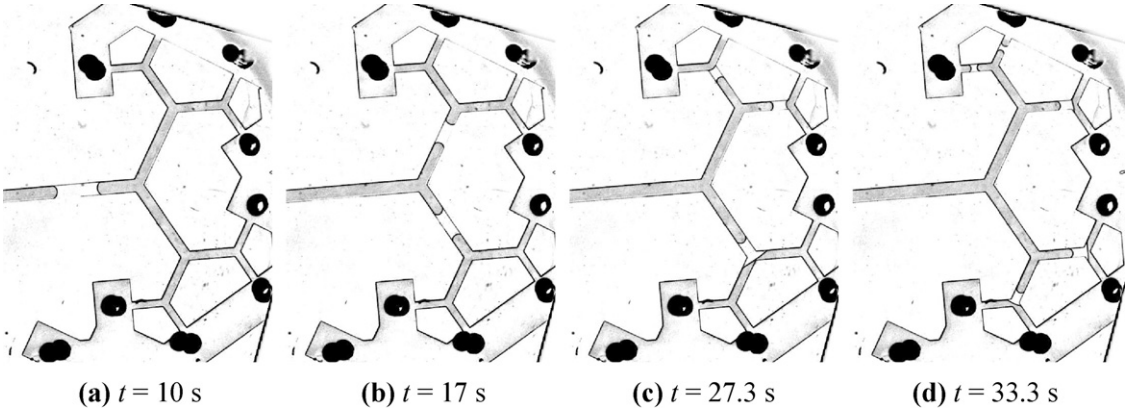

Fig. 11. Image sequence for the half network, obtained from the experiment of constant flow rate driving.

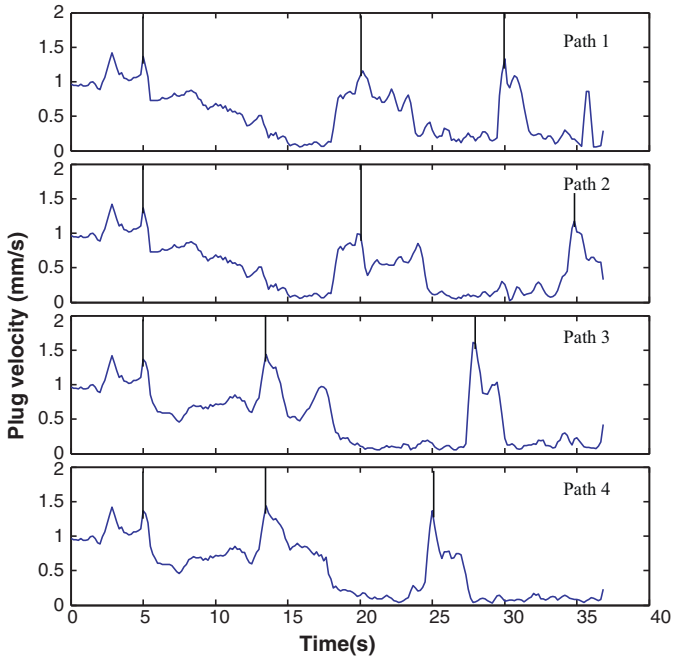

Fig. 12. Velocity evolutions along four paths under the constant flow rate Q_{dr} = 2 μL/min. The vertical line indicates the time when the plug passes a bifurcation.

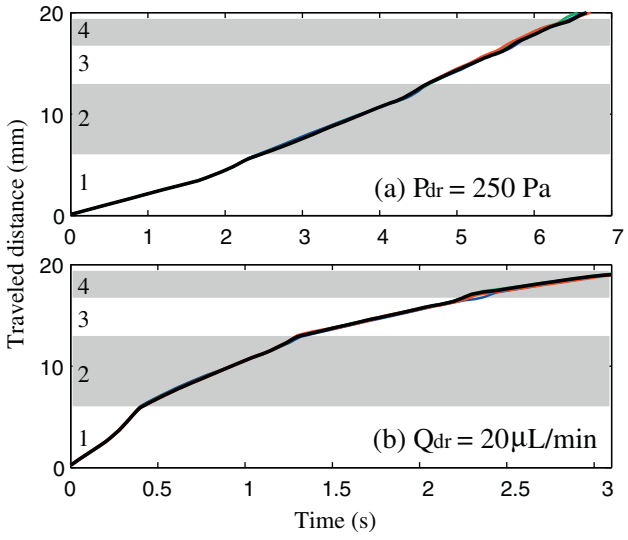

Fig. 14. Distance traveled by daughter plugs along four paths in the network. The shaded and non-shaded areas represent successive generations as labeled on the right of the *y*-axis and the line color is used to indicate the corresponding path shown in Fig. 8. (a) Driving condition P_{dr} = 250 Pa. (b) Driving condition Q_{dr} = 20 μL/min.

driving pressure compared with the threshold to pass a bifurcation, these can result in small values of ΔP, which imply that some plugs advance very slowly through particular bifurcations.

For large driving flow rate (e.g. Q = 20 μL/min) and pressures (P_{dr} > 150 Pa), the plug movement is synchronous in both methods, as seen by the small values of $\overline{\Delta t_i}$. This can also be observed by plotting the positions of the plugs as a function of time, as shown in Fig. 14. In this figure, the position of the rear interface along four representative paths is plotted and all four divide simultaneously both for constant flow rate and constant pressure. However, the distance curves display different evolutions, which allows us to distinguish the driving conditions. While the plugs slightly accelerate as a function of generation number in the case of pressure forcing, they clearly decelerate in the case of flow rate driving, since the number of daughters increases and the flow is distributed over a larger area.

This information can be summarized by measuring the time (T_i) spent traveling in the straight sections in each generation. This is shown in Fig. 15, where each data point is the average over all the plugs in a given generation, averaged over several experimental realizations. T_i is normalized by the total time for an experiment, i.e. the time from the initial plug entering the first bifurcation to the last daughter passing the last bifurcation. For pressure driving, we observe that the time spent in the straight channel decreases as the plugs advance. Since the plug velocity decreases more slowly than the channel length, it takes a shorter time to pass the branch in the later generations. In the case when the plug is pushed at a high flow rate, the travel time remains constant with generation number because the decrease in plug velocity evolves in the same way as the channel length. This result is true by construction and holds for any value of ρ.

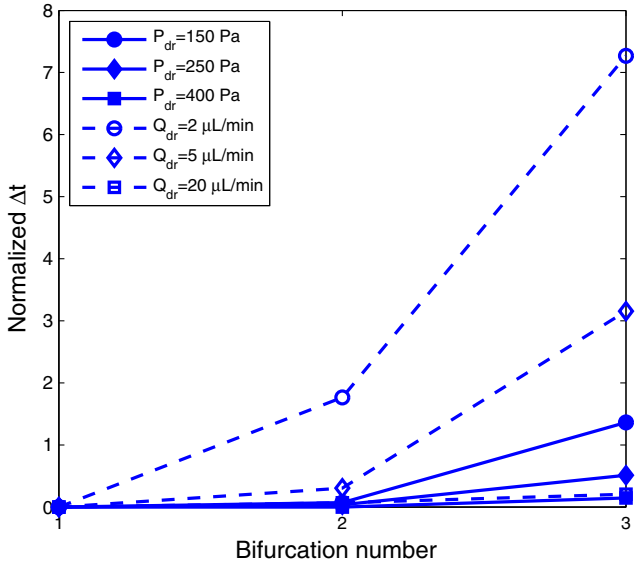

Fig. 13. Time difference of daughters' passage through bifurcations of the same level, data normalized to the average traveling time in the next generation.

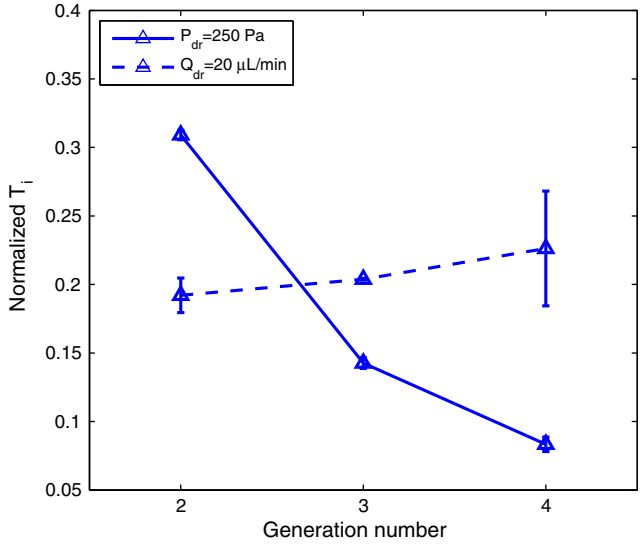

Fig. 15. Comparison of traveling time in each generation for pressure and high flow rate forcing. Both yield symmetric flow patterns.

6. Summary and discussion

In investigating the flow of liquid plugs in a branching network, an empirical relation expressing the pressure–flow rate evolution is derived from the motion of a single plug and found to account for the resistance of the network to the flow of liquid. Given the initial condition of the experiments, e.g. driving pressure and plug lengths, this relation quantitatively predicts the flow rates in the presence of a train of two plugs. This empirical relation indeed provides a better prediction of the flow of a train of plugs than the physical model presented in Ref. [9].

When two successive plugs are separated by a large distance in the network, the resistance associated with the downstream plug is small compared to the resistance of the upstream liquid. This implies that the flow rate in the network is essentially fixed by the upstream plug and the downstream plug perceives a constant flow rate forcing, even if the actual driving condition is through pressure. This may modify the flow distribution in the branching tree through inter-generation effects, which are expected to feed back on the flow everywhere in the network.

Furthermore, the passage through a bifurcation induces strong variations in the capillary pressure jumps across the air–liquid interfaces, which has a major impact on the flow through the branching channels. When considering a single bifurcation, this leads to large variations in the velocity at which the plug advances. It also leads to the existence of a threshold value of the driving pressure necessary to push the plug. A similar threshold is expected to exist in the case of the circular tubes forming the pulmonary airway tree, although its value will strongly depend on the details of the geometry at the bifurcation. Nevertheless, the presence of threshold pressures will have a similar effect on the global organization of flow in the lung as observed in our experiments. Finally, although the threshold values may be small compared with the driving pressure, a sufficiently deep airway tree will always lead to regions in which the local pressure becomes comparable with the value of the threshold.

The influence of the driving condition on the plug propagation in the network has also been explored. The nonlinear pressure–flow rate relation at a bifurcation induces strong long range interactions between plugs in different parts of the network. This is particularly visible in the case of driving the fluids with a low flow rate, in which case some plugs can stop at bifurcations and wait for long periods of time while others continue to advance. Nevertheless, symmetric filling of the network is observed in both conditions. Finally, synchronized filling can be achieved at high pressure and high flow rate driving although different flow evolutions are observed at two conditions. A better understanding of the filling of a branching tree and of the long range interactions in it should lead to improved models of liquid dispersion in the lung, which is an important problem in view of its application to pathology and drug delivery.

Acknowledgments

The authors thank FLUIGENT Company for their kind support. Michael Baudoin was funded by the ANR under the “Santé-Environnement et Santé-Travail” programme.

Conflict of interest

All the authors declare that there is no conflict of interest associated with this work.

References

[1] Grotberg J. Pulmonary flow and transport phenomena. Annu Rev Fluid Mech 1994;26:529–71.
[2] Bilek A, Dee K, Gaver D. Mechanisms of surface-tension-induced epithelial cell damage in a model of pulmonary airway reopening. J Appl Physiol 2003;94(2):770–83.
[3] Huh D, Fujioka H, Tung Y-C, Futai N, Paine R, Grotberg JB, et al. Acoustically detectable cellular-level lung injury induced by fluid mechanical stresses in microfluidic airway systems. Proc Natl Acad Sci USA 2007;104(48):18886–91.
[4] Leach C, Greenspan J, Rubenstein S, Shaffer T, Wolfson M, Jackson J, et al. Partial liquid ventilation with perflubron in premature infants with severe respiratory distress syndrome. N Engl J Med 1996;335(11):761.
[5] Engle WA, the Committee on Fetus & Newborn. Surfactant-replacement therapy for respiratory distress in the preterm and term neonate. Pediatrics 2008;121(2):419–32.
[6] Espinosa F, Kamm R. Bolus dispersal through the lungs in surfactant replacement therapy. J Appl Physiol 1999;86(1):391–410.
[7] Cassidy KJ, Gavriely N, Grotberg JB. Liquid plug flow in straight and bifurcating tubes. J Biomech Eng 2001;123(6):580–9.
[8] Bico J, Quéré D. Falling slugs. J Colloid Interface Sci 2001;243(1):262–4.
[9] Ody CP, Baroud CN, de Langre E. Transport of wetting liquid plugs in bifurcating microfluidic channels. J Colloid Interface Sci 2007;308(1):231–8.
[10] Bretherton FP. The motion of long bubbles in tubes. J Fluid Mech 1961;10(02):166–88.
[11] Baroud CN, Tsikata S, Heil M. The propagation of low-viscosity fingers into fluid-filled branching networks. J Fluid Mech 2006;546(-1):285–94.
[12] Weibel ER. The pathway for oxygen. Cambridge, MA, USA: Harvard Uuniversity Press; 1984.
[13] Stephan K, Pittet P, Renaud L, Kleimann P, Morin P, Ouaini N, et al. Fast prototyping using a dry film photoresist: microfabrication of soft-lithography masters for microfluidic structures. J Micromech Microeng 2007;17(10):N69–74.
[14] Song Y, Manneville P, Baroud CN. Local interactions and the global organization of a two-phase flow in a branching tree. Phys Rev Lett 2010;105:134501.

Scattering of ultrasonic shock waves in suspensions of silica nanoparticles

Michael Baudoin[a] and Jean-Louis Thomas
Institut des NanoSciences de Paris—UMR CNRS 7588, Université Pierre et Marie Curie—Paris 6, 4 place Jussieu, 75252 Paris Cedex 05, France

François Coulouvrat
Institut Jean le Rond d'Alembert—UMR CNRS 7190, Université Pierre et Marie Curie—Paris 6, 4 place Jussieu, 75252 Paris Cedex 05, France

Corinne Chanéac
Laboratoire de Chimie de la Matière Condensée de Paris—UMR CNRS 7574, Université Pierre et Marie Curie – Paris 6, 4 place Jussieu, 75252 Paris Cedex 05, France

(Received 5 February 2010; revised 27 October 2010; accepted 11 December 2010)

Experiments are carried out to assess, for the first time, the validity of a generalized Burgers' equation, introduced first by Davidson [J. Acoust. Soc. Am. **54**, 1331–1342 (1973)] to compute the nonlinear propagation of finite amplitude acoustical waves in suspensions of "rigid" particles. Silica nanoparticles of two sizes (33 and 69 nm) have been synthesized in a water–ethanol mixture and precisely characterized via electron microscopy. An acoustical beam of high amplitude is generated at 1 MHz inside a water tank, leading to the formation of acoustical shock waves through nonlinear steepening. The signal is then measured after propagation in a cylinder containing either a reference solution or suspensions of nanoparticles. In this way, a "nonlinear attenuation" is obtained and compared to the numerical solution of a generalized Burgers' equation adapted to the case of hydrosols. An excellent agreement (corresponding to an error on the particles size estimation of 3 nm) is achieved in the frequency range from 1 to 40 MHz. Both visco-inertial and thermal scattering are significant in the present case, whereas thermal effects can generally be neglected for most hydrosols. This is due to the value of the specific heat ratio of water–ethanol mixture which significantly differs from unity.
 [DOI: 10.1121/1.3533723]

PACS number(s): 43.25.Jh, 43.20.Fn, 43.35.Bf [ROC] Pages: 1209–1220

I. INTRODUCTION

The propagation of finite amplitude acoustic waves in suspensions of "rigid" particles has been first studied theoretically by Davidson in 1973.[1,2] Contrary to the case of high amplitude hydrodynamic shock waves,[3] simplified equations can be obtained through a rigorous asymptotic matching.[1,4] This is due to the small amplitude of acoustical shock waves compared to hydrodynamic shock waves. Davidson[5,6] has derived several generalized Burgers' equations, with one term due to the nonlinear propagation in the continuous phase, and additional relaxation terms due to momentum, heat, and mass transfers between particles and the surrounding medium. We recall that the usual Burgers' equation with thermo-viscous absorption has been first introduced in acoustics by Mendousse,[7] for the propagation of finite amplitude acoustic waves in a viscous perfect gas. The notion of generalized Burgers' equation adapted to any kind of linear dispersion relation is proposed by Blackstock.[8]

A generalized Burgers' equation for two-phase media can be obtained by averaging and simplifying Navier–Stokes equations, providing that (1) the size a of the particles is much smaller than the acoustical wavelength λ, (2) the suspension is dilute, and (3) the response of the particles is linear. Otherwise, nonlinear terms are themselves modified by the presence of nonlinear scatterers. Bubbly media are extensively studied examples.[9,10]

If theoretical aspects[4–6] (equations, dispersion relation, shock structure, etc.) of the propagation of finite amplitude acoustic waves in suspensions have been widely studied, there is still no experimental evidence of the validity of such equations. This gap can be explained by the difficulty of performing such experiments. The propagation of finite amplitude acoustic waves in aerosols requires first the formation of a stable and precisely controlled aerosol, and then the generation of acoustic shock waves in air. Both requirements are hardly compatible in simple in-laboratory experiments. In the case of hydrosol, the shock thickness associated with ultrasonic underwater acoustic shock waves is generally about 10 μm and, therefore, requires the synthesis of suspensions with particles of size within the nano range to meet the above requirements. Recent and tremendous progresses in nanosciences now make this relatively easy to control. We chose to study silica nanoparticles, since particles of controlled and relatively monodisperse size can be simply synthesized. Moreover, the resulting suspension is stable and the particles spatial distribution is statistically homogeneous

[a]Author to whom correspondence should be addressed. Current address: Université Lille 1, Institut d'Electronique, de Microélectronique et de Nanotechnologie (IEMN), avenue Poincaré, BP 60069, 59652 Villeneuve d'Ascq Cedex, France. Electronic mail: michael.baudoin@univ-lille1.fr

TABLE I. Composition of solutions I and II.

	Solution I	Solution II
Suspension A	30 ml TEOS + 30 ml C_2H_5OH	138 ml C_2H_5OH + 27 ml H_2O + 3 ml NH_4OH
Suspension B	30 ml TEOS + 30 ml C_2H_2OH	138 ml C_2H_5OH + 28.2 ml H_2O + 1.8 ml NH_4OH
Solution C	30 ml C_2H_5OH	idem susp. A
Solution D	30 ml C_2H_5OH	idem susp. B

(due to the Brownian motion). Finally, the particles are spherical, which considerably simplifies the theoretical modeling of momentum and heat transfers.

In Sec. II, we describe all aspects of the experimental setup, from the synthesis of the suspensions to the generation and measurement of acoustical shock waves. In Sec. III, we introduce a model based on a generalized Burgers' equation adapted to the present case of a hydrosol with thermal transfers. An adapted computation scheme is also discussed. Finally, in Sec. IV, we compare the experimental absorption measurements to the outputs of the numerical simulations for two different suspensions.

II. EXPERIMENTAL SECTION

A. Nanoparticles synthesis

Two colloidal suspensions A and B of silica nanoparticles diluted in ethanol with different particle sizes have been synthesized following Stöber process.[11] This is an ammonia-catalyzed condensation reaction of tetraethylorthosilicate (TEOS) [$Si(OR)_4$ with $R = C_2H_5$] in ethanol (ROH). A first hydrolysis reaction produces the monomer [$(OR)_3Si(OH)$]:

$$Si(OR)_4 + H_2O \overset{OH-}{\mapsto} (OR)_3Si(OH) + ROH.$$

Then this monomer condenses to form silica particles:

$$(OR)_3Si(OH) + H_2O \mapsto SiO2 \downarrow + 3ROH.$$

This synthesis is obtained at room temperature by mixing two solutions, a first solution (solution I) of TEOS diluted in ethanol and a second one (solution II) of water, ethanol, and ammonia according to quantities given in Table I. Although this synthesis is widely used, the exact mechanism of growth of the particles is still a controversial issue.[12–15] The particles growth is statistically isotropic, resulting in relatively spherical particles (except for the smallest particles). The size of the particles is controlled by the pH of the solution and, therefore, the concentration of ammonia. The produced particles are relatively monodisperse, depending, however, if the pH is constant throughout the addition of solution I in solution II. Two additional *reference* solutions C and D have been prepared by adding the same quantities of water, ethanol, and ammonia as in suspensions A and B, respectively, but without TEOS, hence without particles. Table I sums up the content of the different solutions. The solutions used in our experiments are Carlo Erba ammonia solution 30 wt. % ($\rho_{am} = 892$ kg m^{-3}, $M_{am} = 17$ g mol^{-1}), Normapur absolute ethanol solution ($\rho_{eth} = 789$ kg m^{-3}, $M_{am} = 46$ g mol^{-1}), and Prolabo TEOS solution ($\rho_{TEOS} = 934$ kg m^{-3}, $M_{TEOS} = 208$ g mol^{-1}), where ρ is the density and M is the molar mass.

Finally, as the presence of bubbles can strongly influence the propagation of acoustical waves, the solutions have been carefully degassed in a vacuum chamber.

B. Composition and physical properties of the suspensions

Surface electrical charges prevent the particles from aggregation,[16] and the particles spatial distribution has been considered as statistically homogeneous due to Brownian motion. Indeed, the characteristic length L_{sed} of sedimentation on a time scale Δt is equal for a dilute suspension to $L_{sed} = \frac{2a^2}{9\mu_{co}}(\rho_{do} - \rho_{co})g\Delta t$, where a is the size of the particles, μ_{co}, the viscosity of the liquid, ρ_{co} and ρ_{do} the densities of the continuous and dispersed phase, and g the standard gravity. At the same time, due to Brownian motion, particles will explore a zone whose characteristic size is $L_{br} = \sqrt{\frac{k_bT}{6\pi\mu_{co}a}\Delta t}$, where k_b is the Boltzmann constant and T is the temperature. In this case, the suspensions were mixed with a magnetic stirrer while degassing. Then the experiment was carried out within the day, which means that the characteristic time Δt is <86 400 s. If we report Δt in the above formula, we obtain $L_{sed} \sim L_{br} \sim 2$ mm. Thus, sedimentation is weak and counteracted by Brownian motion which shuffles the suspension.

During the synthesis, some TEOS and water molecules are consumed and some ethanol molecules and silica nanoparticles are formed. We can compute the mass content of the final solutions, if we suppose that *all* TEOS molecules have reacted (see Table II). Indeed, Bogush *et al.*[12] have studied the kinetics of Stöber process. They have shown that all TEOS molecules are consumed during the chemical reaction and that soluble silica (that is, silica that is not condensed into particles) represents at most 0.6% of the silica introduced in the reaction. The percentages given in parenthesis in Table II correspond to the mass fraction of each component of the liquid phase.

The composition of the reference solutions C and D slightly differs from the one of liquid phase in the corresponding

TABLE II. Mass composition of the solutions after chemical reaction.

	C_2H_5OH(g)	H_2O(g)	NH_3(g)	SiO_2(g)
Suspension A (%)	157.3 (86.4)	23.9 (13.2)	0.8 (0.4)	8.1
Suspension B (%)	157.3 (86.3)	24.4 (13.4)	0.3 (0.3)	8.1
Solution C (%)	132.6 (81.8)	28.8 (17.7)	2.7 (0.5)	0
Solution D (%)	132.6 (81.7)	29.2 (18)	1.6 (0.3)	0

TABLE III. Physical properties of the liquid phase (at 18 °C).

	Suspensions A and B	Solutions C and D	Water
Sound speed[a] $c_{co}(ms^{-1})$	1276	1294	1476
Nonlinear parameter β_{nl} (Ref. 17)	6.15	6.2	3.4
Shear viscosity $\mu_c^s(\times 10^{-3}\ kg\,m^{-1}\,s^{-1})$[38,39]	1.7	1.9	1.1
Bulk viscosity $\mu_c^b(\times 10^{-3}\ kg\,m^{-1}\,s^{-1})$[39,40,b]	1.4	1.6	2.9
Density $\rho_{co}(\times 10^{-3}\ kg\ m^{-3})$[38,41]	828	844	998
Isobaric heat capacity $C_c^p(J\ kg^{-1}\ K^{-1})$[42]	2778	2992	—
Isochoric heat capacity $C_c^v(J\ kg^{-1}\ K^{-1})$[43]	2415	2624	—
Specific heat ratio γ_c	1.15	1.14	1.006
Thermal conductivity $\chi_c\ (W\ m^{-1}\ K^{-1})$[44,45]	0.2	0.2	—

[a]Measured by the authors.
[b]The evolution of the bulk viscosity with temperature is assumed to follow the same law as the shear viscosity.

suspensions, as we did not consider the chemical reactions (which consume water and produce ethanol) when preparing them. The properties of the liquid phase used for the comparison of our simulations with experiments are summed up in Table III.

The sound speeds c_{co} for each solution have been determined by measuring the flight time in the different solutions. The nonlinear parameter in a water–ethanol mixture (with concentrations of ethanol ranging from 0 to 100%) has been measured by Jacob *et al.*[17] and Emery *et al.*,[18] respectively, at 27 °C and 20 °C. We can note that the shear viscosity of a water–ethanol mixture is much higher than that of pure water or ethanol solution, even for a small amount of water.[19] The excess density of the mixing is also strongly dependent on the proportion of water and ethanol. This is due to the formation of hydrogen bonds[20] between water and alcohol molecules. Finally, it is interesting to note that unlike most liquids; the specific heat ratio γ_c of ethanol (and consequently ethanol–water mixture) is significantly higher than 1, that is, there is a difference between the isochoric and isobaric heat capacities. If $(\gamma_c - 1) = 6 \times 10^{-3}$ for water, it is, however, approximately equal to 0.15 for our suspensions, that is, 25 times higher. This will play a fundamental role in our suspensions as the temperature variations associated with the acoustic wave,which are proportional to $(\gamma_c - 1)$, cannot be neglected, contrary to most hydrosols.

The only relevant physical properties of the particles for our model are their size, density, heat capacity, and the volume fraction that they occupy. The size distribution of the particles has been determined from images obtained by transmission electron microscopy (TEM). TEM sample was obtained by the deposition of a drop of our suspensions on a carbon coated grid. The relatively monodisperse size of the particles has been fitted to a log normal law (cf. Fig. 1) of the form

$$\Phi(a) = \frac{\exp(-1/2[(\ln(a) - m)/s]^2)}{a\sigma\sqrt{2\pi}},$$

where $\Phi(a)$ is the volume occupied by the particles of size between a and $a + da$, relative to the total volume occupied by the particles. Here m and s are two constants calculated by a best fit process. The average radius of the suspension is related to these parameters according to the law:

$$a_{moy} = \exp(m + s^2/2).$$

For suspension A the average radius is 69 nm and for suspension B, it is 33 nm.

The density of silicon dioxide strongly depends on its molecular structure and porosity. Several authors (see Labrosse and Burneau[21] for a review) have estimated the density of "dry" particles, from measurement of the particles size and the mass of the suspension after evaporation of the liquid phase. The reported values lie in the range from 1980 to 2100 kg m^{-3}. However, silica nanoparticles are porous with a fractal structure, as demonstrated experimentally by Labrosse and Burneau[21] and Szekeres *et al.*[22] Thus, the final

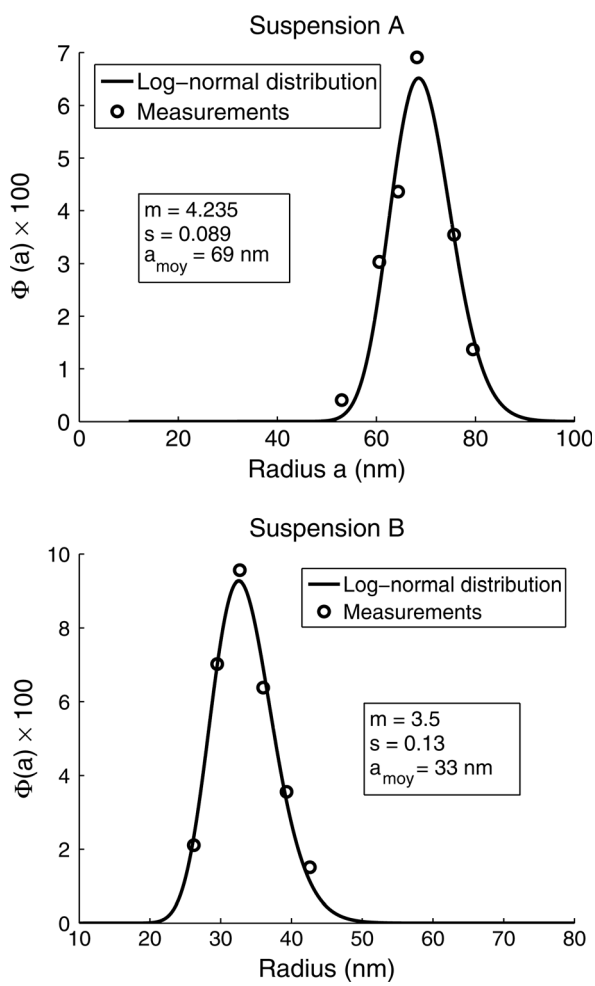

FIG. 1. Particles size distribution measured via electron microscopy (circles) and fitted with a log-normal distribution (solid line).

TABLE IV. Properties of the particles.

Density[23] ρ_{do} (kg m^{-3})	Volume[a] fraction α_{do}	Heat capacity[46] C_d (J kg^{-1} K^{-1})	Therm. conduct.[38] χ_d (W m^{-1} K^{-1})
2200	1.65%	727	1.05

[a]Measured by the authors.

mass of "dried" particles depends on how well the particles have been dried. Indeed, the liquid in the largest pores can evaporate even at room temperature. In intermediate pores, the liquid is trapped and can only evaporate if the temperature is increased above the fusion point of water. Finally, there is also some structural water which remains even when the temperature is increased up to 100 °C. Thus, it is not surprising that discrepancies are reported on the density of "dry" particles, depending on the methods of preparation and measurement. However, in acoustical problems, the density of interest is the density of "wet" nanoparticles. From our knowledge, the only reported value of this wet density comes from acoustical measurement. Hipp *et al.*[23] have measured the linear attenuation of acoustic waves induced by suspension of silica nanoparticles for a large range of frequencies, particle numbers, and concentrations. Their results show a very good agreement between theory and experiments (in the dilute case) for a density of 2200 kg m^{-3}. Since the attenuation is relatively sensitive to this parameter, a wrong value of silica density would have resulted in large discrepancies in their comparison between theory and experiments. This work, therefore, provides an excellent characterization of this parameter. We, therefore, used this value of silica density in our computations.

Finally, the volume fraction occupied by the particles has been computed from the density of the particles and the total mass of silica present in the suspension. Table IV sums up the properties of the dispersed phase. From these data, we can compute the mass fraction $m = \alpha_{do}\rho_{do}/\alpha_{co}\rho_{co} = 4.5 \times 10^{-2}$.

C. Shock wave generation

A sketch of the acoustical experimental setup is represented in Fig. 2. A high amplitude acoustical wave ($P_a = 0.41$ MPa) is emitted at a frequency of $\omega/2\pi = 1$ MHz in a water tank by an array of 256 piezoelectric transducers controlled by a programmable electronics of 128 channels. The transmitted code on each channel is computed with the inverse filter method[24] in order to synthesize within a control plane and the requested spatial wave pattern, a plane wavefront with Gaussian amplitude. A cylindrical cell with lateral poly(methyl methacrylate) (PMMA) walls containing either the suspension or a reference solution (without particles) is set 35 cm away from the array, while the shock formation distance in water is equal to $\rho_\omega c_\omega^3/(\omega\beta_\omega P_a) = 37$ cm, where ρ_w, c_w, and β_w are, respectively, the density, sound speed, and nonlinear parameter of water. The shell is 5.87 cm long and has a radius of 3 cm. Solutions are isolated from water by two lateral mylar membranes, which are approximately acoustically transparent but slightly filter the signal, as detailed later.

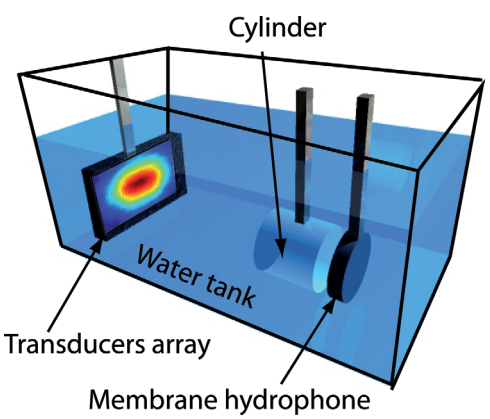

FIG. 2. (Color online) Sketch of the experimental setup.

Through the inverse filter technique, the wavefront shape has been optimized in order to minimize any effects, but the scattering by the particles. A wavefront as plane and broad as possible was synthesized to minimize diffraction, but smaller than 3 cm, in order to minimize the scattering of the acoustical wave by the PMMA walls of the cell. The decrease of the amplitude of the Gaussian beam edge was sufficiently smooth to minimize the interferences between edges and direct waves from the array. Even though the inverse filter is linear and, hence, performed first at low amplitudes, it is very stable to strong nonlinear effects (see Marchiano *et al.*[25,26]). The quality of the synthesis is assessed by Figs. 3 and 4, which show the spatial and temporal shape of the signal measured on a rectangular grid at the entrance of the cylinder. All the measurements are made by moving a membrane hydrophone with a three axis linear stages. The spatial step is fixed to 2 mm on both transverse directions. A strongly steepened signal with a broad harmonic content is visible in Figs. 3(a)–3(c). Figure 3(d) shows the amplitude distribution in the transverse plane after bandpass filtering of the fundamental mode at 1 MHz. Contour plots at −3, −6, and −12dB have been superimposed to emphasize the smooth decrease of the limited aperture of wavefront along this transverse plane. To assess the planarity of the wavefront, the pressure measured on two perpendicular lines crossing at the center of the beam is shown in Figs. 4(a) and 4(b), respectively. The half peak-to-peak maximum amplitude is presented in Figs. 4(c) and 4(d). The smooth decrease on the edge is clearly visible in both directions. These measurements are affected by a relative uncertainty due to the impulse response of the hydrophone. The hydrophone bandwidth is constructor calibrated for frequencies spanning from 1 to 30 MHz. This calibration is performed for the amplitude only and emphasizes the membrane resonance around 30 MHz due to its finite thickness. However, the relative phase between the harmonics is also affected by this

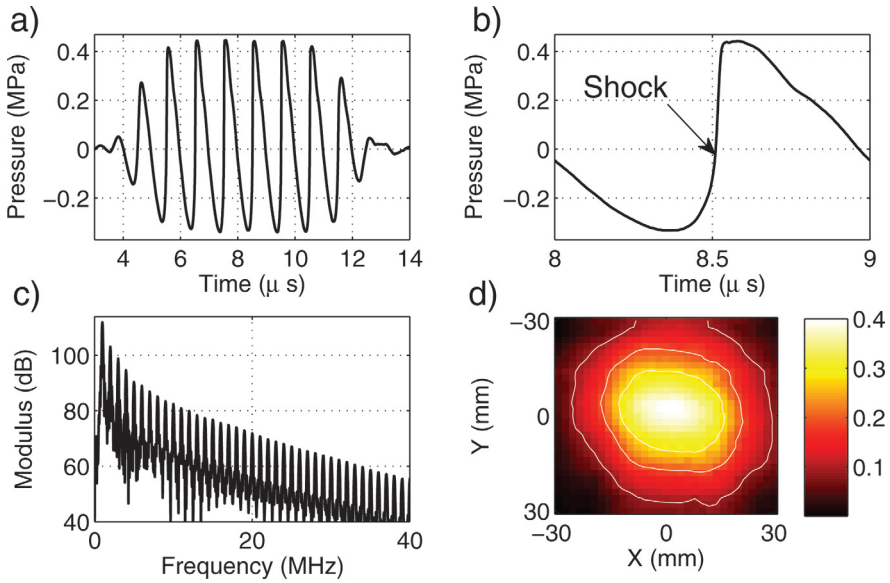

FIG. 3. (Color online) (a) Temporal waveform of the signal measured at the entrance of the cylinder, (b) Zoom on one period, (c) Signal Fourier transform, and (d) Spatial extension of acoustic beam: cross section of the first harmonic. Colorbar: amplitude in MPa.

resonance and is responsible for severe distortion of the signal. To mitigate these effects and obtain the signal presented in Fig. 3, a home-made calibration of amplitude and phase up to 60 MHz was performed. This calibration consists in removing the bell shape variation of phase and amplitude around the resonance frequency. It is important to note, however, that these calibrations are subject to a relative uncertainty. Hence, as will be explained below, the acoustic spectroscopy uses a reference solution to get *relative* measurements independent of the impulse response of the hydrophone.

Finally, the acoustic wave is measured of 15 mm behind the cylinder. Despite our careful design of the experiment, some small side effects are observed. The first one is the diffraction of the acoustic beam by the lateral walls of the cylindrical cell. This effect is visible in Fig. 5, where we see the interference rings on the spatial scan [Fig. 5(b)], and the effects on the temporal signal [Fig. 5(a)].

As the distance covered by the edge wave is higher than the one covered by the direct wave, the expected delay given by the geometry is $\tau = [\sqrt{3^2 + (5.8 + 1.5)^2} - (5.8 + 1.5)] \times 10^{-2}/1200 \sim 5 \times 10^{-6}$, that is, about five periods of the signal (for a measurement on the central axis of the cylinder). We effectively see in Fig. 5(a) (black line), the disturbance appearing about five periods after the beginning of the signal. To minimize this effect, we selected nine spatial locations within the measurement plane, separated from one another by a step of 2 mm and located at the nearest of the propagation axis. Since the scattered wave varies with the measurement point, contrarily to the plane wave, the averaging on these nine locations reduces this adverse effect [see the gray line in Fig. 5(a)]. The second effect (the radiation of acoustic wave by the PMMA) will, on the contrary, affect the beginning of the signal as the sound speed in PMMA ($\sim$2700 ms^{-1}) is higher than the one in our solution ($\sim$1200 ms^{-1}).

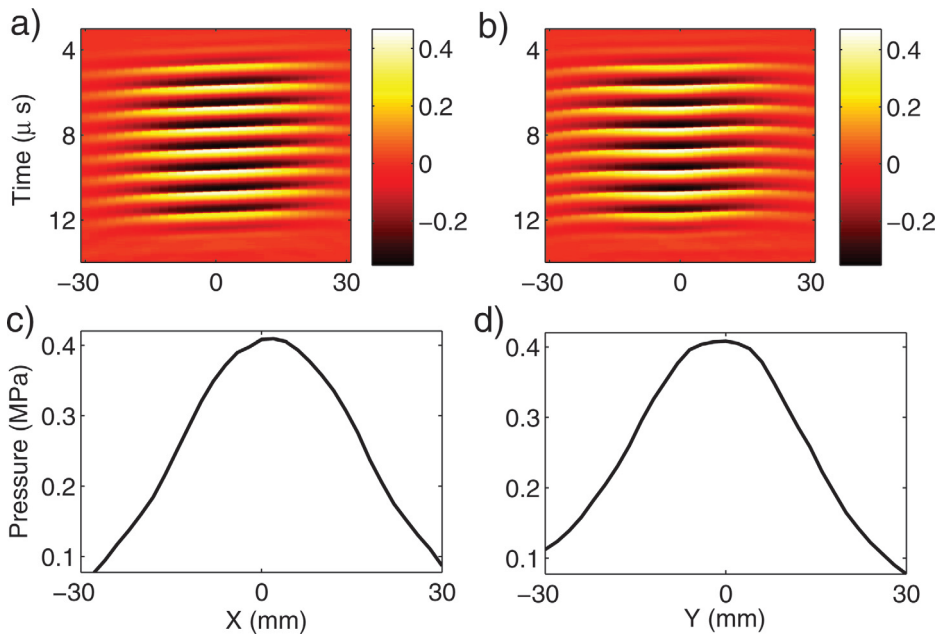

FIG. 4. (Color online) (a) Temporal waveform of the signal measured at the entrance of the cylinder along Ox, (b) temporal waveform of the signal measured at the entrance of the cylinder along Oy, (c) amplitude along Ox, and (d) amplitude along Oy. The origin is located at the center of the incident wavefront. Colorbar: amplitude in MPa.

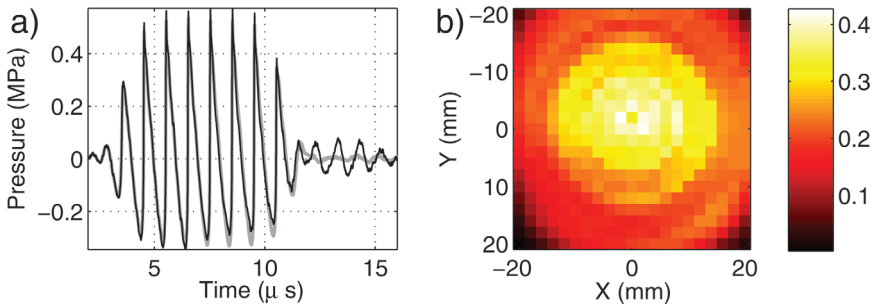

FIG. 5. (Color online) (a) Temporal waveform of the signal measured at the exit of the cylinder before (black line) and after (gray line) averaging. (b) Amplitude (in MPa) of the first harmonic over the beam cross section. Rings are due to the interferences between the direct wave and the signal diffracted at the edge of the cylinder.

Nevertheless both phenomena will mainly affect the first harmonics, as higher harmonics result from nonlinear interaction between first harmonics so that their beam widths are narrower and thus significantly smaller than the cell width (see Fig. 6). Another solution would have been to build a larger cell that would have required a larger volume of solution to fill it. Taking into account the small final impact after spatial averaging, and affecting only the low frequency part of the extra-attenuation measurements, this possibility was disregarded.

III. THEORY

A. Extended Burgers' equation

A generalized Burgers' equation can be used to describe the propagation of finite amplitude acoustical waves in suspensions as demonstrated first by Davidson.[1,2] This equation, obtained by perturbation methods, takes into account the nonlinear effects due to the high amplitude of the impinging wave, scattering effects due to the presence of particles, and classical thermo-viscous dissipation within the continuous phase. They rely on the assumption that the smallest scale associated with the acoustic wave (here the shock thickness) is much larger than the particles. With this hypothesis, the equations can be statistically averaged over the particle configurations, and the medium can be considered as an effective medium. The "geometrical" diffraction of the wave by the particles can also be neglected. This hypothesis is well verified in our experiments, as the sizes of our particles are smaller than 70 nm and the shock thickness is about 10 μm in our case. The validity of these equations is also limited to dilute suspensions, as interactions[23,27,28] between particles are neglected. Davidson has obtained equations for the nonlinear propagation of acoustical waves in aerosols. His results have been generalized by Baudoin[4] for any dilute suspension of spherical rigid particles, that is, for aerosols and also for hydrosols. These two cases differ in terms of the dominant scattering mechanism. In hydrosols, the scattering of the incident wave is usually due to the steady and unsteady momentum transfers induced at small scales by the difference of velocity between the particles and the surrounding medium. The force exerted by the fluid on the particles at these small scales (and, therefore, small associated Reynolds number) can be obtained by considering a moving sphere embedded in a uniform and unsteady velocity field. Uniform field approximation is justified by the small size of the particles relative to the acoustical wavelength. The result is the sum of the Stokes, Basset, Added mass, and Archimed forces.[29] The first term is the classic Stokes drag exerted on a sphere embedded in a steady viscous flow. The Basset hereditary force is an unsteady viscous term due to the time required by the viscous diffusion layer to adapt to new boundary conditions. The Added mass term is linked to the inertia of the liquid, which must be displaced when a sphere

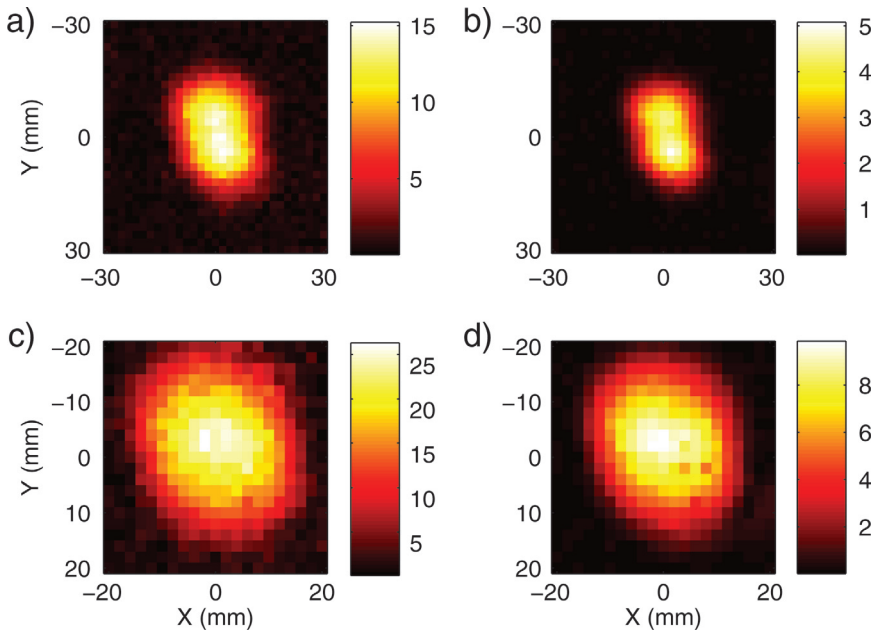

FIG. 6. (Color online) Spatial extension of acoustic beam. Cross section at the entrance of the cylinder: (a) the tenth harmonic and (b) the twentieth harmonic. Cross section at the exit of the cylinder: (c) the tenth harmonic and (d) the twentieth harmonic. Colorbar: amplitude in kPa.

is accelerated or decelerated. Finally the Archimed force is an unsteady inertial force that comes from the difference of density between the particles and the surrounding medium. An additional term is due to the difference of compressibility between the liquid and the particles, which affects the phase velocity but not the attenuation. Thermal exchanges can usually be neglected in hydrosols, as the elevation of temperature associated with the acoustical wave in fluids is proportional to $\gamma_c - 1$, which is very small for most liquids. However, these effects cannot be neglected in the present case, because water–ethanol mixture has a specific heat ratio equal to 1.15. Therefore additional scattering effects arise from steady and unsteady heat transfers between particles and the ambient fluid. The steady term corresponds to the usual Fourier diffusion law for heat transfers between two medium at different temperatures. The unsteady term is the equivalent of the Basset contribution for heat transfers. In the following equations, the temperature inside the particle is assumed to be homogeneous.[30] Indeed, the thermal conductivity of amorphous silica is about five times higher than that of the conductivity of water–ethanol mixture. Hence the diffusion times inside the particles $\tau_d = a^2\rho_{\mathrm{do}}/C_d/\chi_d$ are equal to 8 and 2 ns for particles of 69 and 33 nm, respectively, that is, much smaller times than the ones associated with the main harmonics studied here (1 – 40 MHz), which carry most of the acoustical energy.

If we take into account all relevant effects for hydrosols, we obtain the following set of equations: [4]

$$\frac{\partial v_c}{\partial x} - \frac{\beta_{\mathrm{nl}}}{c_{\mathrm{co}}^2}\left(v_c\frac{\partial v_c}{\partial \tau}\right) - \frac{\Theta}{c_{\mathrm{co}}}\frac{\partial^2 v_c}{\partial \tau^2} = -\frac{m}{2c_{\mathrm{co}}}\left[(1-r)\frac{\partial v_c}{\partial \tau} - \frac{\partial \Delta v}{\partial \tau}\right] + \frac{F}{2c_{\mathrm{co}}}\left[\frac{\partial v_c}{\partial \tau} - \frac{\partial \Delta v}{\partial \tau}\right] - \frac{mC(\gamma_c - 1)}{2c_{\mathrm{co}}}\left[\frac{\partial v_c}{\partial \tau} - \frac{c_{\mathrm{co}}}{\rho_{\mathrm{co}}\left(\frac{\partial T_c}{\partial \rho_c}\right)_{\mathrm{sc}}}\frac{\partial \Delta T}{\partial \tau}\right]. \quad (1)$$

$$(1-r)\frac{\partial v_c}{\partial \tau} - \frac{\partial \Delta v}{\partial \tau} = \frac{1}{\tau_v}\left[\Delta v + \frac{\theta_v}{9}\frac{\partial \Delta v}{\partial \tau} + \sqrt{\frac{\theta_v}{\pi}}\int_{-\infty}^{\tau}\frac{\partial \Delta v}{\partial \tau^*}\frac{d\tau^*}{\sqrt{\tau - \tau^*}}\right]. \quad (2)$$

$$\frac{\rho_{\mathrm{co}}\left(\frac{\partial T_c}{\partial \rho_c}\right)_{\mathrm{sc}}}{c_{\mathrm{co}}}\frac{\partial v_c}{\partial \tau} - \frac{\partial \Delta T}{\partial \tau} = \frac{1}{\tau_T}\left[\Delta T + \sqrt{\frac{\theta_T}{\pi}}\int_{-\infty}^{\tau}\frac{\partial \Delta T}{\partial \tau^*}\frac{d\tau^*}{\sqrt{\tau - \tau^*}}\right]. \quad (3)$$

In the above equations the subscripts "c," "d," and "o" denote, respectively, the continuous fluid phase, the dispersed phase (particles), and the equilibrium state. v_c is the mean velocity of the continuous phase, Δv is the velocity difference between the two phases, T_c is the mean temperature of the continuous phase, ΔT is the temperature difference between the two phases, s_c is the entropy of the continuous phase, $\tau = t - x/c_{\mathrm{co}}$ is the retarded time, β_{nl} is the coefficient of nonlinearity, $F = \alpha_{\mathrm{do}}/\alpha_{\mathrm{co}}$ is the ratio of volume fractions occupied by both phases, $r = \rho_{\mathrm{co}}/\rho_{\mathrm{do}}$ is the ratio of densities, $m = \alpha_{\mathrm{do}}\rho_{\mathrm{do}}/\alpha_{\mathrm{co}}\rho_{\mathrm{co}}$ is the mass fraction, $C = C_d/C_c^p$ is the ratio of isobaric heat capacities of both phases, $\Theta = \mu_c^s/2\rho_{\mathrm{co}}c_{\mathrm{co}}^2(4/3 + \mu_c^b/\mu_c^s + (\gamma_c - 1)/\mathrm{Pr})$ is the characteristic time for classical thermo-viscous dissipation, and $Pr = \mu_c^s C_c^p/\chi_c$ is the fluid Prandtl number. Finally $\tau_v = 2a^2\rho_{\mathrm{do}}/9\mu_c^s$ and $\theta_v = a^2\rho_{\mathrm{co}}/\mu_c^s$ are the characteristic times for the steady and unsteady momentum exchanges, and $\tau_T = a^2\ \rho_{\mathrm{do}}C_d/3\chi_c$ and $\theta_T = a^2\rho_{\mathrm{co}}C_c^p/\chi_c$ are the characteristic times for the steady and unsteady heat transfers.

The first equation is the generalized Burgers' equation, with usual Burgers' equation[7,31] on the left-hand side. The three terms correspond, respectively, to the propagation of the acoustic wave, nonlinear effects, and thermo-viscous absorption. The first term on the right-hand side (rhs) corresponds to steady and unsteady momentum exchanges between the two phases. The contribution of this term is proportional to the mass fraction m, that is, the product of the densities ratio and the volume fraction ratio: the more the particles and the higher the density ratio, the higher will be the scattering of the impinging wave. The second term on the rhs. is a contribution due to the incompressibility of the rigid particles, which therefore modifies the sound speed of the effective medium. The third term on the rhs corresponds to steady and unsteady heat transfers between the particles and the surrounding medium. These exchanges are proportional to mC, which characterizes the thermal inertia of the particles versus temperature changes. It is also proportional to $(\gamma_c - 1)$ which gives the amplitude of temperature variations associated with the acoustical wave.

Two additional equations [Eqs. (2) and (3)] are required to determine, respectively, the velocity and temperature differences between the fluid and solid phases. In the first Eq. (2), we can see that, if the particles have the same density as the surrounding liquid ($r = 1$), the velocity difference between the phases vanishes and the particles, therefore, will move with the same velocity as the surrounding liquid. That is why particles of the same density as the liquid are used for particle image velocimetry (PIV) in hydrodynamic studies. In this case, there is no scattering of the impinging wave. This factor $(1 - r)$ comes from the Archimed force. The first term of the rhs is the Stokes contribution, the second the Added mass, and the last one the Basset history term. As underlined before, we see that the Stokes term is a steady contribution proportional to the velocity difference Δv between the two phases, whereas Added mass and Basset are unsteady terms therefore related to the time derivative of the velocity. The Basset term depends on the "history" of the particle displacement through the time integral. Equation (3) shares the same structure as Eq. (2), but without the Archimed and Added mass terms. Compared to the equations obtained by Davidson[2,6] for aerosols, Eqs. (1)–(3) take into account unsteady momentum and heat transfers. These effects play a fundamental role in hydrosols, whereas they can be neglected in most practical situations in aerosols. The ratio between unsteady and steady characteristic times of momentum and heat transfers is indeed, respectively, equal to $9/2r$ and $3rC$. In hydrosols, the density and specific heat of the dispersed and continuous phases are close. As a result,

TABLE V. Characteristic frequencies.

Characteristic frequencies (MHz)	Suspension A (69 nm)	Suspension B (33 nm)
Steady momentum transfers $1/(2\pi\tau_v)$	122	513
Unsteady momentum transfers $1/(2\pi\theta_v)$	72	312
Steady heat transfers $1/(2\pi\tau_T)$	11	43
Unsteady heat transfers $1/(2\pi\theta_T)$	4	16

unsteady and steady scattering phenomena occur at the same frequencies. In the case of aerosols, however, unsteady transfers occur at much higher frequency due to the huge difference of density between both phases. Therefore, unsteady transfers play a minor role, even when considering the propagation of acoustical shock waves.

B. Analysis based on characteristic parameters

In this section, we will try to compare the different terms and understand which one is significant in the present case. If we try to compare momentum transfers to heat transfers, we see that both are proportional to the mass fraction m, but that the heat transfers are also proportional to $C(\gamma_c-1)$. This factor is approximately equal to 4×10^{-2} in our suspensions. Only based on this first comparison, we might think that thermal effects can be neglected compared to visco-inertial ones. However, the characteristic frequencies of both phenomena also differ. Table V sums up the characteristic frequencies for suspensions A and B.

These characteristic frequencies must be compared to the frequency spectrum (~1 to 40 MHz) associated with the shock wave. We can see that characteristic frequencies associated with thermal transfers are much smaller than their momentum counterparts (a factor 10 for steady transfers and 20 for unsteady transfers) and, therefore, better match with the frequency spectrum associated with the acoustic wave. Despite the smallness of the factor $C(\gamma_c-1)$, thermal effects will therefore play a significant role on the evolution of the acoustic wave. This can be seen in Fig. 7 which compares the linear attenuation and dispersion induced by visco-inertial and thermal effects (due to the presence of the particles), with the classic thermo-viscous dissipation in the corresponding liquid. These curves are computed with the following dispersion relation k_* in terms of the frequency $\omega/2\pi$, obtained from Eqs.(1)–(3)

$$\begin{aligned}\frac{k_* c_{\rm co}}{\omega} &= \left(1-\frac{F}{2}\right)+\frac{i\omega\mu_c^s}{2\rho_{\rm co}c_{\rm co}^2}\left(\frac{4}{3}+\frac{\mu_c^b}{\mu_c^s}+\frac{(\gamma_c-1)\chi_c}{\mu_c^s C_c^p}\right)\\ &\quad+\frac{m}{2}(1-r)h_v+\frac{mC(\gamma_c-1)}{2}h_T\\ &\quad\text{with}\quad h_v=\frac{1-ir\omega\tau_v^*}{1-i\omega\tau_v^*},\quad h_T=\frac{1}{1-i\omega\tau_T^*}\\ \tau_v^* &= \tau_v/\left[1+\frac{1-i}{\sqrt{2}}(\omega\theta_v)^{1/2}-\frac{1}{9}i\omega\theta_v\right]\\ \tau_T^* &= \tau_T/\left[1+\frac{1-i}{\sqrt{2}}(\omega\theta_T)^{1/2}\right].\end{aligned}\tag{4}$$

The first term on the rhs of Eq. (4) is due to the presence of incompressible particles, the second one correspond to classical thermo-viscous dissipation, the third one to momentum transfers between both phases, and the last one to thermal transfers. The complex times τ_v^* and τ_T^* are linked, respectively, to momentum and thermal transfers. We can note that this dispersion relation is equivalent to the one calculated in the linear case by Gumerov *et al.*[30] in the small volume fraction limit, without phase changes and when the temperature inside the particles is supposed to be homogeneous.

The presence of particles induces viscous damping of the acoustic wave because of the difference of velocity between the particles and the fluid, and the small size of the particles. As the particles are small, the associated Reynolds number is also small, and viscous effects play a major role in the dynamics of the particles. Therefore, the differential movement between both phases is damped by viscous effects, so that part of the energy carried out by the acoustical wave is dissipated. In the same way, some energy is dissipated through heat diffusion because of the difference of temperature between the phases. If we look at the phase velocity of the effective medium, it can be estimated as $c_{\rm eff}=\frac{1}{\sqrt{\chi_{\rm eff}\rho_{\rm eff}}}$, where $\rho_{\rm eff}$ is the effective density and $\chi_{\rm eff}$ is the effective compressibility. If the particles have the same temperature and velocity as the liquid, the effective phase velocity will, nevertheless, globally shift because of the increase of the effective density (particles are denser than the surrounding liquid) and the decrease of the compressibility (particles are much less compressible than the surrounding liquid). Figure 7 shows that the increase of the effective density is dominant, as the effective phase velocity globally decreases when we take into account the presence of the particles. On the other hand, the evolution of the effective phase velocity with frequency is due to the velocity and temperature differences between both phases. Of course the classical thermo-viscous dissipation does not affect the phase velocity, but only induces attenuation.

C. Transmission and reflection coefficients

The extremities of the cylinder containing the suspension or the reference solution are mylar membranes. Their thickness (measured with a micrometer directly on the experimental setup) is 13 μm. As a consequence, these membranes are transparent for the lowest harmonics of the acoustic shock wave but slightly filter the highest harmonics. The transmission coefficient can be simply calculated for the first and second membrane from the acoustic impedance of each material and the thickness of the membrane. We get:

$$T=\frac{2}{\left[1+\frac{Z_1}{Z_3}\right]\cos(k_2h)-i\left[\frac{Z_1}{Z_2}+\frac{Z_2}{Z_3}\right]\sin(k_2h)},\tag{5}$$

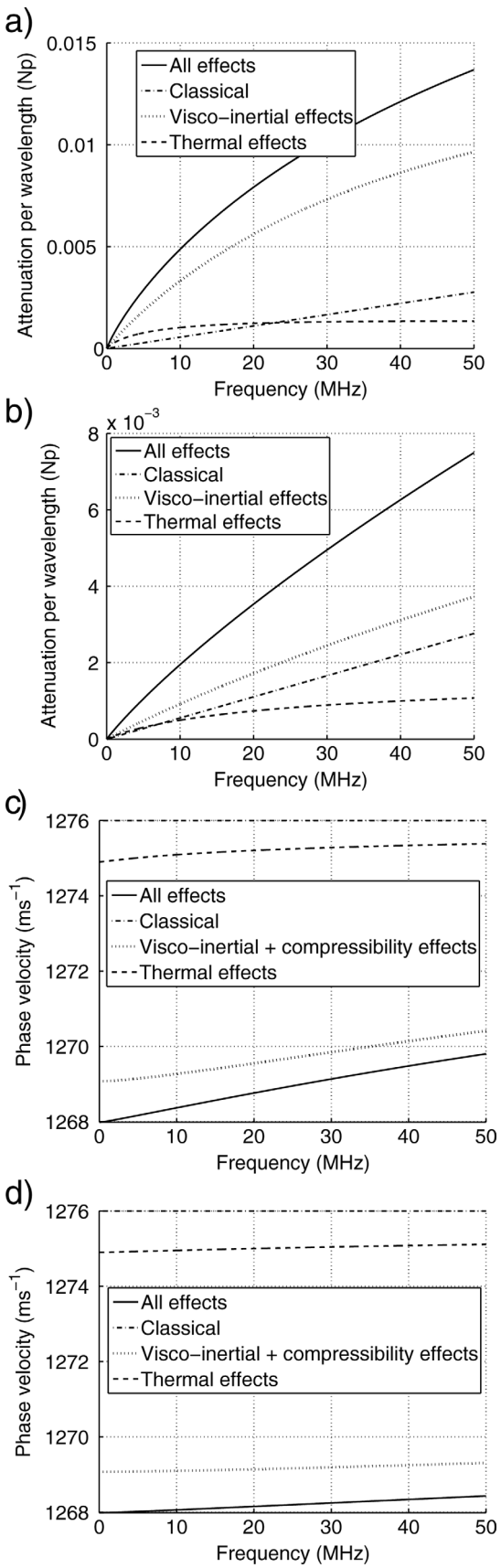

FIG. 7. Comparison of visco-inertial, thermal, and overall effects due to the presence of the particles with the classical thermo-viscous dissipation in the corresponding liquid. (a) Comparison of attenuation in suspension A (69 nm). (b) Comparison of attenuation in suspension B (33 nm). (c) Comparison of phase velocity in suspension A (69 nm). (d) Comparison of phase velocity in suspension B (33 nm).

where T is the transmission coefficient; Z_1, Z_2, and Z_3 are, respectively, the acoustic impedance of the liquid before the membrane, the membrane, and the liquid after the membrane, k_2 is the wave number in the mylar membrane, and h the thickness of the membrane. For our calculations, we took the following properties of mylar membrane (Ref. 32): $\rho_{\mathrm{myl}} = 1180\ \mathrm{kgm}^{-3}$ and $c_{\mathrm{myl}} = 2540\ \mathrm{ms}^{-1}$. With this formula, we can see that if the membrane is sufficiently thin (that is, $k_2 h \ll 1$), the transmission coefficient is equal to $T = 2Z_3/(Z_3 + Z_1)$, so that the membrane plays no role. In our case $k_2 h \sim 0.04$ at 1 MHz and equal to 4 at 100 MHz. Therefore, the membrane will mainly affect the highest harmonics. The transmission coefficient modulus for the first and second membrane is represented in Fig. 8.

D. Computation scheme

Equations (1)–(3) are solved by using a split step numerical scheme. Advancing plane-by-plane from position x to position $x + \Delta x$, nonlinear and scattering effects are considered separately through two successive sub-steps. Nonlinear effects are treated with the so called Burgers–Hayes method[33,34] that provides an analytical solution for shock waves in the inviscid case for the potential (the primitive of the pressure). The attenuation and dispersion, due to the presence of the particles and to classic thermo-viscous dissipation, are taken into account by applying the appropriate dispersion relation [Eq. (4)] in the frequency domain. Note that the numerical algorithm alternating weak shock theory reformulated for the potential flow in the time domain, and linear dispersion/dissipation handled in the frequency domain is a generalization of Pestorius algorithm.[35] It has also been validated for thermoviscosity and molecular relaxation applications to sonic boom.[36] Polydispersion can simply be taken into account by replacing h_V and h_T by their values averaged over the particles size distribution[37]

$$\langle h_j \rangle_a = \int_{\mathrm{amin}}^{\mathrm{amax}} \phi(a) h_j(a) da \quad \text{with } j = v \text{ or } T \tag{6}$$

We first process the signal measured experimentally at the entrance of the cylinder. This process consists in the calibration and the spatial averaging described in Sec. II C. Then, it is propagated numerically along the same path as the one followed experimentally, that is, linear transmission through the first membrane, 5.87 cm of nonlinear propagation in the reference solution or the suspension, linear transmission through the second membrane, and finally 1.5 cm of nonlinear propagation in water up to the hydrophone position. It is important to note, that our measured entrance signal is given within the uncertainty of our membrane hydrophone calibration for frequencies higher than 20 MHz. This is the reason why the cell location was chosen at the point of shock formation. Here the amplitudes of harmonics above 20 MHz are −40 dB less than the fundamental Fig. (3). Most of them will indeed result from nonlinear interaction within the cell (which is enhanced by the larger coefficient of nonlinearity in the water–ethanol mixture). Hence calibration errors above 20 MHz will be negligible when comparing theory and

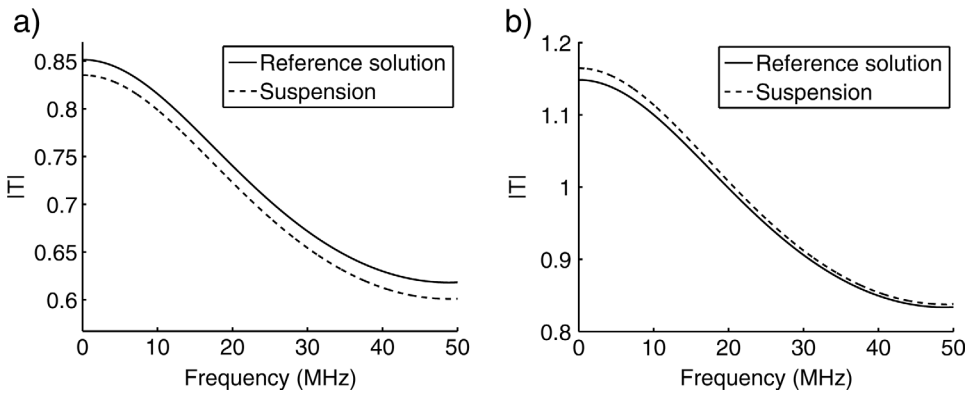

FIG. 8. (a) First interface water/membrane/suspension, dotted lines: transmission coefficient through the water/membrane/suspension interfaces. (b) Second interface suspension/membrane/water. Solid lines are the same, with the suspension replaced by the reference solution.

experiments for *relative* quantities between solutions with or without particles.

IV. RESULTS AND ANALYSIS

A. Comparison of temporal signals and their Fourier transforms

In this section, we compare computed and measured signals and their Fourier transforms after propagation in the two suspensions and the corresponding reference solutions (see Figs. 9 and 10). Simulations have been performed with the literature parameters given in Sec. II without any adjustment. A good agreement is obtained between the simulations and the experiments. The direct comparison of measured temporal signals (or their Fourier transforms) with computed ones, however, leads to small discrepancies, which come from side effects such as (1) the uncertainty on the calibration of the membrane hydrophone (for frequencies above 20 MHz) and (2) the diffraction by the walls of the cell.

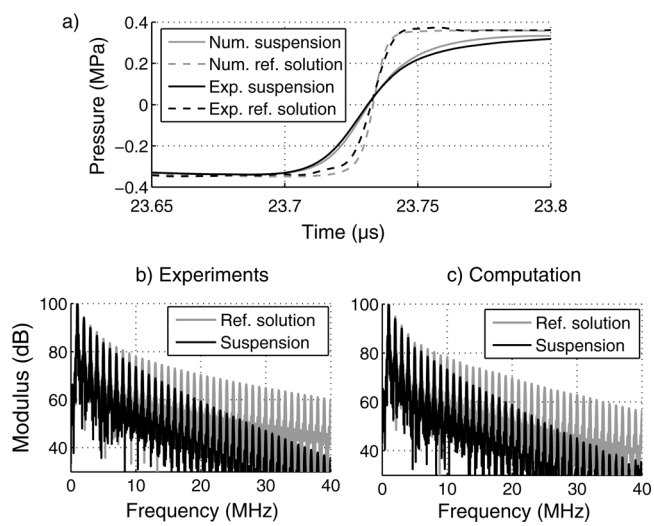

FIG. 9. Comparison of the signals obtained experimentally and numerically after propagation in suspension A (69 nm) and in the reference solution (without particles). (a) Temporal signal: zoom on the acoustical shock at the center of the time waveform. (b) Fourier transforms of the experimental signals. (c) Fourier transforms of the computed signals. Simulations have been performed with an average size of the particles equal to 69 nm.

B. Comparison of "nonlinear" attenuation

The best way to eliminate these side effects is to calculate the ratio between the signals propagated in the suspension and in the reference solution. With this method, a "nonlinear" attenuation is obtained for each harmonic by computing the amplitude of this ratio. It differs from its linear counterpart, as the evolution of the amplitude of the harmonics results from a complex competition between nonlinear effects which transfer energy from the fundamental to the harmonics, and scattering by particles, which tends to dissipate energy. These nonlinear coefficients therefore strongly depend on the distance of propagation through the suspension. We did not compare computed and measured dispersion, as the phase velocity evolution with frequency is very small (about 0.1%) and is within the experimental uncertainties.

Figures 11(a) and 11(b) show the nonlinear attenuation in suspensions A and B, respectively, obtained experimentally and numerically by solving the generalized Burgers' equation. Computations have been performed for different sizes of particles to give an overview of the influence of this parameter. An excellent agreement is obtained for suspension A for the radius measured from TEM images (69 nm).

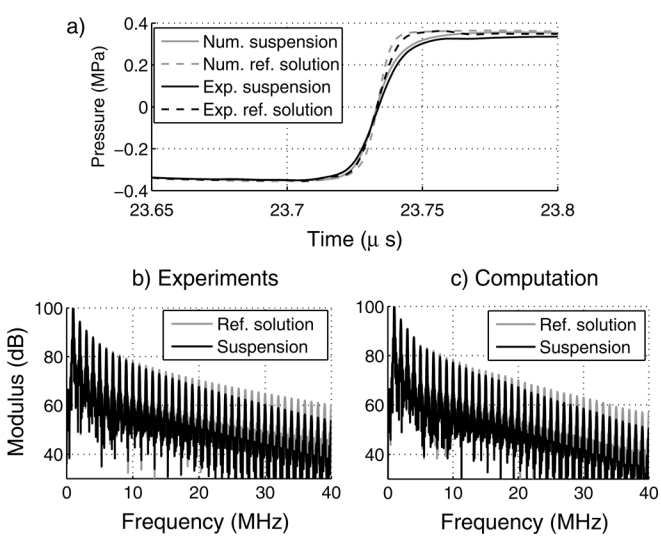

FIG. 10. Same as Fig. (9) for suspension B (33 nm). Simulations have been performed with an average size of the particles equal to 36 nm, which gives the best agreement (see Sec. IV B).

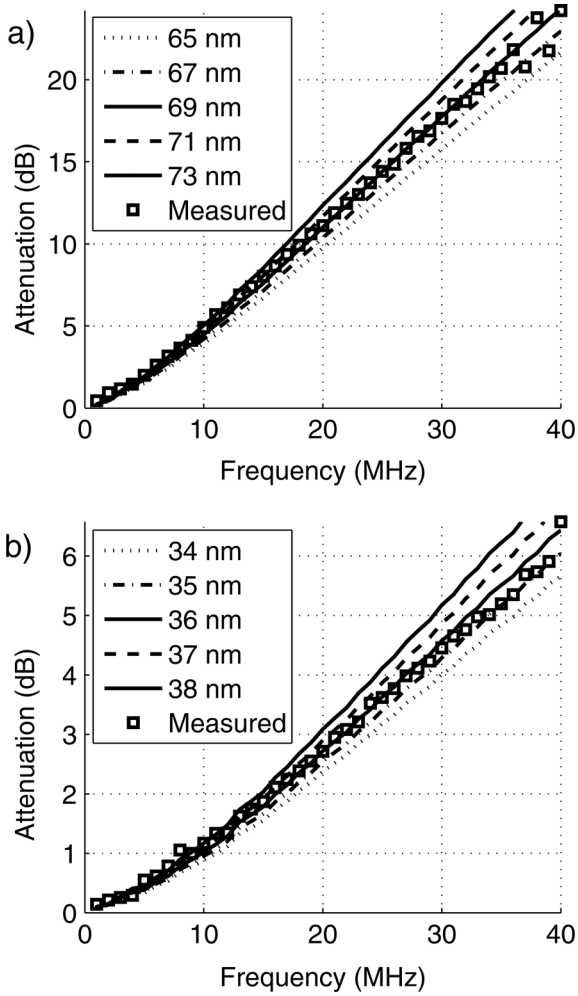

FIG. 11. Comparison of computed and measured "nonlinear" attenuations, that is, the modulus [measured in decibels (dB)] of the ratio between the signal propagated in the suspension and in the reference solution. (a) Suspension A (69 nm) and (b) Suspension B (33 nm).

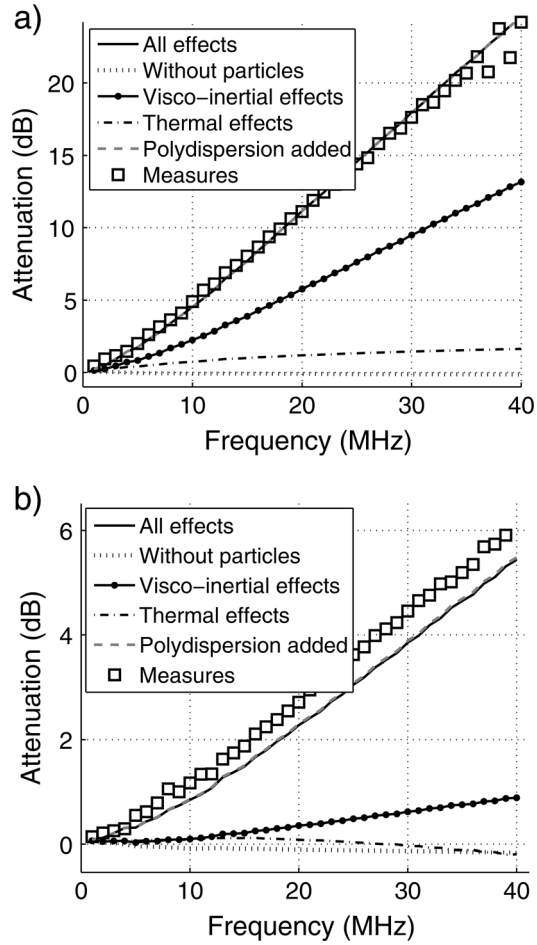

FIG. 12. Numerical comparison of the influence of the various different effects on nonlinear attenuation measured in decibels. (a) Suspension A: simulations are performed for an average size of the particles of 69 nm. (b) Suspension B: simulations are performed for an average size of the particles of 33 nm.

For suspension B (radius measured from TEM images of 33 nm), the best agreement with computations is obtained with a particle size of 36 nm, that is, 3 nm (or 10%) difference. The higher discrepancy between experiments and theory for suspension B could be explained by different factors. First, the nonlinear attenuation is much smaller for this suspension; therefore, the measurement noise may more deeply affect the corresponding results. Second, since the structure of silica nanoparticles is fractal according to Szekeres *et al.*,[22] the density might slightly vary with the size of the particles. Finally, the smaller the particles, the higher is the uncertainty on the TEM determination of the particles size. We can notice a small discrepancy for the first harmonics (the attenuation is higher in the experiments). This difference comes from side effects (described earlier in Sec. II) diffraction of a part of the signal at the edge of the cylinder leads to interferences between the direct and edge waves. Finally, we can notice that the variation of the "nonlinear" attenuation with the size of the particles is rather strong. Therefore its measurement is shown to be a good way to acoustically discriminate this parameter, with a precision in our experiments of the order of 3 nm.

C. Comparative influence of different effects

To conclude, we can compare the influence of the different effects induced by the presence of the particles (see Fig. 12). In the absence of particles, the "nonlinear" attenuation of the harmonics is of course negative because the amplitude of the harmonics is increased through the nonlinear transfer of energy from the fundamental to the higher harmonics. First, we can see that taking into account the polydispersion does not significantly affect the results. The calculation of the dispersion relation with the average radius gives, indeed, a correct estimate of the attenuation. This situation differs from the propagation in fogs,[37] where polydispersion plays a crucial role. Figures 12(a) and 12(b) show the strong influence of thermal effects in our suspensions. Although thermal effects are smaller than visco-inertial ones, neglecting them would lead to a huge underestimation of the attenuation in the suspension. Again this is due, in particular, to the relatively high value of the parameter $\gamma_c - 1$. Hence, the present experiments allow us to assess the validity of generalized Burgers equations (1)–(3) proposed in the theoretical part of this work. They include simultaneously classical thermoviscosity within the ambient solution, and visco-inertial and themal transfers between the fluid and the nanoparticles.

V. CONCLUSION

The evolution of an acoustical shock wave propagating in a suspension of silica nanoparticles has been studied experimentally and compared successfully with a generalized Burgers' equation. This agreement is achieved without any adjustable parameter. Nanoparticles are shown to strongly influence the amplitude and shock structure of the acoustical shock wave. Both visco-inertial effects due to the difference of velocity between the particles and the surrounding liquid, and heat exchanges due to temperature differences, are shown to play a significant role on the acoustical behavior. Finally, we can note that the use of broadband signals such as acoustical shock waves is promising for acoustical spectroscopy. While further investigations would be required to quantify the uncertainty on the particles size estimation, this method might allow to determine the size of the particles with a single signal. This would be interesting to characterize quickly evolving media. Potential applications would be, for example, the *in situ* measurement of particles growth rate during chemical reactions.

[1]G. A. Davidson, "Finite amplitude acoustics of aerosols," J. Acoust. Soc. Am. **53**, 1717–1729 (1973).
[2]G. A. Davidson, "Finite amplitude acoustics phenomena in aerosols from a single governing equation," J. Acoust. Soc. Am. **54**, 1331–1342 (1973).
[3]J. B. Young and A. Guha, "Normal shock wave structure in two-phase vapour droplet flows," J. Fluid Mech. **228**, 243–274 (1991).
[4]M. Baudoin, "Nonlinear acoustics and multiple scattering in suspensions of rigid particles," Ph.D. thesis, Université Pierre et Marie Curie, Paris 6, 2007.
[5]G. A. Davidson, "A Burgers' equation approach for finite amplitude acoustics in fogs," J. Sound Vib. **45** (4), 473–485 (1975).
[6]G. A. Davidson, "A Burgers' equation approach to finite amplitude acoustics in aerosol media," J. Sound Vib. **38**(4), 475–495 (1975).
[7]J. S. Mendousse, "Nonlinear dissipative distortion of progressive sound waves at moderate amplitude," J. Acoust. Soc. Am. **25**, 51–54 (1953).
[8]D. T. Blackstock, "Generalized Burgers' equation for plane waves," J. Acoust. Soc. Am. **77**, 2050–2053 (1985).
[9]Y. A. Kobelev and A. M. Suin, "Difference-frequency sound generation in a liquid containing bubbles of different sizes," Sov. Phys. Acoust. **26**(6), 485–487 (1980).
[10]E. A. Zabolotskaya and S. I. Soluyan, "Emission of harmonic and combination-frequency waves by air bubbles," Sov. Phys. Acoust. **18**(3), 396–398 (1973).
[11]W. Stöber, A. Fink, and E. Bohn, "Controlled growth of monodisperse silica spheres in the micron size range," J. Colloid Interf. Sci. **26**, 62–89 (1968).
[12]G. H. Bogush and C. F. Zukoski, "Studies of the kinetics of the precipitation of uniform silica particles through the hydrolysis and condensation of silicon alkoxides," J. Colloid Interf. Sci. **142**(1), 1–18 (1991).
[13]G. H. Bogush and C. F. Zukoski, "Uniform silica particle precipitation – an aggregative growth model," J. Colloid Interf. Sci. **142**(1), 19–34 (1991).
[14]T. Matsoukas and E. Gulari, "Dynamics of growth of silica particles from ammonia-catalyzed hydrolysis of tetra-ethyl-orthosilicate," J. Colloid Interf. Sci. **124**(1), 252–261 (1988).
[15]T. Matsoukas and E. Gulari, "Monomer-addition growth with a slow initiation step—a growth-model for silica particles from alkoxides," J. Colloid Interf. Sci. **132**(1), 13–21 (1989).
[16]D. F. Evans and H. Wennerström, *The Colloidal Domain* (Wiley, New York, 1994), pp. 401–437.
[17]X. Jacob, "Application of elastic waves interaction to the measurement of nonlinear properties of materials and to high-pressure wave fields characterization," Ph.D. thesis, Université Paris Diderot, 2005.
[18]J. Emery, S. Gasse, and C. Dugué, "Coefficient de non-linéarité acoustique dans les mélanges eau-méthanol et eau-éthanol (Acoustical nonlinearity coefficient in water-methanol and water-ethanol mixtures)," J. Phys. Colloq. C8 **11**, 231 (1979).
[19]E. J. W. Wensink, A. C. Hoffman, P. J. Van Maaren, and D. Van der Spoel, "Dynamic properties of water/alcohol mixtures studies by computer simulation," J. Chem. Phys. **119**(14), 7308–7316 (2003).
[20]I. Bakó, T. Megyes, S. Bálint, T. Grósz, and V. Chihaia, "Water-methanol mixtures: topology of hydrogen bonded network," Phys. Chem. Chem. Phys. **10**, 5004–5011 (2008).
[21]A. Labrosse and A. Burneau, "Characterization of porosity of ammonia catalysed alkoxysilane silica," J. Non-Cryst. Solids **221**, 107–124 (1997).
[22]M. Szekeres, J. Tóth, and Dékány, "Specific surface area of Stöeber silica determined by various experimental methods," Langmuir **18**, 2678–2685 (2002).
[23]A. K. Hipp, G. Storti, and M. Morbidelli," Acoustic characterization of concentrated suspensions and emulsions. 2. Experimental validation," Langmuir **18**, 391–404 (2002).
[24]M. Tanter, J.-L. Thomas, and M. Fink, "Time reversal and the inverse filter," J. Acoust. Soc. Am. **108**, 223–234 (2000).
[25]R. Marchiano, F. Coulouvrat, and J. L. Thomas, "Nonlinear focusing of acoustic shock waves at a caustic cusp," J. Acoust. Soc. Am. **117**, 566–577 (2005).
[26]R. Marchiano, J. L. Thomas, and F. Coulouvrat, "Experimental simulation of supersonic superboom in a water tank: Nonlinear focusing of weak shock wave at a fold caustic," Phys. Rev. Lett. **91**(18), 184301 (2003).
[27]M. Baudoin, J. L. Thomas, and F. Coulouvrat, "On the influence of spatial correlations on sound propagation in concentrated solutions of rigid particles," J. Acoust. Soc. Am. **123**(6), 4127–4139 (2008).
[28]M. Baudoin, J. L. Thomas, F. Coulouvrat, and D. Lhuillier, "An extended coupled phase theory for the sound propagation in polydisperse suspensions of rigid particles," J. Acoust. Soc. Am. **121**, 3386–3397 (2007).
[29]Yu. A. Buyevich and V. G. Markov, "Rheology of concentrated mixtures of fluids with small particles," PMM **36**(3), 480–493 (1972).
[30]N. A. Gumerov, A. I. Ivandaev, and R. I Nigmatulin, "Sound waves in monodisperse gas-particle or vapour-droplet mixtures," J. Fluid Mech. **193**, 53–74 (1988).
[31]J. M. Burgers, "A mathematical model illustrating the theory of turbulence," Adv. Appl. Mech. **1**, 171–199 (1948).
[32]http://www.ondacorp.com (date last viewed January 1, 2011).
[33]F. Coulouvrat, "A quasi-analytical shock solution for general nonlinear progressive waves," Wave Motion **46**(2), 97–107 (2009).
[34]W. D. Hayes, R. C. Haefeli, and H. E. Kulsrud, "Sonic boom propagation through stratified atmosphere with computer programme," Technical Report, NASA CR–1299, 1969.
[35]F. M. Pestorius, "Propagation of plane acoustic noise of finite amplitude," Technical Report ARL-TR-73-23, Applied Research Laboratories, The University of Texas, Austin, 1973.
[36]A. Loubeau and F. Coulouvrat, "Effect of meteorological variability on sonic boom propagation from hypersonic aircraft," AIAA J. **47**(11), 2632–2641 (2009).
[37]D. A Gubaidullin and R. I. Nigmatulin, "On the theory of acoustic waves in polydispersed gas-vapor-droplet suspensions," Int. J. of Multiphase Flow **26**, 207–228 (2000).
[38]D. R. Lide, editor. *Handbook of Chemistry and Physics*, 89th ed (CRC Press Inc, Boca Raton, FL, 2008–2009), pp. 8–56, 12–213.
[39]B. N. Misra and Y. P. Varshni, "Viscosity-temperature relation for solutions," J. Chem. Eng. Data **6**(2), 194–196 (1961).
[40]M. Brai and U. Kaatze, "Ultrasonic and hypersonic relaxations of monohydric alcohol/water mixtures," J. Phys. Chem. **96**, 8946–8955 (1992).
[41]G. D'Arrigo and A. Paparelli, "Sound propagation in water-ethanol mixtures at low temperatures. I. Ultrasonic velocity," J. Chem. Phys. **88**(1), 405–415 (1988).
[42]G. C. Benson and P. J. d'Arcy, "Excess isobaric heat capacities of water-n-alcohol mixtures," J. Chem. Eng. Data **27**(4), 439–442 (1982).
[43]H. Kitajima, N. Kagawa, H. Endo, S. Tsurono, and J. W. Magee, "Isochoric heat capacities of alkanols and their aqueous mixtures," J. Chem. Eng. Data **48**, 1583–1586 (2003).
[44]Q. F. Lei, R. S. Lin, and D. Y Ni, "Thermal conductivities of some organic solvents and their binary mixtures," J. Chem. Eng. Data **42**(5), 971–974 (1997).
[45]S. A. Putnam, D. G. Cahil, and P. V. Braun, "Thermal conductivity of nanoparticles suspensions," J. Appl. Phys. **99**, 084308 (2006).
[46]F. L. Franck, V. Drach, and J. Fricke, "Determination of thermal conductivity and specific heat by a combined 3*w*/decay technique," Rev. Sci. Instrum. **64**, 760–765 (1993).

Sound, infrasound, and sonic boom absorption by atmospheric clouds

Michaël Baudoin and François Coulouvrat[a)]
Université Pierre et Marie Curie, Institut Jean Le Rond d'Alembert, UMR CNRS 7190, 4 place Jussieu, 75252 Paris cedex 05, France

Jean-Louis Thomas
Université Pierre et Marie Curie, Institut des NanoSciences de Paris, UMR CNRS 7588, 4 place Jussieu, 75252 Paris cedex 05, France

(Received 26 January 2011; revised 24 June 2011; accepted 1 July 2011)

This study quantifies the influence of atmospheric clouds on propagation of sound and infrasound, based on an existing model [Gubaidulin and Nigmatulin, Int. J. Multiphase Flow **26**, 207–228 (2000)]. Clouds are considered as a dilute and polydisperse suspension of liquid water droplets within a mixture of dry air and water vapor, both considered as perfect gases. The model is limited to low and medium altitude clouds, with a small ice content. Four physical mechanisms are taken into account: viscoinertial effects, heat transfer, water phase changes (evaporation and condensation), and vapor diffusion. Physical properties of atmospheric clouds (altitude, thickness, water content and droplet size distribution) are collected, along with values of the thermodynamical coefficients. Different types of clouds have been selected. Quantitative evaluation shows that, for low audible and infrasound frequencies, absorption within clouds is several orders of magnitude larger than classical absorption. The importance of phase changes and vapor diffusion is outlined. Finally, numerical simulations for nonlinear propagation of sonic booms indicate that, for thick clouds, attenuation can lead to a very large decay of the boom at the ground level.
 [DOI: 10.1121/1.3619789]

PACS number(s): 43.28.Bj, 43.28.Dm, 43.20.Hq, 43.28.Mw [ROC] Pages: 1142–1153

I. INTRODUCTION

Water droplets in suspensions considerably modify sound propagation. This was first studied by Sewell,[1] who considered only momentum transfers between ambient air and fixed particles. Lamb[2] modified this model by allowing particle motion. Isakovich[3] outlines the importance of heat transfer. Epstein and Carhart[4] introduce a new formalism to take into account particles elasticity. This work, limited to the low frequency range, is extended by Allegra and Hawley[5] to emulsions and aqueous suspensions without frequency limitation. This approach, now referred as the ECAH theory, is most suitable for solid particles or emulsions as it cannot take into account phase changes at the particle surface. Viglin[6] and Oswatitsch[7] investigate the effects of evaporation and condensation, assuming in a simplified analysis the two phases have the same speed and temperature. This approach is extended by Marble,[8] Marble and Wooden,[9] Cole and Dobbins,[10] and Ivandaev and Nigmatulin[11] to the case of different speeds and temperatures for the two phases. In particular, a peak of the attenuation per wavelength associated with phase change effects is predicted. Marble and Wooden[9] and Cole and Dobbins[10] consider a liquid particle surrounded by a mixture of its vapor and an inert gas. The evaporation rate is assumed to be dominated by the diffusion of vapor within the gas. On the contrary, Ivandaev and Nigmatulin[11] investigate the case of a liquid droplet in suspension within its vapor only. The evaporation rate is determined by the Hertz–Knudsen–Langmuir formula[12–14] involving the so-called evaporation coefficient. In all these models, transfers of mass, momentum and energy are modeled by stationary terms. Unsteady effects are included by Gumerov *et al.*[15] for the case of a liquid in suspension within its vapor only. That model is finally extended by Gubaidullin and Nigmatullin[16] to include polydispersed droplets within a gaseous mixture of vapor and inert gas. Duraiswami and Prosperetti[17] show that, when the effects of phase changes on the acoustic wave propagation are maximum, the Knudsen number is necessarily of order one. They therefore propose some corrections to the transfers terms to be taken into account when the droplet size is comparable to the gas mean free path. They also include the presence of an inert gas. However, the model used in the present study is the one of Gubaidullin and Nigmatullin,[16] as it is, to our knowledge, the only one to include simultaneously polydispersion, unsteady effects, mass (evaporation/condensation), momentum and energy surface transfers. It will be shown that the polydispersion plays a major role in the propagation of acoustic waves in clouds, while the Knudsen number remains in practice small enough to neglect the corrections proposed by Duraiswami and Prosperetti.[17]

From the experimental point of view, Knudsen[18] is likely the first to have made qualitative observations. Dobbins and Temkin[19,20] measure attenuation and dispersion in a mixture of oleic acid within nitrogen. However, the frequencies are too large for evaporation and condensation effects to be observed, so that their results are very similar to those of

a)Author to whom correspondence should be addressed. Electronic mail: francois.coulouvrat@upmc.fr

aerosols with solid particles. The influence of phase changes has been measured only in the experiment of Cole and Dobbins in 1971,[21] performed within a Wilson chamber filled with a water cloud. Droplet concentration is controlled by spark-induced condensation nuclei. The water mass ratio is about 10^{-2}, about 10 times larger than in atmospheric clouds. Concentration and droplet size are controlled optically by Mie diffusion of a light source. Radii range from 1.8 to 10 μm. Sound attenuation is measured through the time decay of a stationary wave at a fixed frequency (80 Hz), and attenuation is plotted versus a dimensionless frequency proportional to the mass ratio. Experimental uncertainty, a 15% error margin very sensitive to optical measurements, is smaller than the mismatch with theory, with experimental attenuation about 35% smaller than in theory. Nevertheless, these experiments remain to our knowledge the only ones measuring quantitatively the influence of phase changes on sound absorption within an aerosol made of water droplets in air.

Since these experiments have been realized, the model[16] has been established with clear theoretical foundations. It is able to handle all effects likely to influence sound propagation in an aerosol of water droplets in air. These effects are, namely, (i) the viscoinertial effects associated to the motion of the droplets relative to the ambient fluid oscillations, (ii) the thermal transfers due to the temperature difference between the gas and the droplets, and (iii) the evaporation/condensation of water, also due to the local disturbance of the thermodynamic equilibrium of the aerosol by the sound field. Phase changes are also affected by (iv) vapor diffusion within dry air, that may limit them by preventing the vapor molecules produced at the droplet surface to diffuse within the air. Hence, the first objective of this paper is to examine the adequacy of Gubaidullin and Nigmatulin's model to predict attenuation of sound and infrasound. We will see in particular that the model is limited to relatively low altitudes (typically less than 4000 m) and low frequency (less than 100 Hz). Then by collecting physical and thermodynamical data for clouds, we will quantify the magnitude of the absorption effect for various types of clouds. Cloud absorption will be compared to classical absorption (due to bulk thermoviscosity and molecular relaxation of nitrogen and oxygen). Finally, a realistic case of application concerning sonic boom propagation will exemplify in a quantitative way the importance of atmospheric clouds.

II. PHYSICAL DATA FOR CLOUDS

In the model, the required physical data about clouds are the mean radius a_0 of the water droplets, the statistical distribution $N(a)$ of droplets size a, the liquid water concentration w_L, the height h of the cloud basis above the ground, and the cloud thickness d. For a given type of cloud, only mean "typical" values are considered. Variability between clouds of the same type is not examined.

Atmospheric clouds are considered as suspensions of almost perfectly spherical liquid water droplets. Only clouds with a small ice content are adequately modeled. Clouds at a temperature higher than 0 °C contain only liquid water. In order to freeze at temperatures higher than − 40 °C, liquid water needs nuclei in order to initiate the solidification reaction. Water freezes spontaneously only at temperatures below − 40 °C. In the atmosphere, the number of nuclei is generally insufficient, and a large part of the water remains in the liquid phase. This is the supercooling (or undercooling) phenomenon. Data[22] (p. 39) indicate that, between 0 °C and − 10 °C, the liquid water content remains dominant (more than 50%) over the ice content. Hence, the present model is applicable to temperatures higher than approximately − 10 °C. For ICAO standard atmosphere,[23] this corresponds to altitudes lower than about 3850 m above sea level.

Given this constraint, seven types of clouds observed at altitudes lower than 4000 m have been selected: stratus (fog - ST), altostratus (AS), stratocumulus (SC), early stage cumulus (CE), growing stage cumulus (CG), final stage cumulus (CF) and cumulonimbus (CN). Typical values[22] are collected in Table I. Liquid water concentration is measured as w_L in grams of water per cubic meter. These data are only mean, representative values. As many meteorological phenomena, extreme values can be observed from time to time, such as water contents up to 14 g/m^3 for some thunder clouds for instance. The distribution function, where $N(a)da$ is the number of particles per unit volume whose radius lies between a and $a+da$, is given by[22] (pp. 26–27):

$$N(a) = Aa^2 \exp(-Ka), \tag{1}$$

where A and K are related to the mean radius, the water content and the liquid water specific mass ρ_{lo} by:

$$a_0 = \frac{\int_0^{+\infty} aN(a)da}{\int_0^{+\infty} N(a)da} \quad \text{and} \quad K = \frac{3}{a_0} \quad \text{and} \quad A = \frac{10^{-3} w_L K^6}{160\pi\rho_{lo}}. \tag{2}$$

III. THE THEORETICAL MODEL

A. Qualitative description of absorption mechanisms

In an atmospheric cloud, droplets (with radius on the order of 10 to 30 μm —see Table I) are in suspension within a gas composed of a mixture of water vapor and air, which itself is a mixture of mostly molecular nitrogen N_2, molecular oxygen O_2 and argon Ar. At thermodynamic equilibrium, the partial vapor pressure p_v is equal to the saturation pressure $p_{vs}(T)$ given by the Clausius-Clapeyron relation. A sound wave disturbs that equilibrium. In case of an expansion, temperature drops, vapor pressure gets larger than its equilibrium value and, in order to restore equilibrium, some

TABLE I. Physical data for atmospheric clouds.

Type	h (km)	d (m)	w_L (g/m^3)	a_0 (μm)
Fog	0	500	0.05 to 0.5	10
Altostratus	2.0 to 4.5	2000	0.2 to 0.5	20
Stratocumulus	0.6 to 2.0	800	0.1 to 0.5	20
Cumulus				
Early stage	0.5 to 2.0	500	0.2 to 0.5	10
Growing stage	0.5 to 2.0	1500	0.5 to 1.0	20
Final stage	0.5 to 2.0	2500	0.5 to 3.0	30
Cumulonimbus	0.5 to 2.0	5000	0.5 to 3.0	30

vapor has to condense. That phase change requires some energy under the form of latent heat, that is pumped from the acoustical wave. A spectacular illustration of this effect is seen on some photographs of condensation clouds taking the form of a Mach cone around aircraft flying supersonically at low altitudes. Similarly, a compression wave induces a partial vaporization of the water droplets. However phase changes are not instantaneous. For high frequencies, the cloud cannot adapt to the fast temperature changes and it appears as "frozen" in its initial thermodynamic state. On the contrary, for low frequencies, the cloud always remains at thermodynamic equilibrium, and no sound absorption is induced. Hence, sound absorption due to phase changes is most efficient in some intermediate frequency range. We will see the critical frequency is around 0.1 Hz, a value controlled simultaneously by vapor diffusion, and by water mass concentration. Indeed phase changes occur at the surface of the droplets. A strong evaporation may induce a surface accumulation of vapor molecules that also need time to diffuse within the ambient air to restore an equal spatial repartition. The second effect that may affect sound propagation is momentum transfers between the droplets and the gas. Indeed, a particle relative motion within a fluid induces a viscous drag that dissipates part of the energy producing that motion. Acoustic motion being unsteady, it also induces an inertial Archimedes force on the droplet that contributes to the velocity mismatch between the air and the liquid, and hence to the viscous drag. Finally, droplets and air have different thermal properties and do not adapt in phase to the acoustical temperature. Hence a temperature mismatch occurs, that leads to a dissipative heat flux. Because phase changes are controlled by temperature, mass and heat transfers at the surface of water droplets are strongly coupled to one another.

B. Outline of the model

The two-phase model of Gubaidulin and Nigmatulin[16] is obtained by spatial averaging of Navier-Stokes equations over a characteristic volume containing a large number of particles, but nevertheless small enough compared to the acoustic wavelength. Similar equations can be obtained by performing temporal[24] or statistical[25] average. Mass, momentum and energy conservation equations are obtained for each phase (liquid and gas), with an additional equation required to describe the mass conservation of vapor. The necessary following conditions are to be fulfilled. (1) The average of products of fluctuation (the so-called pseudoturbulence) is neglected. (2) Gravity is neglected and there is no heat source. (3) The liquid droplets are supposed to be rigid. (4) The momentum exchanged during phase change is neglected. (5) The suspension is dilute.

$$\frac{\partial\left(\alpha_g\rho_g\right)}{\partial t}+\nabla.\left(\alpha_g\rho_g\mathbf{v}_g\right)=-J, \tag{3}$$

$$\frac{\partial\left(\alpha_g\rho_v\right)}{\partial t}+\nabla.\left(\alpha_g\rho_v\mathbf{v}_g\right)=-J, \tag{4}$$

$$\rho_{lo}\frac{\partial(\alpha_l)}{\partial t}+\rho_{lo}\nabla.(\alpha_l\mathbf{v}_l)=J, \tag{5}$$

$$\alpha_g\rho_g\frac{d_g\upsilon_g}{dt}=-\mathbf{F}-\nabla p_g+\nabla\cdot\Sigma, \tag{6}$$

$$\alpha_l\rho_{lo}\frac{d_l\upsilon_l}{dt}=\mathbf{F}, \tag{7}$$

$$\alpha_g\rho_g C^p_{go}\frac{d_gT_g}{dt}=Q_g+\chi_{go}\nabla^2T+\Sigma:\mathbf{D}, \tag{8}$$

$$\alpha_l\rho_{lo}C_{lo}\frac{d_lT_l}{dt}=Q_l, \tag{9}$$

$$Q_g+Q_l=-Jl_o. \tag{10}$$

Equations (3)–(5) formulate, respectively, the mass conservation of the gaseous, vapor, and liquid phases, Eqs. (6) and (7) the momentum conservation of the gaseous and liquid phases, and Eqs. (8) and (9) the conservation of energy of the gaseous and liquid phase. Equation (10) is the energy balance at the surface of the droplets. The subscripts $k=a,$ $g,$ $l,$ υ designate, respectively, the dry air (inert gas), the gaseous (vapor + dry air) phase, the liquid phase and the vapor. The subscript "o" is used for constant parameters, α_k is the volume fraction occupied by phase $k,$ with the relation $\alpha_g+\alpha_l=1$. Notations ρ_k, T_k, $\mathbf{v_k}$, p_k are, respectively, for the average density, temperature, velocity and pressure of phase $k,$ while $d_k/d_k=\partial/\partial t+v_k.\nabla$ is the convective derivative associated to the motion of phase "k." Then $\mathbf{v}=\alpha_g\mathbf{v}_g+\alpha_l\mathbf{v}_l$, $T=\alpha_gT_g+\alpha_lT_l$ and $\mathbf{D}=1/2(\nabla\mathbf{v}+\nabla\mathbf{v}^T)$ are, respectively, the average velocity, temperature and deformation rate tensor of the suspension. The viscous stress tensor of the suspension is $\Sigma=2\mu_{go}\mathbf{D}+(\zeta_{g0}-2\mu_{go}/3)(\nabla\cdot v)\mathbf{I}$, and μ_{go}, ζ_{go}, C^p_{go}, and χ_{go} represent the dynamic shear and bulk viscosity of the gaseous phase, its heat capacity at constant pressure, and its heat conductivity. C_{lo} and l_o are the heat capacity of the liquid phase and the latent heat of evaporation. Finally, $J,$ $\mathbf{F}$, $Q_{g,}$ and Q_l denote the mass flux induced by phase change, the average force applied on the particles, the heat flux from the gaseous phase toward the interface and the heat flux from the liquid phase toward the interface. Note that only vapor diffusion linked to surface effects of evaporation and condensation is taken into account, while the one due to pressure and temperature bulk gradients induced by the acoustical wave is neglected. Since the suspension is polydisperse, the velocity and temperature field of the liquid phase can be seen as some averages (over the different particle sizes) of the velocity and temperature of droplets of a given size a: $\mathbf{v}_\mathrm{p}(a,\mathrm{x},t)$ and $\mathrm{T}_p(a,\mathrm{x},t)$. Thus, we have $\mathbf{v}_1=\langle\mathbf{v}_p(a,\mathrm{x},t)\rangle_a$ and $T_l=\langle T_p(a,\mathrm{x},t)\rangle_a$, where $\langle f\rangle_a=(1/\alpha_{lo})\int_0^{+\infty}(4/3\pi a^3)f(a)N(a)da$ is the average over the different particle radii of function $f(a)$.

To describe the propagation of a plane sound wave of angular frequency ω, these equations are written in a 1D geometry, expressed in the Fourier space and linearized around thermodynamic equilibrium (defined by the variables α_{go}, α_{lo}, ρ_{go}, ρ_{vo}, $\mathbf{v}_{go}=\mathbf{v}_{lo}=0$, $T_{go}=T_{lo}=T_o$ and p_{go}, which are the equilibrium counterparts of previously defined variables).

Each gaseous species satisfies the ideal gas law $p_k=\rho_kR_kT_g$ with $k=\upsilon,a$ and R_k is the ideal constant of gas k. The total pressure is the sum of the partial ones (Dalton's

law) $p_g = p_v + p_a$. Gas total mass is the sum of its components $\rho_g = \rho_v + \rho_a$. The saturation vapor pressure p_{vs} satisfies the Clausius-Clapeyron relation, with T_Σ the temperature at the droplet surfaces:

$$T_\Sigma(dp_{vs}/dT_\Sigma) = \rho_v l_o. \tag{11}$$

Closure is achieved by providing adequate expressions for the mass, momentum and heat transfers (respectively, J, $\mathbf{F}$, Q_l, and Q_g) between gas and liquid. Since the droplets are small and their motion relatively slow, the Reynolds number associated with the droplet motion is small, so that the force applied on a single droplet can be computed from linear Stokes equations. For an unsteady motion, this force is the sum of the Stokes, Basset, Added mass and Archimedes forces.[26] The first term is the classic Stokes drag applied on a sphere embedded in a steady viscous flow. The Basset hereditary force is an unsteady viscous term due to the time required by the viscous diffusion layer to adapt to new boundary conditions. The added mass term is linked to the inertia of the liquid, which must be displaced when a sphere is accelerated or decelerated. The Archimedes force is an unsteady inertial force which comes from the difference of density between the particles and the surrounding medium. The following expression is obtained in the Fourier space:

$$\mathbf{F} = \alpha_{lo}\rho_{lo}\left\langle \frac{\mathbf{v_g} - \mathbf{v_p}}{\tau_v^*} - \frac{\mathbf{v_g}}{\tau_A^*} \right\rangle_a \tag{12}$$

where τ_v^* is a complex time associated to the sum of Stokes, Basset, and Added mass terms, and τ_A^* is a complex time associated to Archimedes force (defined below).

Heat flux expressions in the gas and liquid phases are obtained by solving the unsteady heat equation inside and outside the droplet with a surface temperature T_Σ:

$$Q_g = -\alpha_{lo}\rho_{lo} r_o C_{go}^p \left\langle \frac{T_g - T_\Sigma}{\tau_{\Sigma_g}^*} \right\rangle_a, \tag{13}$$

$$Q_l = -\alpha_{lo}\rho_{lo} C_{lo} \left\langle \frac{T_l - T_\Sigma}{\tau_{T_l}^*} \right\rangle_a, \tag{14}$$

with $\tau_{\Sigma_g}^*$ and $\tau_{T_l}^*$ the complex characteristic times associated with heat conduction in the gas and liquid, respectively, and r_o the ratio of densities $r_o = \rho_{go}/\rho_{lo}$.

Expression of the mass flux is obtained by equating the flux of evaporation given by Hertz–Knudsen–Langmuir formula J_β, to the flux of diffusion of vapor through the air $J = J_\beta = J_d$ with:

$$J_\beta = \alpha_{lo}\rho_{lo}\frac{r_o}{\rho_{go}}\left\langle \frac{p_v - p_\Sigma}{\tau_\beta} \right\rangle_a, \tag{15}$$

$$J_D = \alpha_{lo}\rho_{lo}\frac{r_o}{\rho_{go}}\left\langle \frac{p_\Sigma - p_{vs}}{\tau_D^*} \right\rangle_a, \tag{16}$$

with p_Σ the vapor pressure reached after evaporation and before diffusion in the inert gas, τ_β the real time associated with phase change and τ_D^* the complex time associated with diffusion through the air.

The times appearing above are defined by the following formula. Times marked with a superscript "*" are complex times. The notation τ is used for steady transfers, and the notation θ for unsteady transfers.

Times associated with

- Momentum transfers

$$\left.\begin{array}{ll} \tau_v = \dfrac{2}{9}\dfrac{\rho_{lo}}{\rho_{go}}\dfrac{a^2}{\nu_{go}} & \theta_v = a^2/\nu_{go} \\ \tau_v^* = \tau_v \Big/ \left[1 - \dfrac{1}{9}i\omega\theta_v + \dfrac{1-i}{\sqrt{2}}\sqrt{\omega\theta_v}\right] & \tau_A^* = -i/(\omega r_o) \end{array}\right\}. \tag{17}$$

  In τ_v^*, the three terms correspond, respectively, to Stokes, Added mass and Basset force (with τ_v associated with steady Stokes drag), and τ_A^* is associated with Archimedes force.

- Heat transfers in the gaseous phase

$$\left.\begin{array}{lll} \tau_T = \dfrac{1}{3}\dfrac{\rho_{lo}}{\rho_{go}}\dfrac{a^2}{\kappa_{go}} & \theta_{T_g} = a^2/\kappa_{go} & z_g = e^{-i\pi/4}\sqrt{\omega\theta_{T_g}} \\ \eta_g = \dfrac{1}{1+z_g} & \tau_{T_g}^* = \dfrac{1}{3}\theta_{T_g}\eta_g & \tau_{\Sigma_g}^* = \dfrac{\alpha_{lo}}{\alpha_{go}}\tau_{T_g}^* \end{array}\right\}, \tag{18}$$

  with τ_T the time associated with steady heat transfers without phase change

- Heat transfers in the liquid phase

$$\left.\begin{array}{ll} \theta_{T_l} = a^2/\kappa_{lo} & z_l = e^{-i\pi/4}\sqrt{\omega\theta_{T_l}} \\ \eta_l = \dfrac{5\left[3z_l\left(3+z_l^2\right)th(z_l)\right]}{z_l^2(th(z_l) - z_l)} & \tau_{T_l}^* \big| = \frac{1}{15}\theta_{T_l}\eta_l \end{array}\right\}. \tag{19}$$

- Vapor diffusion in air

$$\left.\begin{array}{lll} \tau_D = \dfrac{1}{3}\dfrac{\rho_{lo}}{\rho_{go}}\dfrac{a^2}{D} & \theta_D = a^2/D & z_D = e^{-i\pi/4}\sqrt{\omega\theta_D} \\ \eta_D = \dfrac{1}{1+z_D} & \tau_D^* = \dfrac{1}{3}\dfrac{R_v}{R_g}(1-k_{vo})\theta_D & \end{array}\right\}, \tag{20}$$

  with τ_D the time associated with steady vapor diffusion

- Evaporation/condensation

$$\tau_\beta = \frac{1}{3}\sqrt{\frac{2\pi}{\gamma_v}}\frac{\gamma_g c_{vo} a}{\beta c_{go}^2}. \tag{21}$$

The two parameters $m = \alpha_{lo}\rho_{lo}/\alpha_{go}\rho_{go}$ and $k_{vo} = \rho_{vo}/\rho_{go}$ are the most important ones that influence the magnitude of the attenuation induced by the suspension. The attenuation induced by viscoinertial and thermal effects is directly linked to the quantity of droplets present in the suspension and thus to the mass fraction m, while the phase change effects are directly related to the quantity of vapor k_{vo}. In the above expressions, $\nu_{go} = \mu_{go}/\rho_{go}$ is the gas kinematic viscosity, $\kappa_{lo} = \chi_{lo}/\rho_{lo}C_{lo}$ and $\kappa_{go} = \chi_{go}/\rho_{go}C_{go}^p$ are the thermal diffusivity of the liquid and gaseous phases, respectively, D the binary diffusion coefficient of vapor in air, γ_k the heat capacity ratio of phase k, c_{vo} and c_{go} the sound speeds in

vapor and in the gaseous phase, respectively, and β is the evaporation parameter. We can note that τ_v, τ_T, and τ_D on one hand, and θ_v, θ_T, and θ_D on the other hand, share similar written forms. This comes out from the fact that each time arises from the solution of an unsteady diffusion equation (Stokes, heat or diffusion equation). The only difference is that Stokes equation being a vectorial equation, a factor 2/9 instead of 1/3 appears in the expression of τ_v. Complex times τ^* are also similar, but an additional term (the added mass) appears in the expression of τ_v^*. To each time, we can associate a characteristic frequency. We note $f_v = 1/(2\pi\tau_v)$ the frequency of steady momentum transfers, and $f_{pc} = m/(2\pi\tau_D)$ the frequency associated with phase changes. Expression of τ_D^* involves the coefficient $(1 - k_{vo})$, which shows that, in the mass diffusion processes, only gradient concentrations are taken into account. Thermodiffusion, e.g., mass diffusion induced by temperature gradients (Soret effect), is neglected as it is known to be of a smaller order of magnitude. Finally, the expression for the dispersion relation is detailed in the Appendix.

For atmospheric application, the model has to be complemented by data for the dependence of various coefficients with pressure and temperature down to $-10\,^{\circ}$C. Most of them are in Ref. 22 The saturation pressure $p_{vs}(T)$ follows Magnus formula (p. 854) in the temperature range $[-50^{\circ}; +50\,^{\circ}\text{C}]$. Two different expressions for specific heat of liquid water C_{lo} are given (p. 93), either in the range $[-4.2^{\circ}; +35\,^{\circ}\text{C}]$, or in the range $[-37.0^{\circ}; -4.2\,^{\circ}\text{C}]$. For density of liquid water ρ_{lo}, two formula can be found pp. 87, in the range either $[0^{\circ}; 100\,^{\circ}\text{C}]$ or $[-33^{\circ}; 0\,^{\circ}\text{C}]$. Expression for vapor diffusion coefficient D is found pp.503. Evaporation latent heat l_o satisfies Kirchhoff formula (pp. 116). Heat conductivity of vapor χ_{vo}, of dry air χ_{ao} and of the gaseous mixture χ_{go} can all be found p. 508. Ref. 27 provides thermal conductivity of liquid water χ_{lo}, and the specific heat at constant pressure C_{vo}^p and ratio of specific heat γ_v of vapor. Data are extrapolated by a second order polynomial to negative temperatures. Sound speed is deduced by the formula for perfect gases $c_{ko} = \sqrt{\gamma_k R_k T}$. Molar mass is *18* g/mol for vapor and 28.966 g/mol for dry air. Classical formulae to obtain γ_g, R_g, and C_g^p as an ideal mixture of dry air and vapor are used. Given the very low vapor concentration, gas viscosity is identified as that of dry air, following the well-known Sutherland formula.

C. Critical discussion on the model assumptions

The model is limited by a number of various approximations that need a closer examination. The *low frequency* approximation allows to view the cloud as a homogeneous medium at the acoustic wavelength scale $\lambda \gg a_0$. It also enables us to consider the gas locally incompressible at the droplet scale a, so that we can use the classical expression Eq. (12) for the momentum transfer. We are presently interested in the infrasonic and low audible frequency range, lower than 100 Hz (this upper limit value is fixed by another model limitation), which gives a ratio $a/\lambda < 10^{-5}$, indeed very small.

In the *dilute approximation,* interactions between droplets are neglected when estimating the transfers terms. It yields expressions *linear* with particle concentration α_{lo}. Estimating the volume fraction occupied by the liquid water gives $\alpha_{lo} = w_L/\rho_{lo} = 3 \times 10^{-6} \ll 1$. Interactions associated with high concentration of rigid scatterers generally begin to be significant for volume fractions of order 1%, four orders of magnitude larger than the present one. Note the present model (without heat and mass transfers) has been extended to concentrated suspensions of rigid particles[28,29] and compared favorably to experiments for suspensions of nanoparticles in water in the ultrasonic frequency range.

For the *continuum approximation,* Ref. 17 examines wave propagation in fogs in the intermediate regime of Knudsen number Kn of order 1, that maximizes the mass exchanges through evaporation and condensation. This transitional regime between the continuum limit (presently considered) and the free molecular limit $(K_n \gg 1)$ is treated by introducing finite Knudsen corrections to the exchange terms (like Stokes viscous drag or heat flux). However, given values of Table I, we can estimate the Knudsen number for atmospheric clouds to be $\text{Kn} = \mu_{go}/\rho_{go}c_{go}a = 0.0042$ at the ground level ($\rho_{go} = 1.2$ kg/m^3, $\mu_{go} = 1.7 \times 10^{-5}$ Pa s and $c_{go} = 340$ m/s) for the smallest droplets, and $\text{Kn} = 0.0062$ at 4000 m altitude. Hence, the approximation of *small Knudsen number* is very realistic for atmospheric clouds.

According to the *linear approximation,* transfer terms are modeled by linear expressions in terms of velocity, pressure or temperature mismatches, which implies a slow flow motion, or a *small Reynolds number* (Stokes flow). For an acoustical wave of amplitude P_0, the Reynolds number can be estimated to be $\text{Re} = P_0 a/\mu_{go}c_{go}$. For a sonic boom at the ground level with typical Concorde amplitude of 50 Pa (100 Pa with pressure doubling due to ground reflection), this gives a value $\text{Re} = 0.26$, smaller than unity. However, this estimation of the Reynolds number is quite conservative, as it assumes the velocity mismatch between the droplets and the ambient gas is of the same order as the gas velocity itself. This was for instance the erroneous assumption of Sewell's model[1] considering fixed particles. In reality, droplets are convected by the gas, only a small part of the wave field is absorbed, and the velocity mismatch is only a small fraction of the gas velocity. So, for most acoustical applications, including sonic boom, the small Reynolds number assumption is well satisfied. However, for very intense sound field like blast nearfields, amplitudes can reach several thousand Pascals, and that assumption should be examined more carefully. Concerning thermal effects, the conclusion is similar, as both air and water Prandtl numbers are of order one.

The last approximation considers liquid droplets as rigid bodies, and air as a *perfect gas.* The assumption of liquid water as almost incompressible for an aerial acoustic wave is perfectly satisfied because of the very large impedance contrast between air and liquid water (the ratio is about 2.8×10^{-4}). On the contrary, the second approximation is much more constraining. Indeed, at audible frequencies, absorption of acoustic wave is dominated by real gas effects, namely, the vibrational relaxation of diatomic molecules of nitrogen N_2 and oxygen O_2 that make about 99% of the mass of the air.[30] Relaxation frequencies of nitrogen in air saturated with water vapor (100% relative humidity) are typically

of one or several hundreds of Hz, depending on temperature.[31] The quantitative comparison between cloud and classical sound absorption will show that sound absorption in clouds is dominant by several orders of magnitude over the classical one for infrasonic and low audible frequencies, up to typically 100 Hz. However for higher frequencies, the two sources of absorption turn out of the same order of magnitude. Hence real gas effects cannot be neglected anymore in the frequency range 100 Hz to 1 kHz. In order to be applicable in this frequency range, the model should be modified to include real gas effects for dry air. For frequencies higher than 1 kHz, oxygen relaxation and classical thermoviscous effects are dominant, and the effect of water droplets gets negligible. At still higher frequencies there may be droplet resonances also.

IV. SOUND AND INFRASOUND ABSORPTION

A. Mechanisms of sound absorption

The main unknown in the data used in the model is the value of the evaporation coefficient β. This parameter (which appears in Hertz–Knudsen–Langmuir formula) represents the proportion of vapor molecules which condense when impacting the interface. Note that various improvement of the Hertz–Knusden–Langmuir formula exist (see Schrage[14] and Barrett and Clement[12]) and rely on different assumptions about the Maxwellian distribution of vapor molecules close to the interface. Concerning the experimental determination of the parameter β, large differences are reported in the literature, from $\beta = 0.01$ to $\beta = 1$ (for a review see Eames *et al.*[13]). Such discrepancies are likely due to differences in the various experimental processes, especially in the measurement of the surface temperature T_Σ. Recent results[13] for pure water evaporating into a space containing only water vapor, indicate that the true evaporation coefficient is likely to be unity, and is anyway larger than 0.5. However, under real conditions for atmospheric clouds with a gaseous mixture and chemical impurities at the droplet surface, this value may be significantly lower. The question then arises whether this uncertain value significantly influences sound absorption in clouds, as evaporation/condensation is known to be dominant at low frequencies. Hence sound absorption has been computed (Fig. 1) in the frequency range [0.01 Hz – 10 kHz]. The lower value is chosen well above the acoustic cutoff frequency (typically 3.3 mHz) resulting from gravity. Realistic conditions for clouds have been selected regarding their variability according to Table I. These conditions are $a_0 = 10$ μm for a monodisperse suspension, $w_L = 1$ g/m^3 for an altitude of 2000 m ($T_0 = 2\,^\circ$C, $p_{go} = 794$ hPa). Four values of the evaporation coefficient have been retained: 1 (theoretical maximum and likely value in ideal conditions), 0.1, 0.01 (lowest value reported in the literature) and 0 (no evaporation effect). Clearly the figure shows that, as soon as evaporation/condensation is taken into account, it is the dominant effect for (infrasonic) frequencies lower than 10 Hz. Viscous and other thermal effects are dominant only for higher (audible) frequencies. Moreover, the sound attenuation rate is almost the same for $\beta = 0.1$ and $\beta = 1$. In this range, the phenomenon is limited not by the rate of evaporation of molecules at the droplet surface, but by the bulk diffusion of vapor molecules within the gas mixture. Even in the case $\beta = 0.01$, precise values of the absorption coefficient are modified, but their magnitude order keeps the same (between 0.1 and 1 dB/km in the frequency range 0.02 to 10 Hz). Hence, all present conclusions about the importance of sound absorption and evaporation/condensation effects will remain valid, whatever the precise value of the evaporation parameter. Since most recent results suggest β is close to one, and given the weak variations of sound absorption for values of β above 0.1, subsequently we chose $\beta = 1$.

The relative importance of the various absorption mechanisms is now discussed. In the same conditions as for Fig. 1, the absorption coefficient (Fig. 2) and phase velocity (Fig. 3) are displayed versus frequency. The relative importance of the various mechanisms involved is compared, by taking into account only viscous effects, thermal and viscous effects without phase changes, or all effects altogether. Note it is impossible to isolate phase change effects, as they are intimately coupled to thermal ones. Once again, one observes that evaporation and condensation mechanisms (controlled by diffusion) are dominant at low frequencies, with dispersion effects most sensitive below the characteristic frequency of phase change $f_{pc} \approx 0.1$ Hz. Thermal and viscous effects are important only above 10 Hz, slightly below the characteristic frequency of steady viscous effects f_v which is here about 121 Hz at the ground level. We will see later that

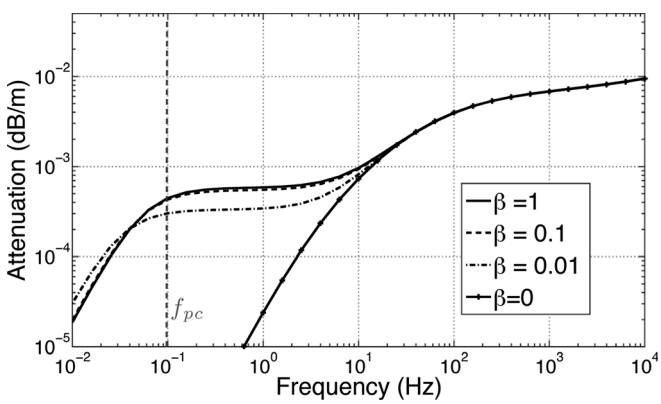

FIG. 1. Influence of the evaporation coefficient parameter on absorption by clouds ($a_0 = 10$ μm, $w_L = 1$ g/m^3, $T_0 = 2\,^\circ$C, $p_{go} = 794$ hPa).

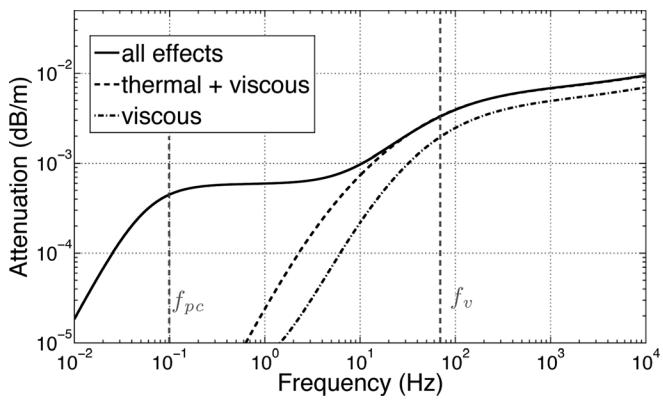

FIG. 2. Influence of various effects on absorption by clouds.

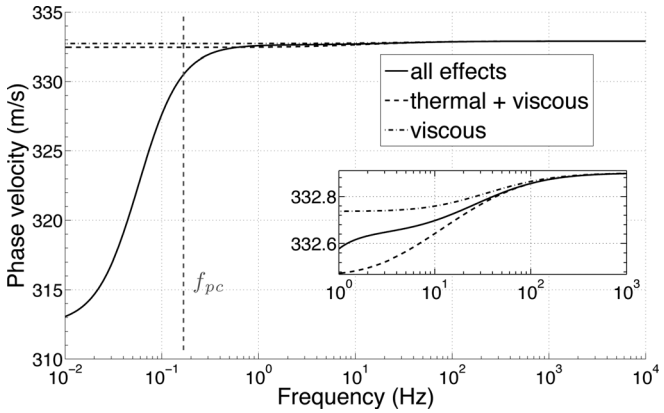

FIG. 3. Influence of various effects on sound speed in clouds.

f_{pc} and f_v are related to one another by $f_{pc} \approx mf_v$ where $m \approx 10^{-3} w_L/(\alpha_{go}\rho_{go})$ is the mass fraction, typically of order 10^{-3} for clouds. Unsteady effects (like Basset history force) play a significant role only at higher frequencies (around 1000 Hz). However, in this high frequency range, real gas effects are anyway dominant. Hence, in any case, unsteady effects are unlikely to play a significant role for absorption of sound in clouds. However, it is an important mechanism to take into account in other cases of suspensions, like solid nanoparticles in water for instance.[32] Viscous and thermal effects have similar behavior with frequency because the Prandtl number of air is close to one, and they are comparable in amplitude.

Thermal and viscous effects introduce very small dispersion, contrarily to phase changes that strongly diminish (by up to 6%) the sound speed at frequencies lower than 1 Hz. Indeed, the effective sound speed is $c_{\text{eff}} = 1/\sqrt{\xi_{\text{eff}}\rho_{\text{eff}}}$ where ρ_{eff} is the effective density and χ_{eff} the effective compressibility. For frequencies $f \gg f_{pc}$, phase changes are frozen, because they are slow compared to acoustic variations. Then, only thermal and viscous exchanges modify the effective density and compressibility of the medium by the introduction of high density and weakly compressible particles. However, these effects are small since they are proportional to the quantity m of liquid present in the suspension, which is small for an atmospheric cloud (see the zoom on Fig. 3). For frequencies $f \ll f_{pc}$, the medium behaves like an effective medium with instantaneous phase changes. In this case, Landau and Lifshitz[33] have shown that the presence of liquid droplets can result into a large effective sound speed decrease. Such variations occur even for a vanishingly small quantity of liquid. This decrease is a consequence of a modification of the thermodynamic behavior of the gazeous phase in the presence of its condensed counterpart. While this effect remains smaller than the one induced by the presence of vapor bubbles in a liquid, it can result into a 10% drop of the sound speed for a suspension of liquid droplets surrounded by its vapor at atmospheric pressure and temperature of 100 °C. The results of Landau, valid for a liquid surrounded by its vapor, have been extended recently[34] in the presence of a neutral gas. The decrease of the sound speed observed in Fig. 3 is consistent with these theoretical predictions.

Two different characteristic times may influence phase change effects: The characteristic time τ_β for the process of evaporation and condensation at the droplet surface, and the characteristic time τ_D for vapor diffusion within air. The first one is very small, on the order of 10^{-8} s, corresponding to frequencies of several MHz. This explains why the present results are quite insensitive to the value of the evaporation coefficient β. In the considered frequency range, phase changes are almost instantaneous. The characteristic time for thermal effects is $\tau_T = \rho_{lo} C_g^p a^2/3\chi_g$. Its ratio to the characteristic time for steady viscous effect τ_v is equal to 3Pr/2. As the Prandtl number of air Pr is of order one, both are of the same orders of magnitude. The ratio τ_D/τ_v is equal to $3Sc/2$ where $Sc = \mu_g/\rho_{g0}\, D$ is the Schmidt number, also of order one for air and vapor. As demonstrated theoretically[9,10] and experimentally[21] in a liquid/gas mixture, there are two coupled thermal modes. The first one (fast mode) is pure *thermal* diffusion. If energy is brought to the medium through a compression, the ambient gas heats, following the state equation. That heating is transmitted through liquid particles by thermal diffusion, hence its dynamic is governed by τ_T. The slow mode induces phase changes. After gas compression and heating, the vapor pressure p_v differs from saturation pressure p_{vs} which has increased through heating. Vapor pressure has to be increased to recover equilibrium, which implies that part of the liquid will vaporize (which is almost instantaneous) and then diffuse. This now induces a *decrease* of the ambient gas and liquid temperatures to pump the necessary latent heat. For this mode, the source of the dynamic relaxation process is the liquid. If the liquid mass concentration is small, that process will be much slower because it is necessarily proportional to the small quantity of liquid present in the suspension (contrarily to the first mechanism which is a transfer of heat from the gas, that is overwhelming relative to the liquid). In this case the characteristic time is τ_D/m. For clouds, m is typically of order 10^{-3}, hence the characteristic frequency of phase change $f_{pc} = m/(2\pi\tau_D) = (3Sc/2)mf_v \approx mf_v$ is about 0.1 Hz. Around this frequency, attenuation per wavelength reaches a maximum value, and the frequency behavior of the coefficient of absorption changes, from a quadratic growth below f_{pc} to a plateau value above.

B. Influence of cloud physical parameters

The absorption coefficient in clouds, being governed by phase change effects at low frequencies, and viscous drag at higher ones, tends to increase with the total mass of water for a given droplet radius (here $a = 10$ μm): the increase in the number of sound absorbers increases sound absorption. This is observed on Fig. 4 in the frequency range 0.1 Hz to 10 kHz, where the water content w_L takes three realistic values ranging from 0.5 to 3.0 g/m^3. However, while the characteristic frequencies of thermal and momentum exchanges are not affected by the water content, the frequency of phase change f_{pc} is directly proportional to the liquid content. Thus, when the water content is decreasing, the characteristic frequency is also decreasing. Clouds with low water content hence have a plateau value of lower amplitude but of wider frequency

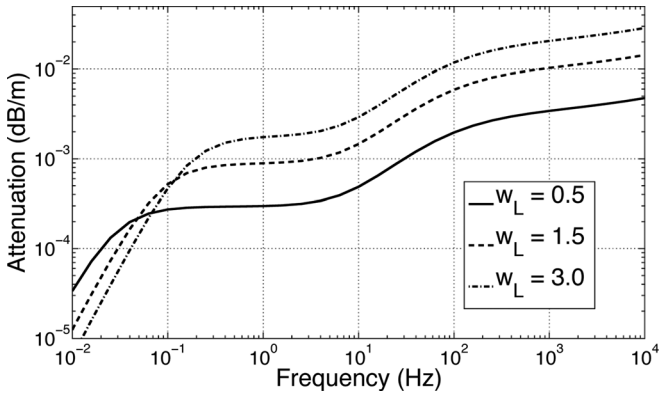

FIG. 4. Influence of water content on absorption by clouds.

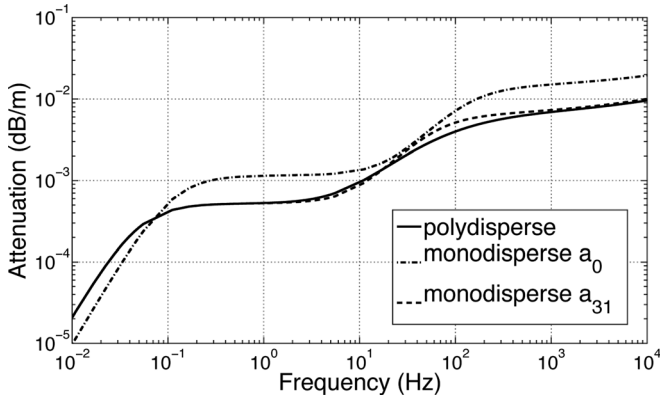

FIG. 6. Influence of polydispersion on absorption by clouds.

extent, so that in the very low frequency range (around 0.01 Hz) the inverse phenomenon is observed: clouds with low water content tend to absorb more infrasound.

The average radius of clouds droplet largely depends on the development stage of the cloud. It can evolve from 5 μm for early stage ones to 40μm for rainy clouds. For a given water mass content (here $w_L = 1$ g/m^3), and when increasing the droplet radius a_0, the total surface of droplets decreases. Since transfers responsible for absorption effects are surface processes, so does the absorption coefficient, see Fig. 5. However, since all characteristic frequencies f_{pc} and f_v are inversely proportional to the square of the droplet radius, the peak of absorption per wavelength is shifted to low frequencies when the droplet radius increases. This results in an inversion of the dependence of the wave attenuation with radius for the lowest frequencies.

Polydispersion plays a significant role as illustrated by Fig. 6 where the monodispersed case (with constant radius $a = 10$ μm) is replaced by a droplet distribution Eq. (1) with the same mean radius a0 = 10 μm. There are significant changes when comparing the monodispersed and polydispersed cases. Taking into account only a mean radius tends to overestimate the absorption, because the influence of large droplets is underestimated and the total surface of droplets is overestimated. Hence a better equivalent mean radius can be defined:[16]

$$a_{31} = \left[\frac{\int a^3 N(a)da}{\int aN(a)da}\right]^{1/2}, \tag{22}$$

based on a mean *surface* defined as the mean volume divided by the mean radius. A much better fit between the polydisperse case and the monodisperse case is then obtained. The same conclusion can be drawn when observing the phase velocity dispersion curves (not shown).

Finally, the influence of altitude is examined on Fig. 7, varying it from 150 to 4000 m, with atmospheric conditions corresponding to ICAO standard atmosphere. When increasing the altitude, the temperature decreases from 14 °C to −11 °C and the pressure from 1013 to 616 hPa. The magnitude of the attenuation induced by phase changes depends on the concentration of vapor k_v, while its characteristic frequency depends on the value of the mass fraction m and the diffusion coefficient D (if the droplet radius remains constant). When the altitude is increased, the diffusion coefficient and mass concentration vary about 9% and 33%, respectively, while the vapor concentration is decreased by a factor 5. As a consequence, while the characteristic frequency of phase change f_{pc} is slightly increased, the dominant effect at low frequencies is a diminution of the attenuation induced by phase change (related to the diminution of vapor concentration). At higher frequencies (above 10 Hz), the dominant absorption mechanisms are momentum and heat transfers whose magnitude depends on the mass fraction m. Thus, the increase of the mass ratio with altitude results in an increase of the attenuation above 10 Hz. We can also note that the characteristic frequency of momentum exchange is little affected by the altitude. Anyway, the

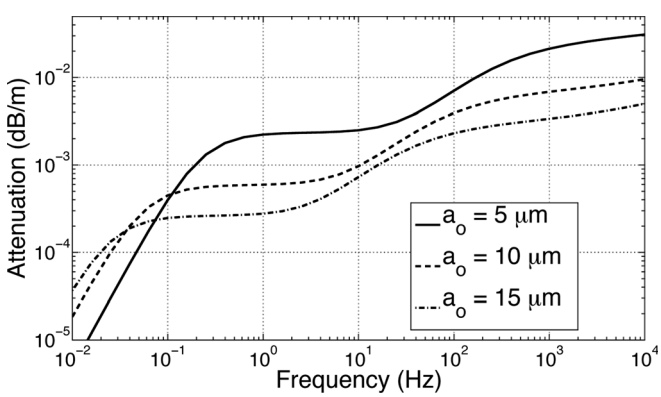

FIG. 5. Influence of droplet radius on absorption by clouds.

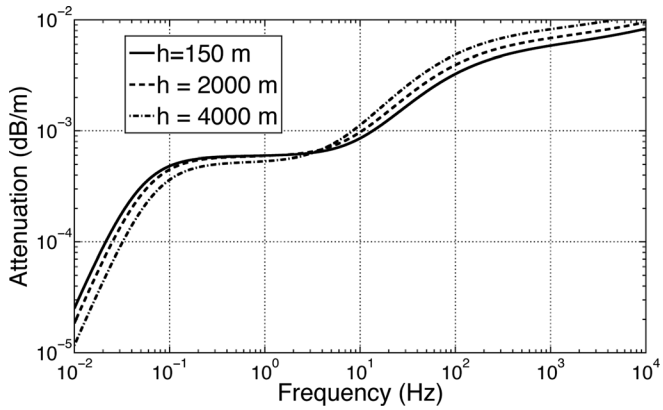

FIG. 7. Influence of altitude on absorption by clouds.

sensitivity of the absorption coefficient to altitude/temperature remains much smaller than sensitivity to other physical parameters.

C. Comparison with standard absorption

Figure 8 compares for various types of clouds the absorption coefficient, computed at the cloud's average altitude according to Table I. Maximum values of water content have been chosen. The resulting absorption is compared to the standard[31] absorption in humid air without clouds, computed at an altitude of 2000 m and a relative humidity of 100%, just prior to condensation. Even though altitudes are not constant, the comparison remains nevertheless significant as either standard or cloud absorption are not deeply modified by altitude (as shown by Fig. 7) in the considered range. Clearly visible on Fig. 8 is the fact that the coefficient of absorption is quite variable with the type of clouds. In the frequency range 1 to 100 Hz, the clouds with the highest water content (such as cumulonimbus or cumulus at intermediate or final stage) tend to be more efficient sound absorbers. At lower frequencies (around 0.1 Hz), influence of droplet radius is more sensitive, and sound absorption in fogs becomes comparable. At very small frequencies (0.01 Hz), variability with clouds is not very large. In magnitude orders, the coefficient of absorption varies from around 4×10^{-5} dB/km at the lowest frequency (0.01 Hz), to around 2×10^{-3} at 100 Hz, e.g., a change of almost two decades in magnitude for four decades in frequency. However, the most important result is that, when compared to standard absorption, absorption within clouds is much larger up to 100 Hz. It is about ten times more important at 100 Hz, hundred times more at 10 Hz and several decades for lower frequencies. When comparing with standard absorption at lower humidities (20% relative humidity) the conclusion is similar although the discrepancy is slightly smaller because standard absorption is larger for dry air. Note the standard absorption gets dominant over the one due to clouds only above 1000 Hz, while the two are comparable in the frequency range 100 to 1000 Hz. This points out one of the main limitation of the cloud model, that is based on a perfect gas assumption for air. Molecular relaxation of diatomic molecules of nitrogen and oxygen is not taken into account, while it is the dominant source of bulk sound absorption up to the MHz range in air without liquid water. Below 100 Hz, the present model is sufficient because droplet absorption is by far dominant. Above 1000 Hz, standard absorption is dominant and droplet influence is negligible. In the intermediate range 100–1000 Hz, both are comparable and the model would need to include real gas effects.

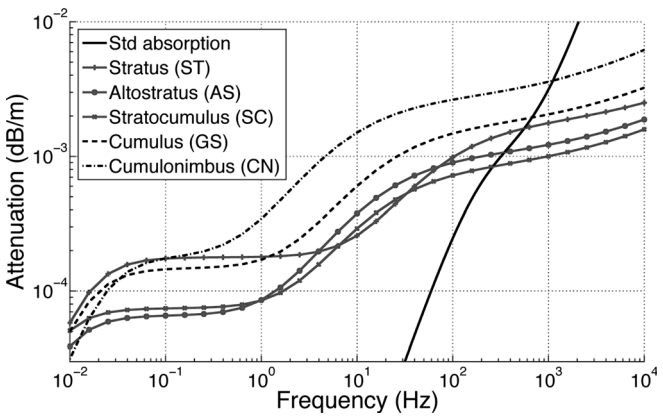

FIG. 8. Comparison of cloud and standard sound absorption.

V. APPLICATION TO SONIC BOOM

Locally, sound absorption within clouds is much larger than standard absorption for frequencies below 100 Hz. Nevertheless, one could argue that, anyway, clouds have only a finite thickness and occupy only a small volume of the atmosphere where sound and infrasound propagate. So the question still remains whether absorption by clouds is really important. Of course, the answer may depend on the type of source, its altitude, frequency range and location relative to clouds and receiver. We here investigate one particular case. A sonic boom is a wideband signal, with main frequency spectrum in the 1 to 10 Hz range but with significant content up to typically 100 Hz. Its source, a supersonic aircraft, is located at high altitudes, well above the cloud, but induces some annoyance at the ground level. It is likely to encounter all types of meteorological situations, with or without clouds. Some flight tests performed in the former Soviet Union on Tu144 indicate a significant effect, with reports[35] on the perception of a loud sonic boom completely modified in presence of thick clouds. To quantify this effect more precisely, we consider a sonic boom emanating from an aircraft flying in steady flight at Mach 1.6 and 15 km altitude. The source signal is the Whitham function[36] associated to a parabolic fuselage 45 m in length, with a volume of 141.3 m^3 and a maximum diameter of 1.4 m. This source has already been used as a reference source for investigating the influence of meteorological variability on sonic boom.[37] It produces at the ground level and in the standard atmosphere without any absorption an ideal N-wave of amplitude 56 Pa and duration 150 ms. This is typical for the sonic boom of a small supersonic aircraft like a business jet or military fighter (without any low boom design). More realistic sources in terms of aerodynamics lead to identical conclusions about the effect of clouds on sonic boom.

Numerical simulations are performed for ICAO standard atmosphere,[23] with the typical relative humidity profile given by the ISO standard.[31] Within the thickness of the selected cloud, that humidity profile has been replaced by a 100% relative humidity. Among values of Table I, the minimal value of height h and the maximal value of the water content w_L are chosen. However, for cumulonimbus, the top of the cloud has been limited to 4000 m, since the model is limited to lower altitudes because of the predominant ice content above. Note the resulting meteorological data may not be fully consistent from a meteorological point of view, as formation of a given type of cloud may be associated to some specific meteorological conditions. However, the point here is to evaluate the importance of clouds on sonic boom absorption, not to provide a fully realistic study of sensitivity of sonic booms to cloudy meteorology.

Numerical simulation is based on a process already described and validated in Ref. 37. Sonic boom is computed through a ray tracing approach. Only the ray emitted perpendicular to the Mach cone at a 0° azimuthal angle in the vertical plane of the aircraft trajectory is considered. Along a given ray, the pressure field satisfies Burgers' equation, augmented with ray-tube area variations for geometrical effects, and linear dispersion and absorption. Standard absorption[31] is considered outside the cloud, and the present model inside the cloudy layer. The cloud is assumed to be a horizontal layer of infinite extent, so that diffraction effects at the edges of the cloudy layer are not considered. The numerical procedure involves a split-step approach. Geometrical effects are taken into account analytically by introducing a linear transformation of the model equation. Nonlinear effects are solved through a quasianalytical shock fitting method[38] based on Poisson solution of the inviscid Burgers' equation. Linear dispersion and absorption are solved numerically in the frequency domain. A second-order Strang split-step is chosen to improve convergence. The problem is voluntarily overdiscretized from a numerical point of view, in order to guarantee numerical convergence. Time pressure waveforms are discretized with 2^{15} points, corresponding to a time step of 7μs, more than 100 times smaller than the actual rise time. The number of spatial steps along the ray is 200, while convergence is generally obtained for values around 30 (thanks to the second-order split-step).

Figure 9 displays the ground pressure waveform when no absorption is considered, for the standard absorption only (no cloud), and for five different clouds. Pressure signal is zoomed on the head shock, to better view the shock structure resulting from the various absorption and dispersion effects. Table II summarizes the main characteristic of the ground pressure field for seven different clouds: (1) peak overpressure (in Pa), (2) rise time (in ms) of the head shock (time necessary for the pressure waveform to go from 10% to 90% of the peak overpressure), and (3) Sound Exposure Level (SEL) with two different frequency A- and C-weightings. ASEL metric is considered (along with Perceived Level) as the best metric for measuring the human response to sonic boom heard outdoor in laboratory conditions.[39] C-weighting is frequently recommended for estimating the human response to loud impulsive noises.[40] In general, standard absorption and clouds tend to preserve the general "N-like" shape of the boom, but reduce the peak overpressure and make shocks smoother. Compared to standard atmosphere, clouds tend to amplify this effect. The effect is moderate for thin cloud (fog or altostratus) but is very significant for thick clouds (cumulus at final stage or cumulonimbus). In the last case, the peak overpressure is more than halved compared to the standard case. Indeed, sound absorption in clouds is much more efficient than standard absorption at frequencies corresponding to the peak of the boom spectrum (1 to 10 Hz). While standard absorption barely affects this part of the boom spectrum, cloud absorption does. The effect is small for thin clouds because propagation path is too short (500 m vertically for fog), but large for thick clouds (4000 m for cumulonimbus). The nonzero value (7 μs) of the rise time in the nonabsorbing case is due to the finite time discretization, with the head shock spread over two grid points only. Rise time in the standard case (no cloud) is on the order of 0.8 ms. Clouds systematically increase that rise time. That increase is almost insignificant for fog, but once again very large for thick clouds. When examining overall sound exposure levels, one again observes a decrease compared to the standard case, in any metric. That effect is almost insignificant for thin clouds (on the order of 0.5 dB for fog), but is extremely large for thick clouds (more than 10 dB for cumulonimbus and A-weighting, 8.5 dB for C-weighting).

TABLE II. Sonic boom absorption by atmospheric clouds.

Type	P_{max} (Pa)	t_m (ms)	SEL (dBA)	SEL (dBC)
No absorption	56.08	0.007	94.48	105.90
No cloud	50.63	0.869	90.58	104.98
Stratocumulus	48.03	0.762	90.50	104.56
Fog	47.78	1.073	90.21	104.42
Altostratus	43.89	1.116	88.82	103.61
Cumulus				
Early stage	47.61	1.159	89.63	104.36
Growing stage	41.50	1.341	88.52	103.15
Final stage	28.92	4.024	83.41	98.88
Cumulonimbus	24.31	7.029	80.40	96.48

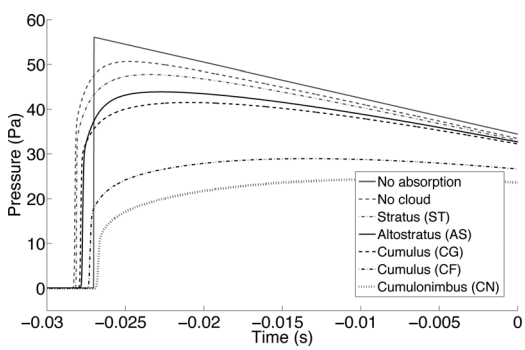

FIG. 9. Sonic boom attenuation by clouds: head shocks.

VI. CONCLUSION

This study examines and quantifies the influence of atmospheric clouds on propagation of sound and infrasound. Two main limitations of an existing model[16] have been outlined. First, it is limited to temperatures higher than about − 10 °C. For colder conditions, the ice content would be too large and a four phase model (air, vapor, liquid water, and ice) would be necessary. Second, the assumption of perfect gases neglects relaxation effects associated to the diatomic nature of nitrogen and oxygen molecules. This effect gets predominant compared to droplet effects within clouds for frequencies over 1000 Hz, and the present model is applicable only for frequencies lower than 100 Hz. In this frequency range, absorption by clouds turns out to be one or several magnitude orders larger than standard absorption. The model shows that phase change effects are predominant at low frequencies (below 1 Hz), while steady thermal and viscous drag is the leading effect above 10 Hz. Unsteady effects are negligible in the considered frequency range. Even though the value of the evaporation parameter is pretty uncertain,

the overall absorption is anyway almost insensitive to this parameter. This is explained by the fact that phase changes are limited by the diffusion of vapor in air. Sound absorption in clouds is mostly sensitive to the radius of water droplets and the total water content. For frequencies above 0.01 Hz, clouds with small droplets and high water content absorb more because they maximize the total surface of droplets. Sound absorption in clouds is much less sensitive to altitude. Dispersion in droplet radii is important to take into account. It can be estimated with a good accuracy by considering an adequate mean radius. Application to sonic boom shows that clouds decrease the peak overpressure, increase the rise time of the head shock and decrease the noise level. That effect is small for short propagation paths within clouds (a few hundred meters) but can be very large for thick clouds (several kilometers). Further work would require to improve the model: include real gas effects, and take into account the presence of ice for high altitude clouds. Other applications could consider other types of low frequency or infrasonic sources. Use of database where cloud data is consistent with other meteorological parameters could also be contemplated.

ACKNOWLEDGMENT

This study was supported by Airbus Operations SAS.

APPENDIX: DISPERSION RELATION

From expressions of Sec. III B, the dispersion relation is obtained for a plane harmonic wave of complex wave number $k(\omega)$ under the form $k = (\omega/c_{go})\sqrt{V(\omega)D(\omega)}$ with c_{go} the sound speed in the gaseous phase (air + vapor), $V(\omega)$ the contribution of momentum transfers and $D(\omega)$ the one of thermal transfers and phase change. Expressions of $V(\omega)$ and $D(\omega)$ are given below as a function of parameters and characteristic times introduced in Sec. III B. Both terms $V(\omega)$ and $D(\omega)$ are of the form $1 + m\ldots$, as effects induced by the presence of droplets are directly proportional to the mass concentration m (dilute approximation):

$$
\begin{aligned}
&V(\omega) = 1 + m\frac{(\alpha_{go} - r_o)\langle h_F\rangle_a - \alpha_{go} r_o}{1 + m r_o \langle h_F\rangle_a},\\
&D(\omega) = 1 + m(\gamma_{go} - 1)\frac{\langle h_{T2}\rangle_a - \bar{R}_\upsilon k_{\upsilon o}\gamma_{go}\left(\bar{R}_\upsilon \bar{C}^p_{go}\langle h_{T3}\rangle_a - 2\bar{l}_o r_o\langle h_{T1}\rangle_a - M_1\Lambda\right)}{1 + m\left(\langle h_{T2}\rangle_a - B\langle h_{T3}\rangle_a - M_2\Lambda\right)},\\
&\Lambda = r_o L\langle h_{T1}\rangle_a^2 + \langle h_{T2}\rangle_a\langle h_{T3}\rangle_a,\quad \bar{R}_\upsilon = \frac{R_\upsilon}{R_{go}},\quad \bar{l}_o = \frac{l_o}{c_{go}^2},\quad \bar{C}^p_{go} = \frac{C^p_{go}}{\gamma_{go}R_{go}} = \frac{1}{\gamma_{go}-1},\quad \bar{C}_{lo} = \frac{C_{lo}}{\gamma_{go}R_{go}},\\
&h_F = \left(1 - \tau^*_\upsilon/\tau^*_A\right)/\left(1 - iw\tau^*_\upsilon\right),\quad h_{T1} = Ze_2,\quad h_{T2} = Z(e_1 - Le_2),\quad h_{T3} = Ze_2(r_o - i\omega\tau^*_{\Sigma_g}e_1),\\
&B = (1 - \bar{R}_\upsilon k_{\upsilon o})\bar{R}_\upsilon,\quad L = r_o\gamma_{go}\left(\gamma_{go} - 1\right)k_{\upsilon o}\bar{l}_o^2,\quad M_1 = m\bar{R}_\upsilon\bar{C}^p_{go}\left(\gamma_{go} - 1 + \bar{R}_\upsilon k_{\upsilon o}\right),\quad M_2 = mB,\\
&Z = r_o/[r_o - i\omega\tau^*_{\Sigma_g}(e_1 - \rho_{\upsilon o}r_o l_o\bar{l}_o(\gamma_{go} - 1)e_2)/p_{go}],\quad e_1 = (C_{lo}/C^p_{go})(1 - i\omega\tau^*_{T_l})^{-1},\quad e_2 = (i\omega(\tau^*_D + \tau_\beta))^{-1}.
\end{aligned}
\tag{A1}
$$

Note that we found a few differences with expressions from Ref. 16 First, we find a coefficient1/15 instead of 1/3 in the expression of $\tau^*_{T_l}$ Second, in the expression of τ_β, we have $\sqrt{2\pi/\gamma_{vo}}$ instead of $\sqrt{2\pi/\gamma_{vo}}$ Finally we have $l_o\bar{l}$ instead of l_o, in the expression of Z.

[1]C. J. T. Sewell, "On the extinction of sound in a viscous atmosphere by small obstacles of cylindrical and spherical form," Philos. Trans. R. Soc. London **210**, 239–270 (1910).
[2]H. Lamb, *Hydrodynamics* (Dover, New York, 1945), pp. 659–661.
[3]M. A. Isakovich, "On the propagation of sound in emulsions," Zh. Exp. Teor. Fiz. **18**, 907–912 (1948).
[4]P. S. Epstein and R. R. Carhart, "The absorption of sound in suspensions and emulsions. I. Waterfog in air," J. Acoust. Soc. Am. **25**, 553–565 (1953).
[5]J. R. Allegra and S. A. Hawley, "Attenuation of sound in suspensions and emulsions: Theory and experiments," J. Acoust. Soc. Am. **51**, 1545–1564 (1972).
[6]A. Viglin, "Propagation of vibrations in a two-phase vapour-liquid system," Zh. Tekh. Fiz. 275–285 (1938).
[7]K. von Oswatitsch, "Die Dispersion und Absorption des Shalles in Wolken (Sound dispersion and absorption in clouds)," Phys. A **42**, 365–378 (1941).
[8]F. E. Marble, "Dynamic of dusty gases," Ann. Rev. Fluid Mech. **2**, 397–446 (1970).
[9]F. E. Marble and D. C. Wooten, "Sound attenuation in a condensing vapor," Phys. Fluids **13**, 2657–2664 (1970).
[10]J. E. Cole and R. A. Dobbins, "Propagation of sound through atmospheric fog," J. Atmos. Sci. **27**, 426–434 (1970).
[11]A. I. Ivandaev and R. I. Nigmatulin, "On the propagation of weak perturbations in two phase media with phase transformations," Zh. Prikl. Mekh. Tekh. Fiz. **5**, 73–77 (1970).
[12]J. Barrett and C. Clement, "Kinetic evaporation and condensation rates and their coefficient," J. Colloid Interface Sci. **150**, 352–364 (1992).
[13]I. W. Eames, N. J. Marr, and H. Sabir, "The evaporation coefficient of water: a review," Int. J. Heat Mass Transfer **40**, 2963–2973 (1997).
[14]R. W. Schrage, *A Theoretical Study of Interphase Mass Transfer* (Columbia University Press, New York, 1953), pp. 25–43.
[15]N. A. Gumerov, A. I. Ivandaev, and R. I. Nigmatulin, "Sound waves in monodisperse gas-particle or vapour-droplet mixtures," J. Fluid Mech. **193**, 53–74 (1988).
[16]R. A. Gubaidullin and R. I. Nigmatulin, "On the theory of acoustic waves in polydispersed gaz-vapor-droplet suspensions," Int. J. Multiphase Flow **26**, 207–228 (2000).
[17]R. Duraiswaimi and A. Prosperetti, "Linear pressure wave in fogs," J. Fluid Mech. **299**, 187–215 (1995).
[18]V. O. Knudsen, J. V. Wilson, and N. S. Anderson, "The attenuation of audible sound in fog and smoke," J. Acoust. Soc. Am. **20**, 849–857 (1948).
[19]R. A. Dobbins and S. Temkin, "Measurement of particulate acoustic attenuation," AIAA J. **2**, 1106–1111 (1964).
[20]S. Temkin and R. Dobbins, "Attenuation and dispersion of sound by particulate-relaxation processes," J. Acoust. Soc. Am. **40**, 317–324 (1966).

[21]J. E. Cole and R. A. Dobbins, "Measurement of the attenuation of sound by a warm air fog," J. Atmos. Sci. **28**, 202–209 (1971).
[22]H. R. Pruppacher and J. D. Klett, *Microphysics of Clouds and Precipitation* (Kluwer Academic, Dordrecht, 1978), pp. 26–27, 39, 87, 93, 116, 503, 854.
[23]ICAO, "Manual of the ICAO standard atmosphere (extended to 80 km)," Technical Report, ICAO, Doc 7488-third edition (1993).
[24]M. Ishii and T. Hibiki, *Thermo-Fluid Dynamic Theory of Two-Phase Flow* (Springer, New York, 2006), pp. 93–117.
[25]Y. A. Buyevich and I. N. Shchelchkova, "Flow of dense suspensions," Prog. Aerospace Sci. **18**, 121–151 (1978).
[26]Y. A. Buyevich and V. G. Markov, "Rheology of concentrated mixtures of fluids with small particles," PMM **36**, 480–493 (1972).
[27]National Institute of Standards and Technology, "Webbook of Chemistry," http://webbook.nist.gov/chemistry (Last viewed 22 July 2011).
[28]M. Baudoin, J.-L. Thomas, and F. Coulouvrat, "On the influence of the particles correlations in position on the sound propagation in concentrated solutions of rigid particles," J. Acoust. Soc. Am. **123**, 4127–4139 (2008).
[29]M. Baudoin, J.-L. Thomas, F. Coulouvrat, and D. Lhuillier, "An extended coupled phase theory for the sound propagation in polydisperse suspensions of rigid particles," J. Acoust. Soc. Am. **121**, 3386–3397 (2007).
[30]H. E. Bass, L. Sutherland, J. Piercy, and L. Evans, "Absorption of sound by the atmosphere," in *Physical Acoustics: Principles and Methods*, (Academic, Orlando, 1984), Vol. XVII, pp. 145–232.
[31]ISO 9613-1 "Acoustics - Attenuation of sound during propagation outdoors - part 1: Calculation of the absorption of sound by the atmosphere," International Organization for Standardization, Genève (1993).
[32]M. Baudoin, J.-L. Thomas, F. Coulouvrat, and C. Chanéac, "Scattering of ultrasonic shock waves in suspensions of silica nanoparticles," J. Acoust. Soc. Am. **129**, 1209–1220 (2011).
[33]L. D. Landau and E. M. Lifshitz, *Course of Theoretical Physics. Vol. 6. Fluid Mechanics*, 2nd ed. (Butterworth-Heinemann, Oxford, 1987), p. 254.
[34]A. Perelomova, "A small-signal sound speed and parameter of non-linearity B/A in a ternary mixture. Examples on calculations of mixture consisting of air, water and water vapour," Acta Acust. Acust. **91**, 809–816 (2005).
[35]V. S. Gratchev, Y. A. Zaverchnev, A. D. Ivanov, I. A. Mironov, and A. V. Rodnov, "Experimental study of the influence of turbulence and nebulosity on sonic boom," Technical Report, ONERA (incomplete French translation of a Soviet report in Russian without reference) (1966).
[36]G. B. Whitham, "The flow pattern of a supersonic projectile," Commun. Pure Appl. Math. **5**, 301–348 (1952).
[37]A. Loubeau and F. Coulouvrat, "Effects of meteorological variability on sonic boom propagation from hypersonic aircraft," AIAA J. **47**, 2632–2641 (2009).
[38]F. Coulouvrat, "A quasi exact shock fitting algorithm for general nonlinear progressive waves," Wave Motion **49**, 97–107 (2009).
[39]J. D. Leatherwood, B. M. Sullivan, K. P. Shepherd, D. A. McCurdy, and S. A. Brown, "Summary of recent NASA studies of human response to sonic booms," J. Acoust. Soc. Am. **111**, 586–598 (2002).
[40]CHABA, "Community Response to High-Energy Impulsive Sounds: An Assessment of the Field Since 1981," *Committee on Hearing, Bioacoustics and Biomechanics (CHABA)* (National Academy Press, Washington, DC, 1996), pp. 20–21.

AIP | Applied Physics Letters

Low power sessile droplets actuation via modulated surface acoustic waves

Michael Baudoin, Philippe Brunet, Olivier Bou Matar, and Etienne Herth

Citation: Appl. Phys. Lett. **100**, 154102 (2012); doi: 10.1063/1.3701725
View online: http://dx.doi.org/10.1063/1.3701725
View Table of Contents: http://apl.aip.org/resource/1/APPLAB/v100/i15
Published by the American Institute of Physics.

Low power sessile droplets actuation via modulated surface acoustic waves

Michael Baudoin,[1,a)] Philippe Brunet,[2] Olivier Bou Matar,[1] and Etienne Herth[1]
[1]*International Associated Laboratory LEMAC, IEMN, UMR CNRS 8520, Université des Sciences et Technologies de Lille and EC Lille, 59652 Villeneuve dAscq Cédex, France*
[2]*Laboratoire MSC, UMR 75057, 10 rue Alice Domon et Léonie Duquet, 75205 Paris, France*

(Received 20 January 2012; accepted 15 March 2012; published online 9 April 2012)

Low power actuation of sessile droplets is of primary interest for portable or hybrid lab-on-a-chip and harmless manipulation of biofluids. In this paper, we show that the acoustic power required to move or deform droplets via surface acoustic waves can be substantially reduced through the forcing of the drops inertio-capillary modes of vibrations. Indeed, harmonic, superharmonic, and subharmonic (parametric) excitation of these modes are observed when the high frequency acoustic signal (19.5 MHz) is modulated around Rayleigh-Lamb inertio-capillary frequencies. This resonant behavior results in larger oscillations and quicker motion of the drops than in the non-modulated case. © *2012 American Institute of Physics*. [http://dx.doi.org/10.1063/1.3701725]

One of the challenges in droplet microfluidics is to overcome surface capillary forces and contact line retention forces, which prevent the motion and deformation of the drop.[1] Different techniques such as electrowetting,[2] optical toolbox[3] based on thermocapillary forces induced by a focused laser, or ultrasonic surface acoustic waves (SAW) have been developed to perform simple operations on droplets. In particular, SAW are efficient to achieve actuation, atomization, jetting, oscillations, or mixing of small quantities of liquid, either lying on a solid substrate or entrapped in confined geometries.[4] However, due to nonlinear coupling between thermal and acoustical mode, SAW can induce quick temperature increase in fluid samples.[5,6] This can be detrimental for the manipulation of biofluids (albumin coagulates in a few seconds when excited by SAW), or for hybrid SPR (surface plasmon resonance)/SAW lab-on-a chip[7] (substrate heating causes a shift in SPR reflectivity). To enhance the droplet response, particular attention has been devoted to the design of the actuators[8] and to the chemical treatment of the surface[9] to reduce hysteresis and modify the contact angle. However, less effort has been dedicated to the optimization of the acoustic signal in relation to the natural frequencies of the drop. Rayleigh in 1879 (Ref. 10) and Lamb in 1932 (Ref. 11) have identified oscillation modes resulting from a competition between inertia and surface tension. While these have been first described for levitating drops, they can also be adapted to sessile drops. In this case, the droplet vibration is affected by the wettability of the surface[12] and the pinning of the contact line.[13]

These low-frequency oscillations (typically from 10 to 200 Hz for millimeter-sized drops) are observed when a drop lying on a solid substrate is subjected to sinusoidal SAW of much higher frequency (about 20 MHz).[14,15] The free surface deformation results from nonlinear acoustic forces (acoustic radiation pressure and acoustic streaming bulk force), while the detailed mechanism of excitation of these modes has not been elucidated yet. The acoustic radiation pressure induces a stress at the surface of the drop, while acoustic streaming induces internal flow, which can also contribute to the droplet deformation. The respective magnitudes of these two force fields depend on the properties of the acoustic field inside the drop and thus on the frequency of excitation, the size of the drop, and the acoustic attenuation length.[15,16]

In this paper, we show that modulations of the acoustic signal around Rayleigh-Lamb characteristic frequency and twice this frequency result, respectively, in harmonic and parametric response. This latter was predicted theoretically by Papoular and Parayre for levitating drops,[17] but not observed experimentally. This resonant behavior leads to higher amplitude drop oscillations compared to the non-modulated case at same input acoustic power. We also show that these oscillations promote droplets mobility.

SAW are generated at the surface of a 1.05 mm thick piezoelectric substrate (X-cut niobate lithium $LiNbO_3$) by a transducer consisting of interdigitated fingers, Fig. 1. These fingers are designed with the following process: (1) A titanium (Ti) layer of 20 nm and a gold (Au) layer of 200 nm are successively sputtered on a $LiNbO_3$ substrate, (2) the substrate is coated with AZnlof2020 resist, which is patterned by conventional photolithography technique, (3) the Au/Ti layers are successively wet-etched by potassium iodide (KI) and hydrofluoric acid (HF 50%), and (4) AZnlof2020 is removed by acetone. The width of the fingers and their distance are both equal to 43.75 μm, leading to a characteristic frequency of 19.5 MHz, which is used as the carrier

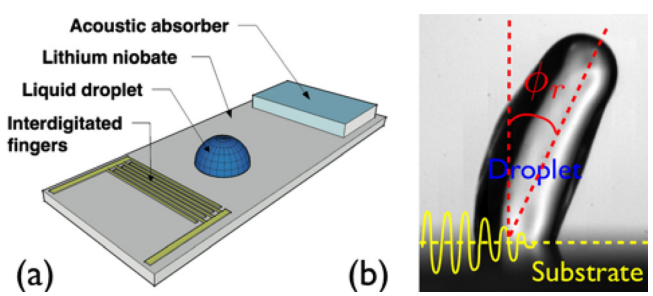

FIG. 1. (a) Sketch of the experimental setup. (b) Drop undergoing large deformation along the acoustic wave refraction angle ϕ_r.

[a)]Electronic mail: michael.baudoin@univ-lille1.fr.

frequency f_c. A periodic sinusoidal voltage is applied at this frequency with a high frequency generator (IFR 2023A) and amplified with a home made amplifier. This carrier signal is modulated by a square wave switching between 1 and 0, at frequency $f_m \ll f_c$. The amplitude d of the SAW is measured with a Mach-Zender laser interferometer (BMI-SH130). The surface of the substrate is treated with hydrophobic coating (monolayer of OTS) leading to advancing and receding contact angles of $\theta_a = 108^\circ$ and $\theta_r = 99^\circ$, respectively, measured with a Kruss DSA100 goniometer. A 7.5 μl droplet of water is then placed on the substrate (a sensitivity analysis of the droplet response according to its volume has been conducted in Ref. 15). The droplet dynamics is observed via a high speed camera (Photron SA3) and recorded at 2000 frames per second. To avoid pollution of the surface by impurities and to obtain reproducible results, all the experiments have been carried out in our laboratory class 1000 clean room.

At rest, the drop remains essentially hemispherical, since its radius ($R \sim 1.5$ mm) does not exceed the capillary length ($l_c \sim 2.5$ mm for water at room temperature) and thus surface tension overcomes gravity. The acoustic energy transmitted to the fluid induces zonal drop oscillations, of degree $l = 2$ (in spherical-harmonics basis), and a tilt of the drop to the right, as shown in Fig. 2. This left-right asymmetry is due to the asymmetry of the acoustic field, which is radiated in the drop according to a refraction angle $\phi_r \approx 25^\circ$ given by Snell-Descartes law, see Fig. 1. When the drop is sufficiently tilted for the rear and front contact angles to exceed their hysteretic value, one additionally observes drop motion. The vertical amplitude Δh and frequency f_r of oscillation depend on both f_m and d, see Fig. 3. According to these parameters, either a harmonic response at frequency $f_r = f_m$, a subharmonic response at $f_r = 1/2 f_m$, or a superharmonic response at $f_r = 2 f_m$ is observed (see also accompanying movies in the supplemental material[18]).

Harmonic region: Shift of resonance. In the blue area of Fig. 3, a peak of response is obtained when f_m reaches the inertio-capillary characteristic frequency f_o, which can be estimated from Rayleigh formula: $f_o = (8\gamma/3\pi\rho V)^{1/2} \approx 89$ Hz for the dipolar ($l = 2$) oscillation of a 7.5 μl droplet, with γ the surface tension and V the droplet volume. At intermediate power ($d = 1.10$ nm and $d = 1.38$ nm), the peak is asymmetric, with a skewness directed to low frequencies and the resonance frequency decreases with the amplitude of oscillation. This response is typical of an *anharmonic* oscillator with softening spring ($\beta < 0$)

$$\ddot{x} + 2\lambda\dot{x} + \omega_o^2 x + \alpha x^2 + \beta x^3 = F\cos(\Omega t), \qquad (1)$$

where x is the dynamic variable (here the deformation of the drop), t the time, λ the damping coefficient, $\omega_o = 2\pi f_o$ the angular eigen frequency, α and β two nonlinearity coefficients, F the amplitude of excitation, and Ω the excitation frequency. Such nonlinear behavior has already been reported by Perez *et al.*[19] for levitating drops larger than the capillary length and more recently by Miyamoto *et al.*[20] for sessile droplets smaller than the capillary length, with pinned contact line. These authors determine the coefficient appearing in Eq. (1) from experiments and compare the frequency response of the drop to theoretical predictions. In our system, the oscillation damping is due to dissipation in the viscous boundary layer and in the neighborhood of the contact line.[21] The nonlinear response of droplets appears when they undergo finite-amplitude deformations,[22,23] leading to a shift of the resonance frequency to lower frequencies as the amplitude of oscillation increases. For sessile drop, additional nonlinearity results from the up-down asymmetry of boundaries and the presence of a contact line.

Superharmonic region: Combination of modes. In the green region of Fig. 3, low f_m and large Δh, the drop response is a combination of harmonic and superharmonic modes. Indeed, the drop is pushed by the acoustic wave when the signal is on. Then, the drop keeps bouncing in the period with no forcing (signal is off) and oscillates a whole cycle before the next push. After a transient phase, this synchronization of forced and natural bouncing results in large drop oscillations.

Subharmonic region: Parametric resonance. In the red region of Fig. 3, the droplet responds at $f_m/2$. This subharmonic response appears only above a threshold: $d \geq 1.42$ nm, with a frequency window broadening progressively with the amplitude of oscillation Δh. This is typical of a so-called *Arnold Tongue*. Furthermore, the amplitude of the subharmonic response at fixed f_m is independent of the amplitude of

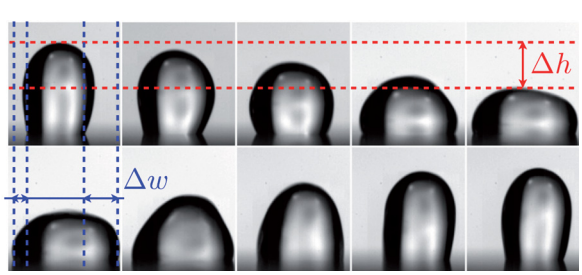

FIG. 2. Dipolar (degree $l = 2$) zonal oscillations of a drop of 7.5 μl subjected to a SAW of carrier frequency $f_c = 19.5$ MHz, modulation frequency $f_m = 52.5$ Hz, and amplitude $d = 1.38$ nm. The time elapsed between two successive snapshots is 2 ms. Δh and Δw are, respectively, the longitudinal and lateral amplitude of oscillation.

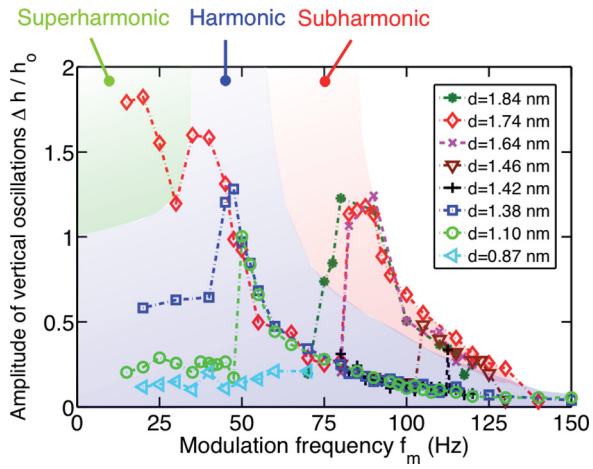

FIG. 3. Amplitude of vertical oscillations of the drop Δh divided by the initial height of the droplet h_o as a function of the modulation frequency f_m for different amplitudes d of the surface acoustic wave. In the green, blue, and red region, the droplet response is, respectively, superharmonic, harmonic, and subharmonic (compared to the frequency of modulation).

excitation d. All of these properties are characteristic of parametric resonance. Parametric instability of an oscillator is enabled when its characteristic frequency ω_o is modulated in time near $2\omega_o$.[24] It can be modeled with a Mathieu equation

$$\ddot{x} + 2\lambda\dot{x} + \omega_o^2[1 + A\cos(2\omega_o + \epsilon)t]x = 0. \quad (2)$$

with $\epsilon \ll \omega_o$. Such Mathieu equation can be obtained when an anharmonic oscillator described by Eq. (1) is excited near $2\omega_o$, $\Omega = 2\omega_o + \epsilon$.[25] Indeed, from the asymptotic expansion of the variable x in Eq. (1) $x = x_1 + x_2$, with x_1 the solution of the harmonic oscillator and $x_2 \ll x_1$, we obtain at second order

$$\ddot{x_2} + 2\lambda\dot{x_2} + \omega_o^2\left[1 - \frac{2\alpha F}{3w_o^4}\cos(2\omega_o + \epsilon)t + \ldots\right] = 0. \quad (3)$$

The parametric excitation of *zonal* oscillation modes was predicted theoretically by Papoular and Parayre[17] for levitating drops, but not observed experimentally. Indeed, parametric resonance appears for anharmonic oscillators above an amplitude threshold $F_t = 6\lambda\omega_o^3/|\alpha|$, which decreases with the nonlinearity coefficient α. This latter is related to the asymmetry of the oscillator stiffness for prolate and oblate deformation ($x < 0$ or $x > 0$), which is increased by the presence of the substrate. Thus, the observation of the parametric response in the present experiments could be explained by a larger nonlinearity of the system and larger excitations than in the system of Papoular and Parayre.

The parametric mode appears after a transient phase, as shown in the spatio-temporal diagram on Fig. 4. At first, the droplet oscillates at the same frequency as the excitation $f_m = 100$ Hz between t = 0 and 0.15 s. Between t = 0.15 and t = 0.32 s, the parametric instability grows. Finally, the droplet reaches a stationary regime of oscillation at half the frequency of modulation $f_r = 1/2f_m$. Between initial harmonic and later parametric response, the amplitude of droplet lateral oscillations Δw is increased by a factor of 4.8. This large increase of Δw comes along with an increase of the droplet

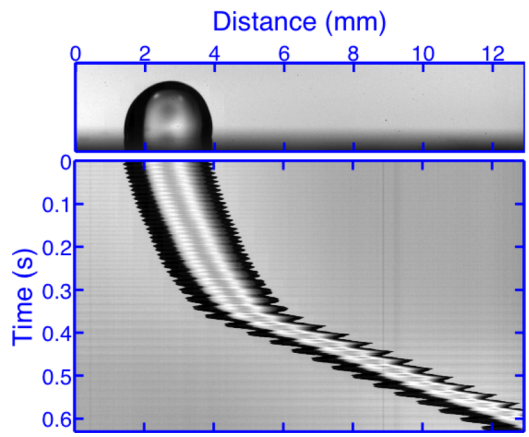

FIG. 4. Evolution of a 7.5 μl droplet excited by an acoustic wave of amplitude $d = 1.55$ nm and modulation frequency $f_m = 100$ Hz. The top picture shows the initial shape of the drop. The spatio-temporal diagram below is obtained by taking the base line of the drop (dashed blue line on top picture) and showing its evolution as a function of time. The average slope of the front or rear curve delimiting the drop gives the velocity of the drop.

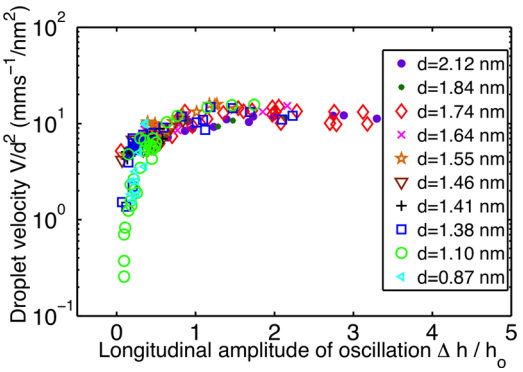

FIG. 5. Velocity of the drop divided by the square of the surface acoustic wave amplitude d^2 (corresponding to the acoustic power radiated into the drop up to a prefactor) as a function of the longitudinal amplitude of oscillation $\Delta h/h_o$. Each marker corresponds to a specific amplitude d.

velocity by a factor of 4, see the rupture of slope at t = 0.35 s in Fig. 4.

In all the previously described experiments, there is indeed a correlation between the droplets velocity V and their amplitude of oscillation $\Delta h/h_o$, see Fig. 5. Indeed, the drop velocity divided by the applied acoustic power collapse into a single curve, which increases with the amplitude of oscillation up to $\Delta h/h_o = 1$, and then reaches a plateau. From this figure, we can conclude that (1) the droplet velocity is basically proportional to the surface acoustic wave power and (2) that droplets oscillations promote their mobility.

Indeed, the velocity of a drop is determined by the equilibrium between the driving forces and the retention forces. The motion is due to the contact angle difference between the front and rear interfaces and thus to the asymmetry of the drop, see e.g., Ref. 21. An increase of the acoustic wave amplitude d naturally leads to larger droplet deformations and, therefore, larger asymmetry and velocities of the drop. The signal modulation does not affect the acoustic power. Nevertheless, it can affect both the driving and retention forces into different ways. First, it is important to mention that while some authors, see e.g., Ref. 26, have observed a decrease of the hysteresis of the contact line due to its continuous depinning, such variations are not observed in the present study and cannot explain the increase of drop velocity. Second, as seen previously, the droplet *static* shape is not much affected by gravity, since the droplet radius is smaller than the capillary length. However, when the drop is highly stretched with a left/right asymmetry component (see e.g., Fig. 1(b)), gravity plays a significant role during the retraction phase. The drop is not simply pulled back by capillary forces but also the upper part of the liquid drop falls vertically by gravity (see accompanying movie "superharmonic" in supplemental material[18]): this strengthens even further the left/right asymmetry and should contribute to the drop motion. Finally, the acoustic energy transferred to the drop and the retention force depend, respectively, on the contact surface with the substrate and the perimeter of the contact line. Thus, a stretching of the drop contributes to a reduction of the retention force but also a reduction of the amount of energy transferred to the drop. This might explain the existence of the plateau region in Fig. 5. To conclude, we can compare the velocities obtained

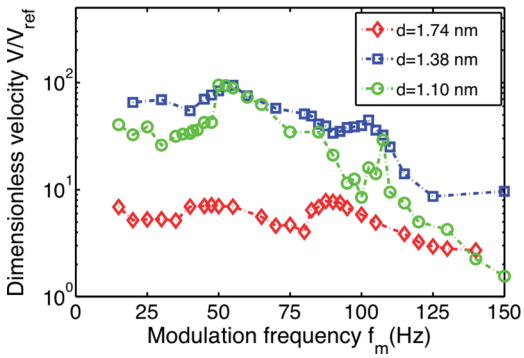

FIG. 6. Velocity of the drop V measured with a modulated signal divided by a reference velocity V_{ref} obtained at same acoustic power when the modulation is turned off, as a function of the modulation frequency f_m.

with and without signal modulation at same acoustic power (see Fig. 6 and accompanying movies in the supplemental material[18]). The drop velocity can be increased by a factor 100 thanks to the modulation.

In this paper, we have shown that inertio-capillary modes of oscillations can be excited either directly or parametrically by modulating the acoustic signal around once or twice the Rayleigh-Lamb characteristic frequency. This modulation introduces an original way to decrease the acoustic power required to stir inside, to stretch, or to move a sessile droplet with SAWs. Compared to the non-modulated case, the minimum acoustic power required to move a droplet at a non-zero speed, and a speed of 5 mm s^{-1} are reduced by a factor of 2 and 3, respectively, while the minimum power required to stretch the droplet vertically by a factor $\Delta h/h_o$ of 0.2 and 1 are reduced by a factor 5 and 3, respectively. This is especially important for the harmless manipulations of biofluids, which could be damaged by the temperature increase due to the dissipation of acoustic energy. It is also of primary interest for portable lab-on-a-chip, which requires low power consumption.

[1]H. Stone, A. Stroock, and A. Adjari, Ann. Rev. Fluid Mech. **36**, 381 (2004).
[2]M. Pollack, R. Fair, and A. Shenderov, Appl. Phys. Lett. **77**, 1725 (2000).
[3]C. Baroud, M. Robert de Saint Vincent, and J. Delville, Lab Chip **7**, 1029 (2007).
[4]J. Friend and L. Yeo, Rev. Mod. Phys. **83**, 647 (2011).
[5]J. Kondoh, N. Shimizu, Y. Matsui, M. Sugimoto, and S. Shiokawa, Sens. Actuators, A **149**, 292 (2009).
[6]D. Beyssen, Ph.D. dissertation, Université Henri Poincaré, 2006.
[7]A. Renaudin, V. Chabot, E. Grondin, V. Aimez, and P. Charette, Lab Chip **10**, 111 (2010).
[8]M. Tan, J. Friend, and L. Yeo, Phys. Rev. Lett. **103**, 024501 (2009).
[9]A. Wixforth, Superlattices Microstruct. **33**, 389 (2003).
[10]J. Rayleigh, Proc. R. Soc. London **29**, 71 (1879).
[11]H. Lamb, *Hydrodynamics* (Cambridge University Press, England, 1932).
[12]M. Strani and F. Sabetta, J. Fluid Mech. **141**, 233 (1984).
[13]X. Noblin, A. Buguin, and F. Brochard-Wyart, Eur. Phys. J. E **14**, 395 (2004).
[14]S. Yamakita, Y. Matsui, and S. Shiokawa, Jpn. J. Appl. Phys., Part 1 **38**, 3127 (1999).
[15]P. Brunet, M. Baudoin, O. Matar, and F. Zoueshtiagh, Phys. Rev. E **81**, 036315 (2010).
[16]S. Alzuaga, J. Manceau, and F. Bastien, J. Sound Vib. **282**, 151 (2005).
[17]M. Papoular and C. Parayre, Phys. Rev. Lett. **78**, 2120 (1997).
[18]See supplementary material at http://dx.doi.org/10.1063/1.3701725 for movies showing subharmonic, harmonic, and superharmonic response of a drop excited with a modulated signal and an additional movie showing the response of a drop at same acoustic power but without modulation.
[19]M. Perez, L. Salvo, M. Suéry, Y. Bréchet, and M. Papoular, Phys. Rev. E **61**, 2669 (2000).
[20]K. Miyamoto, S. Nagamoto, Y. Matsui, and S. Shiokawa, Jpn. J. Appl. Phys., Part 1 **41**, 3465 (2002).
[21]D. Bonn, J. Eggers, J. Indekeu, J. Meunier, and E. Rolley, Rev. Mod. Phys. **81**, 739 (2009).
[22]R. Tsamopoulos and R. Brown, J. Fluid Mech. **127**, 519 (1983).
[23]W. Smith, J. Fluid Mech. **654**, 141 (2010).
[24]M. Faraday, Philos. Trans. R. Soc. London **121**, 299 (1831).
[25]L. Landau and E. M. Lifshitz, *Course of theoretical Physics, Mechanics* (Pergamon, New York, 1959).
[26]E. Decker and S. Garoff, Langmuir **12**, 2100 (1996).

Airway reopening through catastrophic events in a hierarchical network

Michael Baudoin[a,b], Yu Song[a], Paul Manneville[a], and Charles N. Baroud[a,1]

[a]Laboratoire d'Hydrodynamique (LadHyX) and Department of Mechanics, École Polytechnique, Centre National de la Recherche Scientifique (CNRS), 91128 Palaiseau, France; and [b]Institut d'Electronique de Microélectronique et de Nanotechnologie (IEMN), Université des Sciences et Technologies de Lille, UMR CNRS 8520, 59652 Villeneuve d'Ascq, France

Edited by William R. Schowalter, Princeton University, Princeton, NJ, and approved November 27, 2012 (received for review July 9, 2012)

When you reach with your straw for the final drops of a milkshake, the liquid forms a train of plugs that flow slowly initially because of the high viscosity. They then suddenly rupture and are replaced with a rapid airflow with the characteristic slurping sound. Trains of liquid plugs also are observed in complex geometries, such as porous media during petroleum extraction, in microfluidic two-phase flows, or in flows in the pulmonary airway tree under pathological conditions. The dynamics of rupture events in these geometries play the dominant role in the spatial distribution of the flow and in determining how much of the medium remains occluded. Here we show that the flow of a train of plugs in a straight channel is always unstable to breaking through a cascade of ruptures. Collective effects considerably modify the rupture dynamics of plug trains: Interactions among nearest neighbors take place through the wetting films and slow down the cascade, whereas global interactions, through the total resistance to flow of the train, accelerate the dynamics after each plug rupture. In a branching tree of microchannels, similar cascades occur along paths that connect the input to a particular output. This divides the initial tree into several independent subnetworks, which then evolve independently of one another. The spatiotemporal distribution of the cascades is random, owing to strong sensitivity to the plug divisions at the bifurcations.

microfluidics | respiratory flow

The motion of liquid plugs through a connected network of channels may involve many degrees of freedom evolving via a similarly large number of interactions: each immiscible interface introduces a degree of freedom into the problem owing to its ability to deform and to move, whereas each connecting branch between different areas introduces an interaction path that allows the flow in one region to influence the behavior in other areas of the network. The resulting flow pattern determines, among other things, how water or oil is extracted from porous media (1–3), the imbibition of paper (4, 5), and the stability of flow in a microfluidic device (6, 7).

Liquid–gas two-phase flows also occur in the pulmonary airway tree, which is constantly coated with a thin liquid film. When the thickness of this film increases beyond some limit, plugs of liquid may form (8, 9) and therefore occlude the flow of air to the distal branches. Evidence of such behavior has been observed in pathologies ranging from asthma (10, 11) to cystic fibrosis (12). Furthermore, liquid plugs may be used as means to deliver medical treatment into the lung, e.g., in surfactant replacement therapy (13), and these plugs were observed to go through complex divisions, breaking and reforming before reaching their intended target (14).

The structure of the lung as a branching binary tree has motivated many studies on the motion of gas–liquid flows into bifurcating channels (15–20), with numerical work also taking into account the elasticity of the pulmonary walls, (e.g refs. 21 and 22). However, nearly all the model experiments and simulations have considered the simplest situations, either studying the motion of a single liquid plug or gas finger or concentrating on the flow through a single bifurcation, or both. This reduces the number of independent degrees of freedom and, by the same token, the range of behaviors those models can explore.

These studies therefore cannot account for complex interactions that involve many levels in the tree, which are observed in the real lung. Indeed, experiments on animal lungs have shown that multilevel interactions are primordial during the reinflation of a collapsed lung. Alencar et al. (23, 24) reported that reopening takes place through an avalanche of events in which distinct regions are reopened in nearly singular bursts. However, ex vivo observations of the spatial behavior during reinflation are prohibitively complex, therefore limiting the comparison between the experiments and the theoretical models to measurements at the root of the tree (25).

Here we study the flow and rupture of liquid plugs that initially occlude microfluidic channels, as they are submitted to an imposed pressure head. Our experiments are conducted in microfluidic systems consisting of a straight channel or a branching network of channels, formed in a polydimethylsiloxane (PDMS) substrate using conventional soft lithography techniques. We show that the dynamics of a train of plugs differ from those of a single occlusion because the plugs interact via both short- and long-range mechanisms. The physics underlying plug interactions are first deduced from the reopening of a single straight channel, by comparing experimental measurements with the results of a one-dimensional analytical model. Experiments in a branching tree are then performed, showing the existence of cascades of ruptures that occur along well-defined paths through purely hydrodynamic effects.

Collective Behavior of Plugs in a Straight Channel

Single-Plug Behavior. When a single plug of length L_0 is pushed at constant pressure in a channel of width w and height h, it rapidly reaches a velocity V_0 that depends on its initial resistance to flow. In its wake, it leaves a liquid film that remains at rest on the channel wall. This implies a shortening of the plug, which ruptures when its length $L(t)$ reaches zero. The airway then is opened in the sense that the flow of air becomes limited only by the viscous resistance of the gas. An example of such behavior is shown in Fig. 1, which displays snapshots of the experiment, taken at constant time intervals (see also Movie S1). The positions of the rear and front interfaces in each frame are located and interpolated to form two curves whose horizontal distance gives the length $L(t)$ of the plug. The velocity $V(t)$ is given by the slope of the curve for the rear interface. In this experiment, the velocity of the plug varies from 3 cm/s when the pressure head is applied to 28 cm/s when the plug ruptures. This acceleration generates an increase of the thickness of the liquid film left behind the plug and a subsequent rapid decrease of its length, leading to rupture after 24 ms.

Author contributions: M.B., P.M., and C.N.B. designed research; M.B. and Y.S. performed research; M.B. and C.N.B. analyzed data; and M.B., P.M., and C.N.B. wrote the paper.

The authors declare no conflict of interest.

This article is a PNAS Direct Submission.

[1]To whom correspondence should be addressed. E-mail: baroud@ladhyx.polytechnique.fr.

This article contains supporting information online at www.pnas.org/lookup/suppl/doi:10.1073/pnas.1211706110/-/DCSupplemental.

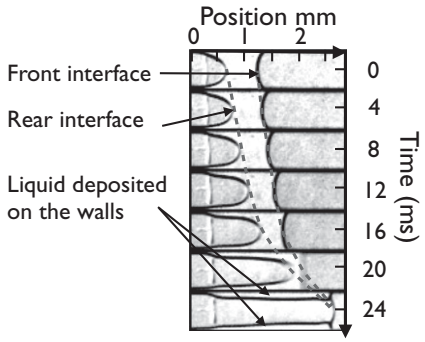

Fig. 1. Spatiotemporal evolution of a single plug of initial length $L_0 = 740$ μm pushed at constant pressure head 2 kPa. The montage is produced by stacking snapshots of the channel taken every 4 ms on top of one another. The liquid appears bright and the air dark. The dashed lines show the positions of the front and rear interfaces as functions of time.

The dynamics of this plug can be understood by introducing an Ohm-like law for the pressure vs. velocity (18, 26), $\Delta P = RV$, where ΔP is the pressure head. The velocity V of the rear interface is a measure of the flow rate, and R is the resistance due to the presence of the liquid in the channel. This resistance is the sum of capillary contributions R^{f} and R^{r} of the front ("f") and rear ("r") interfaces, and a bulk viscous resistance R^{v}. Resistances R^{f} and R^{r} are a result of the deformation of the two interfaces from their rest shape in response to the large velocity gradients in the corners of the moving liquid bridge, and they depend nonlinearly on V. At low capillary number $\mathrm{Ca} = \mu V/\sigma$, where μ is the viscosity of the liquid and σ its surface tension, one gets $R^{\mathrm{f,r}} = F^{\mathrm{f,r}}(h,w)\mathrm{Ca}^{-1/3}$. The explicit expressions of F^{f} and F^{r} are obtained, respectively, from the Hoffman–Tanner law (27, 28) and the Bretherton law (29) adapted to rectangular channels (30). In turn, the bulk resistance of a long-enough plug can be estimated by modeling the flow inside it as a Poiseuille flow in a rectangular channel: $R^{\mathrm{v}} \approx 12\mu L/h^2$ for large aspect ratio w/h (31). The relation between pressure head and speed has been validated experimentally by Ody et al. (18).

The model describing the plug dynamics is closed with an equation for $L(t)$ that accounts for the liquid left in the stationary films on the sidewalls. Bretherton's law (29) provides a way to estimate this thickness for flow at small Ca in circular tubes. We rely for this on the empirical law proposed by Aussillous and Quéré (32) for circular tubes, as extended to channels of rectangular cross-section and larger Ca by de Lózar et al. (33), which we introduce in the mass balance equation for the liquid phase: Let $S = wh$ be the area of the channel cross-section and S^{r} and S^{f} the areas of the lumens open to air behind the plug and ahead of it, respectively. During a time interval $\mathrm{d}t$, the advancing plug absorbs a volume $(S - S^{\mathrm{f}})V\mathrm{d}t$ at its front interface, where V is the velocity. The volume left behind is $(S - S^{\mathrm{r}})V\mathrm{d}t$ and the variation of the plug's volume is $S\mathrm{d}L$, so the balance reads $S\frac{\mathrm{d}}{\mathrm{d}t}L = [S^{\mathrm{r}} - S^{\mathrm{f}}]V$.

Whereas S^{r} is a function of V as recalled above, S^{f} reflects the thickness of the film present ahead of the plug at the considered time. In particular, $S^{\mathrm{f}} \equiv S$ when the plug is moving along a dry channel. Details on the model, its derivation, and its numerical simulation are given in *SI Text*.

The dynamics of a single plug therefore may be understood with the model ingredients described above: When the pressure ΔP is applied, the plug starts moving at a velocity fixed by its initial length and physical parameters. The length then progressively decreases because of liquid deposition, thus lowering the viscous resistance R^{v} so that the plug accelerates. The interfacial resistance scales as $V^{-1/3}$ and therefore also decreases, contributing further to the velocity increase. Finally, when the length of the plug approaches zero, it ruptures. A similar behavior has been observed by Fujioka et al. (34) through direct numerical simulations of the flow field inside a moving plug.

Multiple-Plug Behavior. The evolution of a set of $N = 5$ plugs, forced at constant pressure head 2 kPa, is depicted in the spatiotemporal graph of Fig. 2*A* (see also Movie S2). The plugs are initially distributed as shown in the top image and start advancing when the pressure head is applied at $t = 0$. Plugs are numbered from right to left, beginning with the most advanced one. The distance d_k between the rear interface of plug k and the rear interface of plug $k+1$ remains nearly constant because the air compressibility is negligible at these pressures. As a consequence, all plugs move at the same velocity $V(t)$ and the behavior of the plug train may be characterized by a single capillary number, which is plotted in Fig. 2*A*, *Right*. We observe that Ca stays constant up until $t \simeq 180$ ms, then increases up to the time when plug 1 ruptures at $t \simeq 400$ ms, then more irregularly until $t \simeq 630$ ms (rupture of plug 2), and finally diverges around $t \simeq 800$ ms, when plugs 3–5 break nearly simultaneously.

Examination of this cascade leads us to identify two plug interaction mechanisms: *Long range* effects arise from the superpositions of resistances within the plug train, whereas *short range* interactions take place between nearest neighbors via the wetting film. Indeed, plug k gains some fluid left behind by plug $k-1$ and leaves some fluid, which is taken up by plug $k+1$. Because the film thickness depends on the instantaneous capillary number (see *SI Text* for discussion), the balance between the liquid intake and deposition generates plug length variations when the two layers have different thicknesses. When the train of plugs is forced at a constant velocity—for example, by using a syringe pump—the thickness of the liquid films between the plugs remains constant, so the plugs (except plug 1) always lose as much liquid as they gain and thus keep their initial length. When the plugs are pushed at constant pressure, as in Fig. 2, their velocity changes, leading to

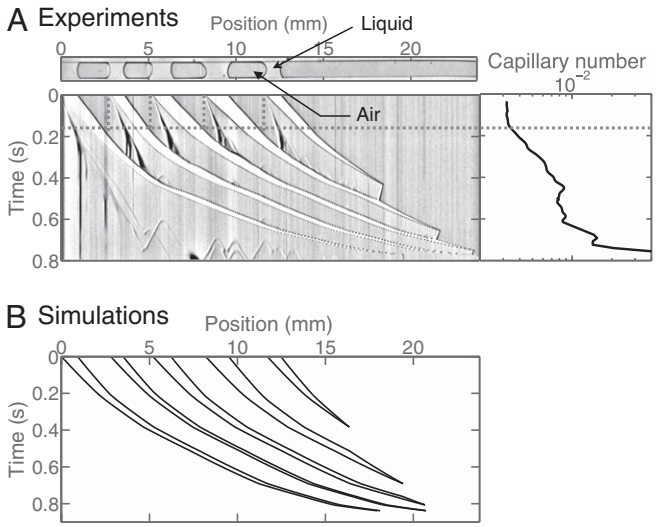

Fig. 2. Dynamics of a set of equally spaced monodisperse plugs. The initial length of the plugs is $L_{k,0} = 800$ μm, and the distance separating two adjacent plugs is $d_k \simeq 2$ mm. The whole train is pushed at constant pressure head 2.0 kPa. (*A*) Image corresponding to the experiment. (*Upper*) Initial plug configuration; liquid (air) appears light (dark) gray. (*Lower*) Spatiotemporal diagram displaying the gray values along the center line of the channel as a function of time. Velocities and lengths of the plugs are obtained from the slopes of the boundaries and the distances between them, respectively. The gray dashed line indicates the moment when the plugs reach the initial position of their immediate predecessor. (*Right*) Capillary number of the plug train as a function of time. (*B*) Spatiotemporal diagram obtained numerically from the model for the same conditions as in *A*.

variations in the film thickness. These variations couple back with the resistance to flow and velocities in two ways, as discussed below.

First, the resistance R^f associated with the displacement of the front interface decreases as the thickness of the precursor film increases. This has been demonstrated experimentally (26) and justified theoretically (35) for a single plug in a prewetted channel. In our experiment, the thickness of the film left behind a plug may display large changes, as seen in Fig. 1, which generates resistance variations for the following plug. In a train of plugs, the capillary number of a plug affects the next one with a delay equal to the time required to cover the distance that separates them. So when plug k arrives at the position initially occupied by plug $k-1$, it encounters a thicker film that decreases the resistance of its front interface and leads to an increase in velocity. This sudden acceleration is observed at $t \simeq 180$ ms, as marked by the dotted horizontal line in Fig. 2*A*. The second way in which neighboring plugs interact is via the mass balance. Like the lubrication effect, this takes place with a delay because the plugs are traveling at finite speed. Liquid exchange tends to lengthen the cascade duration because the fluid taken up by a plug increases its length. The two short-range effects therefore are antagonistic.

Using an analogy with electrical circuits, the train of plugs submitted to a constant pressure head ΔP may be viewed as a series of resistors and the total resistance as the sum of the individual resistances. Therefore, rupture of plug k leads to long-range effects because it corresponds to a sudden drop to zero of the corresponding resistance. Consequently, the speed of the remaining plugs suddenly increases, further hastening the deposition of the wetting film and inducing new ruptures. This catastrophic speeding-up is at the origin of the cascade observed in our experiments. It is easier to observe when the initial distribution of plugs is irregular and their size polydisperse. An example is shown in Fig. S1, in which a train of 10 plugs is pushed at constant pressure head (see also Movie S3). The evolution of the train is dominated mainly by short-range interactions until $t = 300$ ms (dotted line), when three plugs break nearly simultaneously. The velocity of the remaining plugs then displays a large increase, and the subsequent ruptures take place within shorter and shorter time intervals, with all the remaining plugs broken between $t \simeq 320$ ms and $t \simeq 370$ ms. The rapid variation of the velocity points to the finite-time singularity nature of the cascade.

Model and Simulations. Because at a given time all plugs move at the same speed, interactions between plugs may be treated by generalizing the equation for a single plug to a series of plugs: $\Delta P = \sum_{k=1}^{N} R_k V$, where R_k is the resistance ascribed to plug k. The lubricating role of the wetting film thickness is taken into account by expressing the front interface resistance R_k^f as a function of the cross-sectional area $S(x,t)$ of the lumen open to air ahead of plug k. This area is given by $S(x_k + L_k, t)$, which is determined by the history of the previous plugs $k-1, k-2, \ldots$ The surface in front of plug 1 is just $S(x > x_1 + L_1) = wh$. The fluid distribution in the channel then may be computed as a function of time, once the conservation of liquid is expressed. For each plug, we get $\frac{d}{dt} L_k = -[1 - S(x_k)/S(x_k + L_k)]V$. The area $S(x_k)$ of the lumen behind plug k then serves as an input in the computation for plug $k+1$. Plug rupture takes place when $L_k = 0$ and is accounted for by setting $R_k = 0$. The positions of the plugs may be obtained by integrating the velocity V, as discussed in *SI Text*.

The results of the model are shown in the bottom panels of Fig. 2 (monodisperse) and in Fig. S1 (polydisperse). In both cases, the motion of the plugs and the order of plug ruptures are reproduced correctly. Quantitative predictions from the model were compared with results from experiments with trains made of one to seven plugs. Two quantities were measured: (*i*) the time t_c required for complete reopening of the airway (all plugs have ruptured), called "cascade duration," and (*ii*) the penetration length L_c, which is the distance between the initial position of plug 1 and its position when it breaks, also indicating the necessary channel length for a cascade to be observed. Results are presented in Fig. 3, in which each square marks a single run. (The simulation derivation is supported by Figs. S2–S6 and the physical parameters are listed in Tables S1 and S2.)

The solid line corresponds to the predictions obtained with the full model, which takes into account all the processes described above. In contrast, the dash/dotted lines in Fig. 3 *A* and *B* show the predictions when short-range effects are neglected, i.e., when the

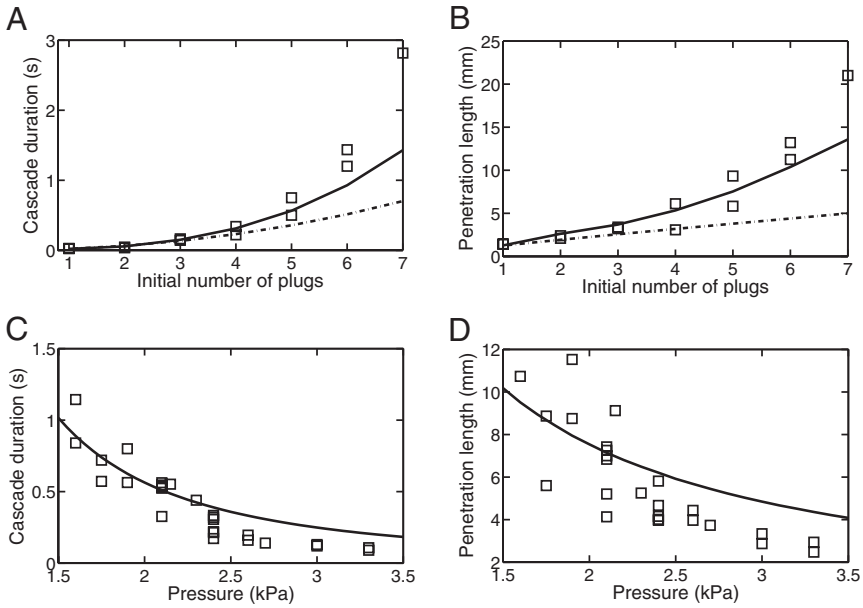

Fig. 3. Evolution of the cascade duration (*A* and *C*) and the penetration length (*B* and *D*) as functions of the number of plugs (*A* and *B*) and applied pressure (*C* and *D*) for a set of monodisperse plugs of length 0.78 mm separated by 2.1 mm. In *A* and *B*, the pressure head is 2.0 kPa. Squares correspond to experiments, solid lines to the full model, and dash/dotted curves to predictions from the model without plug interactions.

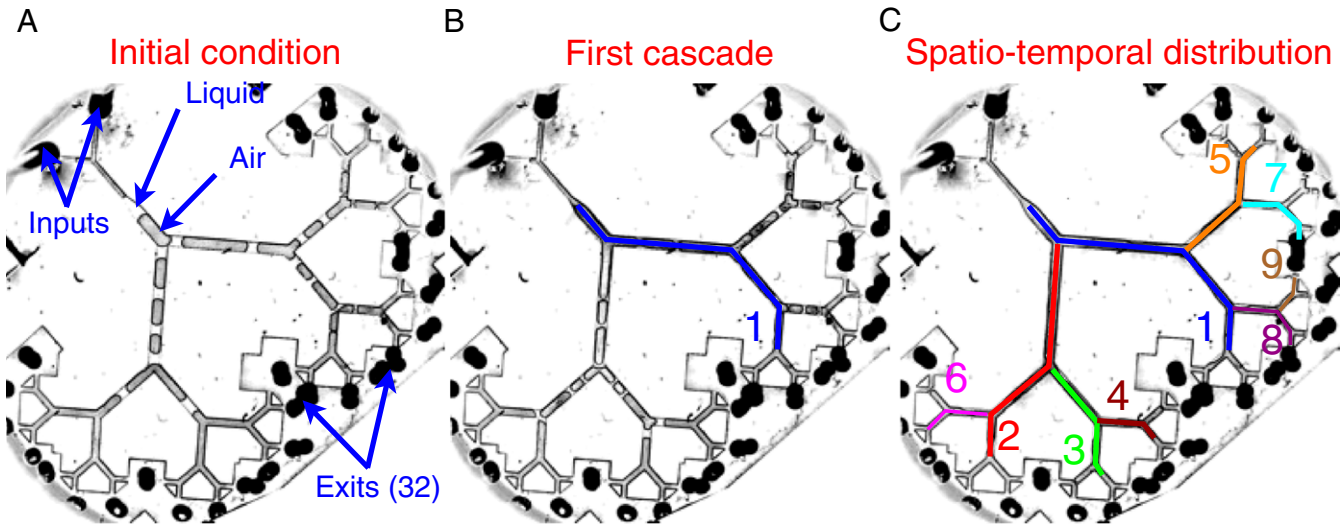

Fig. 4. Initial distribution of plugs and spatial distribution of successive airway reopenings obtained by pushing an initial set of liquid plugs by $\Delta P = 3.5$ kPa in a six-generation network. A given path is "open" when all the plugs obstructing the airflow from the entrance to the exit have ruptured. (*A*) Initial plug distribution in the network. (*B*) The path taken by the first cascade. (*C*) Spatio temporal distribution of successive cascades. Paths are numbered according to the order in which they reopen.

resistances of all plugs are just summed as if each of them were alone in the channel: $\Delta P = NR_sV$, with N the total number of plugs and R_s the resistance of an isolated plug. When the interactions are neglected, the cascade duration and the penetration length are grossly underestimated and the discrepancy increases with the number of plugs, stressing the role of liquid exchange between plugs. This shows that the interactions play a dominant role in the dynamics of the train, increasing the quantities of interest by a large factor. The experiments were repeated to measure the cascade duration and penetration length as functions of the imposed pressure head; the results are shown in Fig. 3 *C* and *D*. The model agrees quantitatively with the experiments at low pressures, but discrepancies appear above 2.5 kPa. This departure is attributed to the fact that the theoretical expressions used for interface resistances are valid only at low capillary numbers. Although individual resistances are not sufficiently well estimated during the fastest part of the cascade, the model still may serve as a good basis for predicting the cascade duration and penetration lengths in straight rectangular channels.

Cascade of Plug Ruptures in a Bifurcating Network

When considering an initially occluded tree structure, such as the pulmonary airway, the processes described above must be adapted to account for geometric effects: the division of plugs at bifurcations and the interactions across different regions in the network (19). This has been studied in a series of reopening experiments performed by replacing the straight channel with a six-generation tree network, as shown in Fig. 4. The widths of the channels in successive generations are chosen according to the diameter ratio in Weibel's symmetric model of the human lung (36), i.e., $w_{i+1}/w_i = 2^{-1/3}$, where w_i is the width of channels in generation i and $w_1 = 720$ μm. The height of channels is 45 μm everywhere.

The same protocol as for the straight channels is used. The experiment begins by alternately injecting liquid and air into the root channel to form seven successive plugs that are distributed into the tree. Indeed, each plug splits into two daughters when it reaches a bifurcation in the branching tree, thus distributing the liquid into all regions of the network (19, 20). Although the sequence of pressures during the plug formation is computer controlled and kept unchanged for all runs, slight perturbations affect the plug divisions at each run. The initial distributions therefore differ slightly from one experiment to the next despite the network symmetry.

A typical experiment is shown in Fig. 4 (see also Movie S4). Once the initial plug distribution is installed (Fig. 4*A*), after waiting sufficient time to make sure the system is at rest, a high pressure head (3.5–5.5 kPa) is applied at the root, whereas the exits of the network are maintained at atmospheric pressure. The flow rate in each path is determined by the pressure difference, which is equilibrated by the sum of the resistances through each branch of the path. The small differences in initial distribution of plugs lead to variations in flow rates among paths, which then are amplified as the liquid plugs make their way in the network. Ultimately, one path reopens through a cascade of plug ruptures (Fig. 4*B*).

This first cascade is followed by several others, each opening a different path, as shown in Fig. 4*C*, in which the numbers indicate the order in which cascades occur. The spatial distribution of the cascades is irregular; they may take place either in adjacent paths (e.g., 3 and 4) or in well-separated paths (e.g., 4 and 5). Each cascade divides the network into independent subnetworks that evolve separately from the rest.

The pressure driving each subnetwork may be inferred by considering the airflow in the reopened path. Because the pressures P_{in} at the root and P_{out} at the exit are fixed, the flow of air that takes place in the reopened path determines the intermediate values of the pressure along the path. A typical situation is shown in Fig. 5, in which the last five generations of the network are displayed before and just after reopening of path A. The whole subnetwork

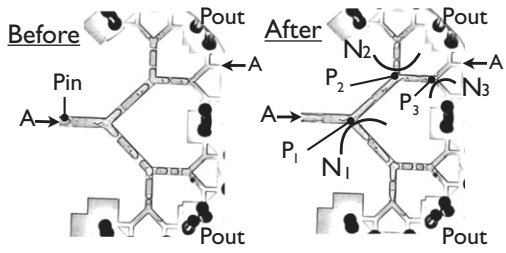

Fig. 5. Snapshots taken before and after the reopening of path A, corresponding to the first cascade in the network. P_{in} and P_{out} are the pressures at the entrance and exit of the tree. P_1, P_2, and P_3 indicate the intermediate pressures at the first, second, and third nodes after reopening, with $P_1 > P_2 > P_3$.

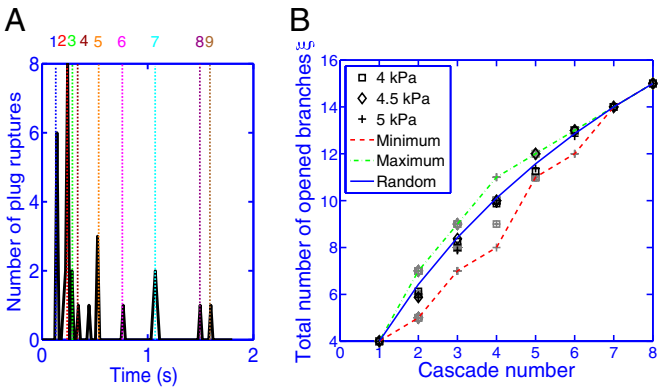

Fig. 6. (*A*) Histogram of the number of plug ruptures as a function of time for the same experiment as in Fig. 4. The dotted line numbering corresponds to the cascades identified on the image. (*B*) Total number ξ of opened branches (in which air can flow freely) measured after each cascade. The black symbols show the variations of ξ obtained experimentally for the driving pressures shown in the legend by averaging results over eight experiments for each pressure. The gray symbols correspond to individual experiments. The curves connect maximum (dash/dotted green) and minimum (dashed red) values of ξ observed and the average predicted value for supposedly random openings.

initially is driven at the common pressure P_{in}. However, once the cascade takes place along path A, the tree gets separated into three subnetworks, N1, N2, N3, driven at three intermediate values of the pressure, P_1, P_2, and P_3. The smaller the subnetwork, the lower the pressure head driving it. On the other hand, the smaller the subnetwork, the fewer plugs it contains, and hence the lower the resistance to flow. It therefore is not possible to predict the path that will be followed by the next cascade.

The readjustment of the driving pressure after each cascade leads to a delay of successive cascades in time. This is shown in Fig. 6*A*, which displays a histogram of individual plug ruptures plotted as a function of time. Ruptures are clustered in groups that correspond to each cascade, which we label using the same numbering scheme as in Fig. 4. The initial cascades develop when a large part of the network is still occluded and therefore involve many simultaneous plug ruptures. In contrast, later cascades involve fewer plugs and affect shorter paths of the tree. The time separating successive cascades, initially short, gradually increases in all experiments.

The spatial distribution of reopenings is characterized by introducing a quantity $\xi(N)$ that measures the cumulated number of branches, between the root and generation 4, that are reopened by cascades 1 to N (Fig. 6*B*). The first cascade always corresponds to $\xi(1)=4$, because all four generations are initially occluded. However, the evolution of ξ between successive cascades depends on the size of the reopened subnetwork and thus on the spatial distribution of successive reopenings. The minimum and maximum possible evolutions of $\xi(N)$, shown in Fig. 6*B*, may be calculated by simulating different reopening scenarios in the network. Alternatively, the evolution of $\xi(N)$ for a random distribution of reopenings is calculated numerically by performing a Monte Carlo simulation of the successive paths and taking the mean value of $\xi(N)$ for a large number of realizations.

Measurements of ξ were performed for three different driving pressures, 4.0, 4.5, and 5.0 kPa, by repeating each experiment eight times. The average value of $\xi(N)$ for the eight realizations is indistinguishable from the random prediction, as shown by the black symbols in Fig. 6*B*. The results for a particular experiment, however, may fall anywhere between the minimum and maximum values, as shown by the light-gray symbols. The value of ξ is statistically random over a set of runs.

This large difference between particular runs is a result of the complexity of fluid redistribution when a plug divides at a bifurcation. Indeed, the exact timing of the cascade with respect to the plug passage through a bifurcation may lead to two different outcomes: If the plug passes a bifurcation before the cascade takes place, it separates into two daughter plugs, one in each of the daughter branches, only one of which will rupture during the cascade (Fig. S2). Conversely, if the plug bursts before the division, the occluded subnetwork does not acquire an extra plug. Therefore, the resistance in the occluded subnetwork, and the time necessary to reopen it, may display large fluctuations between individual runs. Indeed, the timing of the cascades and the distribution of the liquid were found to display extreme sensitivity to the initial conditions, making the prediction of the cascade path impossible. On average, Fig. 6 shows that the behavior is indistinguishable from a random distribution.

Discussion

The geometry of the bifurcating tree introduces several modifications to the physical picture developed for the cascades in straight channels. First, the plug divisions at the successive bifurcations add a strong random component to the dynamics in the network, as described above. This greatly limits the ability to predict the cascade timing or path. Second, the model proposed for the straight channels is insufficient to describe the cascades in the network because the plugs in a given path of the network do not flow at the same velocity in all generations. Instead, the velocity of the plugs decreases with the generation number, because the cross-section increases. This means that plugs closer to the root have higher capillary numbers than those close to the exits, so the value of the resistance R_k of each plug depends on the generation number in which the plug is flowing.

The network's geometry also implies that the distance between plugs may vary in time, through two mechanisms: (*i*) Plugs that are in different generations get closer together as they advance into the network because those closer to the root of the network are traveling faster. (*ii*) The distances separating them may change if an air bubble, which separates two plugs, divides asymmetrically at a bifurcation. These mechanisms imply that the short-range interactions also become more complex in the network.

These modifications in plug distances and velocities imply that reopening the microfluidic network is more efficient when the plugs have not yet penetrated deep into the tree, particularly because the stabilizing short-range interactions play a smaller role in this case. Therefore, the strategy for reopening such a network should be to work at high driving pressures. When extrapolating this statement to the lung reopening, however, one should consider biological factors such as the effects of the shear stresses and pressure fluctuations on the epithelial cells, both during the motion of the plugs (37) and at the location of rupture (38). The magnitude of these efforts in vivo cannot be obtained from the current model.

Indeed, the relevance of our study to pulmonary airway reopening is limited in that we consider a highly idealized system. In contrast, the actual lung involves many supplementary mechanisms, such as surfactant (15, 39) or elastic interconnected airways (21, 40), in addition to being made up of rough tubes bifurcating asymmetrically. All these effects will complicate the behavior compared with what is observed here. For instance, surfactants will introduce several effects. They may retard the plug bursting compared with clean interfaces, as in the case of soap bubbles, but they also may enhance the liquid deposition on the walls (39), in addition to inducing deformations in the leading films that may increase the shear stress on the wall (37).

A more complete model must also include a description of airway deformation, which is particularly important because breathing takes place through the dilation of the diaphragm and rib cage, which induces a negative pressure that draws the air

into the lung. Because a plug's length and resistance are coupled with the cross-section of the tube containing it, an increase in tube diameter will reduce the resistance to flow, leading to faster cascades.

Nevertheless, our simple model has allowed us to identify some basic mechanisms that will remain important in real pulmonary flows. Indeed, the lung will still display the collective behavior that we have observed for a train of plugs, namely through local and global interactions, and the choice of a particular path in the network for each cascade. Only the quantitative details will be modified as more ingredients are added to the airway model but not the qualitative behavior.

Materials and Methods

Microfluidics and Observations. The microfluidic devices are prepared using dry-film soft lithography techniques (41). The channels are etched in PDMS and bonded on a PDMS-covered glass slide. Perfluorodecalin is used as the working fluid because of its good wetting properties (contact angle 23° with PDMS) and its compatibility with PDMS (42). The pressure at the network inlet and driving the liquid is imposed using a Fluigent MFCS-8C controller, which is programmed to achieve specific pressure sequences. The observations are performed through a stereomicroscope using a fast camera (Photron Fastcam 1024) filming at 1,000 frames per second. The image sequences then are analyzed using MatLab and ImageJ.

Experimental Protocol. A train of liquid plugs is created inside the channels by alternately pushing liquid and air slowly through a Y-junction (18). The Y-junction then leads to the experimental region, which consists of either a straight channel (rectangular cross-section of width $w = 700$ μm and height $h = 55$ μm) or a branching network. Once the plugs are created and placed, the pressure is set to zero for a few seconds to achieve a stationary initial condition, after which a constant pressure head ΔP is applied at the channel entrance of the channel. More details are given in *SI Materials and Methods*.

ACKNOWLEDGMENTS. The authors thank Tim Pedley for a careful reading of and comments on the manuscript. C.B. acknowledges early discussions of this work with Jihad Touma. This work was funded by the Agence Nationale de Recherche under the "Transport et Transfert via le Système Pulmonaire Humain" project (M.B.). The Fluigent corporation generously lent us the MFCS-8C pressure source.

1. Lenormand R, Zarcone C, Sarr A (1983) Mechanisms of the displacement of one fluid by another in a network of capillary ducts. *J Fluid Mech* 135:337–353.
2. Dias MM, Payatakes AC (1986) Network models for two-phase flow in porous media Part 1. Immiscible microdisplacement of non-wetting fluids. *J Fluid Mech* 164:305–336.
3. Stark J, Manga M (2000) The motion of long bubbles in a network of tubes. *Transp Porous Media* 40:201–218.
4. Davis SH, Hocking LM (1999) Spreading and imbibition of viscous liquid on a porous base. *Phys Fluids* 11:48–57.
5. Rost M, Laurson L, Dubé M, Alava M (2007) Fluctuations in fluid invasion into disordered media. *Phys Rev Lett* 98(5):054502.
6. Engl W, Roche M, Colin A, Panizza P, Ajdari A (2005) Droplet traffic at a simple junction at low capillary numbers. *Phys Rev Lett* 95(20):208304.
7. Champagne N, Vasseur R, Montourcy A, Bartolo D (2010) Traffic jams and intermittent flows in microfluidic networks. *Phys Rev Lett* 105(4):044502.
8. Duclaux V, Clanet C, Quéré D (2006) The effects of gravity on the capillary instability in tubes. *J Fluid Mech* 556(1):217–226.
9. Heil M, Hazel AL, Smith JA (2008) The mechanics of airway closure. *Respir Physiol Neurobiol* 163(1-3):214–221.
10. Wright SM, et al. (2000) Altered airway surfactant phospholipid composition and reduced lung function in asthma. *J Appl Physiol* 89(4):1283–1292.
11. Hohlfeld JM, et al. (2002) The role of surfactant in asthma. *Respir Res* 3(4):1–8.
12. Griese M, Birrer P, Demirsoy A (1997) Pulmonary surfactant in cystic fibrosis. *Eur Respir J* 10(9):1983–1988.
13. Engle WA; American Academy of Pediatrics Committee on Fetus and Newborn (2008) Surfactant-replacement therapy for respiratory distress in the preterm and term neonate. *Pediatrics* 121(2):419–432.
14. Cassidy KJ, et al. (2001) A rat lung model of instilled liquid transport in the pulmonary airways. *J Appl Physiol* 90(5):1955–1967.
15. Espinosa FF, Kamm RD (1999) Bolus dispersal through the lungs in surfactant replacement therapy. *J Appl Physiol* 86(1):391–410.
16. Cassidy KJ, Gavriely N, Grotberg JB (2001) Liquid plug flow in straight and bifurcating tubes. *J Biomech Eng* 123(6):580–589.
17. Zheng Y, Anderson JC, Suresh V, Grotberg JB (2005) Effect of gravity on liquid plug transport through an airway bifurcation model. *J Biomech Eng* 127(5):798–806.
18. Ody CP, Baroud CN, de Langre E (2007) Transport of wetting liquid plugs in bifurcating microfluidic channels. *J Colloid Interface Sci* 308(1):231–238.
19. Song Y, Manneville P, Baroud CN (2010) Local interactions and the global organization of a two-phase flow in a branching tree. *Phys Rev Lett* 105(13):134501.
20. Song Y, Baudoin M, Manneville P, Baroud CN (2011) The air-liquid flow in a microfluidic airway tree. *Med Eng Phys* 33(7):849–856.
21. Howell PD, Waters SL, Grotberg JB (2000) The propagation of a liquid bolus along a liquid-lined flexible tube. *J Fluid Mech* 406:309–335.
22. Grotberg JB, Jensen OE (2004) Biofluid mechanics in flexible tubes. *Annu Rev Fluid Mech* 36:121–147.
23. Alencar AM, Buldyrev SV, Majumdar A, Stanley HE, Suki B (2001) Avalanche dynamics of crackle sound in the lung. *Phys Rev Lett* 87(8):088101.
24. Alencar AM, et al. (2002) Physiology: Dynamic instabilities in the inflating lung. *Nature* 417(6891):809–811.
25. Majumdar A, et al. (2003) Fluid transport in branched structures with temporary closures: A model for quasistatic lung inflation. *Phys Rev E Stat Nonlin Soft Matter Phys* 67(3 Pt 1):031912.
26. Bico J, Quéré D (2001) Falling slugs. *J Colloid Interface Sci* 243(1):262–264.
27. Hoffman RL (1975) Study of advancing interface. A. Interface shape in liquid-gas systems. *J Colloid Interface Sci* 50(2):228–241.
28. Tanner LH (1979) Spreading of silicone oil drops on horizontal surfaces. *J. Phys. D* 12: 1473–1484.
29. Bretherton FP (1971) The motion of long bubbles in tubes. *J Fluid Mech* 10:166–188.
30. Hazel AL, Heil M (2002) The steady propagation of a semi-infinite bubble into a tube of elliptical or rectangular cross-section. *J Fluid Mech* 470:91–114.
31. White FM (1991) *Viscous Fluid Flow* (McGraw-Hill, New York), 2nd Ed.
32. Aussillous P, Quéré D (2000) Quick deposition of a fluid on the wall of a tube. *Phys Fluids* 12(10):2367–2371.
33. de Lózar A, Hazel AL, Juel A (2007) Scaling properties of coating flows in rectangular channels. *Phys Rev Lett* 99(23):234501.
34. Fujioka H, Takayama S, Grotberg JB (2008) Unsteady propagation of a liquid plug in a liquid-lined straight tube. *Phys Fluids* 20(6):062104.
35. Chebbi R (2003) Deformation of advancing gas-liquid interfaces in capillary tubes. *J Colloid Interface Sci* 265(1):166–173.
36. Weibel ER (1984) *The Pathway for Oxygen. Structure and Function in the Mammalian Respiratory System* (Harvard Univ Press, Cambridge, MA).
37. Fujioka H, Grotberg JB (2005) The steady propagation of a surfactant-laden liquid plug in a two-dimensional channel. *Phys Fluids* 17(8):082102.
38. Huh D, et al. (2007) Acoustically detectable cellular-level lung injury induced by fluid mechanical stresses in microfluidic airway systems. *Proc Natl Acad Sci USA* 104(48): 18886–18891.
39. Tavana H, et al. (2010) Dynamics of liquid plugs of buffer and surfactant solutions in a micro-engineered pulmonary airway model. *Langmuir* 26(5):3744–3752.
40. Halpern D, Naire S, Jensen OE, Gaver DP (2005) Unsteady bubble propagation in a flexible channel: Predictions of a viscous stick-slip instability. *J Fluid Mech* 528:53–86.
41. Stephan K, et al. (2007) Fast prototyping using a dry film photoresist: Microfabrication of soft-lithography masters for microfluidic structures. *J Micromech Microeng* 17(69–N):74.
42. Dangla R, Gallaire F, Baroud CN (2010) Microchannel deformations due to solvent-induced pdms swelling. *Lab Chip* 10(21):2032–2045.

Supporting Information

Baudoin et al. 10.1073/pnas.1211706110

SI Materials and Methods

The experiments were performed in microchannels made using standard soft lithography techniques. First, a mold was etched by depositing a dry-film photoresist on a glass slide and exposing it to a UV lamp through a photomask. The film then was developed in an aqueous solution of potassium to yield the negative of the channel design. This then constituted a mold over which polydimethylsiloxane was poured and allowed to polymerize. This microchannel was then cut out and bonded on another glass slide by passing the two surfaces in an oxygen plasma.

We used perfluorodecalin (PFD) to form the liquid plugs because of its good wetting properties (contact angle ~23°) and inertness. PFD is a fluorocarbon oil with viscosity $\mu = 5.1 \times 10^{-3}$ Pa·s and surface tension $\gamma = 19.3 \times 10^{-3}$ N/m. The plugs were separated by air bubbles. The fluids were controlled using either a water column, whose height determined the pressure head, or a programmable pressure controller (Fluigent MFCS-8C, generously lent by Fluigent S.A.), which provided precise and programmable pressure control.

The microchannel geometry presented a narrow Y-shaped junction (width = 200 μm) upstream of the test section (Fig. 5). This narrow region provided the ability to form liquid plugs reliably. The channel width then increased downstream of this junction, thus reducing the plug length equivalently. This geometry therefore provided better control of plug formation and length than using channels with constant width.

Experiments were recorded with a high-speed camera (Photron Fastcam 1024 PCI) through a stereomicroscope at 0.7× magnification. The resolution of the camera was 1,024 × 1,024 pixels, which yielded 1 pixel for 24.8 μm. The camera allowed image sequences to be captured at frame rates up to 1,000 images per second at full resolution. Image analysis was then performed using ImageJ software.

SI Model of Plug Motion and Rupture

In this section, we develop an analytical model to describe the motion of the gas–liquid train as the plugs change in size and eventually rupture in a straight channel. In this model, we ignore the effects of gravity and inertia by recalling that the Bond and Weber numbers are small. Moreover, because the experiments take place at small to moderate Reynolds and capillary numbers (Table S2), we limit ourselves to a minimal one-dimensional model that treats the plugs as discrete resistors. The aim, therefore, is not to describe the hydrodynamic behavior of our system in detail but to capture the essential mechanisms that lead to the cascade of ruptures.

As in the main text, we suppose that the total resistance to flow can be written as the sum of the resistances for individual plugs, which in turn can be separated into three contributions (1). The first one, R^{v}, is due to viscous dissipation in the bulk of the liquid; the other two correspond to capillary resistance at the front and rear interfaces, R^{f} and R^{r}, respectively. We also note that the fluid velocity V is nearly conserved at all locations in the channel. We therefore write the balance between driving pressure and resistance to flow as:

$$\Delta P = \sum_k R_k V = \sum_k \left[R_k^{\mathrm{v}} + R_k^{\mathrm{f}} + R_k^{\mathrm{r}}\right] V. \qquad \textbf{[S1]}$$

The theoretical description aims at estimating the different resistance terms and their coupling with the plug velocities. An event-driven model of the coupling yields the evolution in time of the velocities and resistances, as discussed in the main text.

Problem Formulation. We consider a train of N liquid plugs pushed at a constant pressure head ΔP in a straight rectangular microchannel of height h and width w. The variables, defined in Fig. S3, are the positions $x_k(t)$ of the plugs' rear interfaces (numbered from right to left, beginning with the most advanced one); their lengths $L_k(t)$; the radii $\varepsilon_k^{\mathrm{r}}(t)$ and $\varepsilon_k^{\mathrm{f}}(t)$ of their rear and front menisci; and the cross-sectional area $S(x,t)$ of the lumens open to air at position x between the plugs. This description of the meniscus shape introduces two effects in the one-dimensional model developed here. First, the radii ε^{f} and ε^{r} determine the location at which fluid is exchanged with the films on the walls. Second, the front–rear asymmetry between the two curvatures leads to an additional resistance to flow, as described below.

The plugs leave a liquid film on the walls, whose thickness is variable: we define the cross-sectional area open to air behind plug k as $S_k^{\mathrm{r}}(t) = S(x_k - \varepsilon_k^{\mathrm{r}}, t)$, whereas one has $S_k^{\mathrm{f}} = S(x_k + L_k + \varepsilon_k^{\mathrm{f}}, t)$ in front of the plug. The amount of liquid deposited on the wall behind each plug depends on its velocity V_k (2–4), defined as the speed of its rear interface, $V_k(t) = \mathrm{d}x_k(t)/\mathrm{d}t$. On the other hand, the plug velocities are related to the flow rate $Q(t)$ through $V_k(t) = Q(t)/S_k^{\mathrm{r}}(t)$.

The velocity of each plug may be different from its neighbors in principle, because they each can leave a film of different thickness. Nevertheless, experimental observations show that the plug velocities remain within less than 10% of one another for all experiments, as shown, for example, in Fig. S4 or observed in Figs. 2 and 3 in the main text. In the present model, the problem therefore is simplified by assuming that the plugs all travel at the same velocity $V(t)$, which comes to equating the thickness of the rear films. Therefore, we can simplify the notation by writing $S_k^{\mathrm{r}}(V_k) = S^{\mathrm{r}}(V)$.

Based on the parameters above, the dimensionless equations are obtained by introducing a characteristic length $\ell = \sqrt{wh}$, a characteristic pressure $\Delta P = 2\sigma/\ell$, and the viscocapillary timescale $\tau = \mu\ell/\sigma$. Using these definitions, the dimensionless speed of the plug train is just the capillary number $\mathrm{Ca} = \mu V/\sigma$. In the following text, variables with tildes indicate dimensionless quantities.

Evolution of plug lengths. The equation giving the variation of the plug length as a function of time is obtained by expressing a balance between the fluid collected from the previous plug and the fluid left behind. Let $S_0 = wh = \ell^2$, then, during a time interval δt the length of the plug changes by δL, the volume of the plug changes by $S_0 \delta L$, the fluid collected ahead is $(S_0 - S_k^{\mathrm{f}})V\delta t$, and the fluid left behind is $(S_0 - S^{\mathrm{r}}(V))V\delta t$; hence,

$$S_0 \delta L = \left(S_0 - S_k^{\mathrm{f}}\right) V \delta t - (S_0 - S^{\mathrm{r}}(V)) V \delta t. \qquad \textbf{[S2]}$$

After simplification, rewriting Eq. **S2** in dimensionless form yields

$$\frac{\mathrm{d}\tilde{L}_k}{\mathrm{d}\tilde{t}} = \left[\tilde{S}^{\mathrm{r}}(\mathrm{Ca}) - \tilde{S}_k^{\mathrm{f}}\left(\tilde{X}, \tilde{t}\right)\right] \mathrm{Ca}. \qquad \textbf{[S3]}$$

A relation between $\tilde{S}^{\mathrm{r}}$ and the capillary number Ca can be obtained by combining the scaling law proposed by Aussillous and Quéré (5) for the thickness of the liquid layer left behind a moving plug in a cylindrical channel and the empirical extension of this formula obtained by de Lózar et al. (6) for rectangular channels. By noting that $1 - \tilde{S}^{\mathrm{r}}$ is nothing but what they call the wet fraction, we obtain

$$\tilde{S}^{\mathrm{r}} = 1 - \frac{A + B\,\widehat{\mathrm{Ca}}^{2/3}}{1 + C\,\widehat{\mathrm{Ca}}^{2/3}}, \qquad \textbf{[S4]}$$

where A, B, and C are constants and

$$\widehat{\mathrm{Ca}} = \left[1 + 0.12(\alpha - 1) + 0.018(\alpha - 1)^2\right]\mathrm{Ca}$$

is an effective capillary number correcting for the departure of the aspect ratio $\alpha = w/h$ away from the square case $\alpha = 1$. The best fit with the experimental data displayed in figure 3 in ref. 6 for $\alpha = 12$ provides $A = 0.021$, $B = 3.4$, and $C = 5.2$ in the range of capillary numbers of interest.

The section of air in front of each plug $\tilde{S}_k^{\mathrm{f}}$ is obtained by keeping track of the amount of liquid left on the wall by the preceding plug.

Pressure balance and plug velocities. A second set of equations is obtained by equilibrating the driving pressure head with the pressure drops from viscous dissipation in the bulk of the liquid plugs $\Delta\tilde{P}_{\mathrm{v}}$ and at the successive liquid–air interfaces $\Delta\tilde{P}_{\mathrm{i}}$:

$$\Delta\tilde{P} = \Delta\tilde{P}_{\mathrm{v}} + \Delta\tilde{P}_{\mathrm{i}}. \qquad \textbf{[S5]}$$

The viscous pressure drop is obtained by recalling the pressure-flow rate relation for a single fluid flowing in a rectangular channel (7):

$$\Delta P_v = \frac{12\mu}{wh^3}QL, \qquad \textbf{[S6]}$$

where Q is the flow rate and L is the length of the plug. It is common to extend this formula to account for the viscous pressure drop in a train of plugs, when they are sufficiently long and sufficiently far apart, by summing the individual contributions (see, e.g., ref 1):

$$\Delta P_v = \sum_k \frac{12\mu}{wh^3}QL_k. \qquad \textbf{[S7]}$$

Recalling that $Q = S^{\mathrm{r}}V$, in dimensionless form Eq. **S7** reads:

$$\Delta\tilde{P}_{\mathrm{v}} = 6\ \mathrm{Ca}\ \tilde{S}^{\mathrm{r}}\alpha\sum_k \tilde{L}_k. \qquad \textbf{[S8]}$$

The interface pressure differences are the result of deformations of the interfaces away from their static shapes. Indeed, for plugs at rest, curvatures at the front and the rear compensate their effects, leading to a uniform pressure within each plug. When the plugs move, interfaces depart from their static shapes, which leads to pressure drop corrections at both the front and rear interfaces, $\Delta\tilde{P}_{\mathrm{i}}^{\mathrm{f}}$ and $\Delta\tilde{P}_{\mathrm{i}}^{\mathrm{r}}$, respectively:

$$\Delta\tilde{P}_{\mathrm{i}} = \Delta\tilde{P}_{\mathrm{i}}^{\mathrm{f}} + \Delta\tilde{P}_{\mathrm{i}}^{\mathrm{r}}. \qquad \textbf{[S9]}$$

Quantity $\Delta\tilde{P}_{\mathrm{i}}^{\mathrm{r}}$ can be estimated from the study of an air finger flowing in a channel, viewed as the tip of the following air bubble. The formula obtained by Bretherton (2), valid at low capillary numbers for a cylindrical tube, has been extended by Wong et al. (3) for a square channel, and more recently to the rectangular case by Hazel and Heil (4). By means of numerical simulations, these authors have shown that $\Delta P^{\mathrm{r}}(\alpha, \mathrm{Ca}) = f(\alpha)\Delta P^{\mathrm{r}}(\alpha = 1, \mathrm{Ca})$, tabulating $f(\alpha)$ for $\alpha \in [1, 2]$. It turns out that in this range, their data are well fitted by the expression $\alpha f(\alpha) = 1 + 0.52(\alpha - 1)$, that is, $f(\alpha) = 0.52 + 0.48/\alpha$. This expression is not surprising because the pressure difference should scale as the shear with, in a first approximation, additive contributions from the two directions, cross-stream in $1/h$ and spanwise in $1/w = 1/\alpha h$. Accordingly, we are confident that the extrapolation to our conditions $\alpha = 12.7$ is reliable.

On the other hand, Hazel and Heil have corrected the result of Wong et al. (3) for the finiteness of Ca. Their data for the dynamical contribution to ΔP in a square channel are in the form $D\mathrm{Ca}^{2/3}$, where D is a constant. Our fitting of their data in figure 8 of ref. 4, over the range $\mathrm{Ca} \in [10^{-3}, 0.3]$, yields $D = 4.1$. Turning to dimensionless quantities, we finally obtain

$$\Delta\tilde{P}_{\mathrm{i}}^{\mathrm{r}} = D\alpha^{1/2}f(\alpha)\mathrm{Ca}^{2/3}$$

[and $D\alpha^{1/2}f(\alpha) = 8.1$ for $\alpha = 12.7$]. Thus, for a set of N plugs moving at the same velocity, we obtain:

$$\Delta\tilde{P}_{\mathrm{i}}^{\mathrm{r}} = ND\alpha^{1/2}f(\alpha)\mathrm{Ca}^{2/3}. \qquad \textbf{[S10]}$$

Finally, as to the front interfaces, following Ody et al. (8) and assuming that the apparent dynamic contact angle θ^{a} of the front meniscus [as defined by Chebbi (9)] is the same in the two principal directions, the pressure jump at the front interface of a single plug can be computed from

$$\Delta P_{\mathrm{i}}^{\mathrm{f}} = \sigma\left[\frac{2}{w} + \frac{2}{h}\right](1 - \cos\theta^{\mathrm{a}}). \qquad \textbf{[S11]}$$

The apparent contact angles of each plug are not necessarily identical because the macroscopic films covering the channel wall ahead of them may be different. The dimensionless expression for the train of plugs then reads

$$\Delta\tilde{P}_{\mathrm{i}}^{\mathrm{f}} = \sum_k \frac{h + w}{\ell}(1 - \cos\theta_k^a). \qquad \textbf{[S12]}$$

The first plug moves on a dry substrate, with an apparent dynamic contact angle obtained from the Hoffman-Tanner law (10, 11):

$$\theta_1^a = E\mathrm{Ca}^{1/3}, \qquad \textbf{[S13]}$$

in which the constant E has been determined for PFD plugs moving in rectangular microchannels by Ody et al. (8) as $E = 4.9$. The following plugs move on a substrate that is prewetted by a macroscopic film. According to Chebbi (9), the apparent dynamic contact angle at the front of a plug advancing in a cylindrical tube of radius R over a fluid film of thickness e_∞ far away from the meniscus is given by

$$\tan\theta^{\mathrm{a}} = (3\mathrm{Ca})^{1/3}F\left((3\mathrm{Ca})^{-2/3}\tilde{e}\,\cos\theta^{\mathrm{a}}\right), \qquad \textbf{[S14]}$$

where

$$F(y) = \sum_{j=0}^{3} b_n[\log_{10} y]^n, \qquad \textbf{[S15]}$$

where $\tilde{e} = e_\infty/R$ and the b_n are tabulated in ref. 9; values rounded to two significant figures are given here for the reader's convenience: $b_0 = 1.4$, $b_1 = -0.59$, $b_2 = -3.2\times10^{-2}$, and $b_3 = 3.1\times10^{-3}$. To adapt this formula to our case, we estimate the relative fluid thickness $\tilde{e}$ as $(1 - \tilde{S}_k^{\mathrm{r}})^{1/2}$. Furthermore, because apparently no extension of this formula to the rectangular geometry exists, we introduce an empirical correction coefficient K so that in dimensionless form, we obtain

$$\tan\theta_k^{\mathrm{a}} = K(3\mathrm{Ca})^{1/3} F\left((3\mathrm{Ca})^{-2/3}\left(1-\tilde{S}_k^{\mathrm{f}}(\tilde{X},\tilde{t})^{1/2}\right)\cos\theta_k^{\mathrm{a}}\right). \quad \textbf{[S16]}$$

The coefficient K, the only quantity not directly extracted from the literature, has been fixed to adjust time scales in the simulations to those of the laboratory experiments. We find $K \simeq 1.3$.

Plug dynamics. The equations derived above allow us to solve the coupled problem of the plug lengths and liquid deposition, resistance to flow, and plug velocity. By inverting this system, one obtains the capillary number at each time and thus computes the positions of the plugs. The model therefore provides a closed set of equations used to predict the dynamics of a train of plugs pushed at constant pressure head.

Application. The formulation above now can be expanded to be solved numerically. Eqs. **S8** and **S10** allow us to write

$$R_{\mathrm{v}} = \frac{2\mu}{\ell}\left[6\tilde{S}^{\mathrm{r}} \;\alpha\sum_k \tilde{L}_k\right], \quad \textbf{[S17]}$$

$$R^{\mathrm{r}} = \frac{2\mu}{\ell} N D\alpha^{1/2} f(\alpha)\mathrm{Ca}^{-1/3}. \quad \textbf{[S18]}$$

At low capillary number, expanding Eqs. **S12** and **S16** at lowest order yields

$$\Delta\tilde{P}_{\mathrm{i}}^{\mathrm{f}} = \frac{h+w}{2\ell}\sum_k \theta_k^{\mathrm{a}2}, \quad \textbf{[S19]}$$

$$\theta_k^{\mathrm{a}} = K(3\mathrm{Ca})^{1/3} F\left((3\mathrm{Ca})^{-2/3}\left(1-\tilde{S}_k^{\mathrm{f}}(\tilde{X},\tilde{t})^{1/2}\right)\right), \quad \textbf{[S20]}$$

which leads to

$$R^{\mathrm{f}} = \frac{\mu}{\ell}\left[\frac{h+w}{\ell}\right]\mathrm{Ca}^{-1/3}\left[12+3^{2/3}K^2\sum_{k=2}^{N}F^2\left((3\mathrm{Ca})^{-2/3}\left(1-\tilde{S}_k^{\mathrm{f}}(\tilde{X},\tilde{t})^{1/2}\right)\right)\right]. \quad \textbf{[S21]}$$

Fig. S5 displays the predicted variation of the front interface resistance of a single plug moving in a prewetted channel as a function of the capillary number for different relative thicknesses of the macroscopic film ahead of the plug $\tilde{e}$. It shows that Eq. **S20**, which is the lowest-order approximation to Eq. **S16**, gives sufficiently accurate results in the range of capillary numbers of interest. Accordingly we may rely on Eq. **S21**, which both provides a better insight into the physics of the problem and is simpler to implement. The important phenomenon to be seen in Fig. S5 is the systematic decrease of the front interface resistance with $\tilde{e}$ for all values of the capillary number, which we call the "lubrication effect."

Finally, Fig. S6 shows the variation of the total interfacial resistance $R_{\mathrm{i}} = R_{\mathrm{i}}^{\mathrm{f}} + R_{\mathrm{i}}^{\mathrm{r}}$ of the first plug (dashed curve) and the following plugs (full lines) as a function of the capillary number Ca and the relative thickness of the liquid film $\tilde{e}$. A monotonic decrease of the interfacial resistance is observed when the capillary number increases for all values of $\tilde{e}$ between 10^{-1} and 10^{-5}, as well as for the dry substrate ($\tilde{e}=0$).

Physical Origin of the Cascade. Initially, a train of plugs is created by alternately pushing some air and some liquid in a Y-junction with low input pressure. The initial state therefore is a set of N plugs separated by air bubbles coated by a thin layer of liquid, with dry substrate ahead of the first plug. When a large pressure head ΔP is applied at the beginning of an experiment, all the liquid plugs leave a larger amount of liquid on the walls than what they may recover from the liquid film ahead of them. The amount of liquid left indeed increases with the capillary number, according to Eq. **S4**. This leads to a decrease in the plugs' length, Eq. **S3**, and thus of the viscous resistance, Eq. **S17**. Because $\Delta P = RV$ and the pressure head is constant, this resistance decrease induces an increase in the plug velocity. In turn, this velocity increase is exacerbated by the decrease in the interface resistance $R_{\mathrm{i}} = R_{\mathrm{i}}^{\mathrm{f}} + R_{\mathrm{i}}^{\mathrm{r}}$ (Fig. S6). Another phenomenon contributing to the reduction of the front interface resistance is the lubrication effect generated by the interplug liquid film. As its thickness increases with the plug velocity, a further reduction in the front interface resistance results (Fig. S5).

Finally, each plug rupture provokes a brutal decrease in the interfacial resistance due to the reduction in the number of interfaces, which locally thickens the prewetting film. This leads to a large acceleration of the plugs and thus to more and more plug ruptures.

Computation. The system of equations has been solved using an event-driven code: Between two plug ruptures, the system is solved by a finite difference method. Each time a rupture takes place, the interfacial resistance is updated. Owing to the large increase in the plug velocities, mesh refinement was performed to determine the time step between two computations and to maintain accuracy.

Input Parameters. Table S1 summarizes the parameters used in our simulations. Using the value of the capillary number shown in Fig. S4 for the capillary number, which corresponds to a maximum velocity of $V \simeq 4\times10^{-2}$ m/s, we obtain the estimates quoted in Table S2 for the dimensionless parameters of the problem.

1. Baroud CN, Gallaire F, Dangla R (2010) Dynamics of microfluidic droplets. *Lab Chip* 10 (16):2032–2045.
2. Bretherton FP (1971) The motion of long bubbles in tubes. *J Fluid Mech* 10(2):166–188.
3. Wong H, Radke CJ, Morris S (1995) The motion of long bubbles in polygonal capillaries. Part. 2. Drag, fluid pressure and fluid flow. *J Fluid Mech* 292:95–110.
4. Hazel AL, Heil M (2002) The steady propagation of a semi-infinite bubble into a tube of elliptical or rectangular cross-section. *J Fluid Mech* 470:91–114.
5. Aussillous P, Quéré D (2000) Quick deposition of a fluid on the wall of a tube. *Phys Fluids* 12(10):2367–2371.
6. de Lózar A, Hazel AL, Juel A (2007) Scaling properties of coating flows in rectangular channels. *Phys Rev Lett* 99(23):234501.
7. White FM (1991) *Viscous Fluid Flow* (McGraw-Hill, New York), 2nd Ed.
8. Ody CP, Baroud CN, de Langre E (2007) Transport of wetting liquid plugs in bifurcating microfluidic channels. *J Colloid Interface Sci* 308(1):231–238.
9. Chebbi R (2003) Deformation of advancing gas-liquid interfaces in capillary tubes. *J Colloid Interface Sci* 265(1):166–173.
10. Hoffman RL (1975) Study of advancing interface. A. Interface shape in liquid-gas systems. *J Colloid Interface Sci* 50(2):228–241.
11. Tanner LH (1979) Spreading of silicone oil drops on horizontal surfaces. *J. Phys. D* 12(9): 1473.

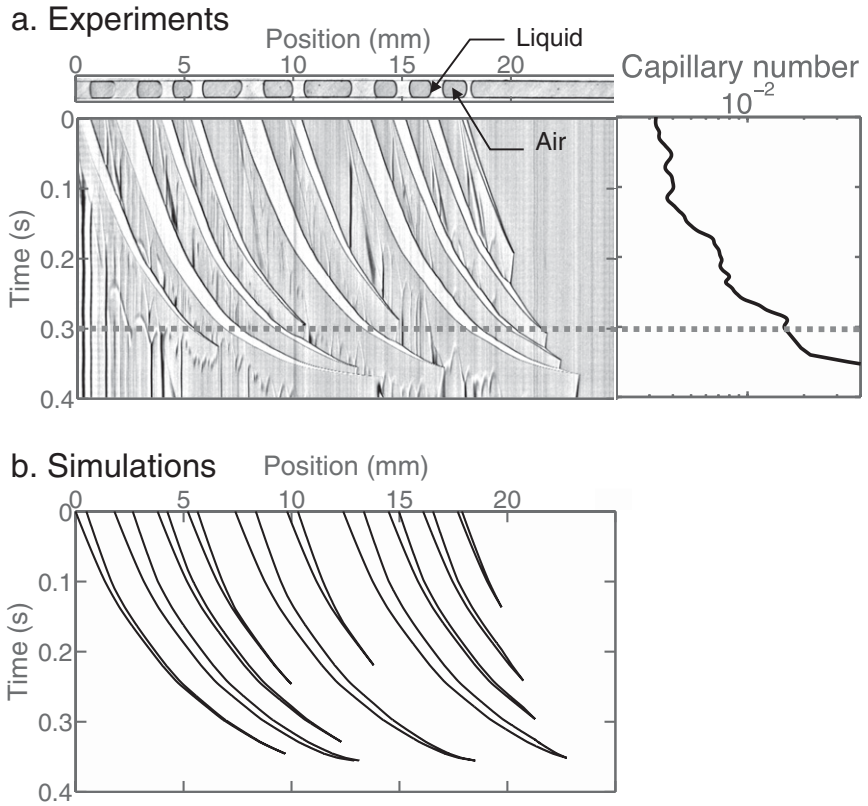

Fig. S1. Dynamics of a set of polydisperse plugs pushed at constant pressure head 4.8 kPa. (*A* and *B*) Plug positions as functions of time, experimental and simulated, respectively. The variation in the capillary number with time is given to the right of *A*, where the gray dashed line indicates the time when several plugs break almost simultaneously.

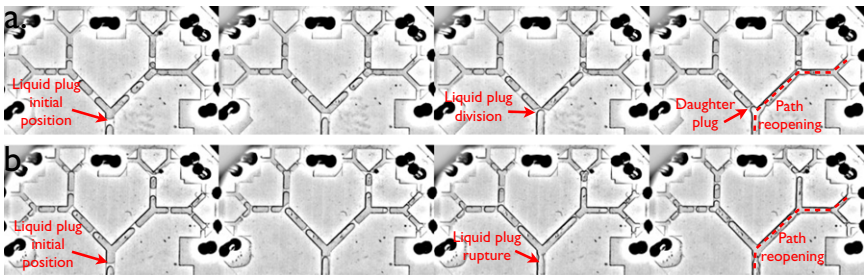

Fig. S2. Influence of bifurcations on the fluid redistribution in the network. (*A* and *B*) Two sequences show the evolution of plugs inside the last five generations of the network driven at a pressure head of 3.5 kPa with slightly different timing. In *A*, the liquid plug in the first generation divides before the cascade takes place; thus, only one of the daughter plugs is broken while the adjacent path is reinforced by the other daughter. In *B*, the plug ruptures before the bifurcation and the adjacent path remains weakened. The time separating the two images is 14 ms.

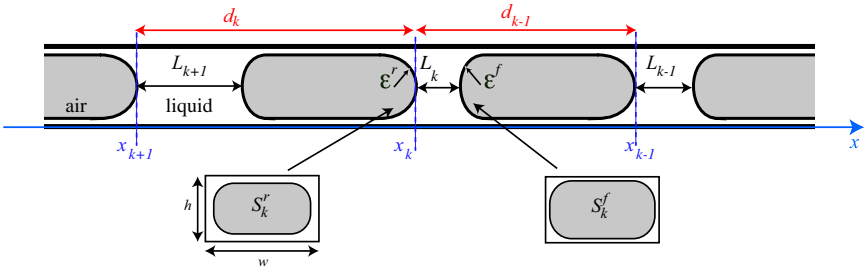

Fig. S3. Sketch of the problem, showing plug k surrounded by plugs $k-1$ and $k+1$. Liquid is shown in white and air in gray. The moving plugs (velocity $V_k = \mathrm{d}x_k/\mathrm{d}t$) leave a film behind them thicker than the film they encounter in front. The cross-sectional area open to air behind plug k (S_k^r) therefore may be different from the air surface in front (S_k^f). The wetting liquid forms menisci of radius ε^r at the rear and ε^f at the front.

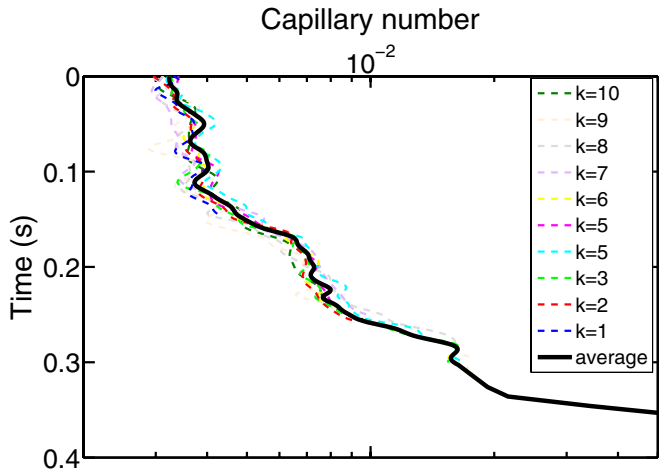

Fig. S4. Evolution of the capillary number $\mu V_k/\sigma$ associated with the rear interface of 10 plugs pushed at a constant pressure head 4.8 kPa. Each dashed line corresponds to the capillary number of a given plug k, and the plain line corresponds to the capillary averaged over all the plugs. This figure corresponds to Fig. 3 in the main text.

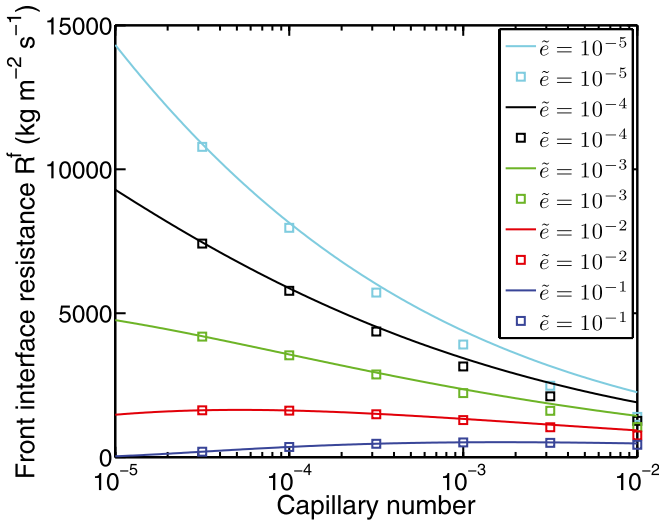

Fig. S5. Evolution of the front interface resistance of a plug moving in a prewetted channel as a function of the capillary number Ca for different values of the relative thickness of the macroscopic film preceding the plug ë. The squares correspond to solutions of the exact (Eq. **S16**) and the lines to its lowest-order expansion (Eq. **S20**).

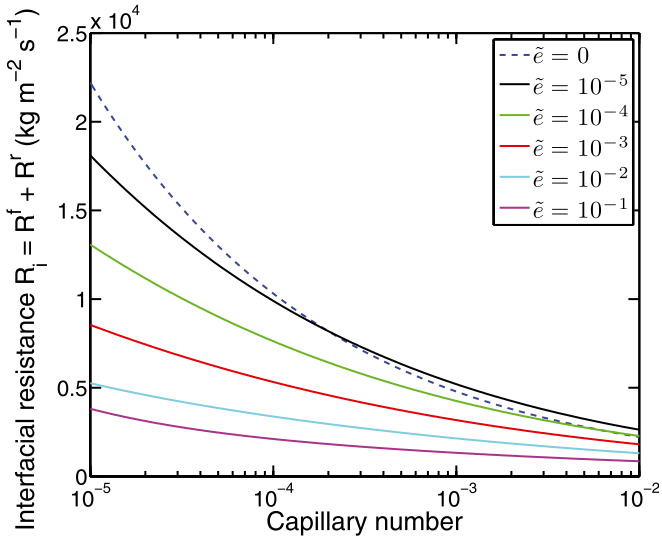

Fig. S6. Interfacial resistance $R_i = R_i^f + R_i^r$ of a single plug as a function of the capillary number Ca, moving on a substrate either dry (dashed line) or prewetted by a macroscopic film for different relative thicknesses $\tilde{e}$ (solid lines).

Table S1. Value of parameters used in our simulations

Parameter	Symbol	Value	Unit
Channel width	w	700	μm
Channel height	h	55	μm
Surface tension	σ	19.3×10^{-3}	N/m
Viscosity	μ	5.1×10^{-3}	kg/m·s^2
Density	ρ	2×10^3	kg/m^3

Table S2. Value of dimensionless parameters in the problem

Number	Formula	Maximum value
Re	$\rho V \ell / \mu$	10
Ca	$\mu V / \sigma$	10^{-2}
We	$\rho V^2 \ell / \sigma$	10^{-1}
Bo	$\rho g h^2 / \sigma$	0.2

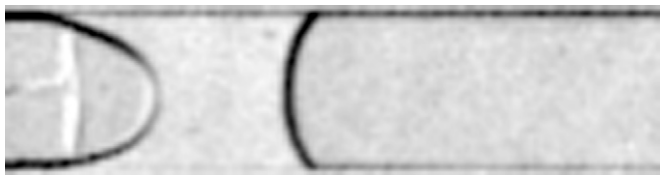

Movie S1. Evolution of a single plug of initial length $L_0 = 740$ μm pushed at constant pressure head 2 kPa. Time is slowed by a factor of 250. This movie illustrates Fig. 1 in the main text.

Movie S1

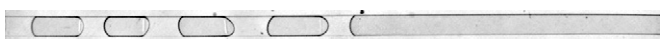

Movie S2. Dynamics of a set of equally spaced monodisperse plugs. The initial length of the plugs is $L_{k,0} = 780$ μm, and the distance separating two adjacent plugs is $d_k \simeq 2$ mm. The whole train is pushed at constant pressure head 2.0 kPa. Time is slowed by a factor of 10. This movie illustrates Fig. 2 in the main text.

Movie S2

Movie S3. Dynamics of a set of polydisperse plugs pushed at constant pressure head 4.8 kPa. Time is slowed by a factor of 10. This movie illustrates Fig. 3 in the main text.

Movie S3

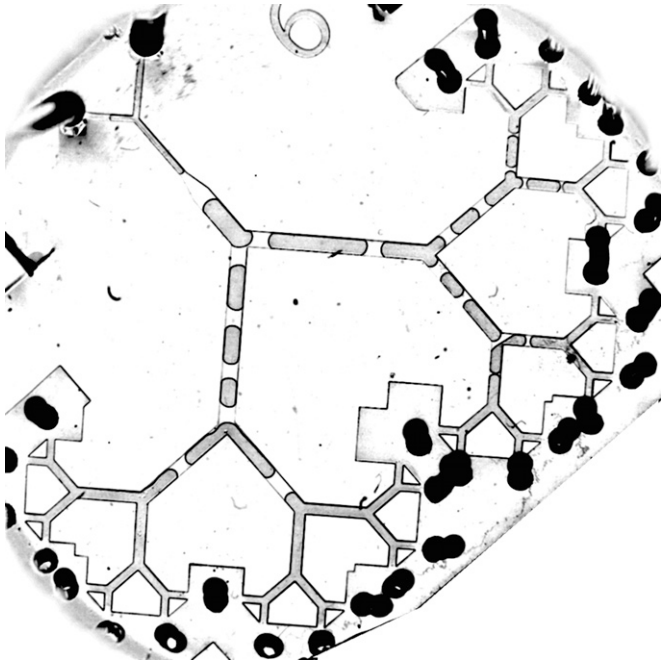

Movie S4. Dynamics of an initial set of liquid plugs pushed at a constant pressure head $\Delta P = 3.5$ kPa in a six-generation bifurcating network. Time is slowed by a factor of 10. This movie illustrates Fig. 5 in the main text.

Movie S4

PHYSICAL REVIEW E **90**, 013008 (2014)

Cyclones and attractive streaming generated by acoustical vortices

Antoine Riaud,[1,2] Michael Baudoin,[1,*] Jean-Louis Thomas,[2] and Olivier Bou Matar[1]

[1]*Institut d'Electronique, de Microélectronique et Nanotechnologie (IEMN), LIA LICS, Université Lille 1 and EC Lille, UMR CNRS 8520, 59652 Villeneuve d'Ascq, France*

[2]*CNRS UMR 7588, UPMC Université Paris 06, Institut des NanoSciences de Paris (INSP), F-75005 Paris, France*

(Received 17 December 2013; published 14 July 2014)

Acoustical and optical vortices have attracted great interest due to their ability to capture and manipulate particles with the use of radiation pressure. Here we show that acoustical vortices can also induce axial vortical flow reminiscent of cyclones, whose topology can be controlled by adjusting the properties of the acoustical beam. In confined geometry, the phase singularity enables generating "attractive streaming" with the flow directed toward the transducer. This opens perspectives for contactless vortical flow control.

DOI: 10.1103/PhysRevE.90.013008 PACS number(s): 47.15.G−, 43.25.Nm, 43.25.+y, 47.61.Ne

I. INTRODUCTION

Acoustic streaming, that is, vortical flow generated by sound, plays a fundamental role in a variety of industrial and medical applications such as sonochemical reactors [1], megasonic cleaning processes [2], ultrasonic processing [3], acoustophoresis [4], and therapeutic ultrasound [5,6]. More recently, acoustic streaming has been the subject of a burst of interest with the development of microfluidic applications [7,8]. For instance, it is at the core of the physics involved in droplet actuation with surface acoustic waves [9] for laboratory-on-a-chip facilities, providing a versatile tool for droplet displacement [10–12], atomization [13], jetting [14,15], or vibration [12,16,17]. Moreover, vorticity associated with acoustic streaming is the main phenomenon envisioned to ensure efficient mixing of liquids [18,19].

Different forms of streaming are generally distinguished according to the underlying physical mechanism [20,21]. *Boundary-layer-driven streaming* [22] arises when an acoustic wave impinges a fluid-solid interface due to viscous stresses inside the viscous boundary layer. This form of streaming can be divided into *inner streaming*, also called Schlichting streaming [23], occurring inside the viscous boundary layer, and counter-rotating *outer streaming*, outside it [24]. The former is not exclusive to acoustics since it does not require compressibility of the fluid, but only the relative vibration of a fluid and a solid. The latter, first enlightened by Lord Rayleigh, can be seen either as the fluid entrainment outside the boundary layer induced by Schlichting streaming or as a consequence of the tangential velocity continuity requirement for an acoustic wave at a fluid-solid boundary. Finally, *bulk streaming*, or so-called Eckart streaming [25], is due to the thermoviscous dissipation of acoustic waves and the resulting pseudomomentum transfer to the fluid [26,27]. Since the early work of Rayleigh [24], many studies have been dedicated to acoustic streaming and investigation of the influence of various phenomena on the resulting flow such as unsteady excitation [28–30], nonlinear acoustic-wave propagation [31,32], and high hydrodynamic Reynolds numbers [33,34]. However, in all these studies, only plane or focalized acoustical waves [35] are considered.

In this paper, we report on bulk acoustic streaming generated by specific solutions of the Helmholtz equation called *acoustical vortices*. New acoustic streaming configurations are obtained with cyclone-like flows, whose topology mainly depends on the one of the acoustical vortex. Flow streamlines are not only poloidal, as in classic bulk streaming [25], but also toroidal, due to the orbital momentum transfer. This special feature provides an acoustical control of the axial vorticity, while in all forms of acoustic streaming reported up to now, the topology of the induced hydrodynamical vortices is mainly determined by the boundary conditions. Finally, in confined geometries, the azimuthal vorticity can also be tailored by adjusting the properties of the acoustic beam. In this way, attractor and repeller hydrodynamic vortices, corresponding, respectively, to flow directed toward and away from the sound source, can be obtained.

II. THEORETICAL ANALYSIS

Acoustical vortices (or Bessel beams) are helical waves possessing a pseudo-orbital angular momentum and a phase singularity on their axis (for orders $\geqslant 1$). The pitch of the helix l is called the order or topological charge [36]. These waves are separated variable general solutions of the Helmholtz equation in cylindrical coordinates and are therefore not exclusive to acoustics (see, e.g., [37] for their optical counterparts). Separated variable solutions mean that their axial and radial behavior are independent; i.e., the diffraction is canceled for infinite aperture and remains weak in other cases [38]. This enables their controlled synthesis even in confined geometries. Acoustical vortices can be generated by firing an array of piezoelectric transducers with a circular phase shift [39] or using inverse filtering techniques [40–42]. As few as four transducers are enough to develop a first-order vortex [39]. Recently, it has been observed that their orbital momentum can be transferred to dissipative media, which results in a measurable torque for solids [43,44] or azimuthal rotation for fluids [45].

In the following, we derive the equations of the flow generated by an attenuated collimated *Bessel beam* of finite radial extension r_1 [Fig. 1(a)], traveling along the z axis of an unbounded cylindrical tube of radius r_0. This model constitutes an extension of Eckart's perturbation theory [25] initially limited to *plane waves*. In the case of Bessel beams [39], the density variation ρ_1 induced by the acoustical wave takes the

*michael.baudoin@univ-lille1.fr

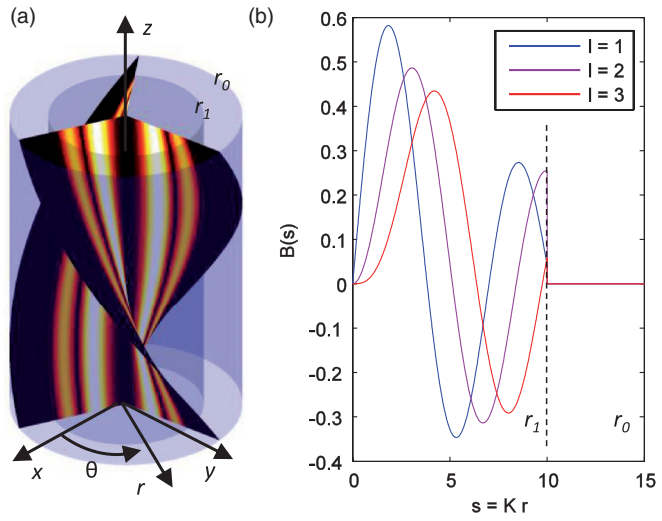

FIG. 1. (Color online) (a) Acoustical vortex with topological charge $l = 3$, $\tan(\alpha) = 1.21$, and $Kr_1 = 10$ (z axis was enlarged 10 times). Surfaces correspond to the phase $l\theta + k_z z = \pi/2$, while colors indicate the magnitude of the radial function B. (b) Corresponding radial function $B(Kr)$ for $l = 1$ to 3.

form

$$\rho_1(r,\theta,z,t) = \hat{\rho}_1 B(s)\sin(l\theta + k_z z - \omega t), \tag{1}$$

$$B(s) = A(s)J_l(s). \tag{2}$$

In these equations, $\hat{\rho}_1, l, \theta, k_z, \omega, t$, and J_l denote, respectively, the amplitude of the acoustical wave, the topological charge of the Bessel beam, the angular coordinate, the projection of the wave vector on the z axis, the wave angular frequency, the time, and the cylindrical Bessel function of order l. The spatial window function, $A(s)$, is used to limit the infinite lateral extension of the Bessel function. The phase of such a vortex is given by $\phi = l\theta + k_z z - \omega t$, yielding to helicoidal equiphase surfaces as shown in Fig. 1(a). We introduce the shorthand notation $s = Kr$ and, by analogy $s_1 = Kr_1, s_0 = Kr_0$, with K the transversal component of the wave vector. It is defined by the dispersion relation of a Bessel beam: $K^2 + k_z^2 = \omega^2/c^2$, with c the sound speed. We also introduce the variable α, measuring the helicoidal nature of the flow and defined by $\tan(\alpha) = k_z/K$. The radial dependence in Eq. (1) is based on Bessel functions, which are plotted in Fig. 1(b). Provided that $l \geqslant 1$, these functions cancel at $s = 0$, where destructive interference between the wavelets from opposite sides of the vortex occurs. Consequently, the core of the vortex is not solely a phase singularity, but also a shadow area.

Following Eckart [25], acoustic streaming can be calculated by decomposing the flow into a first-order compressible and irrotational flow (corresponding to the propagating acoustical wave) and a second-order incompressible vortical flow (describing the bulk acoustic streaming). The insertion of this decomposition into Navier-Stokes compressible equations yields Eckart's diffusion equation for the second-order vorticity field $\vec{\Omega}_2 = \vec{\nabla} \times \vec{u}_2$, with $\vec{u}_2$ the second-order velocity field. This diffusion is forced by a nonlinear combination of first-order terms and simplifies at steady state into

$$\Delta\vec{\Omega}_2 = -\frac{b}{\rho_0^2}\vec{\nabla}\rho_1 \times \vec{\nabla}\frac{\partial\rho_1}{\partial t}, \tag{3}$$

with $b = 4/3 + \mu'/\mu$, μ' the bulk viscosity, μ the shear viscosity, ρ_0 the density of the fluid at rest, and ρ_1 the first-order density variation. Since the streaming flow is incompressible, we can introduce the vector potential $\vec{\Psi}_2$ such that $\vec{u}_2 = \vec{\nabla} \times \vec{\Psi}_2$, with the Coulomb gauge fixing condition: $\vec{\nabla} \times \vec{\Psi}_2 = \vec{0}$. The resolution of Eq. (3) thus amounts to the resolution of the inhomogeneous biharmonic equation: $\Delta^2\vec{\Psi}_2 = -\frac{b}{\rho_0^2}\vec{\nabla}\rho_1 \times \vec{\nabla}\frac{\partial\rho_1}{\partial t}$. Originally, this equation was integrated by Eckart for truncated plane waves. In the present work, we solve it in the case of Bessel beams, whose expression is given by Eqs. (1) and (2). Owing to the linear nature of this partial differential equation, we consider only solutions verifying the symmetries imposed by the forcing term and the boundary conditions: the no-slip condition on the walls, an infinite cylinder in the z direction, and no net flow along the channel. In this case, the problem reduces to a set of two linear ordinary differential equations, which were integrated with standard methods. The complete procedure is detailed in Appendix A.

Results are given by Eqs. (4) to (11):

$$u_2^z = 2\frac{\Omega_\theta^\star}{K}\left[\left(1 - \frac{s^2}{s_0^2}\right)f(s_0) + \frac{1}{2}\left(\frac{s^2}{s_0{}^2}\Lambda_z^l(s_0) - \Lambda_z^l(s)\right)\right], \tag{4}$$

$$u_2^\theta = \frac{\Omega_z^\star}{K}\left(\frac{s}{s_0{}^2}\Lambda_\theta^l(s_0) - \frac{1}{s}\Lambda_\theta^l(s)\right), \tag{5}$$

$$\text{with} \quad f(s) = -\frac{1}{2}\Lambda_z^l(s) + \frac{2}{s^2}\int_0^s x_1\Lambda_z^l(x_1)dx_1, \tag{6}$$

$$\Lambda_\theta^l(s) = \int_0^s x_2\int_0^{x_2}\frac{B^2(x_1)}{x_1}dx_1dx_2, \tag{7}$$

$$\Lambda_z^l(s) = \int_0^s \frac{1}{x_2}\int_0^{x_2} x_1B^2(x_1)dx_1dx_2, \tag{8}$$

$$\Omega_\theta^\star = \frac{1}{2}\frac{\omega b\tan(\alpha)}{\rho_0 c^2}E_1, \tag{9}$$

$$\Omega_z^\star = \frac{1}{2}\frac{\omega bl}{\rho_0 c^2}E_1, \tag{10}$$

$$E_1 = c^2\frac{(\hat{\rho}_1)^2}{\rho_0}. \tag{11}$$

In these expressions, we see that the ratio between the axial and the azimuthal velocities u_2^z/u_2^θ is proportional to the ratio $\Omega_\theta^\star/\Omega_z^\star = \tan(\alpha)/l$, indicating that as α decays or l increases (increasing the gradients along the r and θ directions, respectively), the azimuthal velocity tends to dominate over its axial counterpart. Both speeds are proportional to the acoustic energy rather than the amplitude, emphasizing the fundamental nonlinear nature of acoustic streaming. Furthermore, both terms are linearly proportional to ω such that its product with the elastic potential energy, (11), refers to the power flux carried by the wave.

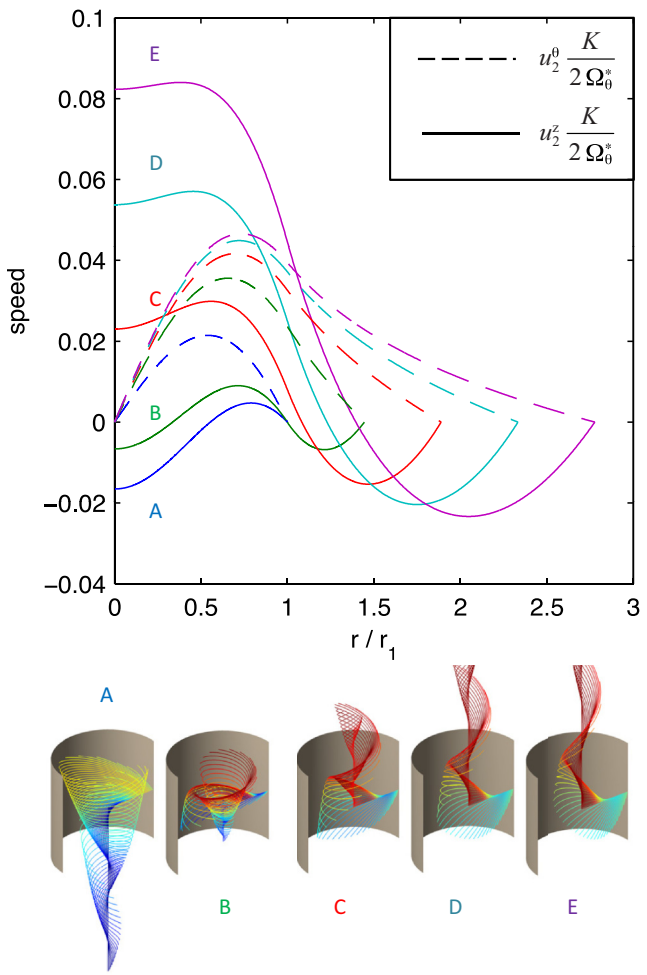

FIG. 2. (Color online) Top: Nondimensional velocities for $l = 1$, $\tan(\alpha) = 1.21$, and $Kr_1 = 1.84$ for progressively increased cavity geometrical proportions $r_0/r_1 = [1\ (A), 1.44\ (B), 1.89\ (C), 2.33\ (D), 2.78\ (E)]$. Axial velocity is represented by solid lines, and the azimuthal component by dashed ones. Bottom: Flow streamlines. Colors are indicative of the speed magnitude along u_2^z: extrema are represented by the most intense colors, red for positive and blue for negative.

Equations (4) to (11) were integrated numerically to compute the velocity field. A square spatial window function for $A(s)$ (whose expression is given in Appendix (B1)) is chosen to simplify the algebra. In the following, we investigate the case $l = 1$, $\tan(\alpha) = 1.21$, and $Kr_1 = 1.84$ to get an overview of the flow pattern when the geometric ratio r_0/r_1 is tuned. The resulting velocity profiles and the associated streamlines are presented in Fig. 2. They show a combination of axial and azimuthal vortical structures whose topology depends on the ratio r_0/r_1.

III. REPELLER AND ATTRACTOR VORTICES

It is commonly accepted that Eckart's streaming is the result of pseudomomentum transfer from the sound wave to the fluid [26]. Consequently, the acoustic beam ($r < r_1$) should push the fluid away from the transducer. This is what actually occurs in weakly confined geometry, that is, for the highest ratios r_0/r_1 (see Fig. 2, C to E). In these cases, confinement and mass conservation impose a backflow at the periphery of the acoustic beam, resulting in azimuthal vorticity similar to that observed by Eckart. But Bessel beams also carry an angular momentum, which is transmitted to the fluid and results in axial vorticity [45]. Since for $l > 0$ the wave is rotating in the positive direction (when time increases, equiphase is obtained for growing θ), the azimuthal velocity is also positive.

However, this analysis does not hold when applied to very confined geometries such as A and B in Fig. 2, where the beam covers almost all the cylindrical channel. Under these conditions, radial variations of the beam intensity must be considered. Indeed, in Fig. 1 we clearly see that the Bessel beam offers a shadow area in the neighborhood of its axis, where the wave amplitude cancels. This holds for all non-zero-order vortices. The backflow generally appears where the wave forcing is weaker. Hence, the fluid recirculation can occur either near the walls or at the core of the beam, which becomes the only option as the free space at the periphery of the vortex shrinks to 0, as in case A. Let us call these vortices *attractor vortices* since they tend to drive fluid particles towards the sound source, and their opposite *repeller vortices*, since they push fluid particles away from the source. Although streaming pushing the fluid away from a transducer is common, (i) it is not usually associated with axial vorticity, and (ii) the vorticity topology depends on the boundary conditions. Furthermore, Bessel beams enable for the first time the synthesis of attractive vortices, offering original prospects for flow control and particle sorting in confined geometries.

Intrigued by this reverse-flow motion, we performed a systematic investigation of the conditions of its appearance. Looking at the expression of the velocity, we note that the sign of $u_2^z(r = 0)$ is independent of $\tan(\alpha)$, such that the set of parameters reduces to the topological charge l, the typical dimension Kr_1, and the geometrical ratio r_0/r_1. All these parameters are gathered in Fig. 3 to give an overview of the streaming induced by Bessel beams in confined space. Looking at the flow map for $l = 1$, we first note that there is a bounded set of parameters leading to attractor vortices. Indeed, these vortices are squeezed by two restrictions: the beam must be confined enough (ratio r_0/r_1 close to 1) as previously explained, and the value of Kr_1 has to be small. Looking back at Fig. 1(b), we note that as Kr_1 increases, the Bessel function amplitude decreases at the periphery, which facilitates the flow recirculation close to the channel walls. This trend is reinforced by the apparition of new nodes of the Bessel function for higher values of Kr_1 and the quadratic dependence of the streaming flow. In addition, as the beam gets wider, the envelope of the beam weakens for increasing r, and hence, the recirculation preferentially flows towards the periphery.

Introducing the topological order l as a free parameter, we note the progressive broadening of the attractor domain. Referring to Fig. 1(b), it appears that Bessel functions of higher order roughly translate towards increased Kr_1 or, reciprocally, need a higher Kr_1 to reach the analog extremum. This explains the Kr_1 part of the broadening, whereas the r_0/r_1 is due to the progressive flattening of Bessel functions, which, nonetheless, rapidly saturates. Using the asymptotic forms of Bessel development, we compute this limit in

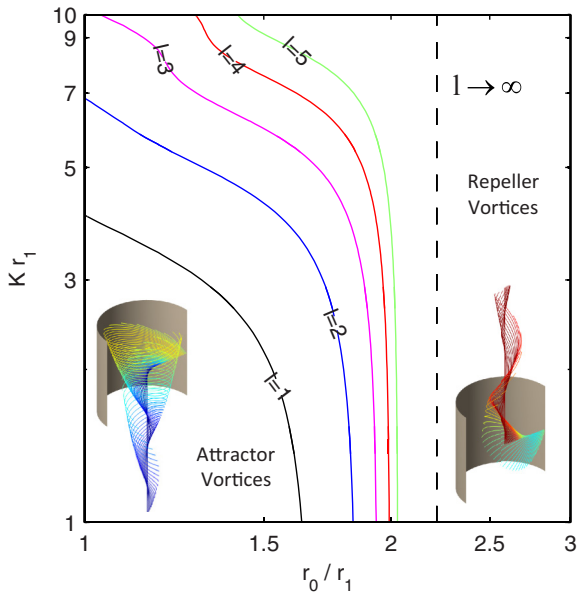

FIG. 3. (Color online) Contour plot of $u_2^z(r=0)=0$ at various topological charges l, typical dimension Kr_1, and geometrical ratio r_0/r_1. The parameter plane is partitioned into two areas: one close to the origin, corresponding to *attractor* vortices, with negative axial velocities at $r=0$, and the other corresponding to *repeller* vortices. The dashed line at $r_0/r_1 \sim 2.218$ indicates an asymptotic limit obtained for large l values.

Appendix B. The extreme value is given solving the equation $\ln(x) = 1 - 1/x^2$,with $x = r_0/r_1$. The existence of this upper bound highlights the essential condition of the confined nature of the channel.

To compute these last results, we use a window function, $A(s)$, with a sharp cutoff to ease the comparison with Eckart results. If we relax this condition, no change is expected in the case of weakly confined beams, $Kr_1 \gg 1$. For such a beam, the flow will recirculate preferentially at the periphery due to the radial decrease in the Bessel function. The strictly confined case $r_0/r_1 = 1$ is possible since Bessel beams are the modes of cylindrical wave guides for discrete values of the radial wave number $K = s/r$, i.e., no window $A(s)$ is required. Hence flow reversal at the vortex core should be observable. The intermediate situation of a strongly confined beam, $1 < r_0/r_1 = 1 < 2$, is more challenging to carry out experimentally due to diffraction spreading. However, this problem is mitigated since truncated Bessel beams are weakly diffracting [38].

IV. CONCLUSION

In this paper, we derive the streaming flow induced by Bessel beams (acoustical vortices). The resulting flow topology is reminiscent of cyclones with both axial and azimuthal vorticity. The axial component is solely controlled by the acoustic field. Regarding the azimuthal vorticity, two categories of flow pattern should be distinguished: repeller and attractor vortices. The first category exhibits a positive velocity at the center of the beam and appears when the beam radius is small compared to the fluid cavity, whereas the latter needs a very confined geometry and develops a negative velocity in its core. To the best of our knowledge, streaming-based attractor beams have never been described before and are due to the specific radial dependence of the sound-wave intensity in Bessel beams. This work opens prospects for vorticity control, which is an essential feature in many fluidic systems [46–49]. Moreover, the combination of attractive streaming and radiation pressure [50–52] induced by acoustical vortices could provide an efficient method for particle sorting. Indeed, large particles are known to be more sensitive to radiation pressure, and small particles to streaming [53]. Large particles would therefore be pushed away from the sound source by the radiation pressure, while small particles would be attracted by the flow toward it. Compared to existing techniques relying on radiation pressure generated by standing waves [54,55], the advantage would be that a resonant cavity is not mandatory for sorting particles with acoustical vortices since progressive waves can be used.

ACKNOWLEDGMENT

This work was supported by ANR Project No. ANR-12-279-BS09-0021-01 and Region Nord Pas de Calais.

APPENDIX A: RESOLUTION OF THE ECKART EQUATION FOR ACOUSTICAL VORTICES

Eckart acoustic streaming [25] is adequately described by a set of nonlinear partial differential equations. Although exact analytical solutions have not been found in the general case, the problem can be solved with a perturbation analysis, as long as the acoustic wave propagation is weakly nonlinear (weak acoustical Mach number) and the flow remains laminar (weak Reynolds number). Following Eckart, the flow generated by a transducer can be decomposed into a first-order compressible and irrotational flow (corresponding to the propagating acoustic wave) and a second-order incompressible vortical flow (corresponding to the acoustic streaming) [56]:

$$\rho = \rho_0 + \rho_1 + \rho_2 + \cdots, \tag{A1}$$

$$\vec{u} = \vec{u}_1 + \vec{u}_2 + \cdots, \tag{A2}$$

with $\rho_2 \ll \rho_1 \ll \rho_0$ and $\|\vec{u}_2\| \ll \|\vec{u}_1\|$. Basically the order of magnitude of the ratio between first-order and second-order fields is given by the acoustical Mach number. In this development, we have considered a homogeneous fluid at rest in the absence of an acoustic field. Thus the density ρ_0 is constant in space and time, and the velocity $\vec{u_0} = \vec{0}$.

By replacing this decomposition into Navier-Stokes compressible equations, Eckart showed that the first-order field is the solution of D'Alembert (wave) equation. Acoustical vortices are solutions of this equation in cylindrical coordinates [57] and their expression calculated by Hefner and Marston [39] takes the following form for weakly attenuated waves:

$$\rho_1(r,\theta,z,t) = \hat{\rho}_1 A(Kr) J_l(Kr) \sin(l\theta + k_z z - \omega t). \tag{A3}$$

In this equation, $\phi = l\theta + k_z z - \omega t$ is the phase of the acoustical vortex, l the topological charge of the vortex, θ the angular coordinate, k_z the projection of the wave vector on the z axis, z the height, ω the wave frequency, and t the time. Finally, $\hat{\rho}_1$ is the amplitude of the first-order density fluctuation, which is related to its pressure counterpart $\hat{P}_1$

according to $\hat{\rho_1} = \hat{P}_1/c^2$, and K the transversal component of the wave vector. It is defined by the dispersion relation of an acoustical vortex, $K^2 + k_z^2 = \omega^2/c^2$, with c the sound speed.

Eckart obtained, in his paper, a diffusion equation for the second-order vorticity field $\vec{\Omega}_2 = \vec{\nabla} \times \vec{u}_2$, which can be used to compute the acoustic streaming. In the following, we consider steady streaming generated by a monochromatic acoustic wave with constant amplitude and therefore the Eckart equation reduces to

$$\Delta \vec{\Omega}_2 = -\frac{b}{\rho_0^2} \vec{\nabla} \rho_1 \times \vec{\nabla} \frac{\partial \rho_1}{\partial t}, \tag{A4}$$

$$b = 4/3 + \mu'/\mu, \tag{A5}$$

with μ the shear viscosity and μ' the bulk viscosity. From now on, we use the shorthand notation $s = Kr$, $s_1 = Kr_1$, and $s_0 = Kr_0$. In addition, we introduce B to gather the radial dependence of the beam,

$$B(s) = A(s) J_l(s), \tag{A6}$$

where the function $A(s)$ is introduced to limit the infinite lateral extension of the Bessel function. The derivation of ρ_1 in Eq. (A3) in cylindrical coordinates and the replacement of the result in Eq. (A4) give an inhomogeneous Poisson equation with the first-order field playing the role of the streaming source term:

$$\frac{1}{K^2} \Delta \vec{\Omega}_2(r,\theta,z) = \Omega_\theta^\star \frac{dB^2(s)}{ds} \vec{e}_\theta - \frac{\Omega_z^\star}{s} \frac{dB^2(s)}{ds} \vec{e}_z, \tag{A7}$$

$$\Omega_\theta^\star = \frac{1}{2} \frac{k_z \omega b}{K \rho_0 c^2} E_1, \tag{A8}$$

$$\Omega_z^\star = \frac{1}{2} \frac{\omega b l}{\rho_0 c^2} E_1, \tag{A9}$$

$$E_1 = c^2 \frac{\hat{\rho}_1^2}{\rho_0}. \tag{A10}$$

The beam is assumed to be of infinite extent along z and invariant by rotation θ around this axis, therefore $\vec{\Omega}_2$ has only a radial dependence. Also, the conservative nature of vorticity allows us to drop off the $\vec{e_r}$ component. The resulting solution candidate for $\vec{\Omega}_2$ is

$$\vec{\Omega}_2 = \Omega_2^\theta(s) \vec{e}_\theta + \Omega_2^z(s) \vec{e}_z. \tag{A11}$$

Plugging it into Eq. (A7) gives two linear ordinary differential equations:

$$s^2 \frac{d^2}{ds^2} \Omega_2^\theta + s \frac{d}{ds} \Omega_2^\theta - \Omega_2^\theta = s^2 \Omega_\theta^\star \frac{dB^2(s)}{ds}, \tag{A12}$$

$$s \frac{d^2}{ds^2} \Omega_2^z + \frac{d}{ds} \Omega_2^z = -\Omega_z^\star \frac{dB^2(s)}{ds}. \tag{A13}$$

Using standard methods, the homogeneous (H) and particular (P) solutions are determined:

$$\Omega_2^\theta\big|_H = M_1^\theta s + \frac{N_1^\theta}{s}, \tag{A14}$$

$$\Omega_2^\theta\big|_P = \frac{1}{s} \Omega_\theta^\star \int_0^s x_1 B^2(x_1) dx_1. \tag{A15}$$

The equation along z is treated by introducing $g = \frac{d}{ds} \Omega_2^z$:

$$g|_H = \frac{M_z^1}{s}, \tag{A16}$$

$$g|_P = -\Omega_z^\star \frac{B^2(s)}{s}, \tag{A17}$$

$$\Omega_2^z = N_1^z + M_z^1 \ln(s) - \Omega_z^\star \int_0^s \frac{B^2(x_1)}{x_1} dx_1. \tag{A18}$$

Removing the terms diverging at $s = 0$, we have

$$\vec{\Omega}_2 = \left[M_1^\theta s + \frac{1}{s} \Omega_\theta^\star \int_0^s x_1 B^2(x_1) dx_1 \right] \vec{e}_\theta \tag{A19}$$

$$+ \left[N_1^z - \Omega_z^\star \int_0^s \frac{B^2(x_1)}{x_1} dx_1 \right] \vec{e}_z. \tag{A20}$$

Since the second-order flow (streaming) is incompressible, we can introduce the vector potential $\vec{\Psi}_2$ verifying $\vec{u}_2 = \vec{\nabla} \times \vec{\Psi}_2$ with the gauge $\vec{\nabla} \times \vec{\Psi}_2 = \vec{0}$ to compute the velocity field from the vorticity field:

$$\Delta \vec{\Psi}_2 = -\vec{\Omega}_2. \tag{A21}$$

For symmetry reasons, the flow is assumed to be invariant by rotation θ around z and translation along the propagation axis z, and due to the conservative nature of $\vec{u}_2$, the radial component is dropped off. Consequently, the velocity field is of the form $\vec{u}_2 = u_2^\theta(s) \vec{e}_\theta + u_2^z(s) \vec{e}_z$. Computing the curl of $\vec{\Psi}$ in order to get $\vec{u}_2$, we note that $\vec{\Psi}_2 = \Psi_\theta(s) \vec{e}_\theta + \Psi_z(s) \vec{e}_z$. Equation (A21) is very similar to (A4), except for the source term:

$$s^2 \Psi_\theta'' + s \Psi_\theta' - \Psi_\theta = -\frac{1}{K^2} \left(M_1^\theta s^3 + s \Omega_\theta^\star \int_0^s x_1 B^2(x_1) dx_1 \right),$$

$$s \Psi_z'' + \Psi_z' = \frac{s}{K^2} \left(-N_1^z + \Omega_z^\star \int_0^s \frac{B^2(x_1)}{x_1} dx_1 \right).$$

Using the same procedure as for $\vec{\Omega}_2$ we get the general solution:

$$\Psi_\theta = M_\theta^2 s - \frac{1}{K^2} \left(\frac{M_1^\theta}{8} s^3 + \frac{\Omega_\theta^\star I_\theta(s)}{s} \right), \tag{A22}$$

$$\Psi_z = N_z^2 + \frac{1}{K^2} \left(-N_1^z \frac{s^2}{4} + \Omega_z^\star I_z(s) \right), \tag{A23}$$

$$I_\theta = \int_0^s x_3 \int_0^{x_3} \frac{1}{x_2} \int_0^{x_2} x_1 B^2(x_1) dx_1 dx_2 dx_3, \tag{A24}$$

$$I_z = \int_0^s \frac{1}{x_3} \int_0^{x_3} x_2 \int_0^{x_2} \frac{B^2(x_1)}{x_1} dx_1 dx_2 dx_3. \tag{A25}$$

The resulting velocity field can now be simply obtained by taking the curl of $\vec{\Psi}_2$:

$$u_2^\theta = \frac{1}{K} \left(\frac{1}{2} N_1^z s - \frac{1}{s} \Omega_z^\star \Lambda_\theta^l(s) \right), \tag{A26}$$

$$u_2^z = 2 M_\theta^2 K - \frac{1}{K} \left(\frac{M_1^\theta}{2} s^2 + \Omega_\theta^\star \Lambda_z^l(s) \right), \tag{A27}$$

$$\Lambda_\theta^l(s) = \int_0^s x_2 \int_0^{x_2} \frac{B^2(x_1)}{x_1} dx_1 dx_2, \tag{A28}$$

$$\Lambda_z^l(s) = \int_0^s \frac{1}{x_2} \int_0^{x_2} x_1 B^2(x_1) dx_1 dx_2. \tag{A29}$$

This velocity field must satisfy the adherence boundary condition at the wall of the channel $s = s_0$:

$$u_2^\theta(s_0) = 0, \tag{A30}$$

$$u_2^z(s_0) = 0. \tag{A31}$$

In addition, the steady and incompressible nature of the flow must not violate mass conservation, such that a closure condition is enforced:

$$\begin{aligned} &\int_0^{2\pi} \int_0^{r_0} \rho_0 u_2^z(r) r dr d\theta = 0, \\ &\Leftrightarrow \int_0^{s_0} x_1 u_z(x_1) dx_1 = 0. \end{aligned} \tag{A32}$$

The determinant of the system is equal to $\frac{s_0^4}{8K}$, such that it always admits a unique solution. Solving this linear system of equations, we get

$$N_1^z = \frac{2\Omega_z^\star}{{s_0}^2} \Lambda_\theta^l(s_0), \tag{A33}$$

$$M_\theta^1 = \frac{4\Omega_\theta^\star}{{s_0}^2} \left(f(s_0) - \frac{1}{2} \Lambda_z^l(s_0) \right), \tag{A34}$$

$$M_\theta^2 = \frac{\Omega_\theta^\star}{K^2} f(s_0), \tag{A35}$$

$$f(s) = -\frac{1}{2} \Lambda_z^l(s) + \frac{2}{s^2} \int_0^s x_1 \Lambda_z^l(x_1) dx_1. \tag{A36}$$

Including these boundary conditions in the expressions of the velocity field, we finally obtain

$$u_2^\theta = \frac{\Omega_z^\star}{K} \left(\frac{s}{{s_0}^2} \Lambda_\theta^l(s_0) - \frac{1}{s} \Lambda_\theta^l(s) \right),$$

$$u_z^{(2)} = 2\frac{\Omega_\theta^\star}{K} \left(\left(1 - \frac{s^2}{{s_0}^2} \right) f(s_0) + \frac{1}{2} \left(\frac{s^2}{{s_0}^2} \Lambda_z^l(s_0) - \Lambda_z^l(s) \right) \right).$$

APPENDIX B: ASYMPTOTIC DEVELOPMENT WHEN $Kr_0 \ll 2\sqrt{l+1}$

In this section, we compute an asymptotic development of our final expression when $Kr_0 \ll 2\sqrt{l+1}$. We show that Eckart's result obtained for the plane wave can be recovered as an asymptotic limit of our more general expression. Recovering, the Eckart result dictates the choice of the function $A(s)$:

$$A(s) = \begin{cases} 1 & \text{if} \quad s < s_1, \\ 0 & \text{if} \quad s \geqslant s_1. \end{cases} \tag{B1}$$

1. Asymptotic development

For all $s < s_0 = Kr_0$, we have

$$J_l(s) \sim \frac{1}{l!} \left(\frac{s}{2} \right)^l, \tag{B2}$$

$$\Lambda_z^l(s) \sim \begin{cases} \frac{s^{2l+2}}{(2l+2)^2\, 2^{2l}\, l!^2} & \text{if} \quad s < s_1, \\ {s_1}^{2l+2}\, \frac{1+(2l+2)\ln(s/s_1)}{(2l+2)^2\, 2^{2l}\, l!^2} & \text{if} \quad s \geqslant s_1, \end{cases} \tag{B3}$$

$$f \sim \begin{cases} \frac{s^{2l+2}}{(2l+2)^2\,(2l+4)\,2^{2l}\,l!^2} \left(2 - \frac{2l+4}{2}\right) & \text{if} \quad s < s_1, \\ C_l \left[\begin{array}{l} (s_1/s)^2 \left(l\,(1-(s/s_1)^2) + \frac{1}{l+2} \right) \\ +((l+1)\ln(s/s_1) - (1/2)) \end{array} \right] & \text{if} \quad s \geqslant s_1, \end{cases} \tag{B4}$$

$$\text{with} \quad C_l = \frac{{s_1}^{2l+2}}{(2\,l+2)^2\ 2^{2l}\, l!^2}. \tag{B5}$$

2. Recovering Eckart's streaming with $l = 0$ and $Kr_0 \ll 1$

The case of the plane wave can be recovered from our expression by considering a topological charge equal to 0 and a radius $r_0 \ll 1/K$:

$$\Lambda_z^l(s) \sim \begin{cases} s^2/4 & \text{if} \quad s < s_1, \\ (s_1^2/4)(1 + 2\ln(s/s_1)) & \text{if} \quad s \geqslant s_1; \end{cases} \tag{B6}$$

$$f \sim \begin{cases} 0 & \text{if} \quad s < s_1, \\ (s_1^2/8)[(s_1/s)^2 + 2\ln(s/s_1) - 1] & \text{if} \quad s \geqslant s_1. \end{cases} \tag{B7}$$

In the original paper [25], Eckart introduces the notation $x = s/s_0$ and $y = s_1/s_0$:

$$u_2^z \sim 2\frac{\Omega_\theta^\star}{K} \begin{cases} s_1^2/4[(1/2)(1-(x/y)^2) - (1-y^2/2)(1-x^2) - \ln(y)] & \text{if} \quad s < s_1, \\ -s_1^2/4[(1-y^2/2)(1-x^2) + \ln(x)] & \text{if} \quad s \geqslant s_1. \end{cases} \tag{B8}$$

Equation (B9) is exactly the expression of the acoustic streaming obtained by Eckart [25] for plane waves.

3. Asymptotic limit for large values of l and $Kr_0 \ll 2\sqrt{l+1}$

$$\Lambda_z^l(s) \sim \begin{cases} \frac{s^{2l+2}}{(2l)^2\, 2^{2l}\, l!^2} & \text{if} \quad s < s_1, \\ {s_1}^{2l+2}\, \frac{\ln(s/s_1)}{(2l)\, 2^{2l}\, l!^2} & \text{if} \quad s \geqslant s_1; \end{cases} \tag{B9}$$

$$f \sim \begin{cases} -\frac{s^{2l+2}}{2(2l)^2\, 2^{2l}\, l!^2} & \text{if} \quad s < s_1, \\ C_l \left[\begin{array}{l} (s_1/s)^2(1-(s/s_1)^2) \\ +\ln(s/s_1) \end{array} \right] & \text{if} \quad s \geqslant s_1; \end{cases} \tag{B10}$$

$$C_l = \frac{{s_1}^{2l+2}}{4l\, 2^{2l}\, l!^2}; \tag{B11}$$

$$u_2^z(s=0) = 2\frac{\Omega_\theta^\star}{K} f(s_0). \tag{B12}$$

Using the Eckart [25] notation $y = s_1/s_0$:

$$u_2^z(s=0) = 2\frac{\Omega_\theta^\star C_l}{K}(y^2 - 1 - \ln(y)). \tag{B13}$$

We highlight here that in Eq. (B13) C_l is decreasing extremely rapidly, such that increasing l dramatically decreases the magnitude of $u_2^z(0)$.

[1] A. Kumar, P. Gogate, and A. Pandit, Ind. Eng. Chem. Res. **46**, 4368 (2007).
[2] G. Gale and A. Busnaina, Part. Sci. Technol.: Int. J. **17**, 229 (1999).
[3] X. Li, Y. Yang, and W. Cheng, J. Mater. Sci. **39**, 3211 (2004).
[4] P. Muller, R. Barnkob, M. Jensen, and H. Bruus, Lab Chip **12**, 4617 (2012).
[5] K. Baker, V. Robertson, and F. Duck, Phys. Ther. **81**, 1351 (2001).
[6] L. Crum, J. Acoust. Soc. Am. **117**, 2350 (2006).
[7] M. Wiklund, Lab Chip **12**, 2438 (2012).
[8] J. Friend and L. Yeo, Rev. Mod. Phys. **83**, 647 (2011).
[9] L. Yeo and J. Friend, Annu. Rev. Fluid Mech. **46**, 379 (2014).
[10] A. Wixforth, C. Strobl, C. Gauer, A. Toegl, J. Scriba, and Z. Guttenberg, Anal. Bioanal. Chem. **379**, 982 (2004).
[11] A. Renaudin, P. Tabourier, V. Zang, J. Camart, and C. Druon, Sensors Actuators B **113**, 389 (2006).
[12] P. Brunet, M. Baudoin, O. Matar, and F. Zoueshtiagh, Phys. Rev. E **81**, 036315 (2010).
[13] A. Qi, L. Yeo, and J. Friend, Phys. Fluids **20**, 074103 (2008).
[14] S. Shiokawa, Y. Matsui, and T. Ueda, Jpn. J. Appl. Phys. **29**, 137 (1990).
[15] M. Tan, J. Friend, and L. Yeo, Phys. Rev. Lett. **103**, 024501 (2009).
[16] M. Baudoin, P. Brunet, O. Matar, and E. Herth, Appl. Phys. Lett. **100**, 154102 (2012).
[17] J. Blamey, L. Yeo, and J. Friend, Langmuir **29**, 3835 (2013).
[18] K. Sritharan, C. Strobl, M. Schneider, and A. Wixforth, Appl. Phys. Lett. **88**, 054102 (2006).
[19] T. Frommelt, M. Kostur, M. Wenzel-Schäfer, P. Talkner, P. Hänggi, and A. Wixforth, Phys. Rev. Lett. **100**, 034502 (2008).
[20] R. Beyer, *Nonlinear Acoustics* (Acoustical Society of America, Providence, RI, 1997).
[21] N. Riley, Annu. Rev. Fluid Mech. **33**, 43 (2001).
[22] M. Hamilton, J. Acoust. Soc. Am. **113**, 153 (2003).
[23] H. Schlichting, Phys. Z. **33**, 327 (1932).
[24] L. Rayleigh, Philos. Trans. Roy Soc. London **175**, 1 (1884).
[25] C. Eckart, Phys. Rev. **73**, 68 (1948).
[26] J. Piercy and J. Lamb, Proc. Roy. Soc. London. A **226**, 43 (1954).
[27] M. Sato and T. Fujii, Phys. Rev. E **64**, 026311 (2001).
[28] O. Rudenko and S. Soluyan, Akust. Zh. **17**, 122 (1971).
[29] O. Rudenko and A. Sukhorukov, Acoust. Phys. **44**, 565 (1998).
[30] I. Sou, J. Allen, C. Layman, and C. Ray, Exp. Fluids **51**, 1201 (2011).
[31] E. V. Romanenko, Sov. Phys. Acoust. **6**, 87 (1960).
[32] Y. Statnikov, Sov. Phys. Acoust. **13**, 122 (1967).
[33] L. Menguy and J. Gilbert, J. Acoust. Soc. Am. **105**, 958 (1999).
[34] I. Reyt, V. Daru, H. Bailliet, S. Moreau, J.-C. Valière, D. Baltean-Carlès, and C. Weisman, J. Acoust. Soc. Am. **134**, 1791 (2013).
[35] W. Nyborg, *Nonlinear Acoustics* (Academic Press, New York, 1998), Chap. 7.
[36] J.-L. Thomas, T. Brunet, and F. Coulouvrat, Phys. Rev. E **81**, 016601 (2010).
[37] L. Allen, M. Beijersbergen, R. Spreeuw, and J. Woerdman, Phys. Rev. A **45**, 8185 (1992).
[38] J. Durnin, J. J. Miceli, Jr., and J. Eberly, Phys. Rev. Lett. **58**, 1499 (1987).
[39] B. Hefner and P. Marston, J. Acoust. Soc. Am. **106**, 3313 (1999).
[40] J.-L. Thomas and R. Marchiano, Phys. Rev. Lett. **91**, 244302 (2003).
[41] R. Marchiano and J.-L. Thomas, Phys. Rev. Lett. **101**, 064301 (2008).
[42] T. Brunet, J.-L. Thomas, R. Marchiano, and F. Coulouvrat, New J. Phys. **11**, 013002 (2009).
[43] H. He, M. Friese, N. Heckenberg, and H. Rubinsztein-Dunlop, Phys. Rev. Lett. **75**, 826 (1995).
[44] J. Volke-Sepulveda, A. Santillan, and R. R. Boullosa, Phys. Rev. Lett. **100**, 024302 (2008).
[45] A. Anhauser, R. Wunenburger, and E. Brasselet, Phys. Rev. Lett. **109**, 034301 (2012).
[46] J. Ottino, *The Kinematics of Mixing: Stretching, Chaos, and Transport (Cambridge Texts in Applied Mathematics)* (Cambridge University Press, Cambridge, 1989).
[47] A. Chorin, *Vorticity and Turbulence*, Vol. 103 (Springer, Berlin, 1994).
[48] C. Gmelin and U. Rist, Phys. Fluids **13**, 513 (2001).
[49] Q. Zhu, M. Wolfgang, D. Yue, and M. Triantafyllou, J. Fluid Mech. **468**, 1 (2002).
[50] D. Baresh, J.-L. Thomas, and R. Marchiano, J. Acoust. Soc. Am. **133**, 25 (2013).
[51] M. Settnes and H. Bruus, Phys. Rev. E **85**, 016327 (2012).
[52] L. Zhang and P. Marston, Phys. Rev. E **84**, 035601(R) (2011).
[53] S. Hagsäter, T. Jensen, H. Bruus, and J. Kutter, Lab Chip **7**, 1336 (2007).
[54] F. Petersson, A. Nilsson, C. Holm, H. Jönsson, and T. Laurell, Lab Chip **5**, 20 (2005).

[55] C. Wood, S. Evans, J. Wunningham, and R. O'Rorke, Appl. Phys. Lett. **92**, 044104 (2008).

[56] NB: In his seminal paper, Eckart also computed the irrotational part of the second-order flow corresponding to the effect of nonlinearities on acoustic-wave propagation. Then, using Helmoltz decomposition, he focused on the incompressible part, corresponding to the acoustic streaming. Here we do not consider the effect of nonlinearities on acoustic-wave propagation.

[57] M. D. and K. Dholakia, Contemp. Phys. **46**, 15 (2005).

Lab on a Chip

PAPER

View Article Online
View Journal | View Issue

Cite this: *Lab Chip*, 2014, **14**, 3556

Cell detachment and label-free cell sorting using modulated surface acoustic waves (SAWs) in droplet-based microfluidics

Adrien Bussonnière,[a] Yannick Miron,[b] Michaël Baudoin,*[a] Olivier Bou Matar,[a] Michel Grandbois,[b] Paul Charette*[cd] and Alan Renaudin*[cd]

Received 28th May 2014,
Accepted 30th June 2014

DOI: 10.1039/c4lc00625a

www.rsc.org/loc

We present a droplet-based surface acoustic wave (SAW) system designed to viably detach biological cells from a surface and sort cell types based on differences in adhesion strength (adhesion contrast) without the need to label cells with molecular markers. The system uses modulated SAW to generate pulsatile flows in the droplets and efficiently detach the cells, thereby minimizing the SAW excitation power and exposure time. As a proof of principle, the system shows efficient sorting of HEK 293 from A7r5 cells based on adhesion contrast. Results are obtained in minutes with sorting purity and efficiency reaching 97% and 95%, respectively.

1. Introduction

Cell sorting is critical for many biological and biomedical applications such as cell biology, biomedical engineering, diagnostics and therapeutics. Indeed, numerous biological analyses are based on the separation of different cell types harvested from a raw heterogeneous sample such as whole blood. Fluorescence-activated cell sorting (FACS)[1] and magnetic-activated cell sorting (MACS)[2] are well-established methods for cell and particle sorting and are known for their high throughput and specificity. Both methods, however, require pre-processing to tag cells with markers, an important time and cost expense for some applications.

In contrast, by making use of the differences in the intrinsic physical properties of cells (size, density, adhesion strength, stiffness, electrical and optical polarizability), label-free sorting methods do not require molecular tagging. Compared to FACS and MACS, however, the specificity of label-free methods is often limited owing to insufficient contrast in physical properties, thereby restricting their widespread use. As with tagging-based systems, label-free cell-sorting methods have been implemented in microfluidic devices[3] using techniques such as deterministic lateral displacement,[4] hydrodynamic filtration,[5] dielectrophoresis (DEP),[6,7] optical lattices,[8,9] stiffness separation,[10,11] acoustophoresis[12,13] and adhesion-based sorting.[14–16] In some cases, such as sorting based on adhesion to the substrate, performance was improved by surface nanostructuring[15] and bio-functionalization[16] which enhance adhesion contrast between cell types.

In addition to sorting, the dynamics of cell detachment from solid surfaces is of interest in and of itself, either to harvest cells or to study the mechanisms of cell adhesion to surfaces. Cell dissociation and detachment from a solid substrate are normally achieved by cleaving bonding proteins with trypsin.[17] This process is quite aggressive as cells can be damaged if left exposed to trypsin for too long and a post-treatment rinsing step is required. In contrast, cell detachment based on microfluidic effects alone requires no external agents or rising. Cell detachment under constant fluid shear stresses has been demonstrated using spinning discs,[18] flow chambers[19] and, more recently, using surface acoustic wave (SAW)-actuated flow.[20,21]

The miniaturization of cell-manipulation methods has led to their integration into lab-on-chip (LOC) platforms, where cell detachment and sorting have been widely investigated in flow-based microchannel formats.[19,22,23] Comparatively few studies,[24–27] however, have explored cell separation or detachment in droplet-based microfluidics as in digital microfluidics (DMF).[28] Indeed, the physics of microfluidics in droplets is completely distinct from flow-through closed-channel systems. Microfluidics properties such as bulk and surface modes of vibration, which are unique to droplet-based systems, can be exploited to great effect. In general,

[a] *LIA LEMAC/LICS, Institut d'Eléctronique de Microélectronique et de Nanotechnologies (IEMN) UMR CNRS 8520, Université Lille 1 and EC Lille, Avenue Poincaré, BP 60069, 59652 Villeneuve d'Ascq, France. E-mail: michael.baudoin@univ-lille1.fr*

[b] *Département de Pharmacologie, Falculté de médecine et des sciences de la santé, Université de Sherbrooke, 3001, 12e Avenue Nord Sherbrooke, Sherbrooke, Québec J1H 5N4, Canada*

[c] *Laboratoire Nanotechnologies Nanosystèmes (LN2)- CNRS UMI-3463, Université de Sherbrooke, 3000 Boulevard Université, J1K OA5, Québec, Canada. E-mail: Alan.Renaudin@USherbrooke.ca, Paul.G.Charette@usherbrooke.ca; Fax: +1 (819) 821 7937; Tel: +1 (819) 821 8000 x65788*

[d] *Institut Interdisciplinaire d'Innovation Technologique (3IT), Université de Sherbrooke, 3000 Boulevard Université, J1K OA5, Québec, Canada*

unlike continuous flow systems which are often optimized for high-volume cell sorting, droplet-based systems are best suited for studies of cell properties in small populations of cells, such as cell adhesion modulation mechanisms which are highly complex and of wide-ranging interest.[29,30]

Droplet actuation in DMF is generally accomplished with surface acoustic waves (SAWs),[31–33] electrowetting on dielectrics (EWOD)[34] or dielectrophoresis (DEP).[35] SAW-based DMF has been used in a range of biological applications[36–38] to implement functions as diverse as mixing,[39] droplet displacement,[40,41] and atomization[42] as well as for particle and cell manipulation.[43] Although EWOD has been used successfully to manipulate cells,[25] large or strongly-adhering cells are difficult to detach and/or transport with the relatively weak electrowetting forces exerted by EWOD. In the case of DEP, the oscillatory forces applied to the cell are subject to changes in the physical composition of the membrane,[44] which may or may not be desirable depending on the nature of the experiment. The strong electrical fields involved in DEP also have the potential to alter cell membrane characteristics.[45]

Recently,[46] we presented preliminary results on the use of SAW-based fluid actuation in droplets to detach biological cells from a surface. We showed that under continuous SAW excitation, fully confluent cell layers could be detached *en masse* at sufficiently high SAW power, whereas isolated cells were very resistant to detachment, even at power levels above the threshold for cell viability.[47] In a previous publication, we showed that the acoustic power required to move or deform droplets with SAW can be significantly reduced by using modulated rather than continuous excitation.[48] Based on this work, we demonstrate here that modulated SAW can be used to viably detach cells from a surface and sort cells based on adhesion contrast, without the need for labeling. The experimental results presented show that two distinct cell types can be separated with a final purity of up to 97% and an efficiency greater than 95%. Results are achieved with characteristic processing times on the order of one minute without adversely affecting cell viability or requiring the cell layer to be fully confluent.

2. Methods and materials

2.1. Apparatus set-up and experimental procedure

Experiments were run on cells adhered to the surface of a $LiNbO_3$ substrate and immersed in 20 μl droplets of phosphate-buffered saline (PBS) solution.

Rayleigh-type SAWs were generated at the surface of the $LiNbO_3$ substrate by applying a 17.1 MHz sinusoidal radio frequency (RF) excitation to interdigitated transducer (IDT) thin-film metal electrodes. The excitation frequency was selected to maximize the energy transmission from the substrate surface to the liquid. The IDTs were designed as "electrode width controlled single-phase unidirectional transducers" (EWC-SPUDT),[49] a configuration that ensures that the acoustic energy is directed solely in the forward direction. The excitation signal was supplied by an RF generator (Agilent, model N9310a) and amplified to 30 dBm using an RF amplifier (Empower, model BBM0D3FEL).

Once transmitted to the fluid, the acoustic waves induce interface stresses and internal flow, resulting in deformations of the droplet-free surface due to two types of nonlinear effects: acoustic radiation pressure and acoustic streaming.[40] As explained below, cyclic droplet deformations were induced by switching the SAW excitation on and off with an appropriate period and duty cycle, resulting in large shear stresses in the fluid causing cells to detach.

An 8 × 8 mm^2 "cell-attachment zone" was defined by markers patterned onto the $LiNbO_3$ substrates. The devices were mounted under a phase contrast microscope (Motic, model AE 30/31) with a 10× objective to focus on the cell layer (2 mm diameter field of view). A high-speed 10 bit CMOS camera (PCO, model pco.1200hs) was used to capture the video of cell detachment. The set-up is depicted in Fig. 1.

Image sequences recorded by the camera were processed using ImageJ (NIH, rsbweb.nih.gov/ij) and cell populations were counted using the ImageJ cell counting tool. The two cell types used in the experiments could be easily distinguished in the images based on differences in their morphological characteristics. Following each experiment, short-term cell viability assays were performed by trypan blue exclusion.

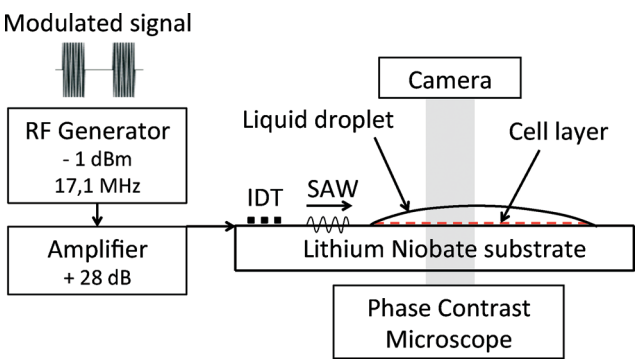

Fig. 1 Schematic diagram of the set-up showing the cell layer (red dashed line) immersed in a 20 μl PBS droplet atop a $LiNbO_3$ piezoelectric substrate. The diagram also shows the interdigitated transducers (IDTs), RF amplifier and signal generator used for Rayleigh type SAW generation. Cell visualization is achieved using a phase contrast microscope, 10× objective, and a CMOS camera.

2.2 SAW device fabrication

The SAW devices were fabricated from 1 mm thickness *X*-cut *Z*-propagating $LiNbO_3$ wafers (Newlight Photonics). This particular cut was chosen for its efficient electromechanical coupling along both *Y* and *Z* perpendicular propagation directions (K_z = 4.9%, K_y = 3.1%), allowing for two-dimensional droplet actuation if required. Indeed, the K^2 values along the two directions are greater than those of a typical 128° *Y*–*X* cut $LiNbO_3$ crystal (K_x = 5.5%, K_y = 1.2%).

The metal IDT electrodes and cell-attachment zone markers were fabricated by photoresist (Shipley S18-13, Microchem) spin-coating on the $LiNbO_3$ wafers, patterning by standard photolithography processes, metal deposition (Ti/Au, 20/200 nm), and lift-off.

2.3. Cell culture and surface preparation

Two cell lines were used in the experiments: adherent vascular smooth muscle cells (A7r5) and human embryonic kidney (HEK 293) cells. These particular cell lines were selected because they have been shown to exhibit surface adhesion strengths comparable to that of cancerous[50] and other normal[51] cell types. Cell adhesion strength, however, is highly dependent on surface preparation specifics. We chose to adhere cells directly to a bare lithium niobate ($LiNbO_3$) substrate, the piezoelectric material most commonly used to generate surface acoustic waves, in order to provide a recognizable point of reference. The adhesion of cells to bare $LiNbO_3$ has been studied by other groups.[52] As shown below, the fluid shear stresses required to detach cells from a bare $LiNbO_3$ surface are in the same range as that reported by others for surface preparations commonly used for cell studies. If required, $LiNbO_3$ can be readily functionalized for specific surface preparations.[53,54] Cells were adhered to the device surfaces either by growing the cells directly on the $LiNbO_3$ substrates in the case of single cell line reference experiments or by incubating the $LiNbO_3$ substrates in a solution of pre-grown resuspended cells in the case of single and dual cell line experiments.

A7r5 and HEK 293 cells were grown separately by seeding in 60 mm petri dishes and cultured in growth medium (DMEM supplemented with 10% heat-inactivated fetal bovine serum, 2 mM L-glutamine, 50 IU mL^{-1} penicillin, 50 μg mL^{-1} streptomycin, Wisent) under an atmosphere of 5% CO_2 at 37 °C for 24 h. For experiments requiring cells to be grown directly onto $LiNbO_3$ surfaces, the $LiNbO_3$ substrates were placed at the bottom of the petri dish for the duration of the incubation time.

For cells not grown directly onto the $LiNbO_3$ substrates, single cell line resuspended cell solutions were prepared by rinsing the cell cultures in PBS, incubating for 5 min in 500 μl of trypsin–EDTA solution at 37 °C, and resuspending in 2 ml of growth medium to stop the trypsin digestion. After 5 min of centrifugation, cells were resuspended in HEPES-buffered salt solution (HBSS) (20 mM HEPES at pH 7.4, 120 mM NaCl, 5.3 mM KCl, 0.8 mM MgSO4, 1.8 mM $CaCl_2$, and 11.1 mM dextrose). Dual cell line resuspended solutions were prepared by combining HEK 293 and A7r5 resuspended solutions in experimentally determined proportions as required for roughly equal numbers of both cell types to adhere to the surface (Fig. 2). $LiNbO_3$ substrates were placed in a petri dish immersed in resuspended cell solutions for incubation times ranging from 15 to 90 min to study various adhesion states.

Following cell adhesion by either of the two methods above, the $LiNbO_3$ substrates were rinsed with PBS, cells outside the attachment zone were dried and mechanically removed, leaving a uniformly distributed 8 × 8 mm^2 adherent cell layer covered by a thin PBS film. A 20 μl droplet of PBS was added atop the attachment zone using a calibrated micropipette prior to experiments. Note that due to adherent cell secretions, the cell-attachment zone was highly hydrophilic and the droplets spread across the square-shaped area with a high contact angle and a flat profile.

3. Results and discussion

3.1. Droplet dynamics and cell–fluid interaction

As stated earlier, the purpose of this work was to investigate the potential of modulated SAW fluid actuation to selectively detach and sort cells in a droplet. Fig. 3a shows a schematic diagram of the PBS fluid droplet atop the 8 × 8 mm^2 droplet positioning zone on the $LiNbO_3$ substrate, in relation to the SAW electrodes (EWC-SPUDT). Cyclic deformations of the droplets between a relaxed state and a deformed state (side-view camera images shown in Fig. 3b, top and bottom, respectively) were induced by switching the SAW signal on (excitation) and off (relaxation) with an appropriate period and duty cycle. During excitation, internal flow and surface deformation are induced by nonlinear acoustic forces. During relaxation, the potential energy stored as capillary surface energy produces a restoring flow in the opposite direction. Optimal values for the period (200 ms), duty cycle (25%), and power (30 dBm) were based on the droplet intrinsic relaxation time, measured experimentally.

The 50 ms SAW excitation bursts displaced the distal liquid–solid contact line (droplet edge furthest from the SAW

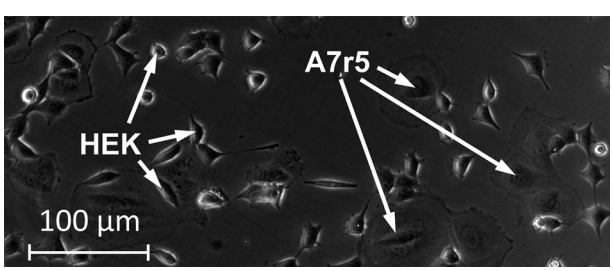

Fig. 2 Photograph of vascular smooth muscle cells (A7r5) and human embryonic kidney (HEK 293) cells adhered to the surface of a $LiNbO_3$ substrate after incubation in a resuspended cell solution at 37 °C. The arrows indicate typical specimens of HEK 293 and A7r5 cells which exhibit significantly different morphological features.

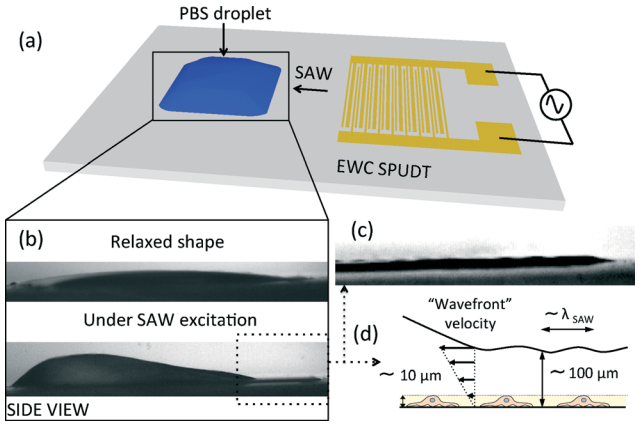

Fig. 3 (a) Schematic diagram of the fluid droplet in its relaxed position spread across the 8 × 8 mm^2 droplet positioning zone atop the $LiNbO_3$ substrate, in relation to the SAW electrodes (EWC-SPUDT); (b) side-view camera images showing the two shape extrema of the droplet during one SAW excitation modulation cycle (ON: 50 ms, OFF: 150 ms). (c) Zoom on the tail section of the drop showing a standing wave pattern. (d) The flow profile of the tail section and characteristic lengths.

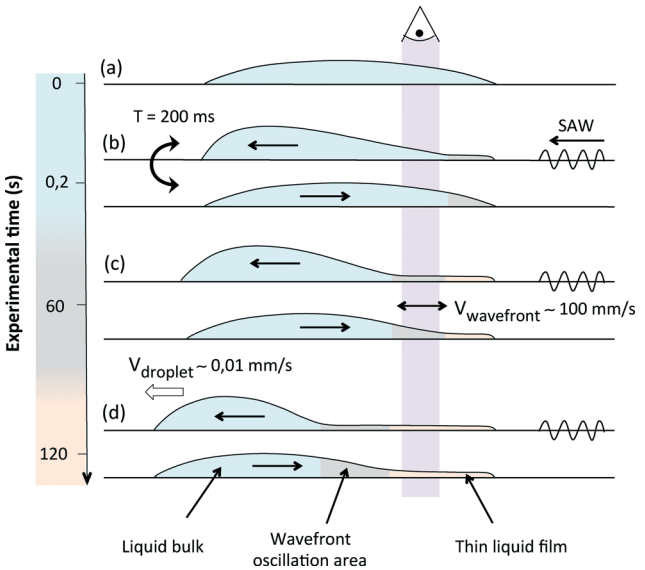

Fig. 4 Schematic diagrams of the different droplet fluid dynamics regimes under modulated SAW actuation (ON: 50 ms, OFF: 150 ms). The vertical bar shows the location of the circular area (2 mm diameter) imaged by the microscope; (a) relaxed shape of the droplet mainly determined by its wetting properties on the cell-covered $LiNbO_3$ substrate; (b) initial shape extrema pair in each excitation/relaxation cycle. (c) After a sufficient number of cycles, a 150 ms relaxation interval between SAW excitation bursts is no longer sufficient to return the droplets to a relaxed symmetric shape of (b). As a result, three distinct fluid dynamics zones can be distinguished: bulk (blue), transient (gray), and thin-film "tail" (orange); (d) eventually, as the droplet spreads sufficiently, the field of view of the camera is confined to the thin-film tail.

electrodes) at a rate of a few microns per cycle while the proximal contact line (droplet edge closest to the SAW electrodes) remained pinned due to the high contact angle hysteresis. As a result, the droplets spread in the direction of SAW propagation at a velocity of ~0.01 mm s^{-1}. As shown in Fig. 4, this expansion elicited three distinct fluidic regimes in the droplets. Since the field of view of the camera (vertical column in Fig. 4) was fixed relative to the spreading droplet, the three fluidic regimes swept sequentially across the field of view and thus could be separated in time in the image sequences.

At the start of the experiments, the expansion was sufficiently small so that the droplets essentially oscillated between the two shape extrema shown schematically in Fig. 4b and in the photographs in Fig. 3b. During SAW excitation (Fig. 4b, top), most of the fluid was displaced in a "bulk" zone at the distal end of the droplet whilst leaving behind a thin film "tail", as previously observed by Rezk *et al.* and Collins *et al.*[55,56] During relaxation, the droplet returned to its relaxed symmetric shape due to surface tension effects (Fig. 4b, bottom).

After a sufficient number of cycles, the distal contact line displacement became significant enough (~0.5 mm) that a 150 ms relaxation interval between SAW excitation bursts was no longer sufficient to return the droplets to a relaxed symmetric shape. As a result, three distinct fluid dynamics regimes (Fig. 4c) could be distinguished in the droplets. As before, the extrema were (1) the bulk (shaded blue area), in which shear stresses result from a combination of large scale vortices induced by Eckart streaming[57] and small-scale vortices due to Rayleigh and Schlichting streaming[58,59] near the viscous boundary layer, and (2) the thin film tail (shaded orange area), in which Schlichting and Rayleigh streaming generated by a standing wave (as evidenced by periodic patterns in Fig. 3c) is dominant.[55] In between the two, a transient zone appeared (gray shaded area), swept by a strong oscillating "wavefront" resulting from the fluid transitions to and from the extrema.

As shown in the experimental results below, the rate of cell detachment from the surface was consistently highest in the transient zone. Eventually, as the droplets spread sufficiently, cells in the field of view of the camera were confined to the thin film tail (Fig. 4d, shaded orange area).

3.2. Magnitude of the shear stresses and unsteady forces in the transient zone

Shear stresses in the fluid acting on the cells were estimated from the image sequences in the transient zone. Assuming no-slip boundary conditions (null velocity at the liquid–solid interface), the vertical shear stress, τ, in the fluid can be linearly approximated (Fig. 3d) by:

$$\tau = \mu \frac{\partial v}{\partial y} \sim \mu \frac{V_{\text{wavefront}}}{h}, \quad (1)$$

where y is the distance perpendicular to the surface, v is the fluid velocity in the direction parallel to the surface at height y, and μ is the dynamic viscosity of the medium (10^{-3} m^2 s^{-1} for PBS at 20 °C). In this formula, $V_{\text{wavefront}}$ and h denote the surface velocity and the height of the thin film, respectively,

estimated from a side-view image sequence (h ~ 100 μm). Under SAW excitation, the "forward" wavefront velocity was about 100 mm s^{-1}, resulting in an estimated vertical shear stress of 1 Pa. When SAW excitation was turned off, the "backward" wavefront velocity was much lower (~10 mm s^{-1}), resulting in an estimated shear stress of 0.1 Pa. For comparison, values of shear stresses reported in the literature to detach cells from treated and untreated surfaces with flow-based systems typically lie between 0.01 and 10 Pa.[16,19,21,60]

In addition to viscous stresses, the pulsatile flow also induces so-called unsteady forces (added mass). The relative magnitudes of viscous and unsteady forces can be quantified by the dimensionless Womersley number $\mathrm{Wo} = \frac{\omega \rho h^2}{\mu}$. In our experiments, Wo was typically ~0.5, meaning that unsteady forces likely also played an important role in cell detachment.

3.3. Cell detachment with a single cell line (HEK 293)

We first investigated the dynamics of cell detachment using our proposed method in experiments with a single cell line (HEK 293). The experiments sought to compare detachment behaviors with substrates prepared using the two protocols described earlier: (1) cells adhered directly to the $LiNbO_3$ substrates after 24 h incubation and (2) $LiNbO_3$ substrates incubated in a solution of resuspended cells (an incubation period of 60 min in this case). In the experiments, ~300 cells were typically adhered initially to the surface in the field of view of the camera.

Because the dynamics of cell detachment from a surface will vary greatly depending on particular conditions, experimental results should be compared in terms of normalized parameters. At a constant rate of detachment, the number of adhered cells will decrease by the same fraction over a time interval of fixed length at any point during the detachment process. As a result, the number of cells adhered to the surface as a function of time, $N(t)$, will follow a decaying exponential profile, $N(t) = N_0 e^{-\sigma t}$, where N_0 is the initial number of attached cells and σ is a detachment rate parameter. Cell detachment dynamics is characterized here in terms of their normalized rate of detachment from the surface, $R(t)$:

$$R(t) = -\frac{1}{N(t)}\frac{\mathrm{d}N(t)}{\mathrm{d}t}. \quad (2)$$

The calculation of $R(t)$ is therefore equivalent to estimating the instantaneous value of the detachment rate parameter, σ, at time t.

Fig. 5 shows the measurements of the fraction of adhered cells over time and the calculated normalized detachment rates under cyclic SAW actuation for experiments with HEK 293 cells prepared with the two adhesion protocols (top: direct to $LiNbO_3$; bottom: incubation in resuspended cells). The three fluid dynamics regimes (bulk, transient and tail) are highlighted by different background colors.

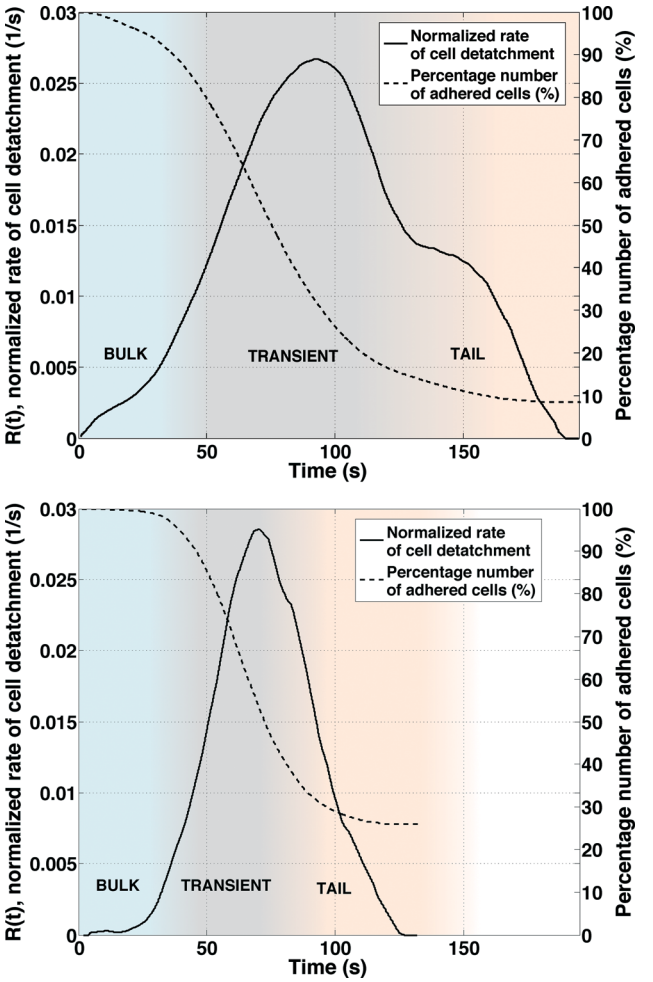

Fig. 5 Normalized detachment rate and percentage of adhered cells over time under cyclic SAW actuation. Top: result from a typical experiment with HEK 293 cells adhered directly to a $LiNbO_3$ substrate after 24 h incubation; bottom: result from a typical experiment with HEK 293 cells adhered to the substrate after incubation in a solution of resuspended cells for 60 min.

Transitions between successive regimes were determined by observing the image sequence where the top of the wavefront in the transient zone could be clearly seen. The uncertainty on estimations of the transition times was on the order of ±5 s. The purpose of these experiments was to explore the relative differences in detachment kinetics between the three fluidic regimes and to extract order of magnitude information if possible about the dynamics. Indeed, a much broader range of experimental conditions would be required to form any kind of quantitative conclusion specific to these particular cell lines.

The results in Fig. 5 clearly show that the cell detachment rate is highest in the transient zone. The two graphs show similar maximum rates of detachment, indicating that both cell adhesion methods can yield similar adhesion strengths to the surface (assuming that detachment rate is an indication of adhesion strength). The inverse of the maximum normalized detachment rate, $1/\max(R(t))$, can be considered as

the "characteristic time" of the system under maximum efficiency, that is to say, the time taken for the number of adhered cells to fall to $(1/e)N_0$ at the maximum rate of detachment. As shown in Fig. 5, this value is ~35 s in both cases. The effect of the duration of the transient regime is also interesting to consider. In Fig. 5 (top), the transient regime is longer (~63 s) resulting in a higher detachment efficacy (>10% residual adhered cells), whereas in Fig. 5 (bottom), due to faster spreading of the droplet, the transient regime is shorter (~46 s) resulting in a lower detachment efficacy (~25% residual adhered cells). In both cases, the majority of cells are detached in minutes, which compares very favorably with the results from other methods.[21,22]

3.4. Cell detachment with dual cell lines (sorting)

We next investigated the selective detachment (sorting) of cell types based on adhesion contrast. $LiNbO_3$ substrates were prepared by incubation in a dual cell solution of resuspended cell lines (A7r5 and HEK293) in a range of incubation periods: 15, 25 and 60 min. Cell sorting performance was characterized by 2 parameters, "purity" and "efficiency", calculated once the system had reached equilibrium, *i.e.* when the number of adhered cells no longer changes (~2 min typically):

$$\text{Purity} = \frac{\%\ \text{HEK 293}_{\text{detached}}}{\%\ \text{HEK 293}_{\text{detached}} + \%\ \text{A7r5}_{\text{detached}}}. \quad (3)$$

$$\text{Efficiency} = \%\ \text{HEK 293}_{\text{detached}}. \quad (4)$$

Fig. 6a shows calculations of cell sorting purity for the three different incubation times. Interestingly, results indicate that purity increases with incubation time. We speculate that this behavior arises because (1) cells require a certain time to achieve complete adhesion and thereby maximizing adhesion contrast between cell types, and (2) it is possible that excretion of the extracellular matrix proteins by A7r5 cells negatively modulates HEK 293 adhesion. Indeed, adhesion modulation by competing species has been observed by other groups, such as the improvement of cancer cell (MCF7) adhesion in the presence of human breast epithelial cells (MCF10A).[15] In all cases, sorting efficiency was greater than 90% (Fig. 6b).

Once detached, cells remained resuspended in the droplets. Short-term viability assays were performed after experiments both with SAW excitation and without SAW as a negative control. Results indicated that SAW excitation only slightly affected the viability (apoptosis rate below 5%).

4. Conclusions

In this paper, we propose a method to selectively and viably detach cells from a solid substrate in fluid droplets using modulated surface acoustic waves (SAWs). Experiments were designed to study the effects of different fluid dynamics regimes by using a fixed imaging field of view with respect to droplet expansion under SAW actuation. Results show that the cell detachment rate is highest in the middle regime, termed "transient regime", where viscous shear stresses are estimated to be of the order of 1 Pa.

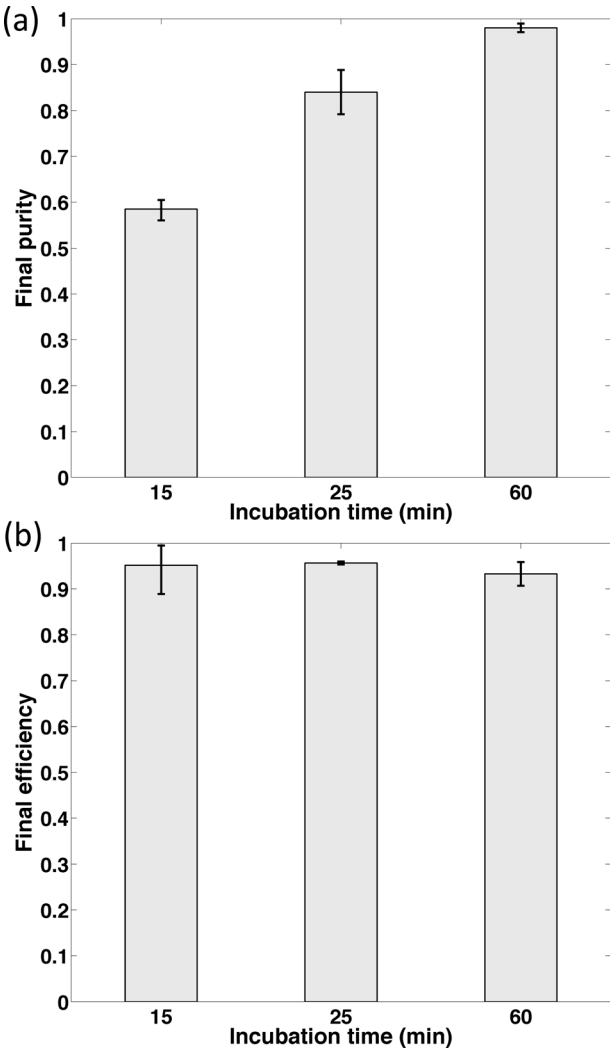

Fig. 6 Cell sorting purity (a) and efficiency (b) for LiNbO3 substrates prepared by incubation in dual cell line resuspended solutions (A7r5 and HEK 293) for a range of incubation periods: 15, 25 and 60 min.

Under the chosen SAW modulation protocol, HEK 293 and A7R5 cells adhered to bare $LiNbO_3$ surfaces were successfully sorted based on adhesion contrast. Results show that cells were detached in the order of minutes and the contrast in adhesion strength varies with incubation time. This method could be generalized to other cell lines exhibiting either intrinsic or controlled (*via* surface bio-functionalization) adhesion contrasts. Importantly, cell adhesion strength is highly dependent on surface preparation specifics and adhesion modulation between competing species. Therefore, SAW excitation parameters required to viably detach and sort cell types under different experimental conditions can be expected to vary according to the characteristics of cell lines,

surface preparation, and adhesion modulation between competing cell species. Similarly, sorting purity and efficiency are expected to be highly dependent on particular experimental conditions.

Interestingly, modulated SAW could be combined with EWOD to detach strongly adhered cells and enhance EWOD cell manipulation and sorting performance. Further investigations with a view to optimizing unsteady forces would also be of interest, for example, with bi-lateral SAW excitation.

Acknowledgements

This work was supported by grants from the Natural Sciences and Engineering Research Council of Canada (NSERC), the Créneau Biotech Santé du Projet ACCORD du Ministère des Finances et de l'Économie (MFEQ) du Québec (Canada), the Agence Nationale pour la Recherche ANR-12-BS09-021-02 et 01 (France), the Direction Générale de l'Armement (France) and Région Nord-Pas-de-Calais (France). The authors would like to thank the Institut Interdisciplinaire d'Innovation Technologique (3IT) at the Université de Sherbrooke (Canada) for technical support.

References

1 L. A. Herzenberg, R. G. Sweet and L. A. Herenberg, *Sci. Am.*, 1976, **234**, 108–117.
2 S. Miltenyi, W. Müller, W. Weichel and A. Radbruch, *Cytometry*, 1990, **11**, 231–238.
3 D. R. Gossett, W. M. Weaver, A. J. Mach, S. C. Hur, H. T. K. Tse, W. Lee, H. Amini and D. Di Carlo, *Anal. Bioanal. Chem.*, 2010, **397**, 3249–3267.
4 L. R. Huang, E. C. Cox, R. H. Austin and J. C. Sturm, *Science*, 2004, **304**, 987–990.
5 M. Yamada and M. Seki, *Lab Chip*, 2005, **5**, 1233–1239.
6 F. F. Becker, X. B. Wang, Y. Huang, R. Pethig, J. Vykoukal and P. R. Gascoyne, *Proc. Natl. Acad. Sci. U. S. A.*, 1995, **92**, 860–864.
7 M. D. Vahey and J. Voldman, *Anal. Chem.*, 2008, **80**, 3135–3143.
8 K. D. M. M. P. MacDonald and G. C. Spalding, *Nat. Biotechnol.*, 2003, **426**, 421–424.
9 A. Jonás and P. Zemánek, *Electrophoresis*, 2008, **29**, 4813–4851.
10 R. Carlson, C. Gabel, S. Chan, R. Austin, J. Brody and J. Winkelman, *Phys. Rev. Lett.*, 1997, **79**, 2149–2152.
11 G. Wang, W. Mao, R. Byler, K. Patel, C. Henegar, A. Alexeev and T. Sulchek, *PLoS One*, 2013, **8**, e75901.
12 T. Laurell, F. Petersson and A. Nilsson, *Chem. Soc. Rev.*, 2007, **36**, 492–506.
13 Y. Ai, C. K. Sanders and B. L. Marrone, *Anal. Chem.*, 2013, **85**, 9126–9134.
14 A. Sin, S. K. Murthy, A. Revzin, R. G. Tompkins and M. Toner, *Biotechnol. Bioeng.*, 2005, **91**, 816–826.
15 K. W. Kwon, S. S. Choi, S. H. Lee, B. Kim, S. N. Lee, M. C. Park, P. Kim, S. Y. Hwang and K. Y. Suh, *Lab Chip*, 2007, **7**, 1461–1468.
16 T. F. Didar and M. Tabrizian, *Lab Chip*, 2010, **10**, 3043–3053.
17 W. Kühne, *Verhandlungen des naturhistorisch-medicinischen Vereins zu Heidelberg, new series*, 1877, vol. 1, pp. 194–198.
18 L. Weiss, *Exp. Cell Res.*, 1961, **8**, 141–153.
19 S. Usami, H. H. Chen, Y. Zhao, S. Chien and R. Skalak, *Ann. Biomed. Eng.*, 1993, **21**, 77–83.
20 M. F. Schneider, Z. Guttenberg, S. W. Schneider, K. Sritharan, V. M. Myles, U. Pamukci and A. Wixforth, *ChemPhysChem*, 2008, **9**, 641–645.
21 A. Hartmann, M. Stamp, R. Kmeth, S. Buchegger, B. Stritzker, B. Saldamli, R. Burgkart, M. F. Schneider and A. Wixforth, *Lab Chip*, 2013, **14**, 542–546.
22 H. Lu, L. Y. Koo, W. M. Wang, D. A. Lauffenburger, L. G. Griffith and K. F. Jensen, *Anal. Chem.*, 2004, **76**, 5257–5264.
23 A. Lenshof and T. Laurell, *Chem. Soc. Rev.*, 2010, **39**, 1203–1217.
24 S.-K. Fan, P.-W. Huang, T.-T. Wang and Y.-H. Peng, *Lab Chip*, 2008, **8**, 1325–1331.
25 G. J. Shah, A. T. Ohta, E. P.-Y. Chiou, M. C. Wu and C.-J. C. J. Kim, *Lab Chip*, 2009, **9**, 1732–1739.
26 G. J. Shah, J. L. Veale, Y. Korin, E. F. Reed, H. A. Gritsch and C.-J. C. Kim, *Biomicrofluidics*, 2010, **4**, 44106.
27 J.-C. Baret, O. J. Miller, V. Taly, M. Ryckelynck, A. El-Harrak, L. Frenz, C. Rick, M. L. Samuels, J. B. Hutchison, J. J. Agresti, D. R. Link, D. A. Weitz and A. D. Griffiths, *Lab Chip*, 2009, **9**, 1850–1858.
28 J. Berthier, *Microdrops and Digital Microfluidics*, William Andrews Publications, 1st edn, 2013.
29 J. T. Parsons, A. R. Horwitz and M. A. Schwartz, *Nat. Rev. Mol. Cell Biol.*, 2010, **11**, 633–643.
30 S. Safran, N. Gov, A. Nicolas, U. Schwarz and T. Tlusty, *Phys. A*, 2005, **352**, 171–201.
31 A. Wixforth, C. Strobl, C. Gauer, A. Toegl, J. Scriba and Z. V. Guttenberg, *Anal. Bioanal. Chem.*, 2004, **379**, 982–991.
32 J. Friend and L. Yeo, *Rev. Mod. Phys.*, 2011, **83**, 647–704.
33 L. Y. Yeo and J. R. Friend, *Annu. Rev. Fluid Mech.*, 2014, **46**, 379–406.
34 W. C. Nelson and C.-J. C. Kim, *J. Adhes. Sci. Technol.*, 2012, **26**, 1–25.
35 M. G. Pollack, R. B. Fair and N. Carolina, *Appl. Phys. Lett.*, 2000, **77**, 1725–1726.
36 Z. Guttenberg, H. Muller, H. Habermüller, A. Geisbauer, J. Pipper, J. Felbel, M. Kielpinski, J. Scriba and A. Wixforth, *Lab Chip*, 2005, **5**, 308–317.
37 T. J. Lyford, P. J. Millard and M. P. Cunha, *IEEE Int. Ultrason. Symp.*, 2012, 1216–1219.
38 A. Renaudin, V. Chabot, E. Grondin, V. Aimez and P. G. Charette, *Lab Chip*, 2010, **10**, 111–115.
39 M. Alghane, Y. Q. Fu, B. X. Chen, Y. Li, M. P. Y. Desmulliez and A. J. Walton, *J. Appl. Phys.*, 2012, **112**, 084902.
40 P. Brunet, M. Baudoin, O. B. Matar and F. Zoueshtiagh, *Phys. Rev. E: Stat., Nonlinear, Soft Matter Phys.*, 2010, **81**, 036315.
41 A. Renaudin, P. Tabourier, V. Zhang, J. Camart and C. Druon, *Sens. Actuators, B*, 2006, **113**, 389–397.
42 A. Qi, L. Y. Yeo and J. R. Friend, *Phys. Fluids*, 2008, **20**, 074103.

43 H. Li, J. R. Friend and L. Y. Yeo, *Biomed. Microdevices*, 2007, **9**, 647–656.
44 Z. Gagnon, J. Gordon, S. Sengupta and H.-C. Chang, *Electrophoresis*, 2008, **29**, 2272–2279.
45 S. Sengupta, J. E. Gordon, H.-C. Chang and N. Dame, *Microfluidic Diagnostic Systems for the Rapid Detection and Quantification of Pathogens*, Springer US, 2009, pp. 271–322.
46 A. Bussonnière, A. Renaudin, Y. Miron, M. Grandbois, M. Baudoin and P. Charette, *Proc. Meetings Acoust.*, 2013, **19**, 045018.
47 H. Li, J. Friend, L. Yeo, A. Dasvarma and K. Traianedes, *Biomicrofluidics*, 2009, **3**, 34102.
48 M. Baudoin, P. Brunet, O. Bou Matar and E. Herth, *Appl. Phys. Lett.*, 2012, **100**, 154102.
49 C. Hartmann and B. Abbott, *Proc. - IEEE Ultrason. Symp.*, 1989, 79–89.
50 B. D. Plouffe, M. Radisic and S. K. Murthy, *Lab Chip*, 2008, **8**, 462–472.
51 C. P. Palmer, M. E. Mycielska, H. Burcu, K. Osman, T. Collins, R. Beckerman, R. Perrett, H. Johnson, E. Aydar and M. B. A. Djamgoz, *Eur. Biophys. J.*, 2008, **37**, 359–368.
52 R. Rodaite-Riseviciene, B. Snopok and V. Snitka, *The 7th IEEE International Conference on Nano/Molecular Medicine and Engineering*, 2013, pp. 7–10.
53 S. Seeger, K. Bierbaum, R. Dahint, C. Feng, M. Mantar and M. Grunze, *Preparation and Characterization of Antibody Films on Lithium Niobate Surfaces*, Springer US, 1992, pp. 53–66.
54 J. Bennès, S. Ballandras and F. Chérioux, *Appl. Surf. Sci.*, 2008, **255**, 1796–1800.
55 A. R. Rezk, O. Manor, J. R. Friend and L. Y. Yeo, *Nat. Commun.*, 2012, **3**, 1167.
56 D. J. Collins, O. Manor, A. Winkler, H. Schmidt, J. R. Friend and L. Y. Yeo, *Phys. Rev. E: Stat., Nonlinear, Soft Matter Phys.*, 2012, **86**, 056312.
57 C. Eckart, *Phys. Rev.*, 1948, **73**, 68–76.
58 L. Rayleigh, *Philos. Trans. R. Soc. London*, 1884, **175**, 1–21.
59 H. Schlichting, *Boundary-Layer Theory*, McGraw-Hill, 1968.
60 A. J. García, P. Ducheyne and D. Boettiger, *Biomaterials*, 1997, **18**, 1091–1098.

Volume 10 | Number 47 | 21 December 2014 | Pages 9375–9586

Soft Matter

www.softmatter.org

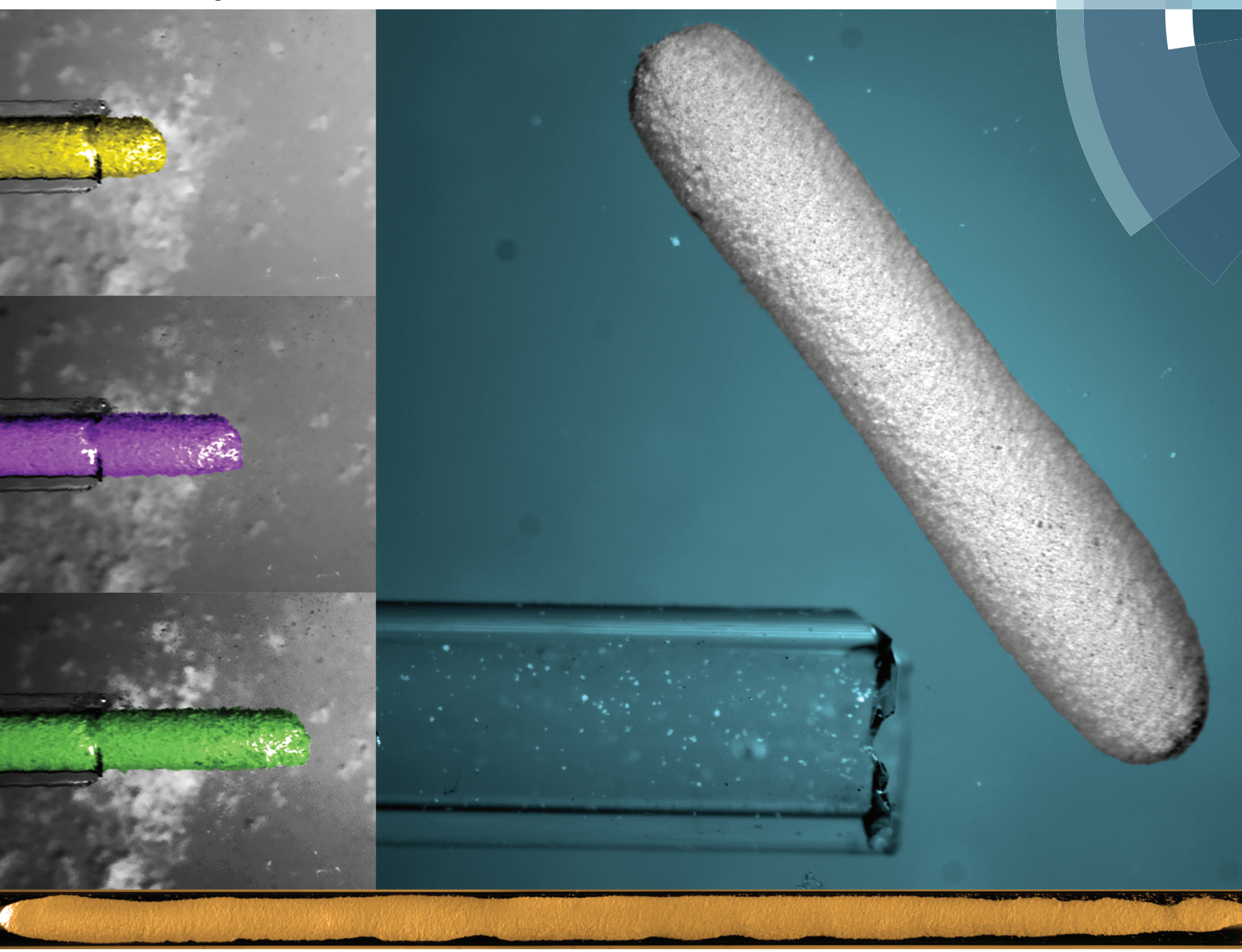

ISSN 1744-683X

ROYAL SOCIETY OF CHEMISTRY

PAPER
Farzam Zoueshtiagh, Michael Baudoin and David Guerrin
Capillary tube wetting induced by particles: towards armoured bubbles tailoring

Soft Matter

PAPER

View Article Online
View Journal | View Issue

Capillary tube wetting induced by particles: towards armoured bubbles tailoring†

Farzam Zoueshtiagh,‡* Michael Baudoin‡* and David Guerrin

Cite this: *Soft Matter*, 2014, **10**, 9403

Received 25th July 2014
Accepted 10th September 2014

DOI: 10.1039/c4sm01648c

www.rsc.org/softmatter

In this paper, we report on the strongly modified dynamics of a liquid finger pushed inside a capillary tube, when partially wettable particles are lying on the walls. Particles promote the appearance of new regimes and enable the tailored synthesis of bubbles encapsulated in a monolayer of particles (so-called "armoured bubbles"). This remarkable behavior arises due to the collection of particles at the air–liquid interface, which modify the global energy balance and stabilize the interface. Armoured-bubbles are of primary interest in industrial processes since they display increased stability, interfacial rigidity and can even sustain non-spherical shapes. This work opens perspective for a low cost bubbles-on-demand technology enabling the synthesis of armoured bubbles with specific sizes, shapes and composition.

1 Introduction

Particle covered interfaces between immiscible fluids are of primary interest in a wide variety of industrial, medical and technological applications: stabilization of bubbly liquids, foams and emulsions,[1–4] flotation-based extraction and separation processes,[5] drug encapsulation,[6] food processing[7] or even surface nanostructuring.[8] Particles drastically alter the behavior of interfaces and make them display solid-like behavior[9] such as interfacial elasticity, buckling instability[10] or cracks formation.[11] When droplets or bubbles are encapsulated in such hybrid interfaces, the "armour" surrounding them strongly modifies their interaction with their environment: Droplets encapsulated inside a layer of partially wettable particles (so-called "liquid marbles") do not wet substrates,[12] thereby suppressing dissipation at the contact line, and also become more stable toward coalescence with other drops.[13] Their bubble counterpart, the "armoured bubbles", have the singular property of sustaining stable non-spherical shape due to the jamming of particles covering their surface.[14] They also exhibit increased stability toward dissolution since they naturally evolve into faceted polyhedral shapes that make the Laplace overpressure vanish.[15] While it has been shown that microfluidic and chemical techniques[16–20] allow the production of spherical droplets with colloidal armour, the tailored production of armoured bubbles with non-spherical shapes, controlled size and composition remains a challenge.

In this paper, we study the dynamics of liquid fingers pushed inside particle-covered capillary tubes. The propagation of liquid fingers in capillary tubes has been largely studied since the early work of Bretherton,[21] Hoffman[22] and Tanner.[23] However, particles have not been considered as a way of modifying the meniscus dynamics and promoting the emergence of new regimes. Bretherton had shown that air blown inside a liquid-filled capillary tube results in the formation of an air finger through the deposition of a liquid film on the walls behind the meniscus. Here we show that the presence of particles on the walls can lead to the mirror situation wherein liquid pushed inside a capillary tube filled with air results in the deposition of a liquid film ahead of the meniscus. This liquid film is covered and stabilized by a single monolayer of closed packed particles. Their jamming prevents the development of Rayleigh-Plateau instability and allows the formation of an encapsulated gas finger with large aspect ratio. This gas finger eventually collapses into an armoured bubble (see Fig. 1) due to an increase of the resistance of the bubbly finger to motion. This system therefore enables the synthesis of armoured bubbles, whose shape and size is prescribed by the geometry of the capillary tube.

Since the appearance of this new regime depends on the global surface energy balance, we investigate here the influence of the wetting properties of the walls and the particles on the evolution of the meniscus. A model is developed and provides a criterion for the formation of armoured bubbles.

2 Materials and methods

2.1 Experimental setup

A liquid finger is either pushed at constant flow rate $Q = 3\ \mu l\ min^{-1}$ with a syringe pump, or at constant pressure head $\Delta P = 0.2$ kPa with a syphon system inside a glass

International Laboratory LEMAC/LICS, IEMN, UMR CNRS 8520, Université Lille 1, Avenue Poincaré, 59652 Villeneuve d'Ascq, France. E-mail: michael.baudoin@univ-lille1.fr; farzam.zoueshtagh@univ-lille1.fr

† Electronic supplementary information (ESI) available. See DOI: 10.1039/c4sm01648c

‡ These authors contributed equally to this work.

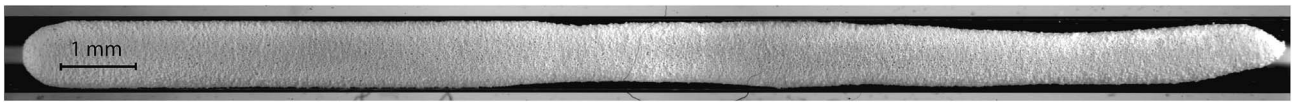

Fig. 1 Cylindrical armoured bubble covered with a monolayer of 15 μm polyamide particle surrounded by water inside a capillary tube of diameter 1 mm.

capillary tube of mean radius $R_w = 501$ μm covered with Rilsan (Polyamide 11) particles of mean radius $R_p = 15$ μm ± 1 μm (see Fig. 2). These particles were scattered in the tube prior to experiments by gently blowing them with an air jet. The dynamics of the moving meniscus is recorded with a CCD camera mounted on a microscope. To avoid diffraction of light by the cylindrical walls, the tube is trapped between two microscope slides and surrounded with an index-matching liquid.

Different wetting configurations were considered (i) by using liquids with different surface tensions (DI water, water/ethanol mixtures, perfluorodecalin) and (ii) by chemically treating the tubes walls to modify their surface energy.

2.2 Capillary tube treatment

Tubes inner walls were treated either with piranha solution (sulfuric acid + hydrogen peroxide), or with Self Assembled Monolayers (SAMs) (silanization process) of different organic molecules: perfluorodecyltrichlorosilane§ (PFTS) or hexamethyldisilazane¶ (HDMS). Piranha solution cleans the organic residues off the glass and leads to perfectly wettable glass walls. SAMs are molecular layers which modify the surface energy of the treated solid in a proportion which depends on the organic molecule adsorbed on the surface.[24,25] SAMs are classically used in labs on chips and droplet microfluidics to turn high energy surfaces such as glass or crystals into hydrophobic surfaces.[26–28]

Capillary tube cleaning. Glass capillaries were freshly cleaned and oxidized to provide a dense array of reactive silanol groups (≡SiOH), which are anchoring sites for the organosilane molecules. Capillaries were first degreased by sonication in dichloromethane, then isopropanol for 5 min. Glass substrates were perfectly dried under nitrogen flow, then in an air oven at 120 °C for 30 min. Then, the samples were dipped into a freshly prepared piranha solution (H_2SO_4, H_2O_2 2 : 1 v/v) at 100 °C for 15 min. They were rinsed thoroughly with deionized water, then were dried under nitrogen stream. To remove water inside capillaries, they were dried in an air oven at 120 °C for 1 h. This cleaning procedure was used to obtain perfectly wettable glass walls but also to prepare the tubes for their silanization. The drying procedure in the last step is very important for silanization since water excess is problematic as it causes hydrolysis and polymerization of organosilane molecules in solution.

Silanization‖. Glass capillaries were coated with SAMs using two organosilanes bearing either methyl (HDMS) or perfluorated (PFTS) functions. By a well-known mechanism (see Fig. 3), these molecules spontaneously react with the silanol ≡SiOH groups on the glass surface providing a hydrophobic molecular film. The silanization reactions were carried out in a glovebox under nitrogen atmosphere since HMDS and PFTS are water sensitive. The cleaned glass capillaries were immersed for 2 h in a 10^{-3} M solution of organosilane in a mixture of *n*-hexane and dichloromethane (70 : 30 v/v). Capillaries were cleaned thoroughly in dichloromethane (2 times) by sonication, then blown with dry nitrogen.

Wetting properties of the walls and particles. The wetting properties of the walls and particles for each surface treatment and liquid were characterized respectively by the static contact angles θ_w and θ_p for negative spreading parameters S_w and S_p. The spreading parameter gauges the ability of a liquid to wet a solid surface. When the spreading coefficient is positive, the liquid wets the surface completely. When it is negative, the liquid wets partially the solid surface and thus the gas interface meets the solid–liquid interface with an angle called the contact angle. The wetting properties of the walls for the different liquids used in our experiments (DI water, water/ethanol mixtures, perfluorodecalin) were measured by applying the

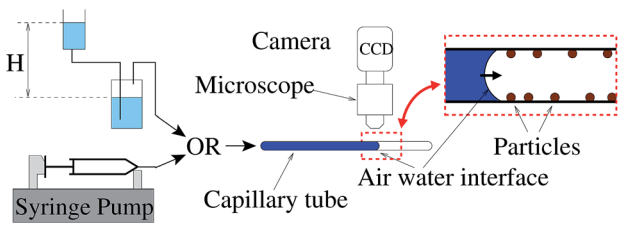

Fig. 2 Experimental setup.

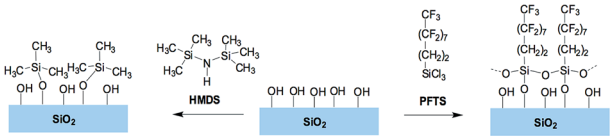

Fig. 3 Silanization process.

§ 1*H*,1*H*,2*H*, 2*H*-Perfluorodecyltrichlorosilane $CF_3(CF_2)_7(CH_2)_2SiCl_3$.

¶ Hexamethyldisilazane $(CH_3)_3SiNHSi(CH_3)_3$.

‖ HMDS and PFTS were obtained from Gelest. Dichloromethane (99.9%, amylene stabilized) was obtained from Scharlau. *n*-Hexane (99%, ACS grade) and isopropanol (99.7%) were purchased from Carlo Erba. Sulfuric acid (98%) and hydrogen peroxide (30% in water) were purchased from Sigma Aldrich. All chemicals were used as received without further purification. Deionized water (18 MΩ cm) was used to rinse substrates.

Table 1 Values of the static contact angle (when the spreading parameter S is negative) with the walls θ_w and particles θ_p for the different liquids used in the experiments and different walls chemical treatments. When the liquid fully wets the walls or the particles, the spreading parameter is positive

	Glass	Glass treated with HDMS	Glass treated with PFTS	Particles
DI water	$S_w > 0$	$\theta_w = 62 \pm 1$	$\theta_w = 106 \pm 8$	$\theta_p = 71 \pm 3$
Water-Eth. 6%	$S_w > 0$	$\theta_w = 62 \pm 1$	$\theta_w = 88 \pm 3$	$\theta_p = 71 \pm 5$
Water-Eth. 27%	$S_w > 0$	$\theta_w = 51 \pm 3$	$\theta_w = 80 \pm 1$	$\theta_p = 48 \pm 1$
Perfluorodecalin	$S_w > 0$	$\theta_w = 10 \pm 4$	$\theta_w = 34 \pm 3$	$S_p > 0$
Ethanol	$S_w > 0$	$S_w > 0$	$\theta_w = 42 \pm 4$	$S_p > 0$

same chemical treatment to a glass wafer as the one applied to the capillary tube and then measuring the static contact angle of a sessile droplet deposited on the substrate. The wetting properties of the particles were characterized by the same method after having coated the glass wafer with a thin film of Rilsan obtained by melting down the particles. These wetting properties are summarized in Table 1.**

3 Experimental results

3.1 Liquid finger pushed at constant flow rate

Experiments have been performed for all wetting configurations described in Table 1. In this section, the liquid is pushed at constant flow rate $Q = 3$ μl min^{-1}. We identified four main regimes with respect to the walls and particles wetting properties (see phase diagram in Fig. 4).

Regime 1. Perfectly wettable particles ($S_p > 0$). Here, particles are weakly affected by the motion of the meniscus for both cases of perfectly ($S_w > 0$) and partially ($S_w < 0$) wettable walls. For perfectly wettable walls ($S_w > 0$), a liquid film is present ahead of the meniscus due to local evaporation and condensation in front of the meniscus. In such a situation, the passage of the meniscus across the particles has no or negligible effect since the particles are already immersed in the liquid film prior to the meniscus arrival (Fig. 5A and Movie S1†). For partially wettable walls however ($S_w < 0$), there is no macroscopic liquid film ahead of the meniscus. As a consequence, particles are attracted by the liquid as soon as they are touched by the interface and then simply released behind the meniscus (Fig. 5B and Movie S2†).

Regime 2. Perfectly wettable walls ($S_w > 0$) and partially wettable particles ($S_p < 0$, $\theta_p \in [0,\pi/2]$). This regime leads to the formation of armoured bubbles. At the beginning, particles are collected at the surface of the meniscus until it becomes entirely covered with a monolayer of packed particles (see Fig. 6B, Movie S3†). Then, the interface keeps growing, through the development of a particle-covered liquid film ahead of the meniscus. This results in the formation of a long gas finger covered with particles (Fig. 6C, Movie S4†). This gas finger eventually collapses (see Fig. 6D, Movie S5†) and forms a long cylindrical armoured bubble (see *e.g.* Fig. 1).

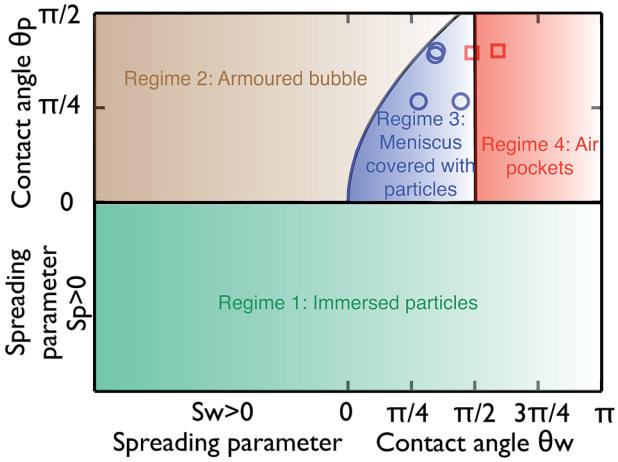

Fig. 4 Phase diagram summarizing the four regimes observed depending on the spreading parameters S_p and S_w of the walls and particles or the contact angles θ_p and θ_w when the spreading parameter is negative. The line separating regimes 2 and 3 has been computed according to eqn (5). Since the values of the spreading parameters is not known when it is positive for the material used in our experiments, only data with $S_p < 0$ and $S_w < 0$ are represented in this graph.

Regime 3. Walls with high wettability ($S_w < 0$, $\theta_w < \pi/2$) and partially wettable particles ($S_p < 0$) with $\theta_p \in [0, \theta_c]$.†† Particles are first collected at the surface of the meniscus until it becomes entirely covered with a monolayer of packed particles (see Fig. 7B), similarly to Regime 2. Then, new particles contribute to the growth of the particle-covered interface through a reduction of the apparent contact angle with the surface down to a limiting value, θ_l. Once this limiting value is reached, new particles which come into contact with the meniscus are immersed inside the liquid finger (see Fig. 7C and Movie S3†).

** The exact value of the spreading parameter when the liquid wets the surface completely ($S > 0$) is difficult to determine since it requires the knowledge of the solid–gas and solid–liquid surface energies. When it is negative however, it is linked to the contact angle θ and the surface tension γ_{GL} according to the formula: $S = \gamma_{GL}(\cos\theta - 1)$.

†† θ_c is the critical contact angle defined by eqn (5).

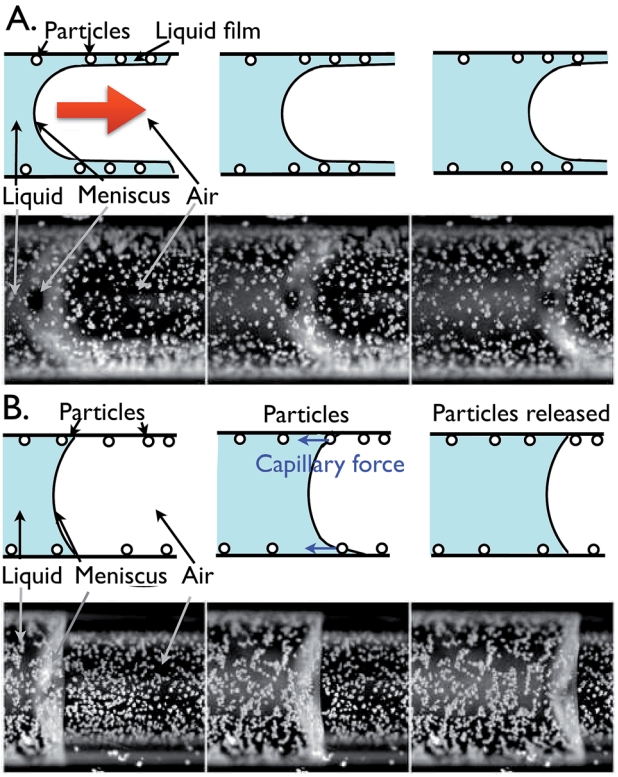

Fig. 5 Regime 1: Schematic and snapshots of experiments showing the evolution of a liquid finger pushed at constant flow rate inside a capillary tube covered with perfectly wettable particles (white dots in the pictures). (A) Perfectly wettable walls (B). Partially wettable walls.

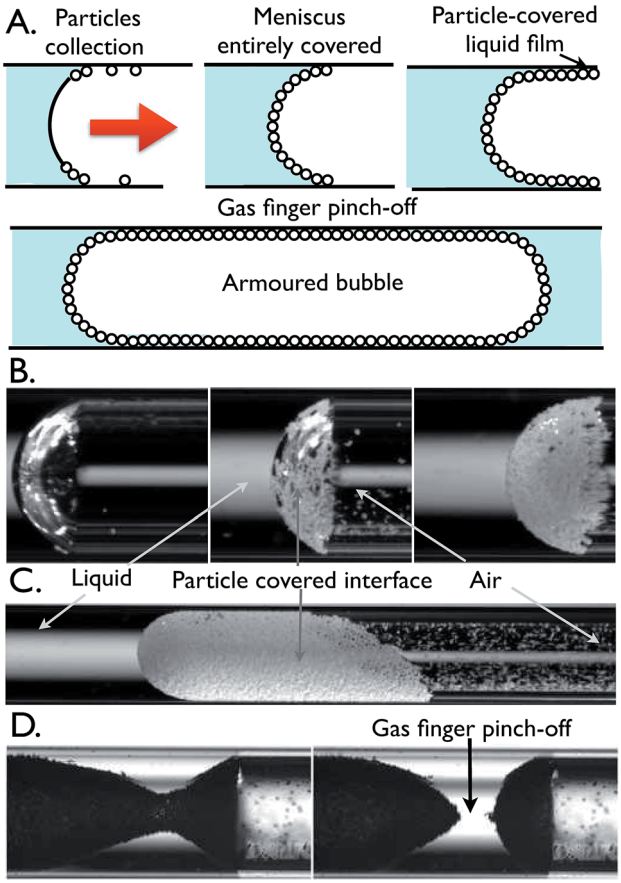

Fig. 6 Regime 2: Liquid finger pushed at constant flow rate inside a perfectly wettable capillary tube covered with partially wettable particles. (A) Schematic of the evolution of the air–liquid interface. (B) Particles are collected until they cover the whole meniscus. (C) A liquid layer covered with a monolayer of particles grows ahead of the meniscus leading to the formation of an encapsulated gas finger. (D) The pinch-off of the gas finger results in the formation of an armoured bubble (Fig. 1). Particles appear in dark in picture D since the lighting conditions were different.

Regime 4. Walls with low wettability ($S_w < 0$, $\theta_w > \pi/2$) and partially wettable particles ($S_p < 0$). In this case, the particles accumulate along the contact line and obstruct its motion. Since the flow rate is imposed, the meniscus eventually bypasses the particles. This gives rise to the formation of air pockets trapped between the tube's wall and the liquid inside the capillary, and whose surface is covered with particles (see Fig. 8 and Movie S7†).

3.2 Liquid finger pushed at constant pressure

Further experiments were conducted in regime 2 to determine the evolution of the encapsulated bubbly finger resistance to motion and gain physical insight of the reason for its collapse into and armoured bubble. In these experiments a long liquid plug is pushed at constant pressure head $\Delta P = 0.2$ kPa inside a perfectly wettable capillary tube covered with Rilsan particles (see Fig. 9A and B and Movies S8 and S9†). In the absence of particles, experiments in the literature[29] indicate that a plug pushed at constant pressure experiences a gradual increase of its velocity due to a progressive decrease of its resistance to motion. Instead, in the present experiment, a gradual decrease in the plug's velocity is observed along with a stick-slip motion of the plug when the length of the encapsulated finger becomes sufficiently large (see Fig. 9C).

4 Discussion and theoretical modeling

In this section, the different regimes observed experimentally are discussed and simple energetic considerations are developed to provide basic understanding of the observed tendencies.‡‡ In all the experiments described above, the Reynolds number $\mathrm{Re} = \rho_l U R_w/\mu_l$, Capillary number $\mathrm{Ca} = \mu_l U/\gamma_{GL}$ and Bond number $\mathrm{Bo} = \rho_l g {R_w}^2/\gamma_{GL}$ remain small:

$$\mathrm{Re} \lesssim 10^{-2}, \mathrm{Bo} \lesssim 10^{-1} \text{ and } \mathrm{Ca} \lesssim 10^{-6}$$

‡‡ As a first approximation, particles are supposed to be perfectly spherical in the following calculations while this is not the case experimentally. Higher order effects could therefore appear in this case such as particle–particle interaction due to the asymmetry of the particles. Nevertheless, they would not fundamentally modify the liquid film deposition mechanism proposed here.

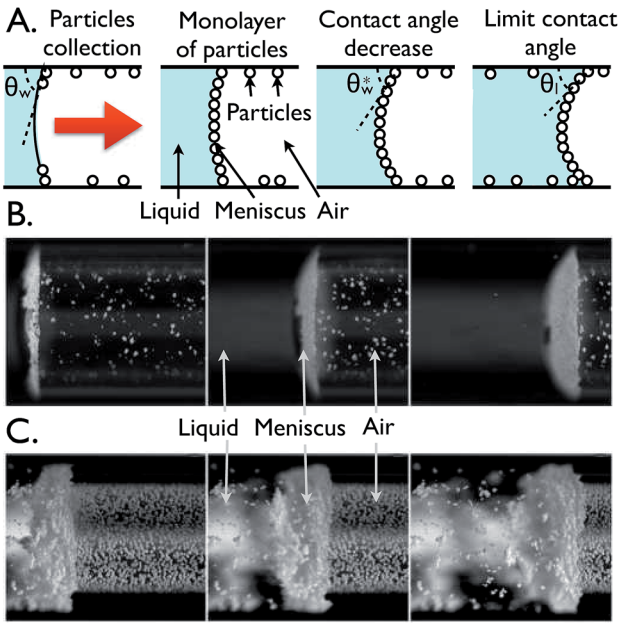

Fig. 7 Regime 3: Liquid finger pushed at constant flow rate inside capillary tubes with highly wettable walls covered with partially wettable particles whose contact angle θ_p is under the critical value θ_c defined by eqn (5). (A) Schematic illustrating the evolution of the meniscus. (B) Snapshots of the capillary tube showing the collection of the particles encountered by the meniscus and the reduction of the contact angle. (C) Evolution of the meniscus once the contact angle has reached a limiting value θ_l.

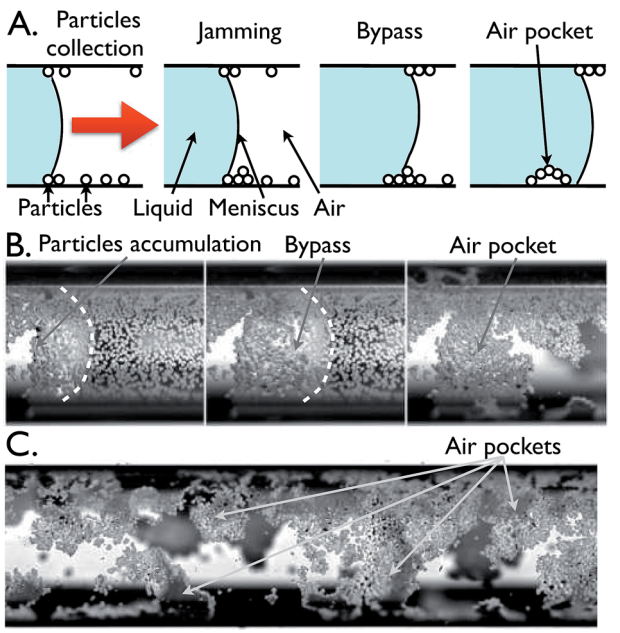

Fig. 8 Regime 4: Liquid finger pushed at constant flow rate inside a capillary tube with low wettability covered with partially wettable particles. (A) Schematic illustrating the evolution of the meniscus. (B) Snapshots showing the formation of an air pocket. The dashed white line indicates the position of the meniscus. (C). Final state after the passage of the meniscus.

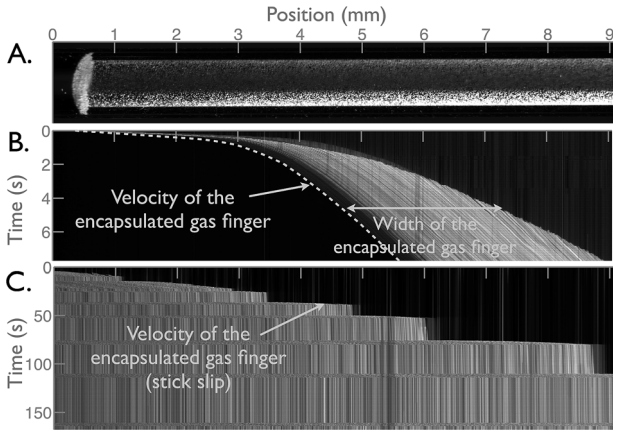

Fig. 9 Evolution of a liquid plug pushed at constant pressure in a wetting tube covered with partially wettable particles. (A) Initial configuration: the front meniscus is covered with a monolayer of particles. (B) Spatiotemporal diagram displaying the grey values along the center line of the channel as a function of time. Velocities and lengths of the encapsulated gas finger are respectively obtained from the slopes of the boundaries of the grey part of the graph and the distance between them. The grey dashed line delimit the left part of the bubble. (C) Spatiotemporal diagram showing the evolution of the right part of the encapsulated gas finger when its length is equal to 1.6 cm. The velocity of the gas-finger is given by the boundary between the grey part (particles) and the dark one (liquid). The steps indicate stick-slip motion.

with ρ_l, μ_l and γ_{GL}, the density, viscosity and surface tension of the considered liquid respectively, $U = Q/(\pi R_w^2)$, the characteristic velocity of the liquid finger and g the gravitational acceleration.§§ This means that, away from the contact line (where the triple line introduces a flow singularity), surface tension effects are dominant over those of inertia, gravitation and viscosity. The shape of the meniscus is therefore only determined by the minimization of surface energy. Furthermore, since the capillary number is extremely small, the dynamic contact angle differs only slightly from the static contact angle¶¶ and thus, the evolution of the meniscus can be considered as quasi-static (that is to say a succession of equilibrium states).

When the first particles come into contact with the meniscus, the system spontaneously selects the configuration which minimizes the total interfacial energy E. The latter is the sum of the gas–liquid (GL), gas–wall (GW), liquid–wall (LW), gas–particle (GP) and liquid-particle (LP) energy:

$$E = \gamma_{GL}A_{GL} + \gamma_{GW}A_{GW} + \gamma_{LW}A_{LW} + \gamma_{GP}A_{GP} + \gamma_{LP}A_{LP}$$

§§ In regime 2, the characteristic velocity of the liquid film is of the same order of magnitude as the velocity U. Indeed, the liquid film velocity is equal to the sum of the meniscus velocity and the expansion velocity of the liquid film. The latter depends on the concentration of particles on the walls prior to the experiment. In the experiments performed here, the characteristic velocity of the liquid film is typically 15% higher than the velocity of the meniscus and thus does not modify the estimation of the capillary number provided in this section.

¶¶ Hoffman–Tanner law[22,23] predicts a dynamic contact angle $\leq 3°$ for a perfectly wetting liquid moving at a capillary number Ca $\sim 10^{-6}$.

where γ and A are the tension and area of the corresponding interface, respectively. The global constraint of minimum energy leads to 3 local constraints: (i) the liquid–gas interface satisfies Young–Laplace's equation and adopts a spherical shape, and the triple lines (ii) on the wall and (iii) at the particle surface satisfy Young–Dupré's equation:

$$\cos\theta_w = \frac{\gamma_{GW} - \gamma_{LW}}{\gamma_{GL}}, \quad \cos\theta_p = \frac{\gamma_{GP} - \gamma_{LP}}{\gamma_{GL}} \tag{1}$$

with θ_w and θ_p, the wall and particle static contact angles, respectively. As a result of condition (iii), perfectly wettable particles ($S_p > 0$) are immersed in the liquid (regime 1) whereas partially wettable particles ($S_p < 0$) are trapped at the interface (regime 2, 3 and 4). For wettable walls ($\theta_w < \pi/2$, regimes 2 and 3), the same condition applies for the successive particles until the meniscus is entirely covered with a monolayer of particles. For walls with low wettability ($\theta_w > \pi/2$) however (regime 4), particles captured at the contact line prevent the liquid from coming into contact with new particles due to jamming (see Fig. 8A) and so, the lowest energy state cannot be reached. Particles accumulate along the contact line and obstruct its motion. As the flow rate is imposed, the liquid finger is pushed forward and the contact line eventually bypasses the pile of particles resulting in the formation of air pockets on the tube's wall (see Fig. 8C).

We will now discuss regimes 3 once the meniscus is entirely covered with a monolayer of particles. When new particles come into contact with the meniscus, three different situations can occur: (i) particles are immersed in the liquid phase, (ii) they are integrated into an extended meniscus, or (iii) they stay in the gas phase. Since in regimes 2 and 3 the particles are partially wettable, interfacial energy is always lower in configuration (ii) as compared to (iii). Thus, situation (iii) cannot occur in the absence of additional constraints.

Now the following calculations are aimed at forecasting the system selection between configurations (i) and (ii) by determining the least energetic configuration according to values of contact angles θ_w and θ_p. To calculate the energy difference δE between configurations (i) and (ii), one can determine the energy required for the transition between these two states.

This transition can be decomposed into two steps (see Fig. 10): (1) the surface of the meniscus increases to leave enough space to integrate a new particle (variation of energy δE^+) and (2) the particle migrates at the air–liquid interface (variation of energy δE^-):

$$\delta E = \delta E^+ + \delta E^- \tag{2}$$

In configuration (ii), the absorption of a new particle by the meniscus requires the expansion of its surface by $\delta S = \pi {R_p}^2/\phi$, where ϕ is the specific surface area as defined by Torquato[30] ($\phi \approx 0.8$ for spheres in a 2D configuration). Indeed due to their shape, the particles occupy only a fraction of the air–liquid interface. For partially wettable walls, this expansion leads to a decrease of the contact angle by $\delta\theta_w^* = [\cos^3(\theta_w)/(2(\sin(\theta_w^*)(2 - \sin(\theta_w^*)) - 1))][R_p^2/(R_w^2\phi)]$, which in turn yields an increase in interfacial energy by:

$$\delta E^+ = \frac{\pi\gamma_{GL}{R_p}^2}{\phi}\left[1 - \frac{\cos(\theta_w)}{\cos(\theta_w^*)}\right]$$

where θ_w^* is the apparent contact angle sustained by the presence of particles at the interface (see Appendix A for details of this calculation). On the other hand, the integration of a new particle to the interface leads to a decrease of interfacial energy by:

$$\delta E^- = -\gamma_{GL}\pi {R_p}^2[1 - \cos(\theta_p)]^2$$

since a partially wettable particle lies in its less energetic configuration when it is trapped at an air–liquid interface with a contact angle θ_p. Thus, configuration (ii) is energetically favorable if:

$$\delta E = \pi\gamma_{GL}{R_p}^2\left[\frac{1}{\phi}\left(1 - \frac{\cos(\theta_w)}{\cos(\theta_w^*)}\right) - \left(1 - \cos(\theta_p)\right)^2\right] < 0. \tag{3}$$

This function is always negative at the beginning when $\theta_w^* = \theta_w$ and results in a decrease in the apparent contact angle θ_w^* until it reaches a limit value θ_l corresponding to $\delta E = 0$:

$$\cos(\theta_l) = F(\theta_p,\theta_w) = \frac{\cos(\theta_w)}{1 - \phi\left(1 - \cos(\theta_p)\right)^2}. \tag{4}$$

Then, new incoming particles are immersed into the liquid phase (regime 3). However, if $F(\theta_p,\theta_w) \geq 1$, that is to say:

$$\theta_p \geq \theta_c = a\cos\left[1 - \sqrt{\frac{1 - \cos(\theta_w)}{\phi}}\right] \tag{5}$$

Eqn (4) has no solution and thus the contact angle decreases down to 0. At this stage, the interface can only expand ahead of the meniscus with the development of a liquid film which recovers the wall (regime 2). Calculations (see Appendix B) indeed show that this liquid expansion is energetically

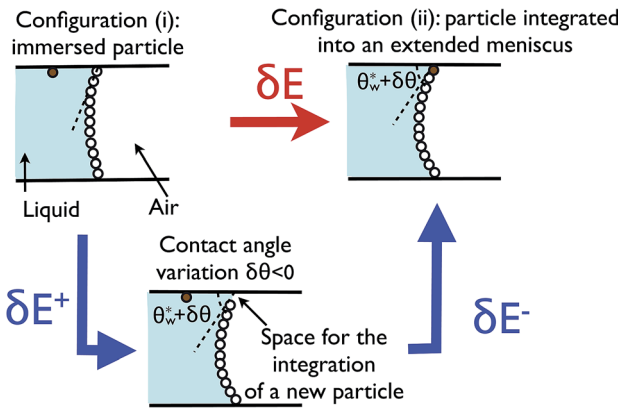

Fig. 10 Transition between configuration (i) and (ii).

favorable when criterion (5) is verified or when the walls are perfectly wetting ($S_w > 0$) and the particles partially wetting ($S_p < 0$). This minimization of the surface energy thus explains the growth of the particle-covered interface through the deposition of a film ahead of the meniscus observed in regime 2.

This liquid film is stabilized by particles jamming in the monolayer, which prevents the development of Rayleigh-Plateau instability. The air finger pinch-off is only enabled by the large pressure head increase resulting from the increase in the resistance of the encapsulated finger to motion. Indeed, the motion of liquid plugs and fingers in micro-channels can be described through an Ohm-like law, $\Delta P = Qr_b$, where ΔP is the pressure drop along the channel and r_b is the liquid plug's or finger's resistance to motion.[29] In Section 3.2, experiments performed at constant pressure indicate a drastic reduction of the velocity of the encapsulated bubbly finger when its size increases through the collection of particles lying on the walls. This reduction of the velocity indicate an increase in the resistance r_b. At constant flow rate, this resistance increase will lead to a large increase in the driving pressure head, which eventually provokes the pinch-off of the gas finger. The prediction of the final size of the armored bubble would require the knowledge of (i) the pressure required for the pinch-off of the bubble and (ii) the evolution of the pressure head resulting from the increase of the bubble resistance to motion. This increase of resistance might have different origins such as the friction of particles with the walls or the viscous dissipation in the liquid film separating the bubble from the tube. Further experiments would be required to determine the comparative contributions of these phenomena.

5 Conclusion and perspectives

In this paper, we study the strongly modified dynamics of a liquid finger pushed inside a capillary tube when particles are lying on the walls. Different regimes are observed according to the wetting configuration. One of these regimes leads to the controlled formation of armoured bubbles covered with a monolayer of particles, whose shape and lateral size is prescribed by the geometry of the capillary tube. This system enables a serial production of such armoured bubbles. Indeed, once an armoured bubbles is formed another starts growing in the remaining part of the tube, and so on until all the particles lying on the walls have been collected. These encapsulated bubbles can then be extracted from the capillary tube by pushing them with a higher flow rate. Once out of the tube, they keep their cylindrical shape since the jamming of particles prevents the reduction of the bubble surface (see Fig. 11). This works opens perspectives for low cost automatic production of armoured bubbles with specific geometries. The production of a large number of identical armoured bubbles would nevertheless require a parallelization and an optimization of the present experimental setup to obtain bubbles with predictable lengths.

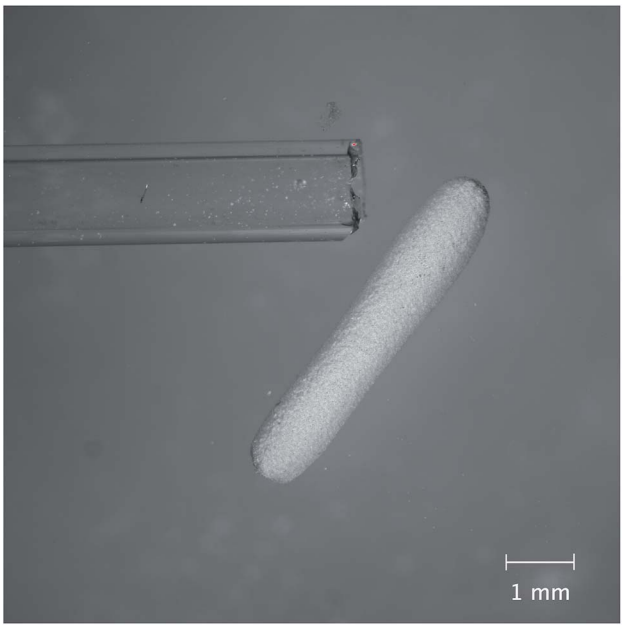

Fig. 11 Stable cylindrical armoured bubble extracted from the tube. It is obtained by pushing the long armored bubble formed in the capillary tube with a higher flow rate into a larger cell. In these preliminary experiments, the buoyancy force resulted in the division of the long armored bubble into smaller bubbles.

The present method might, in principle, be extended to the production of encapsulated bubbles in a colloidal crystal[31,32] or ordered two dimensional arrays[33] if neutral particles are replaced by strongly interacting ones. For macroscopic particles, these interactions can result from the balance of gravity and surface tension, the so-called "Cheerios" effect.[34,35] At smaller scales (micrometer to nanometer range), gravity is negligible and so interaction can be induced by electrical charges,[31,36] irregular shape,[37] roughness,[38] or inhomogeneous wetting properties of the particles.[33] They could also be triggered by interface curvature as demonstrated recently by Würger.[39]

These singular bubbles are interesting for their static properties (stability, original shape); but their strongly nonlinear dynamics also opens new perspective for the design of original acoustical materials such as contrast agents.

Appendix A: decrease of the apparent contact angle induced by the presence of particles on the walls

This appendix is giving the details of calculations for the variations of energy, $\delta E = \delta E^+ + \delta E^-$ expressed in eqn (3). Here, we will only consider particles with small radius R_p compared to the radius of curvature of the meniscus R_c and thus neglect the interface curvature at the scale of a particle. This hypothesis is well verified in our experiments since $R_p/R_c < 2 \times 10^{-2}$. We will also suppose that the evolution is quasi-static, as justified in the main text.

Increase of energy due to the decrease of the contact angle

In absence of particles, the contact angle at the liquid–air–wall triple line is given at rest by Young–Dupré's equation:

$$\cos\theta_w = \frac{\gamma_{GW} - \gamma_{LW}}{\gamma_{GL}} \quad (6)$$

where γ_{GW}, γ_{LW} and γ_{GL} are the gas–wall, liquid–wall and gas–liquid tensions respectively. This equation can be simply deduced from a minimization of the interfacial energy. The integration of an additional particle to the air–liquid interface requires an increase of the meniscus surface δA_{GL} through a reduction of the contact angle $\delta\theta_w^*$. This surface increase, δA_{GL}, yields to an increase of interfacial energy $\delta E^+ = dE_w/d\theta_w^* \delta\theta_w^*$ where $E_w = \gamma_{GL}A_{GL} + \gamma_{GW}A_{GW} + \gamma_{LW}A_{LW}$ is the sum of the gas–liquid, gas–wall and liquid–wall interfacial energy in absence of particles and θ_w^* is the wall apparent contact angle at a certain point of the evolution. We must therefore determine the expressions of $\delta\theta_w^*$ and $E_w(\theta_w^*)$ to estimate δE^+.

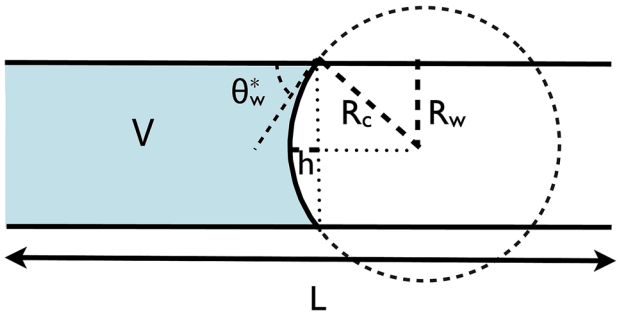

Fig. 12 Schematic of the meniscus.

Computation of $\delta\theta_w^*$. Due to their shape and arrangement, the particles cover only a fraction, ϕ, of the air–liquid interface, called the specific surface area. The air–liquid surface increase δA_{GL} required for the integration of a single particle is therefore:

$$\delta A_{GL} = \pi R_p^2/\phi. \quad (7)$$

Suppose that the wall apparent contact angle at a certain point of the evolution is equal to θ_w^* (with $\theta_w^* = \theta_w$ just prior to meniscus surface increase, *i.e.* when the first additional particle reaches the meniscus which has its surface fully covered by particles). The surface of the meniscus A_{GL} can be expressed as a function of θ_w^* according to (see Fig. 12):

$$A_{GL} = 2\pi R_c h = 2\pi R_c \times (1 - \sin(\theta_w^*))R_c \quad (8)$$

$$= \frac{2\pi R_w^2(1-\sin\theta_w^*)}{\cos^2\theta_w^*} \quad (9)$$

with $R_c = R_w/\cos(\theta_w^*)$ the radius of curvature of the meniscus, R_w the tube radius and h the height of the meniscus. From this formula, we can compute the decrease of contact angle $\delta\theta_w^*$ resulting from the increase of interface δA_{GL}:

$$A_{GL} + \delta A_{GL} = \frac{2\pi R_w^2(1-\sin(\theta_w^* + \delta\theta_w^*))}{\cos^2(\theta_w^* + \delta\theta_w^*)} \quad (10)$$

Since $\delta A_{GL} \ll A_{GL}$ and $\delta\theta_w^* \ll \theta_w^*$, the first order taylor series expansion gives:

$$\delta A_{GL} = [\sin\theta_w^*(2 - \sin\theta_w^*) - 1]\frac{2\pi R_w^2}{\cos^3\theta_w}\delta\theta_w^* \quad (11)$$

Finally the combination of eqn (7) and (11) gives:

$$\delta\theta_w^* = \frac{\cos^3\theta_w^*}{2[2\sin\theta_w^* - \sin^2\theta_w^* - 1]}\frac{R_p^2}{R_w^2\phi} \quad (12)$$

Computation of $E_w(\theta_w^*)$ and its derivative. To compute, the relation between the interfacial energy E_w and the contact angle θ_w^*, we will consider a cylindrical capillary tube of length L and radius R_w partially filled with a volume V of liquid and a volume $\pi R_w^2 L - V$ of gas (see Fig. 12). The interfacial energy E_w is given by:

$$E_w = \gamma_{GL}A_{GL} + \gamma_{GW}A_{GW} + \gamma_{LW}A_{LW}$$

with the interfacial areas A_{LW} and A_{GW} given by:

$$A_{LW} = 2\pi R_w\left[\frac{V}{\pi R_w^2} + \frac{R_w}{3\cos^3\theta_w^*}(1-\sin\theta_w^*)^2(\sin\theta_w^* + 2)\right] \quad (13)$$

$$A_{GW} = 2\pi R_w L - A_{LW} \quad (14)$$

Expression of δE^+. Combination of eqn (7), (12), (13) and (14) gives:

$$\delta E^+ = \frac{dE_w}{d\theta_w^*}\delta\theta_w^* = \frac{d(\gamma_{GW}A_{GW} + \gamma_{LW}A_{LW})}{d\theta_w^*}\delta\theta_w^* + \gamma_{GL}\delta A_{GL}$$
$$= \left[\frac{2\pi R_w^2(\gamma_{GW} - \gamma_{LW})}{2\sin\theta_w^* + (\sin^2\theta_w^* + 1)}\right]$$
$$\times\left[\frac{\cos^3\theta_w^*}{2[2\sin\theta_w^* - (\sin^2\theta_w^* + 1)]}\frac{R_p^2}{R_w^2\phi}\right] + \frac{\gamma_{GL}\pi R_p^2}{\phi} \quad (15)$$

Since $\gamma_{GW} - \gamma_{LW} = \gamma_{GL}\cos\theta_w$ and $[1 - 2\sin^2\theta_w^* + \sin^4\theta_w^*] = \cos^4\theta_w^*$, eqn (15) can be simplified into:

$$\delta E^+ = \frac{\gamma_{GL}\pi R_p^2}{\phi}\left[1 - \frac{\cos\theta_w}{\cos\theta_w^*}\right] \quad (16)$$

In regimes 2 and 3, walls are respectively perfectly and highly wettable ($0 \le \theta_w^* \le \theta_w < \pi/2$) and, as expected, δE^+ is positive.

Decrease of energy due to the integration of a particle at the meniscus

When a particle comes into contact with an air–liquid interface, the system adopts the minimal energy configuration, in absence of additional constraint. A partially wettable particle will therefore be trapped at the air–liquid interface with an angle given by Young Dupré's equation around the particle:

$$\cos\theta_p = \frac{\gamma_{GP} - \gamma_{LP}}{\gamma_{GL}} \quad (17)$$

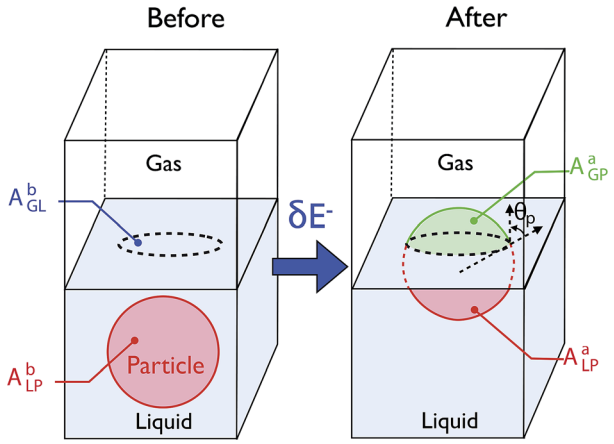

Fig. 13 Migration of a particle to the meniscus.

Therefore, the migration of a particle from the liquid phase to the interface corresponds to a decrease of the interfacial energy δE^-. This variation can be computed by subtracting the interfacial energy before and after the migration of the particle (see Fig. 13):

$$\delta E^- = [\gamma_{GP}A^a_{GP} + \gamma_{LP}A^a_{LP}] - [\gamma_{GL}A^b_{GL} + \gamma_{LP}A^b_{LP}] \quad (18)$$

From Fig. 13, we easily obtain.

$$\delta E^- = \gamma_{GP}[2\pi {R_p}^2(1 - \cos(\theta_p))] + \gamma_{LP}[2\pi {R_p}^2(1 + \cos\theta_p)] - \gamma_{GL}[\pi {R_p}^2 \sin^2\theta_p] - \gamma_{LP}[4\pi {R_p}^2] \quad (19)$$

Combining eqn (17) and (19), we obtain:

$$\delta E^- = -\gamma_{GL}\pi {R_p}^2[1 - \cos\theta_p]^2 \quad (20)$$

This expression is effectively always negative whatever the value of the contact angle θ_p.

Expression of δE

The difference of interfacial energy between configurations (i) and (ii) is now simply obtained by replacing expressions (16) and (20) into eqn (2):

$$\delta E = \delta E^+ + \delta E^- = \gamma_{GL}\pi {R_p}^2\left[\frac{1}{\phi}\left(1 - \frac{\cos\theta_w}{\cos\theta_w^*}\right) - (1 - \cos\theta_p)^2\right] \quad (21)$$

This function is always negative at the beginning when $\theta_w^* = \theta_w$. The minimization of interfacial energy therefore induces the integration of new particles to the interface through a decrease of the apparent contact angle θ_w^* until it reaches a limit value θ_l corresponding to $\delta E = 0$:

$$\cos(\theta_l) = F(\theta_p, \theta_w) = \frac{\cos(\theta_w)}{1 - \phi(1 - \cos(\theta_p))^2}. \quad (22)$$

From then, next particles met by the meniscus enter the liquid phase (regime 3). However, since eqn (4) has a solution only if $F(\theta_p, \theta_w) \leq 1$, that is to say:

$$\theta_p \leq \theta_c = a\cos\left[1 - \sqrt{\frac{1 - \cos(\theta_w)}{\phi}}\right], \quad (23)$$

the contact angle will decrease down to 0 when $\theta_p \geq \theta_c$ (regime 2). Then, the interface can only expand ahead of the meniscus through the development of a liquid film which recovers the walls.

Appendix B: expansion of the interface through the deposition of a liquid film ahead of the meniscus (regime 2)

In this section, we will determine whether the expansion of the air–liquid interface ahead of the meniscus for the integration of new particles is energetically favorable. We therefore have to compare "configuration (a)" where the particle is immersed in the liquid phase and "configuration (b)" where it is incorporated into an extended air–liquid interface. The difference of interfacial energy between these two configurations $\delta E' = E^b - E^a$ can be simply calculated through careful comparison of these two states (see Fig. 14):

$$\begin{aligned}\delta E' = &\left[2\pi {R_p}^2(1 - \cos\theta_p)\gamma_{GP} + \pi {R_p}^2\left(\frac{1}{\phi} - \sin^2(\theta_p)\gamma_{GL}\right)\right. \\ &\left. + 2\pi {R_p}^2(1 + \cos\theta_p) + \frac{\pi {R_p}^2}{\phi}\gamma_{LW}\right] - \left[4\pi {R_p}^2\gamma_{LP}\right. \\ &\left. + \frac{\pi {R_p}^2}{\phi}\gamma_{GW}\right] \\ = &\left[2(1 - \cos\theta_p)(\gamma_{GP} - \gamma_{LP}) + \sin^2\theta_p\gamma_{GL}\right] \\ &- \frac{\pi {R_p}^2}{\phi}[\gamma_{GW} - (\gamma_{LW} + \gamma_{GL})] \end{aligned} \quad (24)$$

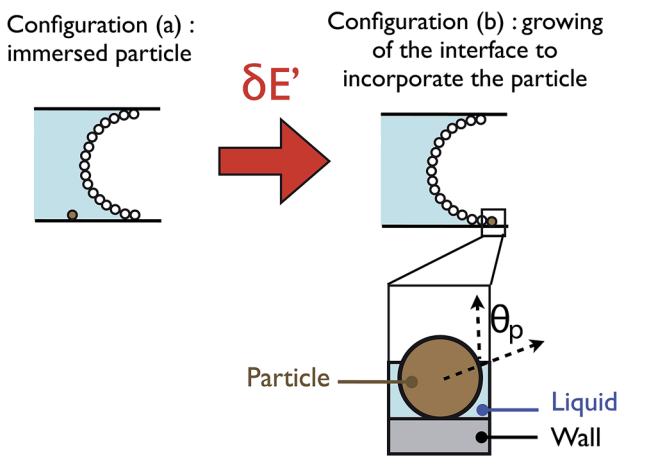

Fig. 14 Expansion of the meniscus.

By combining eqn (6), (17) and (24), one obtains:

$$\delta E' = \gamma_{GL}\pi {R_p}^2\left[-\frac{1}{\phi}S_w - \left(1-\cos\theta_p\right)^2\right] \quad (25)$$

$$= \gamma_{GL}\pi {R_p}^2\left[\frac{1}{\phi}(1-\cos\theta_w) - \left(1-\cos\theta_p\right)^2\right] \quad (26)$$

Note that this expression could have been obtained directly from previous calculation since it is a particular case of eqn (21) when $\theta_w^* = 0$:

$$\delta E' = \delta E(\theta_w^* = 0).$$

Careful examination of eqn (25) and (26) shows that $\delta E'$ is always negative when the walls are perfectly wettable ($S_w > 0$) or when the walls are partially wettable ($S_w < 0$) and $\theta_p \geq \theta_c$, with the expression of θ_c given in eqn (5). Thus in these two cases (corresponding to regime 2) the air–liquid interface covered with particles will expand through the deposition of a liquid film ahead of the meniscus.

Acknowledgements

The authors would like to thank Dr P. Brunet, Dr S. Giordano, Dr M. Gizolme and Dr S. V. Diwakar for their careful reading of the manuscript.

References

1 W. Ramsden, *Proc. R. Soc. London*, 1903, **72**, 156–164.
2 B. Johnson and R. Cooke, *Science*, 1981, **213**, 209–211.
3 B. Binks, *Curr. Opin. Colloid Interface Sci.*, 2002, **7**, 21–41.
4 B. P. Binks and T. S. Horozov, *Angew. Chem.*, 2005, 3722–3725.
5 J. Leja, *Surface chemistry of froth flotation*, Plenum Press, N.Y., 1982.
6 A. Dinsmore, M. Hsu, M. Nikolaides, M. Marquez, A. Bausch and D. Weitz, *Science*, 2002, **298**, 1006–1009.
7 B. Gibbs, S. Kermasha, I. Alli and C. Mulligan, *Int. J. Food. Sci. Nutr.*, 1999, **50**, 213–224.
8 F. Burmeister, W. Badowsky, T. Braun, S. Wieprich, J. Boneberg and P. Leiderer, *Appl. Surf. Sci.*, 1998, **461**, 144–145.
9 A. Subramaniam, M. Ankarian, L. Mahadevan and H. Stone, *Langmuir*, 2006, 10204–10208.
10 D. Vella, P. Aussillous and L. Mahadevan, *Europhys. Lett.*, 2004, **68**, 212–218.
11 D. Vella, H.-Y. Kim, P. Aussillous and L. Mahadevan, *Phys. Rev. Lett.*, 2006, **96**, 178301.
12 P. Aussillous and D. Quéré, *Nature*, 2001, **411**, 924–927.
13 C. Planchette, A.-L. Biance, O. Pitois and E. Lorenceau, *Phys. Fluids*, 2013, **25**, 042104.
14 A. Subramanian, M. Abkarian, L. Mahadevan and H. Stone, *Nature*, 2005, **438**, 930.
15 M. Abkarian, A. Subramaniam, S.-H. Kim, R. Larsen, S.-M. Yang and H. Stone, *Phys. Rev. Lett.*, 2007, **99**, 188301.
16 A. Subramaniam, M. Abkarian and H. Stone, *Nat. Mater.*, 2005, **4**, 553–556.
17 J. Park, Z. Nie, A. Kumachev, A. Abdelrahman, B. Binks, H. Stone and E. Kumacheva, *Angew. Chem., Int. Ed.*, 2009, **48**, 5300–5304.
18 W. Drencklan, *Angew. Chem., Int. Ed.*, 2009, **48**, 5245–5247.
19 M. Lee, V. Prasad and D. Lee, *Langmuir*, 2010, 2227–2230.
20 E. Tumarkin, J. Park, Z. Nie and E. Kumacheva, *Chem. Commun.*, 2011, 12712–12714.
21 F. Bretherton, *J. Fluid Mech.*, 1961, **10**, 166–188.
22 R. Hoffman, *J. Colloid Interface Sci.*, 1975, **50**, 228–241.
23 L. Tanner, *J. Phys. D: Appl. Phys.*, 1979, **12**, 1473.
24 A. Ulman, *Chem. Rev.*, 1996, **96**, 1533–1554.
25 R. Schreiber, *Prog. Surf. Sci.*, 2000, **65**, 151–256.
26 N. Glass, R. Tjeung, P. Chan, L. Yeo and J. Friend, *Biomicrofluidics*, 2011, 036501.
27 Z. Gurard-Levin and M. Mrksich, *Annu. Rev. Anal. Chem.*, 2008, **1**, 767–800.
28 M. Baudoin, P. Brunet, O. Matar and E. Herth, *Appl. Phys. Lett.*, 2012, **100**, 154102.
29 M. Baudoin, Y. Song, P. Manneville and C. Baroud, *Proc. Natl. Acad. Sci. U. S. A.*, 2013, **110**, 859–864.
30 S. Torquato, *Phys. Rev. E: Stat. Phys., Plasmas, Fluids, Relat. Interdiscip. Top.*, 1995, **51**, 3170–3182.
31 P. Pieranski, *Phys. Rev. Lett.*, 1980, **45**, 569–572.
32 W. Irvine, *Nature*, 2010, **468**, 947–950.
33 N. Bowden, A. Tetfort, J. Carbeck and G. Whitesides, *Science*, 1997, **276**, 233–235.
34 M. Nicolson, *Proc. Cambridge Philos. Soc.*, 1949, **45**, 288–295.
35 D. Vella and L. Mahadevan, *Am. J. Phys.*, 2005, **73**, 817–825.
36 M. Nikolaides, A. Bausch, M. Hsu, A. Dinsmore, M. Brenner, C. Gay and D. Weitz, *Nature*, 2002, **420**, 299–301.
37 E. Van Nierop, M. Stinjman and S. Hilgenfeld, *Europhys. Lett.*, 2005, **72**, 671–677.
38 D. Stamous and C. Duschl, *Phys. Rev. E: Stat. Phys., Plasmas, Fluids, Relat. Interdiscip. Top.*, 2000, **62**, 5263–5271.
39 A. Würger, *Phys. Rev. E: Stat., Nonlinear, Soft Matter Phys.*, 2006, **74**, 041402.

Anisotropic Swirling Surface Acoustic Waves from Inverse Filtering for On-Chip Generation of Acoustic Vortices

Antoine Riaud,[1,2] Jean-Louis Thomas,[2] Eric Charron,[2] Adrien Bussonnière,[1] Olivier Bou Matar,[1] and Michael Baudoin[1,*]

[1]*Institut d'Electronique, de Microélectronique et Nanotechnologie (IEMN), LIA LICS, Université Lille 1 and EC Lille, UMR CNRS 8520, 59652 Villeneuve d'Ascq, France*

[2]*Sorbonne Universités, UPMC Univ Paris 06, CNRS, UMR 7588, Institut des NanoSciences de Paris (INSP), F-75005 Paris, France*

(Received 29 April 2015; revised manuscript received 7 July 2015; published 15 September 2015)

From radio-electronics signal analysis to biological sample actuation, surface acoustic waves (SAWs) are involved in a multitude of modern devices. However, only the most simple standing or progressive waves such as plane and focused waves have been explored so far. In this paper, we expand the SAW toolbox with a wave family named "swirling surface acoustic waves" which are the 2D anisotropic analogue of bulk acoustic vortices. Similarly to their 3D counterpart, they appear as concentric structures of bright rings with a phase singularity in their center resulting in a central dark spot. After the rigorous mathematical definition of these waves, we synthesize them experimentally through the inverse filtering technique revisited for surface waves. For this purpose, we design a setup combining arrays of interdigitated transducers and a multichannel electronic that enables one to synthesize any prescribed wave field compatible with the anisotropy of the substrate in a region called the "acoustic scene." This work opens prospects for the design of integrated acoustic vortex generators for on-chip selective acoustic tweezing.

DOI: 10.1103/PhysRevApplied.4.034004

I. INTRODUCTION

Surface acoustic waves (SAWs) have become the cornerstone of microelectromechanical systems. SAWs not only are useful in delay lines and convolution filters [1] but can also monitor temperature variations, strain [2], magnetic fields [3,4], and even chemical or biological composition [5,6]. More recently, the growing field of microfluidics has expressed tremendous interest towards SAWs [7,8], due to their versatility for droplet actuation [9–12], atomization [13,14], jetting [15,16] or mixing [17], but also bubbles, particles, and cell manipulation and sorting [18–21]. Nevertheless, it is remarkable that all these functions rely on the most simple standing or progressive waves such as plane or focused waves.

At the end of the twentieth century, Durnin, Miceli, and Eberly [22] unveiled an exotic family of waves that do not diffract and can self-reconstruct. These waves propagate spinning around a phase singularity where destructive interferences lead to the total cancellation of the beam amplitude (Fig. 1). This concept was subsequently extended beyond optics [22–24] to acoustics [25,26] and even electronic wave functions [27–29]. In all cases, it is shown that vortical waves convey some pseudoangular momentum that exerts a measurable torque on lossy media. The dark core of these waves also plays a key role in trapping objects for optical or acoustic tweezers [30–32]. In the present study, we expand the SAW toolbox with a two-dimensional version of acoustic vortices, called for convenience swirling surface acoustic waves.

In two dimensions, swirling SAWs would appear as a dark spot circled by concentric bright rings of intense vibrations. It is tantamount to cloaking the focus of surface acoustic waves, allowing vigorous actuation of the direct neighborhood of fragile sensors. Furthermore, SAWs easily radiate from a piezoelectric solid to an adjacent liquid, simply by diving the transducer in the fluid. Swirling SAWs could therefore serve as integrated acoustic tweezers [19,20]. This would solve one of the major shortcomings of advanced pointwise acoustic tweezers [32–34], which are complex mechanical assemblies of numerous individual transducers, whereas the present swirling SAW generators are obtained by metal sputtering and photolithography on a single piezoelectric substrate. The radiation of swirling SAWs in adjacent liquid might also be used to monitor cyclonelike flows [35] in cavities by using a nonlinear effect called acoustic streaming. For these reasons, the present paper constitutes a first step towards more advanced acoustofluidic functionalities; the second step—transmission and propagation of swirling SAWs in the liquid phase—also holds several challenges and opportunities. For instance, it was previously observed in 3D optics that isotropic Bessel beams propagating in anisotropic

*Corresponding author.
michael.baudoin@univ-lille1.fr; http://films-lab.univ-lille1.fr

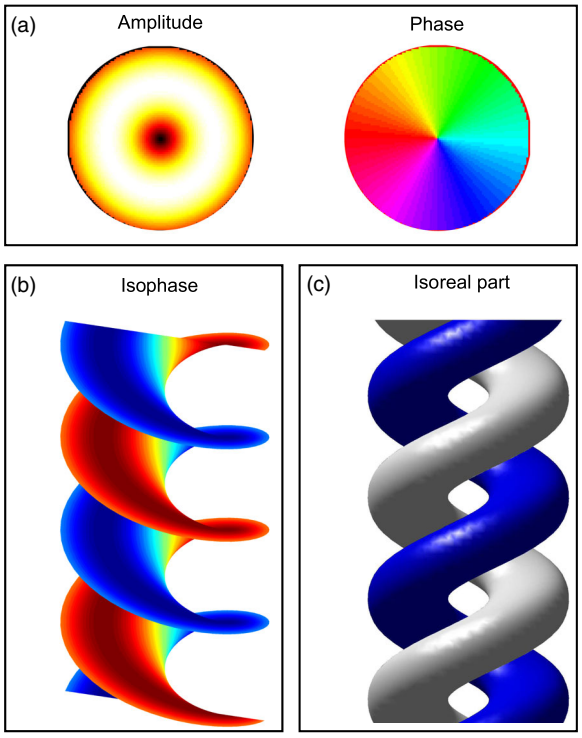

FIG. 1. A particular example of isotropic dark beams: the Bessel beams [Eq. (1) in Sec. II] with $l = 1$, $k_z = 1$, and $k_r = 1$. (a) Beam cross section with a complex phase and amplitude. (b) Isophase surfaces at $l\theta - k_z z = 0$ and $l\theta - k_z z = \pi$ in red and blue, respectively. (c) Isosurface of $\mathrm{Re}(W_l) = -0.3$ and $+0.3$ in blue and white, respectively.

media progressively lose coherence and disintegrate [36–39]. The converse phenomenon (disintegration of an anisotropic Bessel beam propagating in isotropic media) would offer a practical way to confine the acoustic vortex action to a bounded region of space. This subject will be covered in a dedicated report [40], while this one focuses on the definition and synthesis of swirling SAWs.

Since acoustic vortices have been known for a long time, the transition from 3D to 2D waves may appear as an insignificant step and one may wonder why it was not undertaken earlier. It is certainly the case if the wave propagates on a 2D isotropic medium such as perfectly sputtered piezoelectric thin films (AlN or ZnO). However, the best piezoelectric coupling coefficients are obtained when using 2D anisotropic bulk piezoelectric crystals such as $LiNbO_3$, which also happens to be the simplest and cheapest method to generate surface acoustic waves. Twenty years of intense research effort on anisotropic SAW focusing attest to the importance of these practical considerations [41–44]. Hence, in the following, we treat the more general case of an anisotropic medium. This involves two difficulties: First, although SAW synthesis is well mastered for single transducers radiating in specific directions of piezoelectric materials, the design of interdigitated transducer arrays (IDTAs) surrounding a control area is still challenging. Indeed, anisotropy considerably complicates the SAW propagation, leading to a direction-dependent wave velocity, coupling coefficient, and beam-stirring angle (noncollinear wave and energy vectors). Thanks to recent mathematical developments [45–48], SAW far-field propagation is better handled nowadays. Nevertheless, these methods require an accurate depiction of the target field in order to design the generator. The second difficulty is then to define exactly what a swirling SAW is, especially in an anisotropic medium. Since these waves are the fragile result of destructive interference, extreme care must be taken in computing their propagation.

In the present study, we use an adaptive field synthesis method in order to tackle the first issue. For this purpose, a sample of piezoelectric material is covered with a circular array of 32 independent transducers actuated by a programmable electronic. Then, its vibrations are monitored by a Michelson interferometer. The exact input is computed by an advanced calibration procedure called inverse filtering [26,32,49].

Getting rid of the issue of emitter design, we efficiently focus on the definition of swirling surface acoustic waves. Our theoretical work is essentially guided by Laude, Jerez-Hanckes, and Ballandras [48], who unveil and synthesize a zero-order anisotropic Bessel function. In a different context (multipole expansion of electromagnetic waves for numerical computation), Piller and Martin propose a comprehensive extension of Bessel functions to anisotropic media [50]. Our theoretical investigation, described in the first part of the paper, uses the concepts of slowness surface and angular spectrum to fill the gap between Piller and Martin's mathematical expression and surface acoustic waves. The next part of the paper describes our experimental setup, from the transducer design to the SAW measurements. The third part explains how we compute the IDTA signals in order to synthesize swirling SAWs. It provides the key steps of the inverse filtering method adapted to the propagation of surface acoustic waves. Finally, a fourth section exhibits some experimental swirling surface acoustic waves.

II. DEFINITION OF AN ANISOTROPIC BESSEL FUNCTION

A classical solution to the wave equation in isotropic medium is known as the Bessel beam:

$$W_l e^{-i\omega t} = J_l(k_r r) e^{il\theta + ik_z z - i\omega t} = W_l^0 e^{ik_z z - i\omega t}. \quad (1)$$

In this equation, r, θ, z, t, l, W_l, J_l, k_r, k_z, ω, and W_l^0 stand, respectively, for the axisymmetric coordinates, the time, the topological order, the complex wave-field value, the lth-order Bessel function, the radial and axial parts of wave vector, the angular frequency, and the isotropic swirling surface acoustic wave complex value.

The slowness surface and angular spectrum [51] constitute the basic blocks for building anisotropic wave fields. The main idea of these tools is to reduce the problem to a superposition of plane waves. For each single direction and frequency, we solve the 1D propagation equation, which reduces the partial differential equation to a set of ordinary differential equations, whose integration is straightforward. Hence, we first briefly review these concepts and then use them to derive a general 3D anisotropic Bessel beam. We eventually introduce the anisotropic swirling wave as a special case of an anisotropic vortex.

In the following, we work at a given frequency and omit the term $e^{-i\omega t}$ for clarity. In isotropic materials such as water, the wave speed of sound or light is independent of the direction of propagation. Consequently, the magnitude of the wave vector $k = 2\pi/\lambda$ is also a constant, and its locus versus the direction of propagation is a sphere called the slowness surface. Conversely, in the case of an anisotropic material, the wave speed depends on the direction, and so does the wave vector. In the reciprocal space of a 3D medium, we call Φ the azimuth and κ_z the altitude in cylindrical coordinates, so the wave vector reads $\boldsymbol{k}(\phi, \kappa_z)$. The locus of this wave vector, still called the slowness surface, then results in nonspherical shapes depending on the anisotropy of the material [52]. Bessel beams propagate along a specific axis $\boldsymbol{z}$. Consequently, discussions on the surface slowness often refer to $k_r(\phi, \kappa_z)$, the projection of $\mathbf{k}$ on the plane normal to the propagation axis. The axial and radial components of the wave vector k_z and k_r, respectively, are linked by the directionwise dispersion relation:

$$k_z(\phi, \kappa_z)^2 + k_r(\phi, \kappa_z)^2 = \frac{\omega^2}{c(\phi, \kappa_z)^2}. \tag{2}$$

In Eq. (2), we write the coordinates in the reciprocal space κ_i to distinguish them from k_i, which refer to the dispersion relation of the wave and are given physical quantities. For instance, κ_z can take any value, whereas k_z is defined only in a closed interval ($k_z \in [-\omega/c, +\omega/c]$ for an isotropic medium).

The angular spectrum is a multidimensional generalization of the Fourier transform. Since Fourier's pioneering work, it is known that any field can be resolved into a sum of sinusoidal functions. The angular spectrum is a recursive application of the Fourier transform over all the dimensions of the medium:

$$f(x, y, z) = \int_{-\infty}^{+\infty}\int_{-\infty}^{+\infty}\int_{-\infty}^{+\infty} F(\kappa_x, \kappa_y, \kappa_z) e^{i\kappa_x x} d\kappa_x e^{i\kappa_y y} \times d\kappa_y e^{i\kappa_z z} d\kappa_z. \tag{3}$$

We can rearrange the terms in the exponential in order to get $\exp[i(\kappa_x x + \kappa_y y + \kappa_z z)]$ such that Eq. (3) can be interpreted as a sum of plane waves. This means that any physical field in the medium at a given frequency can be seen as a combination of plane waves and therefore must satisfy the dispersion relation or, equivalently, lie on the slowness surface. In this regard, the slowness surface provides a frame for the wave landscape, and choosing the angular spectrum $F(\kappa_x, \kappa_y, \kappa_z)$ amounts to applying the color (complex phase and amplitude) on this frame.

If we express the previous angular spectrum not in Cartesian coordinates but in cylindrical ones, we get

$$f(r, \theta, z) = \int_{-\infty}^{+\infty}\int_{-\pi}^{+\pi}\int_{0}^{+\infty} F(\kappa_r, \phi, \kappa_z) e^{i\kappa_r r\cos(\phi-\theta)} \kappa_r d\kappa_r \times d\phi e^{i\kappa_z z} d\kappa_z. \tag{4}$$

In this expression, the variables κ_r, ϕ, and κ_z refer to the spectral domain, whereas r, θ, and z belong to the spatial one. In order to satisfy the dispersion relation, we know that F must vanish anywhere except on the slowness surface, so $F(\kappa_r, \phi, \kappa_z) = h(\phi, \kappa_z)\delta[\kappa_r - k_r(\phi, \kappa_z)]$, with k_r the magnitude of the wave vector in the (x, y) plane and h an arbitrary function of ϕ and κ_z. This reduces the set of waves that can be created in the medium:

$$f(r, \theta, z) = \int_{-\infty}^{+\infty}\int_{-\pi}^{+\pi} h(\phi, \kappa_z) e^{ik_r(\phi,\kappa_z) r\cos(\phi-\theta)} \times k_r(\phi, \kappa_z) d\phi e^{i\kappa_z z} d\kappa_z. \tag{5}$$

At a given κ_z, the integral in Eq. (5) is the product of two terms: The first one $e^{ik_r(\phi,\kappa_z) r\cos(\phi-\theta)}$ can be reduced to a sum of plane waves thanks to Jacobi-Anger expansion, while the second one hk_r provides the color of each of these plane waves.

We construct anisotropic Bessel functions by splitting the wave angular spectrum in a κ_z-independent part and extracting its coefficients. Since ϕ is the azimuth, it is a periodic function and we can expand hk_r in Fourier series: $hk_r = \sum_{-\infty}^{+\infty} a_l(\kappa_z) e^{il\phi}$. We then get

$$f(r, \theta, z) = \int_{-\infty}^{+\infty} \sum_{l=-\infty}^{+\infty} a_l(\kappa_z) e^{i\kappa_z z} \times \int_{-\pi}^{+\pi} e^{il\phi + ik_r(\phi,\kappa_z) r\cos(\phi-\theta)} d\phi d\kappa_z. \tag{6}$$

As mentioned earlier, the integral can be interpreted as a sum over all the κ_z of some elementary functions. In these functions, κ_z appears as a parameter instead of a variable.

In order to highlight what in this expansion may be reminiscent of a Bessel, we need to write the integral expression of the Bessel function:

$$J_l(x) = \frac{1}{2\pi}\int_{-\pi}^{+\pi} e^{il\eta - ix\sin(\eta)} d\eta. \tag{7}$$

A trivial change of variable $\eta = \phi - \theta - \pi/2$ yields

$$J_l(x) = \frac{1}{2\pi i^l}\int_{-\pi}^{+\pi} e^{il(\phi-\theta)+ix\cos(\phi-\theta)}d\phi. \quad (8)$$

We combine Eqs. (1) and (8) to get the isotropic swirling SAW:

$$W_l^0(r,\theta) = \frac{1}{2\pi i^l}\int_{-\pi}^{+\pi} e^{il\phi+ik_r r\cos(\phi-\theta)}d\phi. \quad (9)$$

By analogy with the isotropic equation, we define an anisotropic swirling wave with a given $\kappa_z = k_z$ as

$$\mathcal{W}_l^0(r,\theta) = \frac{1}{2\pi i^l}\int_{-\pi}^{+\pi} e^{il\phi+ik_r(\phi,k_z)r\cos(\phi-\theta)}d\phi. \quad (10)$$

SAWs appear as a specialization of Eq. (10) to waves that propagate only along the substrate surface, leading to $k_z = 0$. Interestingly, the beam in Eq. (10) shares a common mathematical expression with the electromagnetic multipole used by Piller and Martin [50] for solving anisotropic scattering problems, which augurs that such an anisotropic Bessel beam might be extremely widespread in nature.

Incidentally, any wave in an anisotropic medium can be written as a combination of anisotropic Bessel beams $\mathcal{W}_l = \mathcal{W}_l^0 e^{i\kappa_z z}$:

$$f(r,\theta,z) = \int_{-\infty}^{+\infty}\sum_{l=-\infty}^{+\infty} a_l(\kappa_z)2\pi i^l \mathcal{W}_l^0(r,\theta,\kappa_z)e^{i\kappa_z z}d\kappa_z. \quad (11)$$

In the rest of the paper, we use inverse filtering to generate anisotropic swirling SAW $\mathcal{W}_l^0$ on the surface of an anisotropic piezoelectric crystal.

III. EXPERIMENTAL SETUP

The experimental setup is designed to be as versatile as possible, in order to allow generating a wide variety of waves on an area called the acoustic scene. Starting from an X-cut lithium niobate crystal, 32 unidirectional interdigitated transducers (SPUDT IDTs) are deposited on its periphery (see Fig. 2). In order to widen the range of possible acoustic fields, every spot on the scene should be illuminated by all the transducers. This spatial coverage should be as uniform as possible on the acoustic scene. It is achieved by using IDTs with narrow apertures and disposing them remotely from the acoustic scene to promote diffraction. Furthermore, since any wave can be described as a combination of plane waves, it is essential to generate waves from a wide span of directions. Hence, the quality of the wave-field synthesis critically depends on the span of plane waves provided by the source array in terms of the incident angle, which is the angular spectrum coverage. The best way to achieve such optimal coverage is therefore

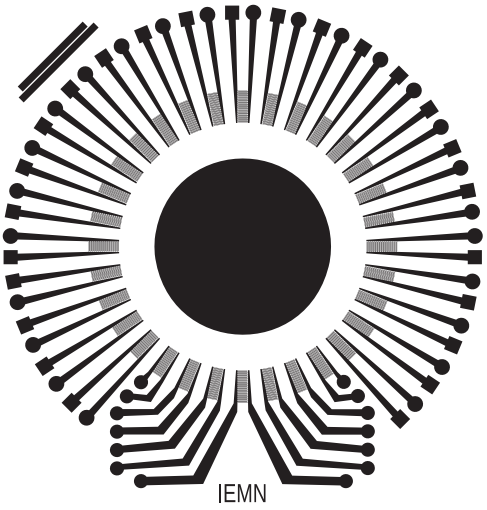

FIG. 2. Interdigitated transducer array used for generating the surface acoustic waves. The central black disk (25-mm diameter) is a gold layer acting as a mirror for interferometric measurements and materializes the maximum extent of the acoustic scene. Vector format image (available online) is used to visualize the fine structure of the electrodes.

to gather many sources from all directions and dispose them radially around a target spot which will be the acoustic scene. These notions of optimal coverage are detailed further in the next section and in the Appendix.

In order to measure the wave field on the acoustic scene, we place the sample under the motorized arm of a polarized Michelson interferometer (Fig. 3). The poor reflection coefficient of lithium niobate is significantly increased by the deposition of a thin layer of gold on the acoustic scene (approximately 200 nm).

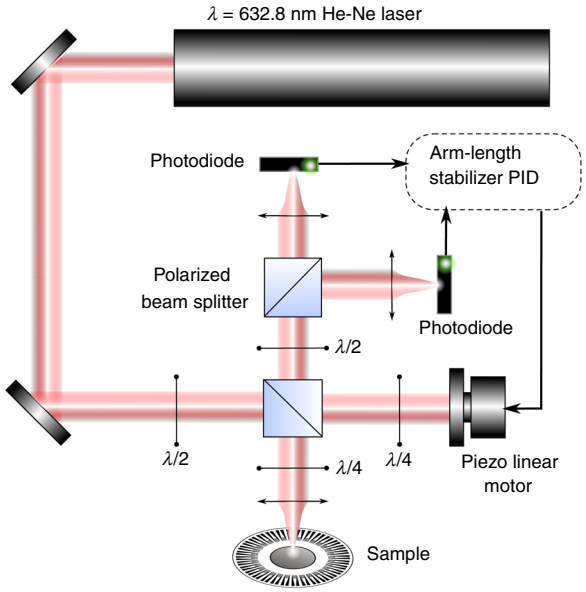

FIG. 3. Polarized Michelson interferometer used for scanning the displacement field associated with surface acoustic waves.

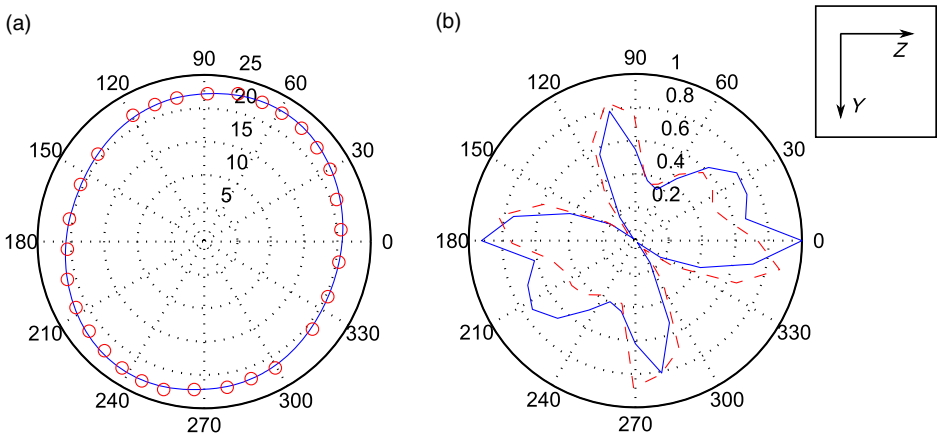

FIG. 4. (a) Theoretical slowness contour (rad/mm, blue solid line) under a very thin gold layer [53] versus the experimentally measured one (red circles). (b) Normalized SAW vertical displacement magnitude at the center of the substrate (theoretical, blue solid line; experimental, red dashed line). The max displacement magnitude is 1.8 nm. Inset: Crystallographic axes.

During the design of the IDTs, special care is given to the anisotropy of the lithium niobate substrate. Indeed, IDTs are high-quality spatiotemporal resonant elements with a spatial period equal to the wavelength. Any deviation from the narrow resonant bandwidth results in a very significant loss of efficiency [1]. We plot in Fig. 4(a) the slowness contour of lithium niobate measured on the gold layer at the working frequency of 12 MHz and compare it to theoretical predictions [53]. The two directions with the lowest SAW magnitude are missing in the experimental data set. The vertical wave motion at the center of substrate is recorded experimentally for each transducer and plotted in Fig. 4(b). The butterfly pattern unambiguously reflects the substrate anisotropy. It is the combination of piezoelectric coupling and beam-stirring effects and can be computed using the Green functions introduced thereafter.

The knowledge of the dispersion relation provides the wave field radiated by a single point source [42,48]:

$$G(r,\theta) \simeq A a(\bar{\phi}) \frac{\exp\{-i\omega r h(\bar{\phi}) - i\frac{\pi}{4}\mathrm{sgn}[h''(\bar{\phi})]\}}{\sqrt{\omega r |h''(\bar{\phi})|}} \qquad (12)$$

with $a(\phi)$ the coupling coefficient between the field to measure and the electrical potential (obtained when solving the SAW equations [53,54]), $\bar{\phi}(\phi)$ the beam-stirring angle, $h(\phi) = \cos(\phi - \theta)k(\phi)/\omega(\phi)$, and $h'' = d^2h[\bar{\phi}(\phi)]/d\phi^2$ related to the focusing factor. The beam-stirring angle is the solution of $h'(\bar{\phi}) = 0$.

Thanks to the superposition principle, we can use the Green function in Eq. (12) to compute the acoustic field radiated by our emitter arrays. The predictions are compared to experiments in Fig. 5. Anisotropy strongly affects the SAW propagation, as we can observe beam widening [(a),(b)], focusing [(c),(d)], and stirring [(e),(f)] depending on the beam direction. Despite a general good agreement between numerical and experimental results, this 2D Green function approach also exhibits some intrinsic limitations. For instance, the lobes on the SAW beam in Fig. 5(b)—confirmed by Fig. 4(b)—are not predicted theoretically. Given the important assumptions of 2D half-space, we believe the suspicious SAW is actually a leaky SAW, and it

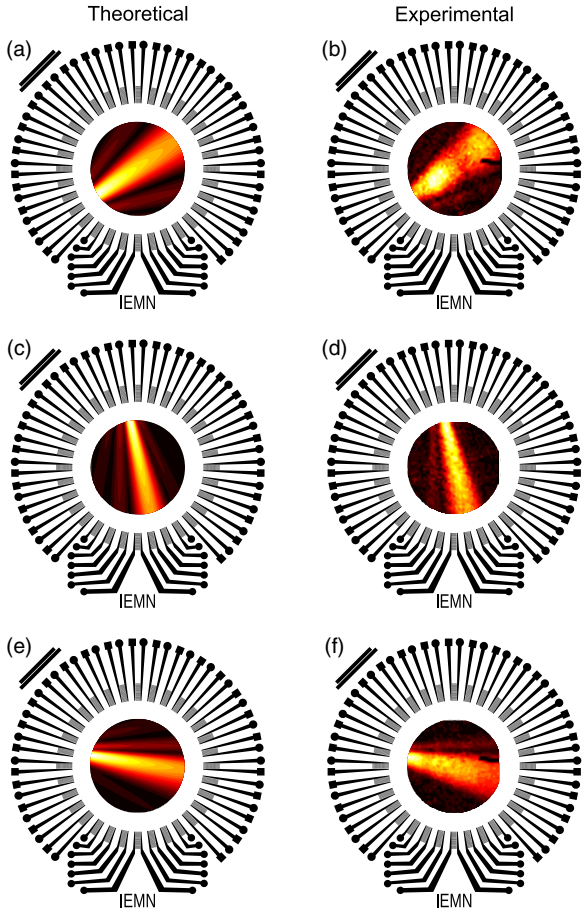

FIG. 5. Influence of anisotropy on the propagation of SAWs generated by single electrodes. (a), (c), (e) Theoretical predictions; (b), (d), (f) experimental measurements. (a), (b) Beam widening; (c), (d) beam focusing; (e), (f) beam stirring. Color represents the beam relative intensity over the substrate and is not indicative of the ratio of intensity between two different transducers.

generates a bulk acoustic wave which bounces between the two faces of the substrate. All these issues of the anisotropic piezoelectric coupling coefficient, beam stirring, and power lobes are significantly alleviated by inverse filtering.

A wide-band high-power multichannel field-programmable gate array (FPGA) (Lecoeur Electronics) powers the 32 emitters with tailored numerical input. The input is specific to each desired wave field and designed through the inverse filtering method.

IV. INVERSE FILTERING THEORY

Inverse filtering [49] is a very general technique for analyzing or synthesizing complex signals that propagate through arbitrary linear medium. This method is especially suited for prototyping, because, given a set of independent programmable sources, it finds the optimal input signal to get a target wave field. When used for this purpose, it is similar to computer-generated holography in optics [55].

The method proceeds in four distinct stages (see Fig. 6): (i) calibration of the transducers, (ii),(iii) computation of the optimal input, and (iv) actuation of the sound sources according to the optimal input.

In the current system, we use a set of 32 emitters and an arbitrary number of control points evenly distributed on the acoustic scene. Their density is governed by the Shanon principle: The distance between two points should not exceed $\lambda/2$. In our acquisition, we use a step of $\lambda/10 = 30\ \mu$m. Moving the arm of the interferometer, we are able to reach individually each of these measurement points. If we call e_i the temporal input of emitter i and s_j the temporal output of control point j located on $\{x_j, y_j\}$, we have for any linear medium

$$s_j = \sum_i h_{ij} * \ e_i, \tag{13}$$

where $*$ refers to the convolution product and h_{ij} is the time response at control point j to an impulse input at emitter e_i. In the spectral domain, $H_{ij} = \mathcal{F}(h_{ij})$ is the Fourier transform of the transfer function at control point j of emitter i and includes the propagation of the wave in the medium. Using the matrix formalism, things get even simpler:

$$|\boldsymbol{S}\rangle = \boldsymbol{H}|\boldsymbol{E}\rangle. \tag{14}$$

In case the transfer matrix is square and well conditioned, it can be inverted to determine the optimal input $|\boldsymbol{E}\rangle$ from a desired output $|\boldsymbol{S}\rangle$. However, the number of independent sources and control points is not necessarily the same, so $\boldsymbol{H}$ is generally not square and often ill conditioned. In the Appendix, we explain the reasons for this ill conditioning from the perspective of the angular spectrum and provide guidelines to minimize it. Although inverse filtering was previously shown to be among the most accurate ones for generating acoustic vortices in 3D isotropic media [26], it was never used for 2D anisotropic media. In previous configurations, the target field is a surface and has a smaller dimensionality (2D) than the propagative medium (3D), whereas the current setup enforces a target field of the same dimensionality as the propagative medium (both 2D). Hence, in the current experiment, the knowledge of the target field explicitly sets an angular spectrum for the propagation medium. However, the wave field in the same medium must fulfill the dispersion relation. Hence, the impulse response matrix is zero everywhere outside the slowness surface. In practice, however, small amplitude noise will always fill these nonpropagative regions. If the target field contains any point outside the slowness surface, the inversion operator would be mistaken as it would rely on the measurement noise to achieve an optimal signal synthesis. Hence, it is essential to define the target field along the slowness curve and resample the impulse

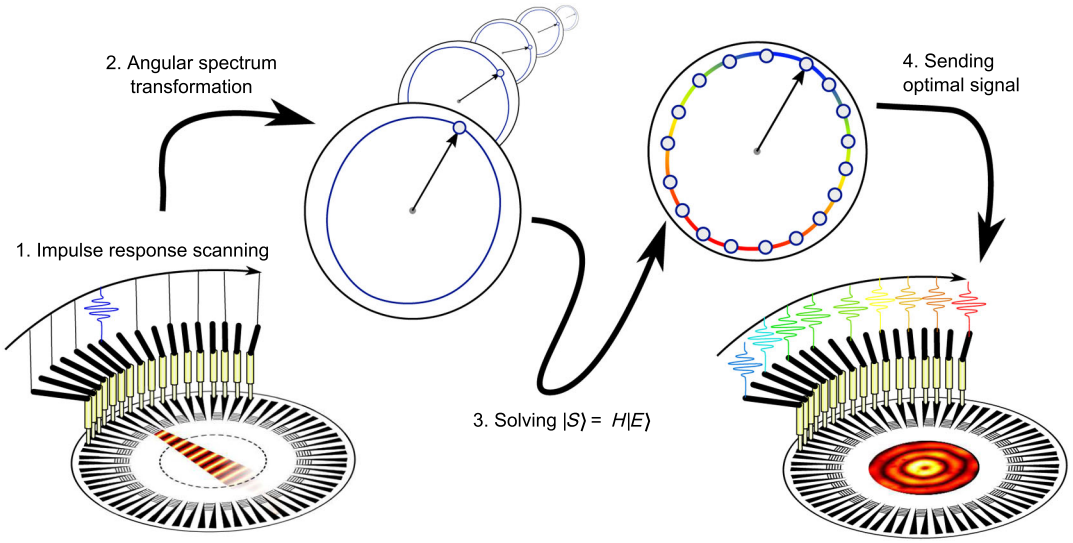

FIG. 6. Inverse filtering flowchart. Inverse filtering happens in four steps. (i) Recording of the spatial impulse response (H matrix) for all transducers. (ii) Transformation of the H matrix from a spatial to spectral domain, where the response is sharper. (iii) Computation of the optimal input $|\boldsymbol{E}\rangle$ for a desired output $|\boldsymbol{S}\rangle$ by pseudoinversion of the matrix $\boldsymbol{H}$. (iv) Generation of the signal from optimal input $|\boldsymbol{E}\rangle$.

response matrix in the same subset of the reciprocal space. We call this method spectral inverse filtering.

As soon as the value of $|\boldsymbol{E}\rangle$ has been computed, the time-dependent input is obtained by inverse Fourier transform and sent to the FPGA amplifier to generate the wave field.

V. EXPERIMENTAL RESULTS

Bessel beams draw large interest for three main reasons: They do not diffract [22], they carry a pseudo-orbital momentum [23,56,57], and they exhibit a dark core (for nonzero order) [32,33]. In addition to these reasons, the zero-order Bessel beam is the optimal beam focusing for a given aperture [42]. In the following section, we start by synthesizing a focused surface acoustic wave $\mathcal{W}_0^0$ and then some simple first-order swirling SAW $\mathcal{W}_1^0$. We seize this opportunity to show the phase singularity and the associated dark spot. The size of the dark spot can easily be tuned, simply by changing the topological charge l, which is done in the third example with seventh-order swirling SAWs.

The zero-order focused $\mathcal{W}_0^0$ Bessel wave phase and amplitude are traced in Fig. 7. It appears that theoretical fields and experimental ones are quite similar. In practice, we have to limit the voltage amplitude of our instrument to about 10% in order to get a linear response of the interferometer (the upper bond is about 40 nm). For high actuation power, we estimate the displacement amplitude based on the second bright ring. When setting the voltage to about 50%, we achieve a displacement amplitude of nearly 180 nm.

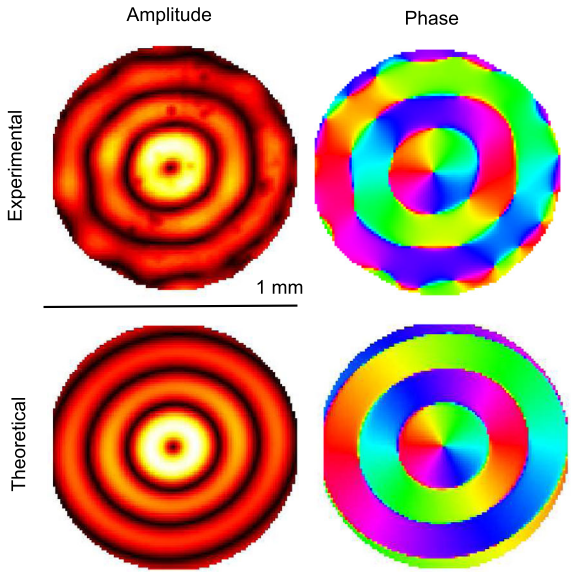

FIG. 8. Experimental and theoretically predicted first-order $\mathcal{W}_1^0$ Bessel wave phase and amplitude. The maximum experimental displacement is 36 nm.

Figure 8 represents the first-order dark beam $\mathcal{W}_1^0$ phase and amplitude. A dark core of zero amplitude with a diameter of 50 μm is clearly visible at the center of the vortex and matches with a phase singularity. This area is contrasted by very bright concentric rings. Despite some blur in the experimental measurements, a good matching between theoretical and experimental vortices is achieved on both the shape and phase.

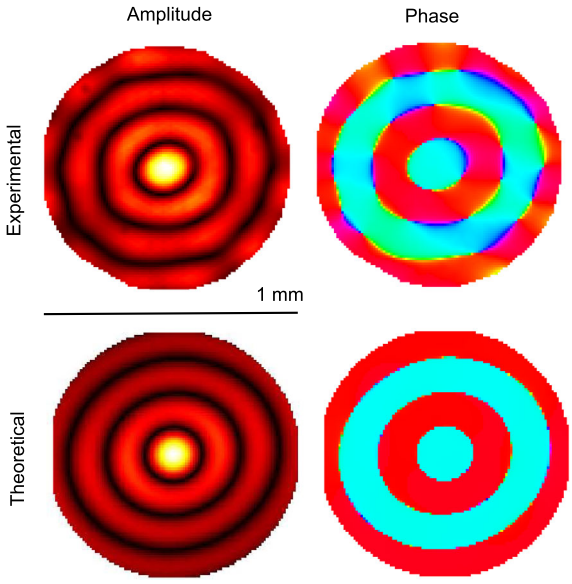

FIG. 7. Experimental and theoretically predicted zero-order focused $\mathcal{W}_0^0$ Bessel wave phase and amplitude. The maximum experimental displacement is 40 nm.

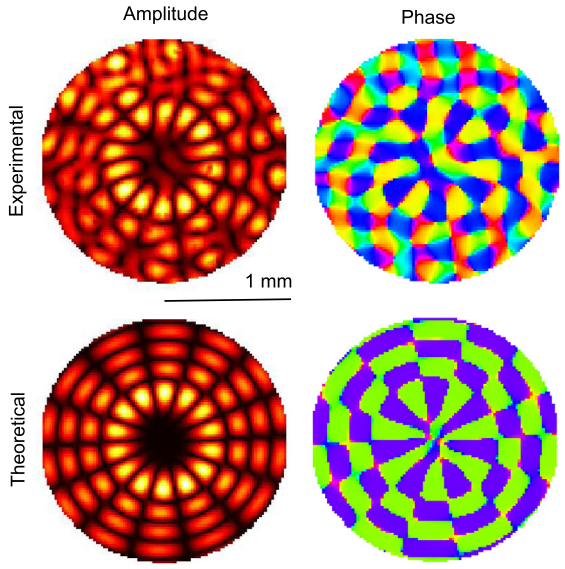

FIG. 9. Experimental and theoretical predictions of the combination of two seventh-order vortices $\mathcal{W}_{\pm 7}^0$ of opposite charge. The maximum experimental displacement is 25 nm.

Swirling SAWs might be useful as integrated transducers for acoustic tweezers or micropumps. Tuning the topological order is essential to these applications for two reasons: It enlarges the first bright ring of the vortex [Olver formula [58] in Eq. (15)], and it increases the pseudoangular momentum of the wave [56]. The second effect itself generates acoustic streaming with an azimuthal flow velocity proportional to the topological charge [35,57]:

$$j'_{l,1} = l(1 + 0.809 \times l^{-2/3}) + O(l^{-7/3}). \qquad (15)$$

In this last example, we suggest a way to increase the ring radius while maintaining zero azimuthal streaming and keep working at the resonance frequency of the electrodes. When two isotropic vortices of opposite charge are combined, they result in a circular stationary wave pattern. In the present case, we sum two seventh-order contrarotating acoustic vortices $\mathcal{W}^0_7 + \mathcal{W}^0_{-7}$. The resulting field, shown in Fig. 9, exhibits a dark core with a diameter of about 500 μm circled by a crown made of 14 extrema of amplitude.

VI. CONCLUSION

In this report, we propose an anisotropic SAW version of acoustic vortices, labeled swirling surface acoustic waves. This implies solving two difficulties: First, the generator has to be designed to accommodate anisotropic propagation, and second, we need to define accurately what are swirling SAWs. The first problem is alleviated using a programmable array of transducers controlled by a two-dimensional spectral inverse filter, while the solution of the second problem confirms earlier theoretical predictions. We synthesize swirling SAWs of different topological charges and large magnitude of displacement. This successful generation provides a pathway for integrated acoustic vortex generators on anisotropic substrates. Furthermore, since these beams are expected to radiate in any adjacent fluid, photolithography fabricated swirling SAW transducers constitute a step towards a credible alternative to the current complicated acoustic tweezer devices made of mechanical assemblies of individual transducers. Beyond the specificities of acoustics, Bessel functions are very widespread in nature, and anisotropic Bessels may offer analytical solutions for a broad class of linear anisotropic problems.

ACKNOWLEDGMENTS

The authors thank Silbe Majrab, who developed and constructed the piezoregulator of the interferometer, and Rémi Marchal, who shared with us precious advice on the art of Michelson interferometry. This work is supported by ANR Project No. ANR-12-BS09-0021-01 and ANR-12-BS09-0021-02, and Région Nord Pas de Calais.

APPENDIX: OPTIMAL CONDITIONING OF INVERSE FILTERING

Inverse filtering is a very versatile method to synthesize an optimal target field from a given number of transducers. As stated in Sec. IV, the method is not exempt from poor conditioning, which would result in large errors in the synthesized field, but some guidelines can significantly improve the quality of the field synthesis. The poor conditioning of inverse filtering has two roots: (i) spectral outliers and (ii) redundant sources.

1. Spectral outliers

At a given frequency, the wave field must fulfill the dispersion relation, which is to have its angular spectrum lying on its slowness surface. When the acoustic scene is a surface (in 2D) or a volume (in 3D), this condition exactly happens. However, experimentally, there is always some noise introduced in the impulse response matrix, making it full rank (any spatial frequency can be created provided there is enough input power). Consequently, a first regularization is to remove the spectral outliers by sampling the target field not on a spatial manifold but on a spectral one and along the slowness surface.

Nevertheless, if the acoustic scene is a line (in 2D) or a surface (in 3D) as in previous implementations [26,49], the spectral condition is relaxed. Indeed, the angular spectrum of the target field is only partially known due to the projection of the field along the line or the surface. In 3D, for instance, if the synthesis happens on an $\{x, y\}$ plane, the system knows the values of k_x and k_y but ignores the ones of k_z, which can then be freely chosen as long as the dispersion relation is fulfilled. In an isotropic medium, this results in $k_z = \pm\sqrt{\omega^2/c^2 - {k_x}^2 - {k_y}^2}$. Note that, in any case, $\omega^2/c^2 > {k_x}^2 + {k_y}^2$, which is the diffraction limit. Hence, spectral outliers in this synthesis appear beyond the $\lambda/2$ boundary.

A third example of spectral outliers is provided by piezoelectric generation on monocrystals. These substrates often exhibit a direction where the piezoelectric coupling coefficient sharply drops to zero. When this happens, no acoustic waves can be generated from this orientation, and the associated angular spectrum coverage is barely zero. Once again, sampling the signal in the spectral space and excluding the zero-coupling directions avoids these outliers and allows an accurate synthesis.

2. Redundant sources

In practice, many transducers are used to ensure an efficient spectral coverage. Above this threshold, adding even more actuators may result in poorer synthesis quality [49]. Indeed, from the inverse filtering perspective, sound sources act like a family of vectors to combine in order to build a target field. When two sources are redundant, the

inversion operator can take any linear combination of them, and this indetermination is solved by comparing the measurement noise associated with each source. A smart way is therefore to regularize the reduced impulse response matrix obtained after removing the spectral outliers. The regularization can be achieved by a singular value decomposition. If two transducers are redundant, they split in a singular value very close to zero and another one much more regular. By knowing the signal-to-noise ratio, it is then possible to discriminate which singular values originate from noise and which do not [49].

[1] Daniel Royer and Eugène Dieulesaint, *Elastic Waves in Solids 2, Generation, Acousto-Optic Interactions, Applications* (Springer, New York, 1996), Chap. 2.1.3.

[2] A. Pohl and F. Seifert, in *Proceedings of the Instrumentation and Measurement Technology Conference* (IEEE, New York, 1996), Vol. 2, pp. 1465–1468.

[3] Odilon D. D. Couto, R. Hey, and P. V. Santos, Spin dynamics in (110) GaAs quantum wells under surface acoustic waves, Phys. Rev. B **78**, 153305 (2008).

[4] Jörg B. Kinzel, Daniel Rudolph, Max Bichler, Gerhard Abstreiter, Jonathan J. Finley, Gregor Koblmüller, Achim Wixforth, and Hubert J. Krenner, Directional and dynamic modulation of the optical emission of an individual GaAs nanowire using surface acoustic waves, Nano Lett. **11**, 1512 (2011).

[5] A. Pohl, A review of wireless SAW sensors, IEEE Trans. Ultrason. Ferroelectr. Freq. Control **47**, 317 (2000).

[6] David Stephen Ballantine, *Acoustic Wave Sensors: Theory, Design, and Physico-Chemical Applications* (Academic, New York, 1997).

[7] Trung Dung Luong and Nam Trung Nguyen, Surface acoustic wave driven microfluidics—A review, Micro Nanosyst. **2**, 217 (2010).

[8] Leslie Y. Yeo and James R. Friend, Surface acoustic wave microfluidics, Annu. Rev. Fluid Mech. **46**, 379 (2014).

[9] Thomas Franke, Adam R. Abate, David A. Weitz, and Achim Wixforth, Surface acoustic wave (SAW) directed droplet flow in microfluidics for PDMS devices, Lab Chip **9**, 2625 (2009).

[10] A. Wixforth, C. Strobl, C. Gauer, A. Toegl, J. Scriba, and Z. Guttenberg, Acoustic manipulation of small droplets, Anal. Bioanal. Chem. **379**, 982 (2004).

[11] A. Renaudin, P. Tabourier, V. Zhang, J. C. Camart, and C. Druon, SAW nanopump for handling droplets in view of biological applications, Sens. Actuators, B **113**, 389 (2006).

[12] M. Baudoin, P. Brunet, O. Bou Matar, and E. Herth, Low power sessile droplets actuation via modulated surface acoustic waves, Appl. Phys. Lett. **100**, 154102 (2012).

[13] K. Chono, N. Shimizu, Y. Matsui, J. Kondoh, and S. Shiokawa, Development of novel atomization system based on SAW streaming, Jpn. J. Appl. Phys. **43**, 2987 (2004).

[14] A. Qi, L. Y. Yeo, and J. R. Friend, Interfacial destabilization and atomization driven by surface acoustic waves, Phys. Fluids **20**, 074103 (2008).

[15] S. Shiokawa, Y. Matsui, and T. Ueda, Study of SAW streaming and its application to fluid device, Jpn. J. Appl. Phys. **29**, 137 (1990).

[16] M. K. Tan, J. R. Friend, and L. Y. Yeo, Interfacial Jetting Phenomena Induced by Focused Surface Vibrations, Phys. Rev. Lett. **103**, 024501 (2009).

[17] T. Frommelt, M. Kostur, M. Wenzel-Schäfer, P. Talkner, P. Hänggi, and A. Wixforth, Microfluidic Mixing via Acoustically Driven Chaotic Advection, Phys. Rev. Lett. **100**, 034502 (2008).

[18] Mikkel Settnes and Henrik Bruus, Forces acting on a small particle in an acoustical field in a viscous fluid, Phys. Rev. E **85**, 016327 (2012).

[19] Xiaoyun Ding, Sz-Chin Steven Lin, Brian Kiraly, Hongjun Yue, Sixing Li, I-Kao Chiang, Jinjie Shi, Stephen J. Benkovic, and Tony Jun Huang, On-chip manipulation of single microparticles, cells, and organisms using surface acoustic waves, Proc. Natl. Acad. Sci. U.S.A. **109**, 11105 (2012).

[20] S. B. Q. Tran, P. Marmottant, and P. Thibault, Fast acoustic tweezers for the two-dimensional manipulation of individual particles in microfluidic channels, Appl. Phys. Lett. **101**, 114103 (2012).

[21] Adrien Bussonnière, Yannick Miron, Michaël Baudoin, Olivier Bou Matar, Michel Grandbois, Paul Charette, and Alan Renaudin, Cell detachment and label-free cell sorting using modulated surface acoustic waves (SAWs) in droplet-based microfluidics, Lab Chip **14**, 3556 (2014).

[22] J. Durnin, J. J. Miceli, and J. H. Eberly, Diffraction-Free Beams, Phys. Rev. Lett. **58**, 1499 (1987).

[23] L. Allen, M. W. Beijersbergen, R. J. C. Spreeuw, and J. P. Woerdman, Orbital angular momentum of light and the transformation of Laguerre-Gaussian laser modes, Phys. Rev. A **45**, 8185 (1992).

[24] H. He, M. E. J. Friese, N. R. Heckenberg, and H. Rubinsztein-Dunlop, Direct Observation of Transfer of Angular Momentum to Absorptive Particles from a Laser Beam with a Phase Singularity, Phys. Rev. Lett. **75**, 826 (1995).

[25] B. T. Hefner and P. L. Marston, An acoustical helicoidal wave transducer with applications for the alignment of ultrasonic and underwater systems, J. Acoust. Soc. Am. **106**, 3313 (1999).

[26] R. Marchiano and J.-L. Thomas, Synthesis and analysis of linear and nonlinear acoustical vortices, Phys. Rev. E **71**, 066616 (2005).

[27] Vincenzo Grillo, Gian Carlo Gazzadi, Erfan Mafakheri, Stefano Frabboni, Ebrahim Karimi, and Robert W. Boyd, Holographic Generation of Highly Twisted Electron Beams, Phys. Rev. Lett. **114**, 034801 (2015).

[28] Roeland Juchtmans, Armand Béché, Artem Abakumov, Maria Batuk, and Jo Verbeeck, Using electron vortex beams to determine chirality of crystals in transmission electron microscopy, Phys. Rev. B **91**, 094112 (2015).

[29] V. G. Sala, D. D. Solnyshkov, I. Carusotto, T. Jacqmin, A. Lemaitre, H. Tercas, A. Nalitov, M. Abbarchi, E. Galopin, I. Sagnes, J. Bloch, G. Malpuech, and A. Amo, Spin-Orbit Coupling for Photons and Polaritons in Microstructures, Phys. Rev. X **5**, 011034 (2015).

[30] A. Anhauser, R. Wunenburger, and E. Brasselet, Acoustic Rotational Manipulation Using Orbital Angular Momentum Transfer, Phys. Rev. Lett. **109**, 034301 (2012).

[31] Philip L. Marston, Axial radiation force of a bessel beam on a sphere and direction reversal of the force, J. Acoust. Soc. Am. **120**, 3518 (2006).

[32] Diego Baresch, Jean-Louis Thomas, and Régis Marchiano, Observation of a single-beam gradient force acoustical trap for elastic particles: Acoustical tweezers, arXiv: 1411.1912.

[33] Alon Grinenko, Paul D. Wilcox, Charles R. P. Courtney, and Bruce W. Drinkwater, Proof of principle study of ultrasonic particle manipulation by a circular array device, Proc. R. Soc. A **468**, 3571 (2012).

[34] Charles R. P. Courtney, Bruce W. Drinkwater, Christine E. M. Demore, Sandy Cochran, Alon Grinenko, and Paul D. Wilcox, Dexterous manipulation of microparticles using bessel-function acoustic pressure fields, Appl. Phys. Lett. **102**, 123508 (2013).

[35] Antoine Riaud, Michael Baudoin, Jean-Louis Thomas, and Olivier Bou Matar, Cyclones and attractive streaming generated by acoustical vortices, Phys. Rev. E **90**, 013008 (2014).

[36] G. Cincotti, A. Ciattoni, and C. Palma, Hermite-Gauss beams in uniaxially anisotropic crystals, IEEE J. Quantum Electron. **37**, 1517 (2001).

[37] Dmitriy H. Zusin, Raman Maksimenka, Valerii V. Filippov, Ruslan V. Chulkov, Michel Perdrix, Olivier Gobert, and Alexander S. Grabtchikov, Bessel beam transformation by anisotropic crystals, J. Opt. Soc. Am. A **27**, 1828 (2010).

[38] Tatyana Fadeyeva, Alexander Rubass, Yuriy Egorov, Alexander Volyar, and Jr. Grover Swartzlander, Quadrefringence of optical vortices in a uniaxial crystal, J. Opt. Soc. Am. A **25**, 1634 (2008).

[39] Xiancong Lu and Lixiang Chen, Anisotropic dynamics of optical vortex-beam propagating in biaxial crystals: A numerical method based on asymptotic expansion, Opt. Express **21**, 8493 (2013).

[40] Antoine Riaud, Jean-Louis Thomas, Michaël Baudoin, and Olivier Bou Matar, Taming the degeneration of Bessel beams at anisotropic-isotropic interface: Toward 3D control of confined vortical waves, arXiv:1508.07980.

[41] S. R. Fang, S. Y. Zhang, and Z. F. Lu, SAW focusing by circular-arc interdigital transducers on YZ-LiNbO3, IEEE Trans. Ultrason. Ferroelectr. Freq. Control **36**, 178 (1989).

[42] Vincent Laude, Davy Gerard, Naima Khelfaoui, Carlos F. Jerez-Hanckes, Sarah Benchabane, and Abdelkrim Khelif, Subwavelength focusing of surface acoustic waves generated by an annular interdigital transducer, Appl. Phys. Lett. **92**, 094104 (2008).

[43] Tsung-Tsong Wu, He-Tai Tang, Yung-Yu Chen, and P.-L. Liu, Analysis and design of focused interdigital transducers, IEEE Trans. Ultrason. Ferroelectr. Freq. Control **52**, 1384 (2005).

[44] Subramanian K. R. S. Sankaranarayanan and Venkat R. Bhethanabotla, Design of efficient focused surface acoustic wave devices for potential microfluidic applications, J. Appl. Phys. **103**, 064518 (2008).

[45] R. C. Peach, A general Green function analysis for SAW devices, Proc. IEEE Ultrasonics Symposium **1**, 221 (1995).

[46] V. P. Plessky and T. Thorvaldsson, Periodic Green's functions analysis of SAW and leaky SAW propagation in a periodic system of electrodes on a piezoelectric crystal, IEEE Trans. Ultrason. Ferroelectr. Freq. Control **42**, 280 (1995).

[47] Donghai Qiao, Wen Liu, and P. M. Smith, General Green's functions for SAW device analysis, IEEE Trans. Ultrason. Ferroelectr. Freq. Control **46**, 1242 (1999).

[48] V. Laude, C. F. Jerez-Hanckes, and S. Ballandras, Surface Green's function of a piezoelectric half-space, IEEE Trans. Ultrason. Ferroelectr. Freq. Control **53**, 420 (2006).

[49] Mickaël Tanter, Jean-Louis Thomas, and Mathias Fink, Time reversal and the inverse filter, J. Acoust. Soc. Am. **108**, 223 (2000).

[50] N. B. Piller and O. J. F. Martin, Extension of the generalized multipole technique to anisotropic medias, Opt. Commun. **150**, 9 (1998).

[51] Juha Fagerholm, Ari T. Friberg, Juhani Huttunen, David P. Morgan, and Martti M. Salomaa, Angular-spectrum representation of nondiffracting X waves, Phys. Rev. E **54**, 4347 (1996).

[52] Daniel Royer and Eugène Dieulesaint, *Elastic Waves in Solids 1, Free and Guided Propagation* (Springer, New York, 1996), Chap. 4.2.5.

[53] J. J. Campbell and W. R. Jones, Propagation of surface waves at the boundary between a piezoelectric crystal and a fluid medium, IEEE Trans. Sonics Ultrason. **17**, 71 (1970).

[54] Olivier Bou Matar, Noura Gasmi, Huan Zhou, Marc Goueygou, and Abdelkrim Talbi, Legendre and Laguerre polynomial approach for modeling of wave propagation in layered magneto-electro-elastic media, J. Acoust. Soc. Am. **133**, 1415 (2013).

[55] N. R. Heckenberg, R. McDuff, C. P. Smith, and A. G. White, Generation of optical phase singularities by computer-generated holograms, Opt. Lett. **17**, 221 (1992).

[56] J.-L. Thomas and R. Marchiano, Pseudoangular Momentum and Topological Charge Conservation for Nonlinear Acoustical Vortices, Phys. Rev. Lett. **91**, 244302 (2003).

[57] K. Volke-Sepulveda, A. O. Santillan, and R. R. Boullosa, Transfer of Angular Momentum to Matter from Acoustical Vortices in Free Space, Phys. Rev. Lett. **100**, 024302 (2008).

[58] F. W. J. Olver, A further method for the evaluation of zeros of bessel functions and some new asymptotic expansions for zeros of functions of large order, Math. Proc. Cambridge Philos. Soc. **47**, 699 (1951).